



**University  
of Antwerp**

Faculty of Science

**Shaping up oligonucleotides:  
aptamer-target recognition investigated by native mass  
spectrometry**

Bepaling van de vorm van oligonucleotiden:  
aptameer-ligand binding onderzocht met natieve  
massaspectrometrie

Thesis submitted to obtain the degree of  
**Doctor in Science: Chemistry**  
at the University of Antwerp to defended by  
**Elise Daems**

Promotors:

Prof. Dr. Karolien De Wael (University of Antwerp)

Prof. Dr. Frank Sobott (University of Leeds)

Antwerp, 2021



## Abstract

Aptamers are short, synthetic DNA or RNA molecules that are characterized by a specific 3D conformation, or fold, which enables specific target recognition. Aptamers are promising tools in many application fields from sensing to therapeutics. One of the major challenges in the aptamer field is understanding the relationship between the sequence and what determines the higher-order structure and specific interactions with targets. Therefore, this PhD thesis focuses on the use of different mass spectrometry (MS) based approaches to characterize aptamers and their interactions. Several of these approaches are already widely applied to study other biomolecules, such as proteins, but are still largely unexplored for aptamers and oligonucleotides in general.

A first focus was put on obtaining information on the higher-order structure and conformational stability of aptamers using a combination of MS and with ion mobility (IM) spectrometry. Several fragmentation methods, i.e. collision-induced dissociation/unfolding (CID/U) and electron transfer dissociation (ETD), were evaluated for this purpose after transferring the aptamers to the gas-phase in native conditions, which means that noncovalent interactions are kept intact. Although CID and ETD did not provide valuable insights in the higher-order structure of aptamers, CIU was shown to hold great promise to analyze the conformational dynamics and gas-phase stabilities of aptamers.

Next, the capabilities and limitations of native IM-MS for the analysis of noncovalent interactions, i.e. target binding, of aptamers were demonstrated. The conformational behavior and interactions of cocaine-binding aptamers were studied and it was found that relative binding affinities of aptamers that only differ slightly in sequence and structure can be determined using native MS. Moreover, native IM-MS allowed the detection of small conformational changes upon binding of a target, which were found to be dependent on the binding mode of the aptamer. An adaptive binding mechanism was suggested for flexible aptamers that require more reorganization upon binding.

In the final part of this thesis, the importance of thoroughly characterizing and validating aptamer-target interactions before using them in an application was emphasized. Moreover, the gathered insights were applied in our own development of a proof-of-concept aptamer-based sensor. This was shown by investigating the interactions of ampicillin aptamers which were found to not bind the target they were

selected for in the first place. A multi-analytical approach combining complementary techniques (i.e. isothermal titration calorimetry, native MS and nuclear magnetic resonance spectroscopy) was used for this purpose since no single technique is generally applicable to characterize all aptamers and their interactions and to obtain a comprehensive picture of the aptamer-target interactions. Furthermore, such multi-analytical approach was used to characterize a testosterone-binding aptamer while developing an aptamer-based electrochemiluminescent sensing strategy for this target. This shows the importance of native MS, in combination with other techniques, to thoroughly understand the aptamer-target interactions in the development of a designed application.

## Samenvatting

Aptameren zijn korte, synthetische DNA of RNA moleculen met een specifieke 3D structuur die de binding van specifieke liganden mogelijk maakt. Aptameren zijn veelbelovend voor het gebruik in verschillende toepassingen: van sensoren tot therapie. Een van de voornaamste uitdagingen in de wereld van de aptameren is het begrijpen van het verband tussen de sequentie, de hogere orde structuur en de specifieke interacties met liganden. Daarom focust deze doctoraatsthesis op het gebruik van verschillende massaspectrometrie (MS) gebaseerde methoden om aptameren en hun interacties te karakteriseren. Meerdere van deze methoden worden al gebruikt om andere biomoleculen, zoals proteïnen, te bestuderen, maar zijn nog grotendeels ongebruikt voor aptameren en oligonucleotiden in het algemeen.

Een eerste nadruk werd gelegd op het verkrijgen van informatie over de hogere orde structuur en de conformationale stabiliteit van aptameren door gebruik te maken van MS in combinatie met ionenmobiliteit (IM) spectrometrie. Hiervoor werden verschillende fragmentatietechnieken, meer bepaald *collision-induced dissociation/unfolding* (CID/U) en *electron transfer dissociation* (ETD), gebruikt nadat de aptameren naar de gasfase werden overgebracht in natieve condities. Dit betekent dat niet-covalente interacties intact gehouden werden. Hoewel CID en ETD geen inzichten boden in de hogere orde structuur van aptameren, bleek CIU potentieel te hebben om de conformationele dynamische eigenschappen en de gasfase stabiliteit van aptameren te analyseren.

Vervolgens werden de mogelijkheden en beperkingen van natieve IM-MS voor de analyse van niet-covalente interacties, meer bepaald ligandbinding, van aptameren onderzocht. Het conformationeel gedrag en de interacties van cocaïne-bindende aptameren werd in detail bestudeerd. Relatieve bindingsaffiniteiten van aptameren, die maar subtiele verschillen in sequentie en structuur vertonen, konden bepaald worden. Bovendien kon natieve IM-MS gebruikt worden om kleine conformationale veranderingen van aptameren bij het binden van het ligand te detecteren. Deze veranderingen konden vervolgens gerelateerd worden aan de bindingsmode van het aptameer. Een adaptief bindingsmechanisme werd voorgesteld voor flexibele aptameren die meer reorganisatie ondergaan bij binding van het ligand.

In het laatste deel van de thesis werd het belang van een goede karakterisering en validatie van aptameer-ligand interacties voordat deze gebruikt worden in een

toepassing benadrukt. Bovendien werden de verworven inzichten toegepast in de ontwikkeling van een *proof-of-concept* aptameer-gebaseerde sensor. Uit onderzoek van de interacties van ampicilline aptameren bleek dat deze aptameren niet binden aan het ligand waarvoor ze geselecteerd werden. Dit werd aangetoond door gebruik te maken van een multi-analytische methode die meerdere complementaire technieken combineert (isotherme titratie calorimetrie, natieve MS en nucleaire magnetische resonantie spectroscopie) aangezien geen enkele techniek algemeen toepasbaar is om alle aptameren en hun interacties te karakteriseren en om een volledig beeld te krijgen van de aptameer-ligand interacties. Tenslotte werd een dergelijke multi-analytische aanpak ook gebruikt om een testosteron-bindend aptameer te karakteriseren parallel aan de ontwikkeling van een elektrochemiluminiscentie detectiestrategie voor testosteron. Dit toont het belang aan van natieve MS, in combinatie met andere technieken, bij het begrijpen van de aptameer-ligand interacties in de ontwikkeling van een bepaalde toepassing.

# Table of contents

Abstract	III
Samenvatting	V
Table of contents	VII
List of abbreviations	VIII
<b>Chapter 1</b> Aptamers and native mass spectrometry: a promising combination	11
<b>Chapter 2</b> Mapping the gaps in chemical analysis for the characterization of aptamer-target interactions	37
<b>Chapter 3</b> Mapping the structure and stability of aptamers	63
<b>Chapter 4</b> Dynamic structure and stability of nucleosomes investigated by native ion mobility mass spectrometry and fragmentation approaches	85
<b>Chapter 5</b> Native mass spectrometry for the design and selection of protein bioreceptors for perfluorinated compounds	105
<b>Chapter 6</b> Aptamer-ligand recognition studied by native ion mobility-mass spectrometry	127
<b>Chapter 7</b> Do aptamers always bind? The need for a multifaceted analytical approach when demonstrating binding affinity between aptamer and low molecular weight compounds	149
<b>Chapter 8</b> Proof-of-concept electrochemiluminescent assay for the aptamer-based detection of small molecules	179
<b>Chapter 9</b> Conclusions and outlook	203
Bibliography	209
Acknowledgements	229
Curriculum vitae	233

## List of abbreviations

### A

AMR	Antimicrobial resistance
ATP	Adenosine triphosphate
AuNP	Gold nanoparticle

### B

BLI	Biolayer interferometry
-----	-------------------------

### C

CCS	Collision cross section
CD	Circular dichroism
CENP-A	Centromere protein A
CENP-A <sup>601</sup>	CENP-A nucleosome on the 601 sequence
CENP-A <sup>NAS</sup>	CENP-A nucleosome on the natural $\alpha$ -satellite sequence
CID	Collision-induced dissociation
CIU	Collision-induced unfolding
cyt c	Cytochrome c

### D and $\Delta$

Da	Dalton
DCA	Deoxycholic acid
DIG	Digoxigenin
DNA	Deoxyribonucleic acid
ds	Double-stranded
$\Delta G$	Gibbs free energy variation
$\Delta H$	Enthalpy variation
$\Delta S$	Entropy variation

### E

ECL	Electrochemiluminescence
EDDA	Ethylenediamine diacetate
EDTA	Ethylenediaminetetraacetic acid
EM	Electron microscopy
ESI	Electrospray ionization

**F**

FA	Fluorescence anisotropy
FP	Fluorescence polarization

**H**

H3 <sup>601</sup>	H3 nucleosome on the 601 sequence
H3 <sup>NAS</sup>	H3 nucleosome on the natural $\alpha$ -satellite sequence
Hb	Hemoglobin
HC	Hydrocortisone
hSA	Human serum albumin
HDX	Hydrogen deuterium exchange

**I**

IM	Ion mobility
IMPACT	Ion Mobility Projection Approximation Calculation Tool
ITC	Isothermal titration calorimetry

**K**

K <sub>d</sub>	Dissociation constant
kDa	Kilodalton
kinITC	Kinetic isothermal titration calorimetry

**L**

LAMP	Loop-mediated isothermal amplification
------	--

**M**

m/z	Mass-to-charge
miRNA	Micro ribonucleic acid
MD	Molecular dynamics
MS	Mass spectrometry
MST	Microscale thermophoresis

**N**

NAS	Natural $\alpha$ -satellite
nESI	Nano-electrospray ionization
NGB	Neuroglobin
NMR	Nuclear magnetic resonance

**P**

PCR	Polymerase chain reaction
PEG	Polyethylene glycol
PFAS	Per- and polyfluorinated alkyl substances
PFG	Pulsed-field-gradient
PFOA	Perfluorooctanoic acid
PFOS	Perfluorooctanesulfonic acid

**Q**

QCM	Quartz crystal microbalance
-----	-----------------------------

**R**

RDE	Rotating droplet electrochemistry
RMSD	Root-mean-square deviation
RNA	Ribonucleic acid
rRNA	Ribosomal ribonucleic acid

**S**

SAXS	Small-angle X-ray scattering
SELEX	Systematic evolution of ligands by exponential enrichment
SERS	Surface-enhanced Raman scattering
SFX	Serial femtosecond crystallography
SPR	Surface plasmon resonance
SPRi	Surface plasmon resonance imaging
ss	Single-stranded

**T**

TEAA	Triethylamine acetate
TPrA	Tripropylamine
tRNA	Transfer ribonucleic acid

**V**

VEGF	Vascular endothelial growth factor
------	------------------------------------

**X**

# 11

Aptamers and native mass spectrometry:  
a promising combination



## Abstract

Aptamers are small synthetic oligonucleotides that recognize with high affinity a given target against which they are selected. They were first discovered in the 1990s and have great potential in many application fields, such as sensing and therapeutics. There is, however, still a lack of understanding of aptamer structures and their specific interactions with targets. Few aptamers are well-characterized regarding their structure, stability and interactions (e.g. selectivity and specificity), which hampers their commercialization. Native mass spectrometry (MS), which is still largely unexplored for aptamers and oligonucleotides in general, offers a promising toolbox for the characterization of aptamers. Especially the combination of native MS with ion mobility spectrometry can provide structural insights into the aptamer-target interactions. Thus, all levels of the structure, from primary (sequence) to quaternary structure (complex formation) can be studied using native MS.

## 1.1 Oligonucleotides

Oligonucleotides are an important class of biomolecules and they are essential for all life forms. Two different types of oligonucleotides can be distinguished: deoxyribonucleic acid (DNA) and ribonucleic acid (RNA). DNA is well-known for storing genetic information and RNA plays a key role in the regulation, transcription and translation of this code to proteins.<sup>1</sup> Oligonucleotides are chains of nucleotides that consist of a heterocyclic base, a pentose sugar and a phosphate group. In DNA, two phosphodiester backbones run in opposite directions and these are joined together by base pairing of the heterocyclic bases. In DNA, four different bases are present: adenine and guanine (i.e. the purines) and cytosine and thymine (i.e. the pyrimidines). RNA also contains four different bases, but thymine is replaced by uracil. These nucleobases can form Watson-Crick base pairs: adenine and thymine are joined together by two hydrogen bonds, and cytosine and guanine form a base pair with three hydrogen bonds.

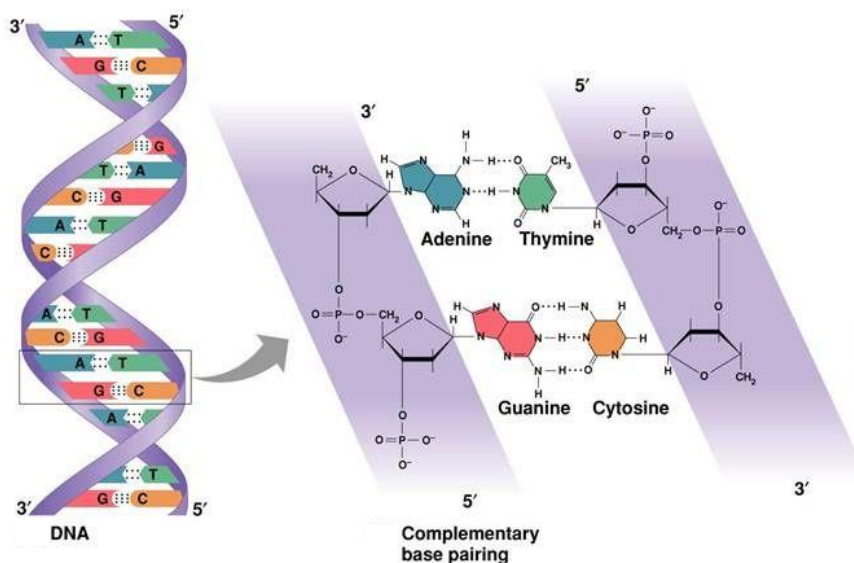


Figure 1. Schematic representation of the double helix structure of DNA (left) and a more detailed representation with the structures of the nucleotides (right).<sup>2</sup>

Besides the well-known DNA and RNA, there are many more naturally occurring (small) RNAs than previously believed. Large parts of the human genome (up to 98 %) were initially labelled as “junk DNA”, while it is now claimed that around 75 % of the noncoding sequence undergoes transcription.<sup>3</sup> These transcripts have important

regulatory functions for the flow of genetic information from DNA to RNA and protein, but also in the defense against bacterial and viral infections.<sup>4</sup> For example, small interfering RNA and microRNA (miRNA) play important roles in post-transcriptional gene regulation. Both RNAs target messenger RNA, the carrier of genetic information before it is translated into amino acid sequences, which makes them interesting targets for therapeutic purposes.<sup>5</sup> Moreover, structured RNAs, such as ribosomal RNA (rRNA) and transfer RNA (tRNA), have important roles in the protein translation process.<sup>1</sup> The rRNA is one of the main component of ribosomes and tRNA carries amino acids to the ribosomes during translation (Figure 2).

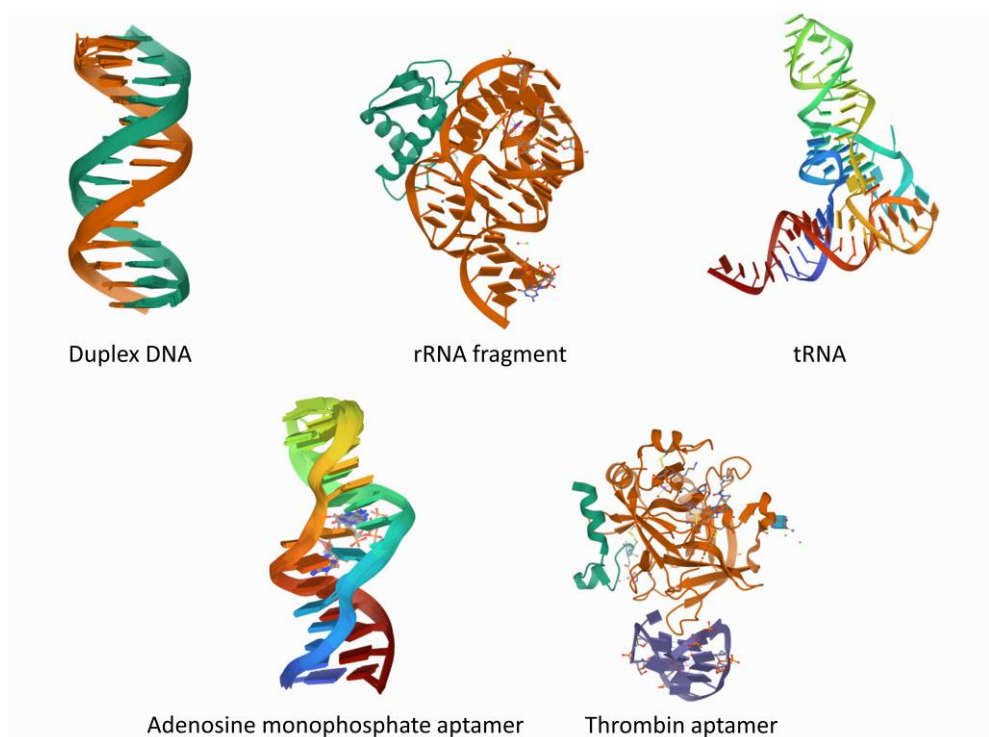


Figure 2. Structures of duplex DNA (PDB code: 2MC2), a 58 nucleotide rRNA fragment (PDB code: 1HC8), tRNA (PDB code: 6UGG), the adenosine monophosphate aptamer (PDB code: 1AW4) and the thrombin aptamer (PDB code: 4DIH).

## 1.2 Aptamers

The structural and functional diversity of oligonucleotides has long been underestimated. In an attempt to utilize some of this functional capability, synthetic biology has had great success with “man-made” oligonucleotides. One particular type

of small oligonucleotides that are currently of great interest are aptamers. The term aptamer is derived from the Latin “*aptus*” meaning “fitting” and the Greek “*meros*” meaning “part”. In essence, aptamers are short single-stranded (ss) DNA or RNA molecules consisting of approximately 20-80 nucleotides, with a molecular mass of 6-30 kDa. They are characterized by a specific 3D conformation, or fold, which enables high-specificity and high-affinity recognition of the target (Figure 2).<sup>6</sup> The specific 3D structure is often a combination of various structural motifs, such as stems, loops, hairpins, bulges, and pseudoknots (Figure 3). To maintain these specific structures, co-factors such as divalent cations (i.e.  $Mg^{2+}$ ) are often needed.<sup>7</sup>

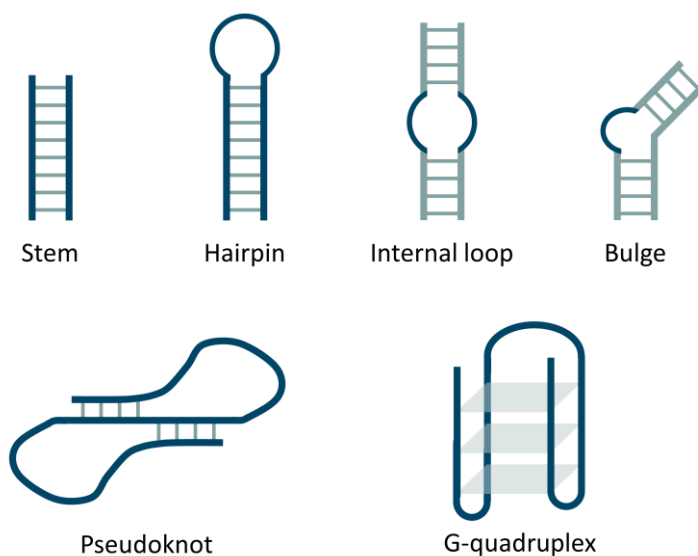


Figure 3. Schematic representation of structural motifs of aptamers.

The high binding affinity and specificity of aptamers render them an attractive alternative to monoclonal antibodies. Moreover, aptamers offer considerable advantages over traditional molecular biorecognition elements such as antibodies or enzymes. First, aptamers are produced chemically with high reproducibility and purity, which reduces the production costs and allows introducing modifications. Second, they have high stability over a wide range of temperature and pH. Furthermore, aptamer sequences are generally not targeted by the innate immune system since their 2'-position of the sugar moiety is often modified for therapeutic purposes (as described later in section 1.2.2) and are therefore not immunogenic.<sup>8,9</sup> Finally, aptamers can be selected against almost every possible analytical target, and nowadays aptamers have been designed to bind e.g. small organic molecules,<sup>10,11</sup> peptides,<sup>12,13</sup> proteins,<sup>14,15</sup> cells,<sup>16</sup> and even viruses.<sup>17</sup>

### 1.2.1 Aptamer selection

Aptamers were first obtained in the 1990s in the labs of Gold<sup>18</sup> and Szostak<sup>19,20</sup> following a procedure called systematic evolution of ligands by exponential enrichment (SELEX). The procedure consists of multiple rounds of binding, separation and amplification (Figure 4).<sup>6,21</sup> Before the selection starts, a large pool of ssDNA or RNA, generally up to  $10^{15}$  unique sequences, is generated. These sequences are then incubated with the target and afterwards the binding sequences are separated from the non-binding sequences. Commonly used methods for this separation are gel electrophoresis and affinity chromatography. After the binding sequences are recovered, they are amplified by using polymerase chain reaction (PCR) or reverse transcription PCR (for RNA). The newly generated library now contains a pool enriched with sequences which can bind the target and the next selection round starts. The selection process continues until the pool consists mainly of sequences that have a high affinity for the target. Afterwards, the aptamer candidates are sequenced and their target recognition characterized using e.g. isothermal titration calorimetry (ITC)<sup>22</sup> or surface plasmon resonance (SPR).<sup>23</sup>

Throughout the years, many modifications were made to the SELEX process. Examples are FluMag SELEX<sup>24</sup> which is nowadays the most commonly used one and combines the advantages of fluorescence labelling of the DNA with a magnetic separation technology, capture-SELEX<sup>25</sup> which was developed specifically for small molecules, and graphene oxide SELEX<sup>26</sup> which does not require immobilization of the aptamer or target in contrast to other SELEX approaches.

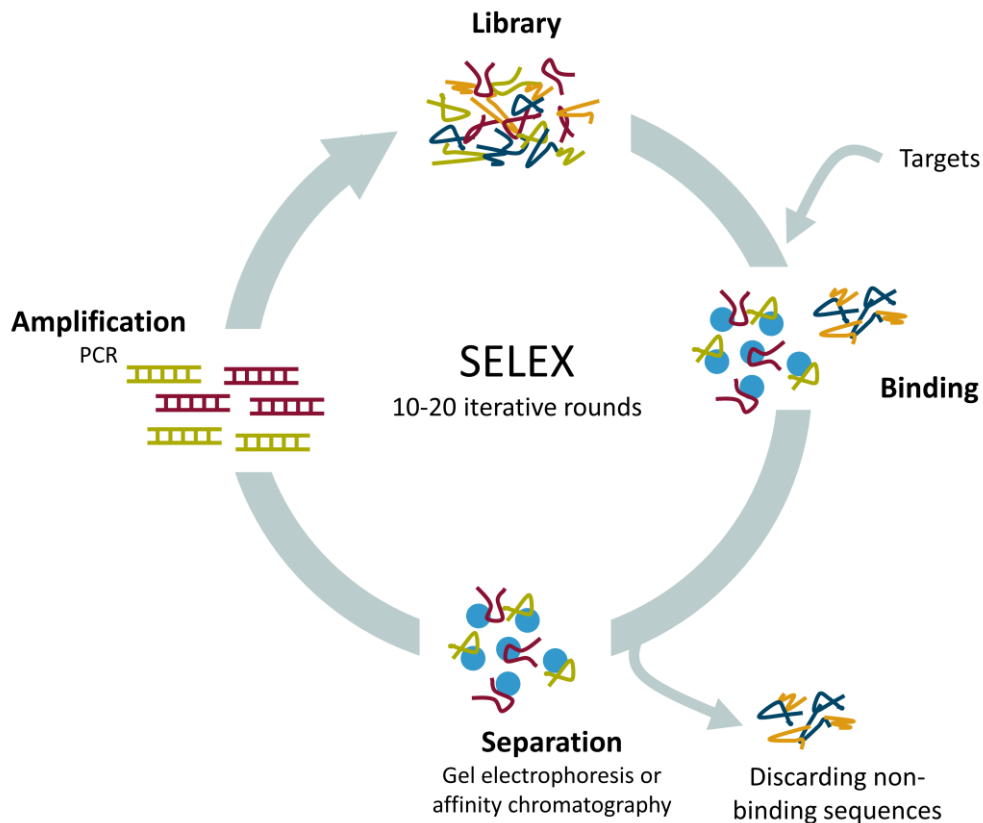


Figure 4. General scheme of the SELEX process. In a first step a library with DNA or RNA sequences is incubated with the target. Afterwards, the non-binding sequences are removed and the binding sequences are amplified. This generates a new pool of sequences which undergoes the next selection round.

### 1.2.2 Applications

Starting at the point of their discovery, aptamers were immediately considered a leap forward in many analytical and biomedical applications and they have been manifested more extensively in recent years. By now, aptamers have been employed in various application fields, with the most common applications further discussed below (Figure 5).

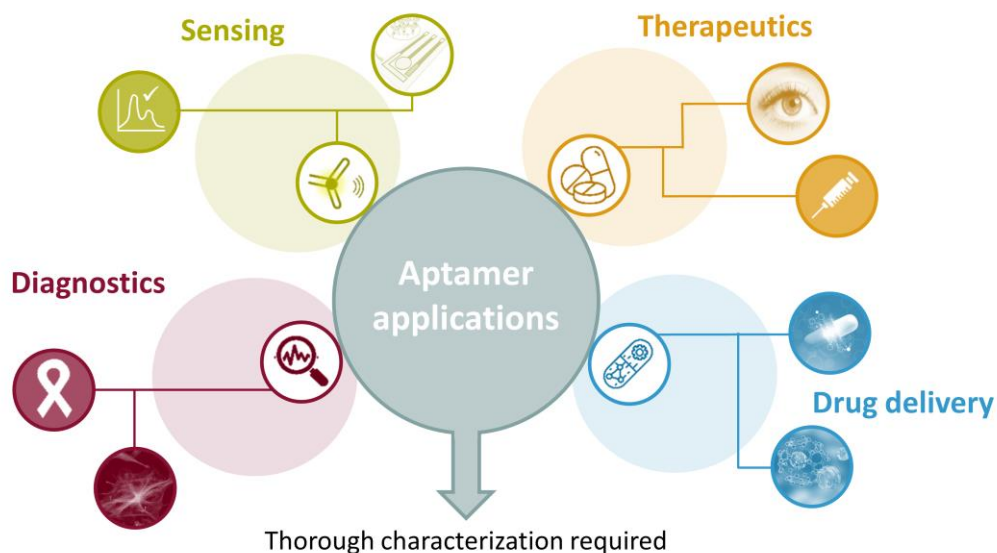


Figure 5. An overview of the main application fields of aptamers; sensing, therapeutics, diagnostics, and targeted drug delivery.

**Sensing.** A substantial amount of the aptamer-based research is going on in the development of biosensors in which an aptamer is used as a biorecognition element, so-called aptasensors. Aptasensors have several advantages, such as their simplicity, high sensitivity, high selectivity, and low cost, compared to biosensors with other biorecognition elements (e.g. antibodies or enzymes). Since the development of the first aptasensors in 1996,<sup>27,28</sup> a variety of sensors was designed for a wide range of targets: from heavy metals<sup>29</sup> to antibiotics<sup>30</sup> and food contaminants.<sup>31</sup> Many detection strategies were used throughout the years and include electrochemical,<sup>32,33</sup> optical (mainly colorimetric<sup>34,35</sup> or fluorimetric<sup>36,37</sup>), and mass-sensitive<sup>38,39</sup> detection platforms. In 2012, NeoVentures Biotechnologies Inc. brought the first commercialized aptasensor to the market to detect ochratoxin A and aflatoxins, both potent carcinogens, in food samples.

**Therapeutics.** There are two possible ways in which an aptamer can function as a therapeutic agent by specifically binding to a protein target: *i*) by inhibiting protein-protein interactions or *ii*) by enhancing the protein's function (due to, for example, stabilization of a particular conformation).<sup>21</sup> Until now there was only one aptamer approved, in 2004, for clinical use by the Food and Drug Administration. This RNA aptamer, called Macugen, is used in the treatment of age-related macular degeneration which causes blindness.<sup>40</sup> Macugen targets a vascular endothelial growth factor (VEGF) and prevents the VEGF from stimulating blood vessel growth and

ultimately vision loss.<sup>6</sup> Several other aptamers are now evaluated in clinical trials for the treatment of various diseases, such as macular degeneration, inflammation, and cancer, emphasizing the considerable activity undertaken to commercialize aptamers as therapeutic agents.<sup>41</sup>

**Diagnostics.** In 1999, Bruno et al.<sup>42</sup> described the first aptamer to be used as a diagnostic tool. The authors developed an aptamer to detect anthrax spores using an electrochemiluminescence (ECL) detection strategy. Since then, several aptamers have been used for the diagnosis of, for example, cancer, infectious diseases and cardiovascular diseases.<sup>21,43</sup> Aptamers can also be used to image certain tissues when they have a signal moiety (e.g. fluorophore) attached. Li et al.<sup>44</sup> used a fluorophore-labelled aptamer to target metastatic colon cancer cells. Tissue imaging results showed that the aptamer was highly specific to the tumor tissue and that it has great potential to become an imaging agent for the early detection of metastatic colon cancer cells.

**Drug delivery.** An aptamer can also be used to selectively deliver therapeutic targets to a defined site or type of cell.<sup>45</sup> In several studies, aptamers were covalently or noncovalently linked to small molecules or RNA. One example is the AS1411 aptamer coupled with the small molecule and chemotherapeutic agent doxorubicin.<sup>46</sup> The aptamer specifically binds to the protein nucleolin, which is overexpressed in many cancer cells. Esposito et al.<sup>47</sup> developed two aptamers which carry miRNAs to deliver these to glioblastoma stem-like cells, and thereby inhibit the propagation of these cells. Occasionally, aptamers are not directly linked to a therapeutic agent, but they are used to coat nanoparticles which encapsulate a drug and act as a biorecognition element to deliver these to a defined site.<sup>48</sup>

The use of aptamers in biomedical applications is hampered by their limited stability in biological environments. Both DNA and RNA are susceptible to degradation by nucleases which results in very short in vivo half-lives.<sup>21</sup> As an example: an unmodified thrombin aptamer was found to have a half-life of less than 2 minutes in animals.<sup>49</sup> Several strategies have been proposed to enhance the resistance of aptamers to degradation by nucleases.<sup>50</sup> First, the 2'-hydroxyl group in RNA can be replaced with other groups (e.g. amino, fluoro or methoxy groups) or can be locked to the 4' carbon of the sugar moiety (the so-called locked nucleic acids). Second, the phosphodiester backbone of aptamers can be replaced with phosphorothioate or methylphosphonate analogues. Finally, the Spiegelmer technology can be applied in which L-enantiomeric nucleotides are used instead of the natural D-forms. Next to the fast degradation by

nucleases, aptamers are excreted rapidly by renal filtration in less than 20 minutes due to their relatively low molecular weight, even when the modifications mentioned above are used.<sup>8,21</sup> To overcome this issue, aptamers are conjugated to bulky moieties such as polyethylene glycol (PEG). The addition of two PEG chains is for example used in the commercial drug Macugen.<sup>51</sup>

### 1.2.3 Challenges in aptamer research

Noncovalent interactions such as van der Waals forces, hydrogen bonding, electrostatic interactions, and hydrophobic interactions mediate aptamer folding and ligand binding. However, the different contributions of these forces are poorly understood. Thus, a thorough understanding of the relationship between the sequence and what determines the higher-order structure and specific interactions of aptamers is lacking.

The above becomes evident by looking at the literature. Several aptamers are reported that do not selectively bind the target against which they were selected in the first place. One of the most famous examples is the cocaine-binding aptamer, which does not only bind cocaine but also a wide range of other targets, such as the antimalaria compound quinine.<sup>52,53</sup> More disturbingly, recent reports in the literature describe aptamers that do not bind the target for which they were selected at all.<sup>54,55</sup> Zong et al.<sup>54</sup> investigated an arsenic-binding aptamer that was already used in more than 20 papers for the detection of As(III). The authors performed various assays and negative controls and concluded that the aptamer could not bind As(III). More recently, Tao et al.<sup>55</sup> found that a truncated chloramphenicol aptamer did not specifically bind the target it was selected for, although it was used by many researchers. These observations hamper the application potential of aptamers which could be fully exploited if they were well-characterized.

Robust experimental methods are needed to characterize the different levels of higher-order structure and the specific interactions which result from it. As the unique 3D structure of an aptamer determines its function – similar to well-established structure-function relationships for proteins – obtaining structural information is key.

Well-established approaches to obtain high-resolution structural information are nuclear magnetic resonance (NMR) spectroscopy and X-ray crystallography. However, both techniques have some limitations and require relatively large amounts of sample

(ca. 0.1 mg). NMR is usually slow and limited to small biomolecules (< 30 kDa).<sup>56</sup> In addition, data analysis for oligonucleotides is difficult since there are only four different bases and signal assignment becomes very hard. On the other hand, X-ray crystallography can determine the structure of larger molecules and is therefore usually used to determine structures of aptamer-protein complexes. It is, however, difficult to obtain crystals that provide suitable quality diffraction data, and it predominantly provides information about the most stable or abundant conformation of a molecule.<sup>57</sup> This means that heterogeneity in samples, e.g. coexisting molecular species with alternative folds or interaction partners, as well as conformational dynamics and flexibility, are not easily detected.

## 1.2.4 Aptamers used in this PhD thesis

Throughout this PhD thesis, multiple aptamer sequences are used for various targets. All aptamers are DNA and an overview is provided in Table 1.

*Table 1. Aptamer sequences and corresponding targets utilized in throughout this PhD thesis.*

<b>Target</b>	<b>Name</b>	<b>Aptamer sequence (5' → 3')</b>
Ampicillin	AMP4	CAC GGC ATG GTG GGC GTC GTG
	AMP17	GCG GGC GGT TGT ATA GCG G
	AMP18	TTA GTT GGG GTT CAG TTG G
Cocaine + quinine	OR7-A	AAA AAC AAG GAA AAT CCT TCA ACG AAG TGG GAA AAA
	OR8-A	AAA AAC AAG GAA AAT CCT TCA ACG AAG TGG GTA AAA
	MN19	GAC AAG GAA AAT CCT TCA ACG AAG TGG GTC
	MN19-A	AAA GAC AAG GAA AAT CCT TCA ACG AAG TGG GTC AAA
	MNS-7.9	GAC AAG GAA AAT CCT TCA ATG AAG TGG GTC
	MN4	GGC GAC AAG GAA AAT CCT TCA ACG AAG TGG GTC GCC
	38-GC	GGG AGA CAA GGA AAA TCC TTC AAC GAA GTG GGT CTC CC
	OR11	GGG CGA CAA GGA AAA TCC TTC AAC GAA GTG GGT CGC CC
L-argininamide	1OLD	GAT CGA AAC GTA GCG CCT TCG ATC
Testosterone	TESS.1	CTC TCG GGA CGA CGG GAT GTC CGG GGT ACG GTG GTT GCA GTT CGT CGT CCC
	TESS.1short	GGG ATG TCC GGG GTA CGG TGG TTG CAG TTC

## 1.3 Native mass spectrometry of oligonucleotides

Mass spectrometry (MS) is capable of determining sequence variations, modifications and heterogeneity (denatured MS) and linking these with 3D structure and interactions (native MS).<sup>58,59</sup> Therefore, MS has great potential for the characterization of aptamers. Native MS is widely applied to study biomolecules<sup>60,61</sup> and recently had a major impact in the study of dynamic and large protein complexes,<sup>62,63</sup> but is still largely unexplored for aptamers and oligonucleotides in general. In native MS, even relatively weak noncovalent interactions are preserved upon transfer to the gas-phase, allowing the analysis of noncovalent complexes. Therefore, native MS provides information about the composition and stoichiometry (provided that the dissociation constant ( $K_d$ ) is in the low- $\mu\text{M}$  to nM range), and allows simultaneous identification and characterization of individual species in a heterogeneous ensemble.<sup>64,65</sup> This presents a strong contrast to many other structural and biophysical techniques which either require homogeneous sample, or report on the ensemble-average or the most prominent state. Advantages of native MS are that only low sample amounts are required (a few  $\mu\text{L}$ ) at relatively low concentrations (low  $\mu\text{M}$ -range), no labelling is required and it is relatively fast (minutes).

### 1.3.1 How to perform native MS?

In order to preserve noncovalent interactions between biomolecules, a number of requirements needs to be fulfilled. This includes sample preparation using a nondenaturing solvent to keep the biomolecules in the native state before the MS analysis, the use of soft ionization techniques for transferring the analyte to the gas-phase, and gentle tuning of the mass spectrometer throughout the analysis.

#### 1.3.1.1 Sample preparation

The main goals of sample preparation for native MS are to remove interfering compounds (e.g. non-volatile salts and typical buffers such as Tris) and to provide a volatile solution to facilitate the transfer to the gas-phase while maintaining noncovalent interactions.<sup>61</sup> This is achieved by performing a buffer exchange to a volatile solvent, usually ammonium acetate, prior to the native MS experiment. There

are several ways to exchange the buffer and the most commonly used ones are dialysis and size-exclusion chromatography using micro-columns. When using a sufficient concentration of ammonium acetate, the excess of  $\text{NH}_4^+$  ions in the positive ionization mode will replace cations, such as  $\text{Na}^+$  and  $\text{K}^+$ , on the oligonucleotide phosphate backbone.<sup>66</sup> During ionization, both components of the ammonium acetate solution, ammonium and acetate, will evaporate easily (as ammonia and acetic acid) to yield protonated oligonucleotides. This leads to less salt adduct formation and, thus, less peak broadening.

In my PhD, the effects of other volatile solvents on the MS spectrum were investigated: triethylamine acetate (TEAA) and ethylenediamine diacetate (EDDA). The native MS spectra of the MN19 cocaine-binding aptamer acquired in the positive ionization mode in these different buffers show clear differences (Figure 6). In ammonium acetate, the aptamer shows a narrow 5+ charge state, while the use of both TEAA and EDDA broadens the peaks and shifts them to higher mass-to-charge ( $m/z$ ) values (lower charge states). In TEAA, the aptamer is heavily adducted with triethylamine, with the most intense peak carrying seven triethylamine adducts. Moreover, the charge state distribution shifted to lower charge states with the main one being the 4+ charge state. Also, the aptamer measured in EDDA shows many buffer adducts. The most intense peak has nine ethylenediamine adducts bound to the aptamer. Neither TEAA or EDDA did enhance the MS spectrum and were therefore not considered further throughout my PhD research.

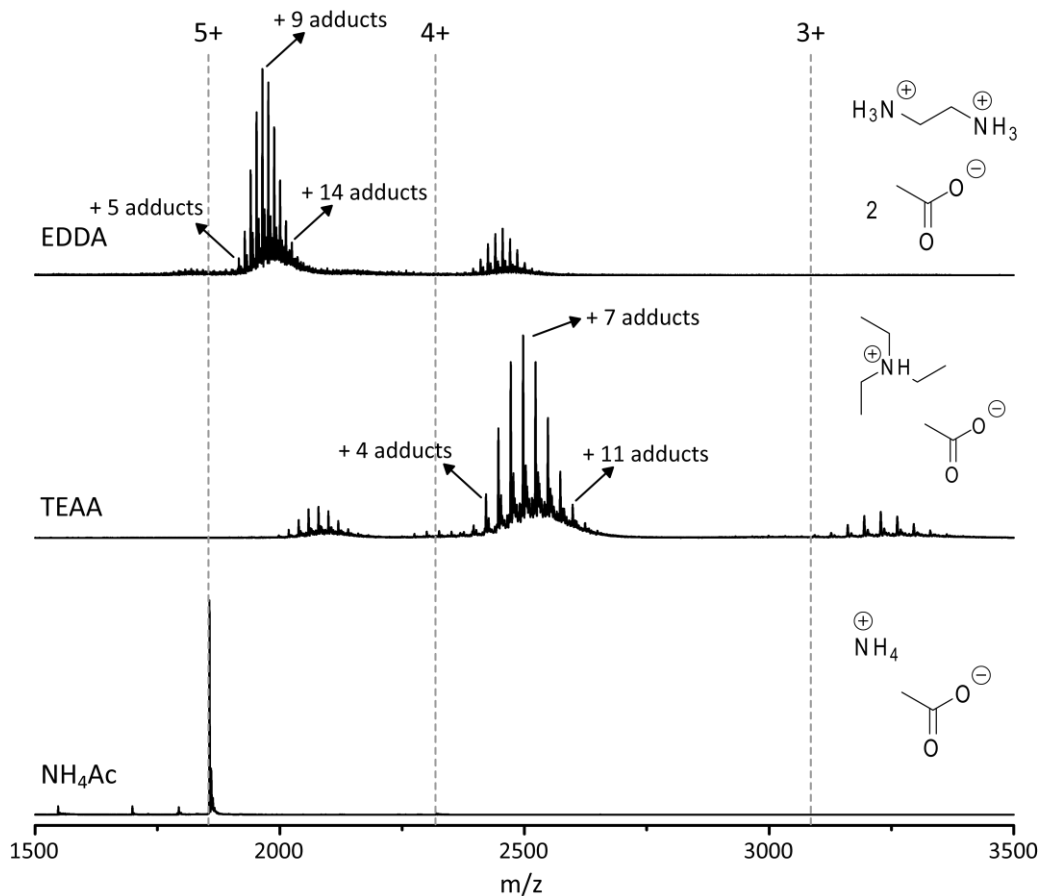


Figure 6. Native MS spectra in the positive ionization mode of the cocaine-binding aptamer MN19 acquired in 300 mM EDDA, TEAA and ammonium acetate ( $\text{NH}_4\text{Ac}$ ). The theoretical  $m/z$ -values of the protonated species are indicated the grey dotted lines. The buffer compositions are shown on the right.

### 1.3.1.2 Soft ionization

In native MS, biomolecules are usually transferred to the gas-phase using the soft ionization technique of electrospray ionization (ESI). During ESI, a voltage difference is applied between a capillary, which contains the sample, and the inlet of the mass spectrometer to generate either positively or negatively charged ions depending on the applied voltage.<sup>67</sup> In case of positive ionization mode, positively charged ions pile up in the so-called Taylor cone which is formed at the tip of the capillary when a voltage is applied, and droplets with an excess of positive ions are emitted (Figure 7). The solvent in these microdroplets evaporates until the Coulombic repulsion is equal to the surface tension (Rayleigh limit), and then the droplets undergo fission to yield smaller droplets.

The fission process continues until finally the remaining solvent evaporates and the charge is transferred to the molecule to generate multiply charged ions in the gas-phase, following the so-called charged residue model.<sup>68</sup>

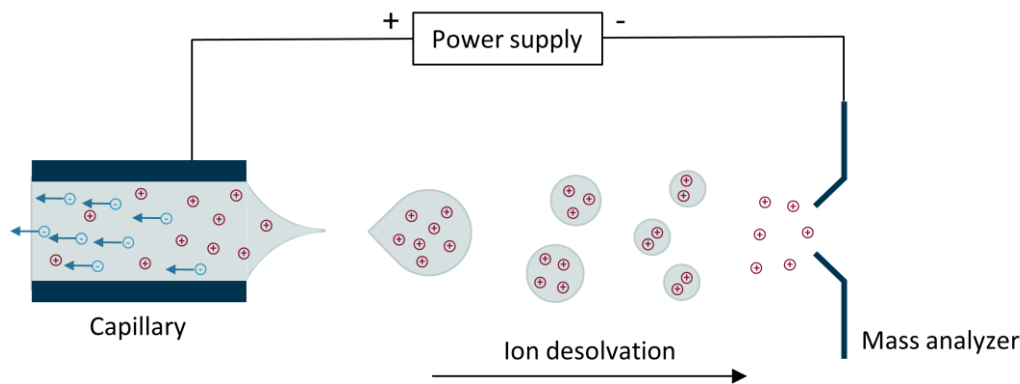


Figure 7. Schematic overview of the ESI process. By applying a voltage between the capillary and the inlet of the mass spectrometer, a spray of droplets is generated. The ions are desolvated and multiply charged ions are formed.

Typically, nano-electrospray ionization (nESI) is used in native MS which generates droplets that are 100 to 1000 times smaller in volume than these generated with conventional ESI.<sup>69</sup> Due to the smaller surface-to-volume ratio of these smaller droplets, less solvent needs to evaporate which enhances the ion desolvation efficiency. In addition this makes the release of the ions into the gas-phase more gentle. Moreover, nESI allows to use lower sample volumes (down to 1  $\mu$ L) and lower flow rates (nL/min).

### 1.3.1.3 Gentle tuning

Once the ions enter the mass spectrometer, it is key to preserve the noncovalent interactions throughout the MS analysis. The instrument should be carefully tuned to balance preservation of the native structure with achieving sufficient declustering (desolvation) in order to obtain well-resolved spectra. For the Synapt G2 HDMS Instrument from Waters (Figure 8), which I mostly used throughout this PhD, mainly the sample cone voltage, extraction cone voltage, trap collision energy, trap DC bias and transfer collision energy need to be tuned gently to maintain noncovalent interactions.

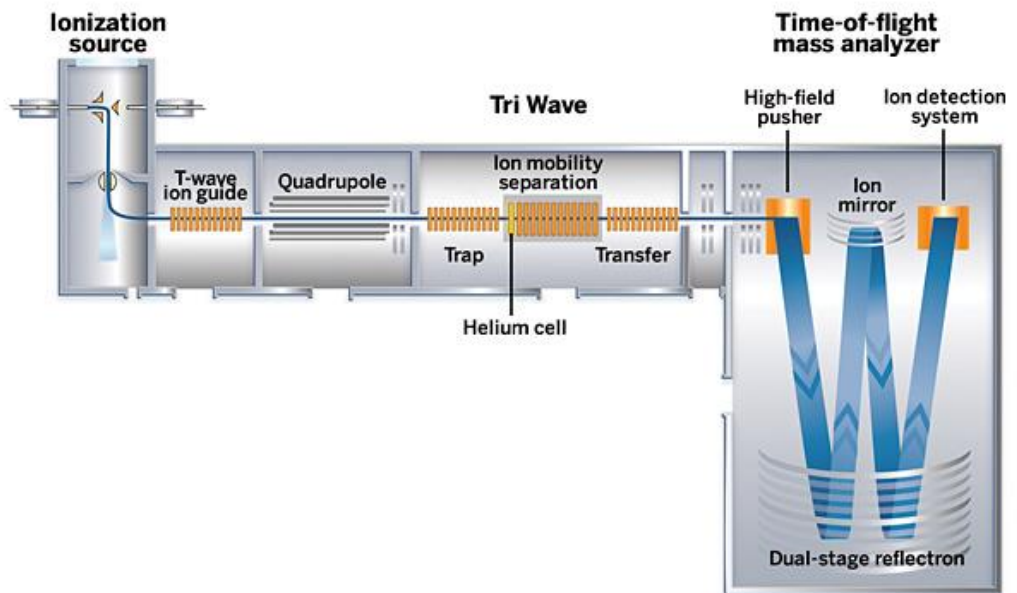


Figure 8. Schematic overview of the Synapt G2 HDMS mass spectrometer from Waters.

Figure 9 shows the effect of the trap collision energy (actually, a voltage offset) on the amount of complex formed between the cocaine-binding aptamer MN19 and quinine. In Figure 9B the amount of complex present is shown in function of the trap collision energy. It is clear that when raising the energy above 15 V, the amount of complex decreases, which means the complex dissociates and the experimental conditions are not keeping the ions in their native state.

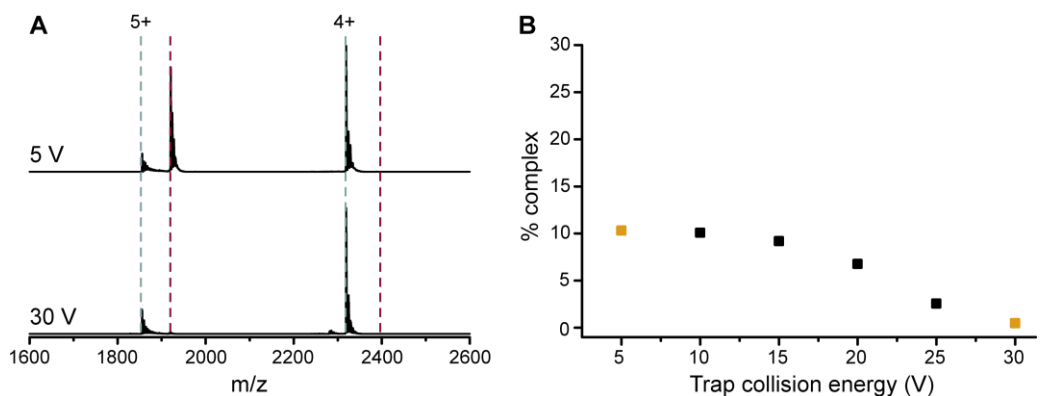


Figure 9. A) MS spectrum of the MN19 cocaine-aptamer in complex with quinine measured using a trap collision energy of 5 V (top) and 30 V (bottom). The theoretical  $m/z$ -values of the aptamer and complex are indicated in grey and red, respectively. B) The percentage of observed complex plotted in function of the trap collision energy.

### 1.3.2 Ion mobility spectrometry

Native MS can be combined with ion mobility (IM) spectrometry. IM spectrometry provides a more detailed view on the global size and shape of the ions, i.e. the conformation, and it can even highlight coexisting conformational states within one charge state. In IM, ions are separated based on their mobility in an inert gas (He or N<sub>2</sub>) under the influence of an electric field.<sup>70</sup> The mobility of an ion depends on its charge, shape, and size. Compact ions, which undergo relatively few collisions with the gas, will travel faster through the IM cell than extended ions with the same charge since these undergo more collisions with the gas and are therefore slowed down (Figure 10). The time the ions spend in the drift region is called the drift time; but most commonly the arrival time, the time an ion needs to move from the beginning of the IM cell to the detector, is used.<sup>71</sup> Thus, compact ions have a smaller arrival time than more extended ions.

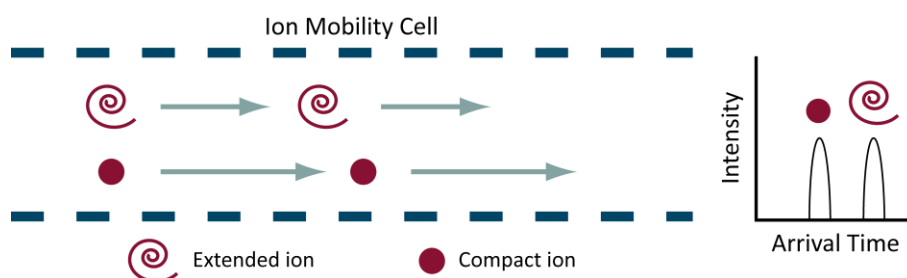
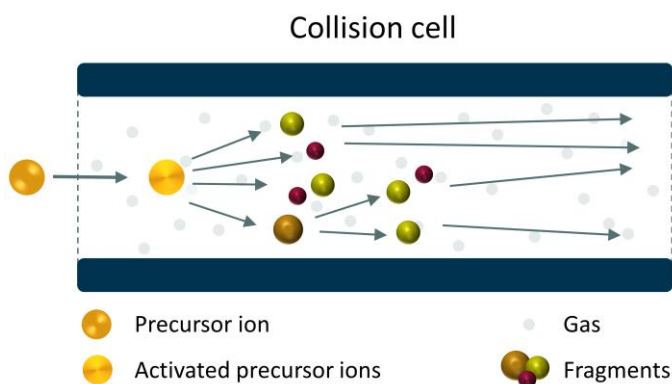


Figure 10. Principle of IM spectrometry. Ions are separated based on their mobility through a gas which is dependent on the charge, shape and size of the ion. Compact ions travel faster through the cell than extended ions (with the same charge) and will therefore have a smaller arrival time.

The measured arrival time of an ion can be converted to a collision cross section (CCS). This CCS value can be considered as the average 'shadow' of the ion through all possible orientations. All orientations are equally occurring since the ion tumbles freely in the IM cell. The CCS distribution of a particle represents its diversity in size and shape. In conventional IM devices, i.e. with a linear drift tube, the arrival time can directly be converted to CCS values.<sup>72</sup> However, often a calibration with ions with a known CCS is required to obtain CCS values.<sup>73–75</sup> This is the case for devices with for example a travelling wave IM cell, such as in the Synapt G2 HDMS (Waters).

### 1.3.3 Collision-induced dissociation and unfolding

Ions can be activated in the gas-phase by collisional heating, which is done as part of a collision-induced dissociation (CID) experiment. CID is a technique often used for sequencing purposes but it is also able to provide higher-order structural information.<sup>59,76</sup> During CID, ions are accelerated into a collision cell by applying a voltage (the so-called collision energy). In the collision cell, the analyte collides multiple times with an inert background gas (Ar or N<sub>2</sub>). Throughout this process, the internal energy of the analyte is increased until the weakest bonds or noncovalent interactions are disrupted (Figure 11). When CID is applied to protein complexes, the noncovalent interactions holding the complex together are broken and the complex dissociates.<sup>77</sup> During CID, asymmetric dissociation of the complex takes place which means a peripheral subunit undergoes unfolding first while taking up many charges and is then ejected from the complex as a highly charged species.<sup>78</sup> If CID is applied to a protein in complex with a small molecule, the target usually dissociates from the protein before the protein unfolds. In case the target is buried in the protein structure, the protein does, however, need to unfold before the target can be released.



*Figure 11. Schematic representation of the CID working principle. The ions undergo multiple collisions with a gas which raises their internal energy until the weakest bonds of the ion are disrupted and the ion falls apart.*

The collisions with a gas do not only induce the dissociation of complexes in the gas-phase, but usually this is preceded by the unfolding of ions or complexes, i.e. as in the asymmetric dissociation described above. This is utilized in so-called collision-induced unfolding (CIU) experiments.<sup>79</sup> This approach allows to examine the conformational stability of biomolecules and their complexes. During a CIU experiment, the arrival time, or CCS, of an ion is monitored when raising the collision energy. Typically,

stepwise changes of the arrival time are observed: once a critical energy is reached, the analyte unfolds, but in between these critical energies the analyte is stable.<sup>80</sup>

### 1.3.4 Native MS of oligonucleotides: state of the art

Native IM-MS has great potential to connect primary (sequence) and higher-order structural information of oligonucleotides and their complexes, and therefore contributes to the characterization of oligonucleotides.

The first report of a DNA duplex measured by ESI-MS dates back to 1993<sup>81</sup> and one year later, the same group published the analysis of a DNA-drug complex.<sup>82</sup> In the beginning, native MS was mainly used to determine stoichiometries of complexes, and it was only several years later that it was first used to determine the  $K_d$  of a double-stranded (ds) oligonucleotide and minor groove binders.<sup>83</sup>

In 2005, a combined IM and molecular modeling study of a rigid four-stranded oligonucleotide complex showed that the experimentally determined CCS matches well with a quadruplex structure, suggesting the higher-order structure was preserved during the native MS analysis,<sup>84</sup> and multiple studies have since used G-quadruplexes as model systems. Gabelica et al.<sup>85</sup> found that the fold of G-quadruplexes is stabilized by  $\text{NH}_4^+$  ions and that the structure was maintained upon transfer to the gas-phase, in a combined IM-MS and molecular dynamics (MD) study. Later, the folding of G-quadruplexes was monitored by both circular dichroism (CD) and IM-MS.<sup>86</sup> The two techniques showed an excellent correlation between their experimental findings and proved that IM spectrometry can be used to investigate the folding of G-quadruplexes. Moreover, the authors found that parallel G-quadruplexes maintain their structures more easily in the gas-phase than antiparallel G-quadruplexes. Balthasart et al.<sup>87</sup> used several G-quadruplexes, among which the thrombin-binding aptamer, to investigate whether ESI-MS reflected the solution-phase species by looking at the amount of  $\text{NH}_4^+$  ions bound to the G-quadruplexes. The authors could detect specific binding of  $\text{NH}_4^+$  ions to the G-quadruplexes, both between G-quartets and on the outside of the external G-quartets. Some of the inner  $\text{NH}_4^+$  ions were, however, too labile to be maintained in the gas-phase indicating the relative abundances observed in solution are not always observed in the gas-phase. This strategy of determining the amount of  $\text{NH}_4^+$  was used to find the optimal instrument tuning conditions in several studies.<sup>87,88</sup>

By employing a temperature-controlled (n)ESI source, it is possible to follow the thermal denaturation of biomolecules. Hommersom et al.<sup>89</sup> investigated the 3D structure of hybridized oligonucleotides and followed conformational changes during the temperature-induced melting with IM-MS. They observed additional drift times above 35 °C indicating a partial unfolding of the dsDNA. Marchand et al.<sup>90</sup> showed that temperature-dependent equilibrium constants could be determined for G-quadruplexes and their complexes. Therefore, also the enthalpic and entropic contributions to the formation of the complexes were identified. By looking at these thermodynamic signatures, insights into the driving forces behind target binding could be obtained. In contrast to G-quadruplexes which appear rigid, short DNA duplexes were found to undergo compaction (over 20 %) in the gas-phase.<sup>91</sup> MD simulations demonstrated this is due to self-solvation of the phosphate groups which prevents electrostatic repulsion between them.

Not only (ds) oligonucleotides and G-quadruplexes were investigated. Baker et al. studied DNA hairpins, pseudoknots, and cruciform structures. The CCS values obtained by IM-MS were compared to those calculated from MD simulations and a match was found with the structures of the lowest charge states.<sup>92</sup>

In addition, Gülbakan, Barylyuk et al.<sup>93</sup> showed that native IM-MS can be used to determine the binding selectivity and stoichiometry of three well-studied small molecule-binding aptamers. Moreover, the authors showed that native MS can provide accurate aptamer-target binding affinities (by incorporating the correct controls) for both specific and nonspecific binding events. The IM-MS data was also able to help refine the model for aptamer-target binding. Yang et al.<sup>94</sup> employed native MS as a fast screening technique to determine the potential binding of target molecules to a thrombin-binding aptamer. The screening allowed to tackle the formation and the coexistence of complexes with different stoichiometries; 1:1 and 1:2. Moreover, by performing competition experiments the authors indirectly proved that one of the alkaloid targets was able to give stacking interactions.

### 1.3.5 Gas-phase vs. solution-phase

During a native MS experiment, oligonucleotides are transferred to the gas-phase by using a soft ionization technique to preserve noncovalent interactions. Moreover, the

mass spectrometer is tuned gently throughout the analysis. Despite these precautions, there are still several differences between the gas-phase and the solution-phase.

Porrini et al.<sup>91</sup> identified a key difference between proteins and nucleic acids in native MS. DNA and RNA duplexes analyzed in  $\geq 100$  mM ammonium acetate, which is typically considered a “native” solution condition, were found to be more compact in the gas-phase compared to their structure in solution. This effect is attributed to the formation of new phosphate-phosphate interactions. The Coulomb repulsion at the low charge states is not sufficient to keep the phosphate groups apart in ammonium acetate. This causes a rearrangement of the backbone and leads to a more compacted structure. It was found that DNA and RNA duplexes can compact over 20 % compared to their initial structure. Important to notice is that the authors found that these new metastable conformations keep some memory of the solution structure.

For aptamer-target binding studies, the type of interaction with the target might play a crucial role in native MS. It is known that hydrophobic interactions are absent in the gas-phase as they rely on the presence of water.<sup>95,96</sup> Since the analytes are analyzed in a vacuum, water is absent and the balance of forces keeping the target bound shifts. This potentially causes a weakening of the aptamer-target complex upon transfer to the gas-phase. All this is in contrast to electrostatic interactions that are strengthened in the gas-phase due to the absence of water.

## 1.4 Goal of the PhD research

Currently, there is still a lack of well-characterized oligonucleotide structures and their specific interactions with targets which hampers their commercialization. A better understanding of the structure and stability of aptamers, together with their interactions, is needed. In this PhD thesis, I explored the use of native MS for DNA aptamer characterization since this technique is still largely unexplored for aptamers, and oligonucleotides in general. Native MS allows to study all levels of the structure, from primary (sequence) to quaternary structure (complex formation) and has therefore great potential to provide a full understanding of the structure, stability and interactions of aptamers. It is, however, unexplored to which extent the properties of aptamers, such as their structure and ligand binding affinity, are maintained in the gas-phase. Therefore, other complementary techniques were used as a reference to support the work. For example, ITC was used as reference for binding affinities and

NMR spectroscopy for information on the structure and conformational dynamics (both from the literature and our own experimental work).

Next to the aptamer work, some characterization approaches were extended to proteins or protein-DNA complexes. For example, aspects of conformational dynamics and stability were not only investigated for aptamers but also for nucleosomes. These protein-DNA macromolecular complexes are very dynamic as they need to be readily accessible during the DNA transcription process and are an ideal system to study structural dynamics. Moreover, the ability to use native MS for the screening of interactions between environmental contaminants and possible protein biorecognition elements was explored. These biorecognition elements could later be used in biosensor development.

A schematic overview of all chapters in this thesis is shown in Figure 12 and a more detailed description of each chapter is provided below.

Chapter 2 provides an overview of currently used analytical techniques for the characterization of aptamer-target complexes. This includes methods to characterize different interactions, to obtain kinetic and thermodynamic information, as well as methods to study the structural and dynamic features of aptamers and their complexes. A focus is put on the fact that the final application of the aptamer should be considered prior to choosing the characterization method since label-free, labelled and immobilized aptamers can behave differently.

In chapter 3, the possibility to employ CID, commonly used to fragment oligonucleotides and obtain information on their sequence, to acquire structural information of aptamers was explored. However, the results only showed the loss of nucleobases independent of the structural features. In a next step, the conformational dynamics and gas-phase stabilities of aptamers with different stem lengths was investigated by performing CIU experiments. More structured aptamers were found to unfold at higher energies than (partially) unstructured aptamers. Finally, electron transfer dissociation (ETD) was explored to fragment aptamers since it should preferentially fragment more exposed sites.

The approach to investigate conformational dynamics and stability of biomolecules was extended from aptamers to nucleosomes in chapter 4. First, the native MS behavior of nucleosomes was studied and it was found that nucleosomes are mainly compact

entities. Second, it was investigated how histone variants and varying DNA sequences affect the conformational dynamics. In particular, we focused on the histone variant centromere protein A (CENP-A) vs. H3 and the 601 DNA sequence (vs. the natural  $\alpha$ -satellite (NAS) sequence). The results indicated that both CENP-A and the NAS sequence contribute to a less compact nucleosome form. Finally, the disassembly pattern of the nucleosomes was examined and it was found that both the type of histone variant and the DNA sequence have an effect on the overall stability and the structural dynamics of the nucleosomes, which enables their highly specified functions.

Chapter 5 continues with proteins and focuses on their tertiary and quaternary structure. Two case studies are reported here to underline the potential of applying native MS in the screening and characterization of biorecognition elements for environmental contaminants such as per- and polyfluorinated alkyl substances (PFAS). In the first case study, the binding capability of delipidated and untreated human serum albumin (hSA) was investigated together with the protein stability. The second case study showed the screening of possible bioreceptors (i.e. hemoglobin (Hb), neuroglobin (NGB) and cytochrome c (cyt c)) for the contaminants.

In chapter 6, a set of cocaine-binding aptamers was used to check to what extent aptamers retain key characteristics of their structure in the gas-phase and preserve key aspects of their folding and ligand recognition. It was demonstrated that aptamer-target complexes can be studied in both the positive and negative ionization mode. Moreover, native MS is able to determine relative binding strengths and rank aptamers according to their affinity. IM-MS allowed to observe small conformational changes upon binding, and related the difference in these changes to the rigidity of the aptamers used. An adaptive binding mechanism was suggested for flexible aptamers that require more reorganization upon binding.

In chapter 7, the need for a thorough characterization of aptamers was brought forward. Aptamers selected for ampicillin were studied using different analytical methodologies, i.e. ITC, native MS and  $^1\text{H}$  NMR spectroscopy, and were found to not bind the target they were selected for. The performance of the techniques was validated with two other well-characterized aptamers. With this chapter we aimed to make the aptamer community aware to more critically think about aptamer performance and to identify the need to validate aptamer-target interactions using multifaceted analytical approaches prior to using aptamers for applications.

Finally, an aptamer-based electrochemiluminescent platform for the detection of testosterone was developed in chapter 8. The incubation and immobilization protocols were optimized, as well as the optimal concentration of the aptamer. Moreover, a multifaceted analytical approach including ITC and native MS was used to obtain a better understanding of the aptamer performance, affinity, and selectivity.

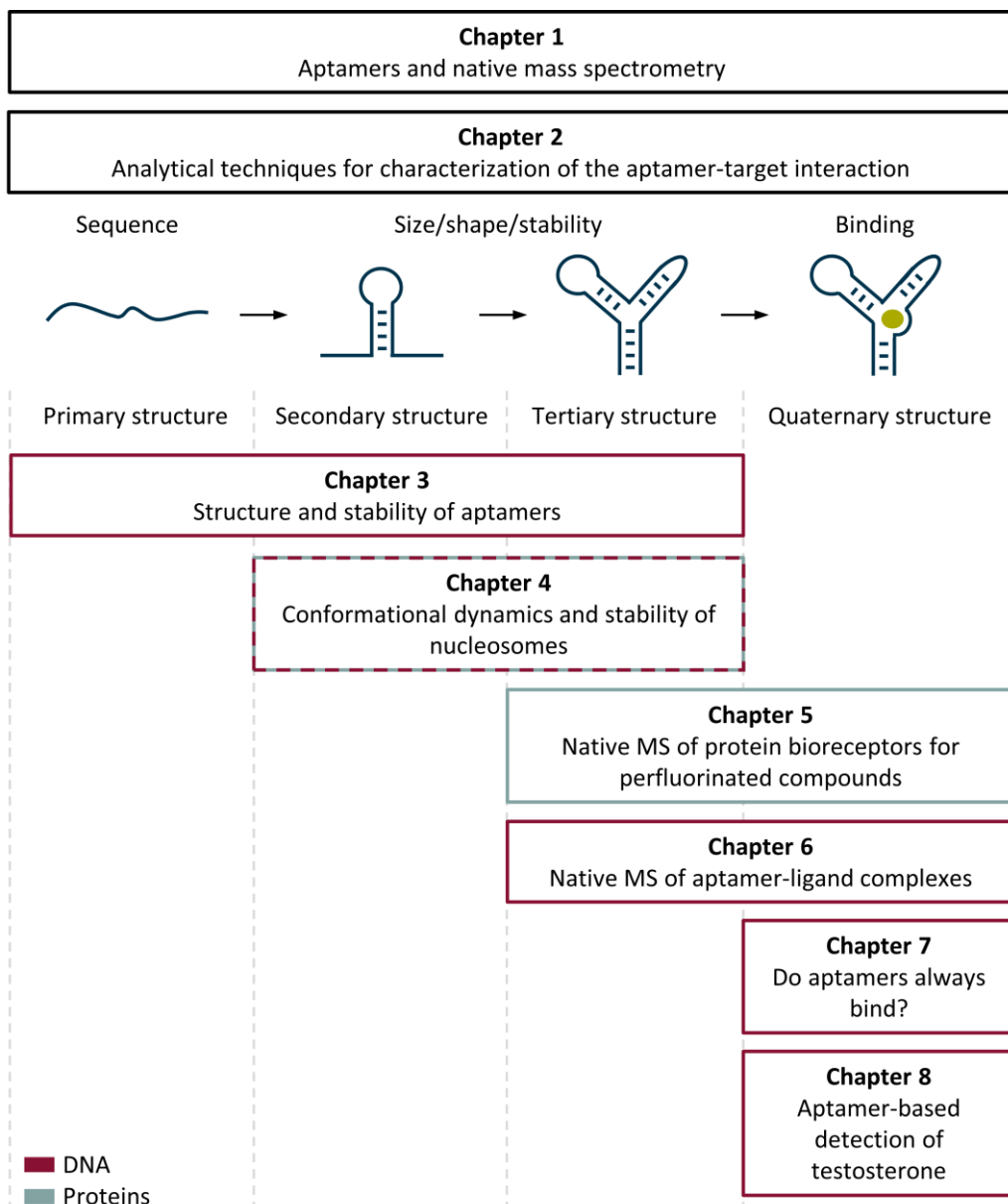


Figure 12. Schematic overview of the conducted PhD research.



# |2

Mapping the gaps in chemical analysis for the characterization of aptamer-target interactions

**Elise Daems\*, Giulia Moro\*, Rui Campos, and Karolien De Wael**

*Adapted from Trends in Analytical Chemistry, 142, 116311 (2021)*

**\* Contributed equally**



## Abstract

Aptamers are promising biorecognition elements with a wide applicability from therapeutics to biosensing. However, to successfully use these biomolecules, a better characterization of their binding performance in the presence of the target is crucial. Several multi-analytical approaches have been reported including techniques to describe kinetic and thermodynamic aspects of the aptamer-target interaction, and techniques which allow an in-depth understanding of the aptamer-target complex structures. Recent literature shows the need of a critical interpretation, a combination of characterization techniques and suggests the key role of the characterization protocol design. Indeed, the final application of the aptamer should be considered prior to choosing the characterization method. All the limitations and capabilities of the analytical tools in use for aptamer characterization should be taken into account. Here, we present a critical overview of the current methods and multi-analytical approaches to study aptamer-target binding interactions, aiming to provide researchers with guidelines for the design of a characterization protocol.

## 2.1. Introduction

In the last 25 years, the number of publications dealing with aptamers and their applications has increased exponentially as shown in Figure 13. Nowadays aptamers are largely applied in therapeutics,<sup>97,98</sup> diagnostics,<sup>99</sup> drug delivery<sup>100,101</sup> and in sensing devices as biorecognition elements.<sup>102–104</sup> There were also developments in the selection process for aptamers and multiple variations exist, such as FluMag SELEX<sup>24</sup>, capture-SELEX<sup>25</sup> and graphene oxide SELEX.<sup>26</sup>

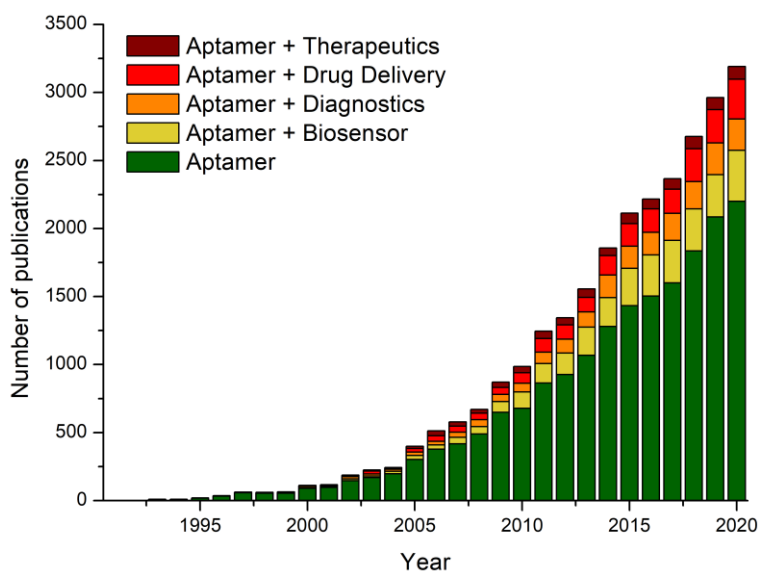


Figure 13. Number of publications per year related to aptamers and their applications. The plot shows the exponential growth of the publications in the field over the last 15 years. Bibliographic analysis performed with Scopus searching for the following keywords: “aptamer\*”, “aptamer\* AND biosensor\*”, “aptamer\* AND therapeutic\*”, “aptamer\* AND drug delivery\*” and “aptamer\* AND diagnostic\*” per year. Data from Scopus retrieved on 14/01/2021.

Despite the advances in SELEX procedures and the variety of aptamers applications, examples of non-functioning aptamers (unable to bind their target) were recently reported in literature, showcasing the key role of a complete characterization of the aptamer-target interactions.<sup>54,55</sup> Zong and Liu<sup>54</sup> reported an arsenic(III)-binding aptamer, which has been used in more than two dozen peer-reviewed articles, and showed that there was no specific binding. In 2020, Tao et al.<sup>55</sup> described the lack of binding of a previously reported chloramphenicol aptamer. These studies were both based on multi-analytical approaches involving complementary techniques. The results emphasize the need for a thorough characterization of aptamers before proceeding to

their application. This need for a critical evaluation of aptamer performance was also claimed during the 2019 meeting of the international society on aptamers, in Oxford (UK). Furthermore, McKeague et al.<sup>105</sup> found that the use of certain techniques can enhance or reduce the affinity of a given aptamer, indicating the need for multiple characterization strategies and a critical choice of these methods depending on the final application.

Here, we provide a critical overview of analytical techniques that can be used for the characterization of aptamer binding and structure. We focus on newer analytical methods rather than classical methods (e.g. equilibrium dialysis, chromatography approaches and gel-based methods) that can be used for studying aptamers. These classical methods were previously discussed by Miranda-Castro et al.<sup>106</sup> First, techniques to retrieve kinetic and thermodynamic information on the binding event are discussed. A distinction is made between techniques used in solution and on a confined surface since immobilization can alter the affinity.<sup>107,108</sup> Moreover, label-free methods and analytical protocols in which a label (such as a fluorophore) is required are addressed separately. Second, we focus on techniques providing information on the aptamer and aptamer-target structures. This part is divided in high- and low-resolution techniques which can provide structural information.

## 2.2. Kinetic and thermodynamic studies of the binding event

Determining the extent to which the aptamer-target interaction occurs represents a fundamental step of aptamer characterization. Kinetic and thermodynamic parameters help in the decision of choosing an aptamer over another. Yang et al.<sup>10</sup> selected aptamers for steroids based on the higher affinity towards the target even though other sequences were also specifically binding to the target.

The analytical methods used in this context can be divided into two main clusters: methods in which interactions are studied in solution (section 2.2.1) and methods in which aptamer-target kinetics are characterized at a confined surface after immobilization of one of the binding partners (section 2.2.2).

## 2.2.1 In solution

Several analytical techniques can provide kinetic or thermodynamic information on the aptamer-target interaction. When studying the interaction in solution, there are two possibilities: using label-free methods (section 2.2.1.1) or methods in which either the aptamer, the target, or both carry a label (section 2.2.1.2).

### 2.2.1.1 Label-free methods

#### **Isothermal titration calorimetry and related methods**

ITC, first described by Wiseman et al.<sup>109</sup> directly measures the heat exchange of biochemical reactions, or molecular interactions, at constant temperature. Experiments are performed by titrating a target into a solution containing the aptamer and the heat which is released or absorbed after each addition is monitored.<sup>110</sup> ITC is regarded as a standard characterization method which enables drawing a detailed thermodynamic picture of aptamer-target molecular interactions not only for small-molecules but also for cell targets.<sup>111,112</sup> From the ITC thermogram, and its corresponding binding curve, it is possible to obtain information on the  $K_d$  and the reaction stoichiometry.

Philip Johnson's group has extensively used ITC to study the cocaine binding aptamer.<sup>53,113–115</sup> In their most recent work<sup>115</sup> they considered the change in the Gibbs free energy ( $\Delta G$ ) to study the (de)stabilising effect of dangling nucleotides on the aptamer-target complex stability. In order to validate the possibility to relate these structural features with the variation of a thermodynamic parameter, such as  $\Delta G$ , the authors used the adenosine triphosphate (ATP) aptamer as a model system. This approach underlined the importance of using appropriate control experiments, such as using a model system and negative controls, depending on the design of the experiment to aid ITC data interpretation.

Despite its potential, ITC can be easily misinterpreted (i.e. non-appropriate fitting). An example is the difference in  $K_d$  values reported by Amato et al.,<sup>116</sup> using ITC, and by Zavyalova et al.,<sup>117</sup> using a turbidimetric assay, when studying the RA36 oligonucleotide which consists of two repeats of the thrombin-binding aptamer. The discrepancy was investigated by Antipova et al.<sup>118</sup> and their findings supported the theory of Zavyalova

et al. that RA36 has two binding sites with a different affinity. Therefore, the difference in  $K_d$  of the original papers could be explained by the use of a one-set-of-site binding model instead of a two-stage binding process. This shows that the method to fit the experimental data is of great importance for correct ITC results.<sup>119</sup> The fitting will be optimal if the so-called  $c$ -value ( $c = NK_d[A]$ , wherein  $N$  is the number of binding sites per aptamer  $A$ ), ranges between 10 and 500. It is, however, not always possible to work in this window of  $c$ -values, particularly for low affinity systems. In case the aptamer concentration cannot be increased to obtain  $c$ -values in this range, fixing the binding stoichiometry ( $N$ ) during data analysis can minimize the error for experiments performed at low  $c$ -values. Another approach could be the use of displacement methods in which a higher affinity target that binds competitively with the target of interest is used.<sup>120,121</sup> These examples show that ITC is a powerful technique that should be handled with care, otherwise it may lead to conclusions that do not reflect the processes taking place.

Additional insights about the binding mechanism can be acquired by performing ITC measurements at different temperatures and considering the enthalpy variation ( $\Delta H$ ) vs. temperature, i.e. by following the changes in the heat capacity. Amano et al.<sup>122</sup> ascribed the negative heat capacity observed for the aptamer-target complex formed between the high-affinity RNA aptamer and its target protein to the burying of a large hydrophobic region upon binding. Thermodynamic parameters ( $\Delta H$  and entropy variation ( $\Delta S$ )) were also used to determine the structure switching mechanism of cocaine aptamers upon binding to the target.<sup>113</sup> Zhang et al.<sup>123</sup> used the adenosine aptamer, that contains multiple binding sites, to show that the combination of rational sequence design and ITC analysis allows the characterization of each binding site separately and the comparison of their thermodynamic behavior. Also a one-site aptamer was developed for adenosine, using ITC to prove the 1:1 binding model and test it towards possible interfering compounds normally interacting with the corresponding wild type aptamer.<sup>124</sup>

Conventional ITC is suitable for studying aptamer-target interactions with a  $K_d$  in the nM -  $\mu$ M-range.<sup>125</sup> For systems which interact more strongly, it becomes unreliable due to the large variation in injection heat when the molar ratio of aptamer/target is only increased slightly. This problem can be overcome by using ligand-displacement ITC as first proposed by Sigurskjold.<sup>125</sup> Kuo et al. were later able to use this method to determine a  $K_d$  in the pM-range for a streptavidin-binding aptamer.<sup>126</sup>

Apart from providing a complete thermodynamic characterization, ITC apparatus and new processing methods allow to directly analyze association kinetics from raw ITC data. Burnouf et al.<sup>127</sup> developed a new processing method named kinetic ITC (kinITC) in which the shape of each injection peak is analyzed to obtain kinetic information. This can be applied to a large variety of systems from folding to ligand binding. ITC-based kinetics was first applied to long timescale reactions aiming to avoid complications related to the time needed for heat flow detection in the calorimeter cell. The optimization of ITC empirical response model enables now to follow reactions occurring in the order of ten seconds.<sup>128</sup> A kinITC method was incorporated in, for example, the AFFINImeter software to obtain a full thermodynamic and kinetic description of one-step interaction systems<sup>129</sup> (a complete introduction can be found in the work of Munoz et al.<sup>130</sup>). Despite these recent advances, the applicability of kinetic-based ITC to aptamer-target systems is still limited and the majority of the examples are related to enzymatic systems (i.e. to tackle inhibitor binding<sup>131</sup>).

## Electrochemical methods

To avoid covalent labelling, redox probes and rotating droplet electrochemistry (RDE) methods can be employed. The kinetic RDE setup developed by Limoges and co-workers, which is depicted in Figure 14, allowed to *i*) work in hydrodynamic conditions (avoiding slow diffusion limitations), *ii*) have a real-time monitoring and *iii*) assure a rapid mixing of the reactants in the microliter droplet.<sup>132</sup> Challier et al.<sup>111</sup> combined RDE with fluorescence polarization (FP), ITC and quartz crystal microbalance (QCM) to characterize the binding process of L-tyrosinamide to its aptamer. The authors found that the interaction occurs via an induced-fit mechanism in which the L-tyrosinamide first binds to the 5'-end of the aptamer after which the aptamer folds around the target.

Redox-active molecules were also used in other approaches. Guyon et al.<sup>133</sup> proposed a displacement strategy in which non-redox-active aminoglycosides bind to an RNA riboswitch, or 16S rRNA, and displace a redox-active target. This increases the diffusion rate of the redox-active target and leads to an enhancement of the electrochemical signal. Paromomycin was found to be an efficient redox spy probe to study the binding of several aminoglycosides. Also loop-mediated isothermal amplification (LAMP) has been used in combination with aptamers and redox-active labels.<sup>134,135</sup> Xie et al.<sup>134</sup> developed an electrochemical method for the detection of Ochratoxin A. In this approach, a situation in presence and absence of the target is compared. In absence of

the target, the aptamer can undergo amplification during the LAMP reaction resulting in a high amount of dsDNA, which is then able to capture the intercalating methylene blue in solution. The aptamer-target complex is, however, less prone to undergo amplification and as a result free methylene blue is present in solution which can undergo the electrochemical reaction and results in a signal. Recently, Martin et al.<sup>136</sup> offered an interesting overview of intercalating and non-intercalating redox probes compatible with dsDNA (such as osmium complexes, methylene blue and derivatives, Nile blue, etc.) by comparing their performance upon the same LAMP reaction. They concluded that intercalating probes result in a higher LAMP sensitivity.

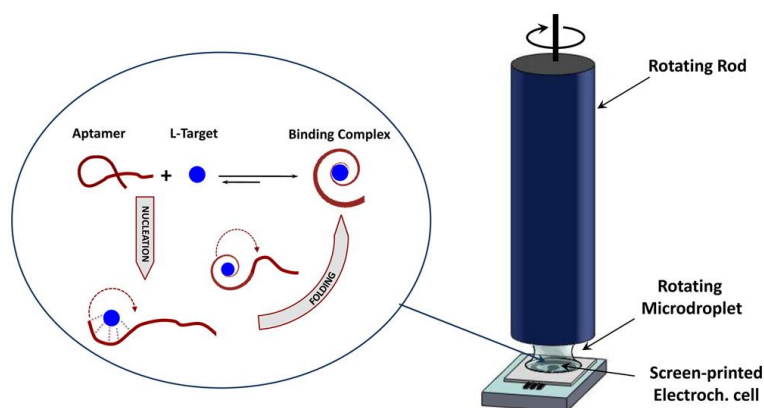


Figure 14. Scheme of the kinetic RDE setup developed by Limoges using a screen-printed three-electrode electrochemical microcell (with a carbon working electrode, a silver reference electrode and a carbon counter-electrode), on the right. Aptamer-target interaction processes investigated with the RDE method, on the left. Reprinted with permission from Challier et al.<sup>111</sup> Copyright (2016) American Chemical Society.

## Fluorescent-based methods

In case the aptamer or target has intrinsic fluorescent properties, these can be used to characterize the aptamer-target interaction in solution although only a few recent examples are available in the literature. Jaeger et al.<sup>137</sup> used the intrinsic fluorescence of ciprofloxacin to study its binding to an RNA aptamer selected for this target. The fluorescence of ciprofloxacin is quenched upon binding to the aptamer and the change in intensity can be correlated to the amount of target bound. This allowed the authors to determine the  $K_d$  of the aptamer-target complex. Moreover, by using derivatives of ciprofloxacin the influence of different side groups was investigated. Fadock et al.<sup>138</sup> used an ochratoxin A aptamer with fluorescent nucleobase analogues at different positions to study the folding and binding. A fluorescent signal is observed upon binding of the target and this can be used to measure the aptamer affinity. Furthermore, since

certain probe locations hampered binding of the target, insights in the binding location were obtained.

#### 2.2.1.2 Labelled methods

Aptamer-target binding kinetics can be characterized in solution also with the help of labelled-based strategies. Once one of the binding partners is labelled with a fluorophore or a quencher, the aptamer-target interaction is indirectly monitored by the changes in fluorescence. These strategies allow estimating aptamer-target kinetics and they are often combined within versatile methods. Additional information regarding the binding mechanism can be acquired by modifying the label or its position (i.e. labelling a different region of the aptamer). In general, the presence of labels may affect the aptamer-target binding process thus labelled-based aptamer-target characterizations require support of other techniques or a complete series of negative controls. The extensive optimization often required for labelled-based strategies makes them more suitable for the characterization of aptamer-target complexes of interest for assays or sensing applications than extensive aptamer screening.

#### Fluorescent-based methods

Well-known for cellular and tissue imaging, fluorophores have been extensively used to label biomolecular complexes, such as protein-protein and DNA/RNA-protein complexes,<sup>139</sup> and to map their interactions even at a single nucleotide level.<sup>140</sup> Once a fluorophore is covalently attached to one of the binding partners, aptamer-target interactions can be monitored by following the changes in the fluorescent quantum yield, through quenching phenomena, fluorescence anisotropy/polarization (FA/FP), etc.

Among these techniques, FA is commonly used in aptamer-target characterization methods.<sup>141</sup> FA records the polarized fluorescence emission of the label in horizontal and vertical directions under polarized excitation light and correlates its rotation speed to the fluorescence lifetime. The changes in anisotropy/polarization reflect the changes in the mobility of the fluorophore (i.e. local rotation or molecular volume), for instance, by the structure-switching of the labelled aptamer upon target binding.

Initially limited to macromolecule-aptamer characterization, FP/FA methods are now also designed for studying aptamers for small-molecules thanks to, for example, molecular mass amplifying strategies<sup>142</sup> or nanomaterial-based enhancement.<sup>143,144</sup> In these methods, the nature and position of the fluorophore label plays a key-role, as exemplified in the study for an aptamer-based FA assay for immunoglobulin E reported by Zhao et al.<sup>141</sup> To optimize the assay, the authors compared a series of aptamers, which differed only in the position of the fluorescein label (Figure 15). Depending on the location of the fluorescein on the DNA sequence, the  $K_d$  was significantly influenced. This also allowed to discriminate close-contact sites and identify the strong affinity binding region. An accurate identification of this region required a large series of experiments in which the target is tested in presence of truncated or modified aptamers, as previously shown in the study of aptamer probes for aflatoxin B1 with tetramethyl rhodamine label.<sup>145</sup> In both examples, the authors underlined that their studies were conceived to be further applied in the design of methods and aptasensors.

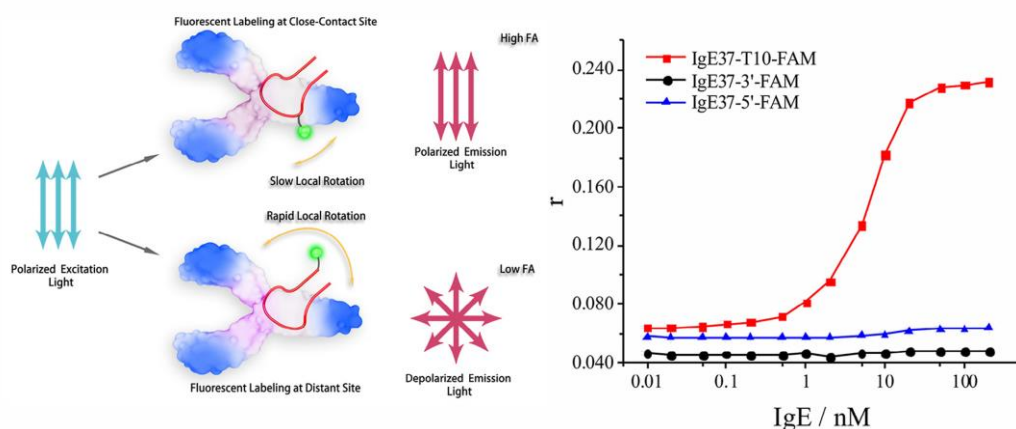


Figure 15. FA analysis of IgE and its aptamer with a single fluorescein label (FAM). The site of the label influences the movement of the label and therefore also the light emitted. Slow local rotations lead to emission of polarized light, while rapid rotations lead to depolarized emission. The results show the label at the T10 position can detect binding of the aptamer to IgE, while the aptamer with label at the 3' or 5' end does not detect the binding. Reprinted with permission from Zhao et al.<sup>141</sup> Copyright (2020) Elsevier.

Indeed, fluorescent-based methods in general are not suitable for simple characterization or screening of aptamer-target kinetics and should be evaluated in consideration to the final aptamer-target application. To optimize the design of the labelled aptamers, a structural characterization by X-ray crystallography can be included, as previously done for fluorescent-labelled RNA aptamers used in transcript tracking.<sup>146</sup> By using a fluorophore-labelled aptamer and a quencher-labelled complementary sequence, Yang et al. investigated the cross-reactivity of aptamers for

steroids.<sup>10</sup> In the presence of a steroid which binds to the aptamer, a fluorescent signal is observed. By comparing the amount of fluorescence observed, the affinity of multiple targets could be distinguished. Fluorophore labels are often combined also with heterogeneous methods. The transition from in-solution to at a confined surface (section 2.2.2) might affect the aptamer performance to a different extent, as discussed by Amaya-González et al.<sup>12</sup> In that work, the authors reported a comparison between biotin and fluorescein labelling showing that fluorescent labels are not always the best choice. Therefore, it is suggested to consider other labelling strategies when relatively high and unreliable  $K_d$  values are obtained with fluorophore labels.

### **Microscale thermophoresis**

Another method in which the fluorescence of a labelled molecule is detected, is microscale thermophoresis (MST). MST is based on the movement of molecules through temperature gradients, the so-called thermophoresis. This movement, which is detected by fluorescence, depends on the size, charge, and hydration shell of an aptamer and at least one of these parameters changes upon binding of a target.<sup>147</sup> Typically, MST is used to determine the binding affinity of an aptamer-target system in which either the target<sup>148</sup> or the aptamer<sup>149,150</sup> is labelled. The technique can, however, also provide some other insights when using multiple aptamers or targets. Rubio et al.<sup>151</sup> showed that two aptamers for the protein  $\beta$ -conglutinin bind to different sites of the proteins using a competitive MST assay. Furthermore, Skouridou et al.<sup>152</sup> investigated a progesterone aptamer and range of steroids with small structural differences. The affinity of the aptamer against all steroids was determined using MST and by overlaying this information with the structures of the steroids, the moieties involved in binding could be identified. MST might not be able to detect binding if the aptamer does not undergo significant conformational changes as shown by Prante et al.<sup>153</sup> using a 25-hydroxyvitamin D aptamer. This aptamer did not show any response at room temperature but at 35 °C, which is closer to the melting temperature of the aptamer, a binding curve could be obtained. This is due to the fact that the aptamer adopts a less structured state at elevated temperatures and folds into its native form upon addition of the target and allows detection using MST.

## 2.2.2 At a confined surface

The first report of an aptamer being used in a biosensor dates back to end of the 20th century when Hieftje et al. showed that aptamers could be used in biosensing by immobilizing a fluorescently labelled anti-thrombin DNA aptamer on a glass support and selectively detecting thrombin in solution.<sup>154</sup> Nowadays aptamer immobilization protocols are commonly used in the design of optical, electrochemical or mass-sensitive aptasensing strategies.<sup>108,155–157</sup> Covalent immobilization protocols were reported requiring to modify the aptamers with specific linkers (chemical functionalities, such as thiols),<sup>158,159</sup> but also noncovalent methods resulted successful, like the electrostatic interaction-based one described by Farjami et al.<sup>160</sup>

Despite its covalent or noncovalent nature, the immobilization process can influence the aptamer-target binding. Potryailo et al. reported beneficial effects in terms of affinity,<sup>154</sup> while other researchers observed a drop in the affinity constants when working at confined surfaces and this drop was ascribed to steric hindrance related to the proximity of the aptamer to the surface of interest.<sup>107,108</sup> Also the nature and length of the linker/spacer used for covalent immobilization was found to influence the affinity.<sup>12,107,157</sup> Increasing the spacer length generally results in a more accessible aptamer and a better affinity towards the target, but too long spacers can reduce the affinity due to a smaller surface density of the aptamer or interaction of the spacer with the aptamer resulting in an incorrect fold.<sup>107,161</sup>

Once at a surface, the aptamer-target binding can be characterized with different methods, which are mostly applied in aptasensing and here briefly though critically discussed. For completeness, even techniques which are not providing binding information, in terms of affinity and conformational changes, are mentioned to emphasize the difference between binding characterization (qualitative and/or quantitative information about the aptamer-target binding) and binding monitoring (verification of the occurrence of the binding).

### 2.2.2.1 Optical methods

Optical detection methods are commonly used in aptasensing strategies to monitor the binding of a target to its aptamer but to a lesser extent for the characterization of aptamer-target interaction. Optical sensing platforms can rely on, e.g., fluorescence or

colorimetric assays,<sup>34</sup> surface-enhanced Raman scattering (SERS),<sup>162</sup> SPR<sup>163,164</sup> and bio-layer interferometry (BLI).<sup>165</sup> Since optical methods are usually used for sensing purposes and not for characterization of aptamers and their complexes, only few examples of optical-based strategies will be presented.

## Surface plasmon resonance

SPR has been extensively used as a label-free method to detect aptamer-target interactions at a confined surface providing information on kinetics and affinity depending on the setup design.<sup>166,167</sup> In general, SPR platforms include a transducing element (planar metal chip), which interrelates the biochemical and optical domain allowing to monitor the changes in reflectivity, and an electronic component.<sup>168,169</sup> The variation in the refractive index (reflectivity) reflects the changes in mass concentration at the chip surface, which is related to the binding event. In a conventional SPR experiment, the reflectivity recorded in resonance units is measured at a fixed angle and wavelength to assure the optimum sensitivity towards the selected aptamer-target complex.

The adaptability of these platforms depends on the possibility to immobilize one of the interacting partners (aptamer or target) on the sensor surface and add the other in solution. In case the target is a small molecule (< 1000 daltons (Da)), it is usually the target that is immobilized while the aptamer is in solution to obtain a detectable variation in reflectivity. Once the architecture is optimized, a wide range of binding conditions can be screened as showed by Minagawa et al. in the selection and characterization of a salivary  $\alpha$ -amylase aptamer.<sup>170</sup> After measuring the  $K_d$  of the candidate sequences, the authors studied the binding specificity of the one with higher affinity by testing it in presence of other related salivary biomarkers. Importantly, the binding affinities determined via SPR platforms cannot be directly compared with these obtained with other techniques, as clearly showed by the dataset presented by Sass et al.<sup>150</sup> Here, the  $K_d$  for an anthracycline aptamer and a truncated form calculated via SPR was two orders of magnitude higher than that determined using MST, which is a labelled immobilization-free strategy. This example underlines how the immobilization step can influence the binding and suggests the importance of designing the characterization protocol of an aptamer by considering its final application. Also the aptamer surface density can have a significant influence on the target binding as shown by Simon et al.<sup>171</sup> The authors used a high throughput SPR imaging system (SPRi) and

showed that the optimal surface density of the aptamer is dependent on the target size; they did so by studying two different aptamers, one for the protein immunoglobulin E and one for the peptide 6xHis-tag.

In addition, SPR was directly combined with SELEX to select an aptamer against a structured RNA, derived from the transcription factor *XBP1*. SPR was allowed to follow the evolution of the aptamers throughout the SELEX cycles and the SPR-SELEX combination resulted in a simultaneous aptamer selection and real-time evaluation of their binding affinity.<sup>172</sup> A similar principle was reported by Jia et al.<sup>173</sup> in which SPRi was combined with SELEX to select and characterize aptamers against the protein lipocalin-1.

### **Surface-enhanced Raman scattering**

SERS showed a wide applicability in multi-analytical aptamer-target characterization studies. Since 2009, the potential of SERS for monitoring aptamer conformational changes was described. Conformational changes can be quantified by a spectral cross-correlation function, as described by Neumann et al.<sup>174</sup> making SERS a suitable complementary technique in aptamer binding studies. Recently, Cui et al.<sup>175</sup> successfully combined the data obtained via BLI, SERS and MD simulations for determining the affinity and conformational changes of the theophylline-binding aptamer upon binding of its target, as summarized in Figure 16. The authors took advantage from the label-free, sensitive and real-time technology of BLI to first evaluate the affinity, which often proceeds aptasensing design<sup>176,177</sup> but does not allow to gain information about conformation changes. The latter were monitored indirectly by comparison of the differences in the SERS spectra and carefully analysing the signals related to the aptamer nucleobases.

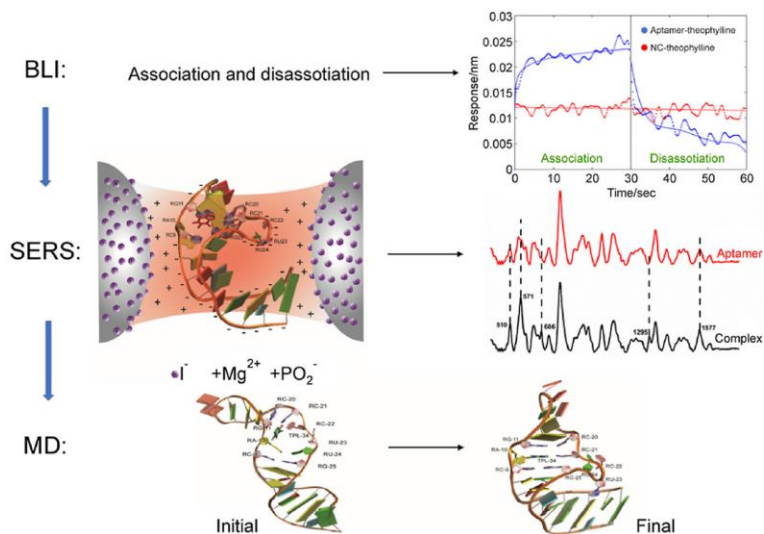


Figure 16. The kinetic parameters of theophylline binding to its aptamer were determined using BLI. The combination with SERS and MD simulations allowed the authors to analyze the conformational changes of the aptamer and finally an in-depth understanding of the aptamer-theophylline binding process was obtained. Reprinted with permission from Cui et al.<sup>175</sup> Copyright (2020) Elsevier.

### 2.2.2.2 Electrochemical techniques

Highly sensitive electrochemical techniques, such as electrochemical impedance spectroscopy, but also potentiometric and amperometric techniques, are widely applied in aptasensing.<sup>178–180</sup> However, their application is often limited to monitoring the aptamer-target binding event and not to the evaluating of kinetic or affinity parameters. Nevertheless, Eissa et al. reported an electrochemical SELEX platform in which the  $K_d$  values of aptamers against 11-deoxycortisol, immobilized at the electrode surface, were determined via square wave voltammetry by estimating peak current changes upon aptamer binding.<sup>181</sup> Afterwards, the authors selected one aptamer and applied this in a voltammetric label-free aptasensor. Despite the sensitivity of electrochemical-based sensing strategies, even down to the sub-picomolar range,<sup>182</sup> they cannot be used to gain further information about the binding event itself.

### 2.2.2.3 Mass-sensitive techniques

QCM is a label-free, mass-sensitive technique in which the resonance frequency of a quartz crystal varies when the mass on the crystal surface changes.<sup>183</sup> Challier et al.<sup>111</sup>

used QCM, with dissipation monitoring, to study the effect of surface immobilization of a L-tyrosinamide-binding aptamer. The  $K_d$  was estimated from these experiments by looking at shifts in QCM frequency at various concentrations of the target and fitting these data. It was found that these values were up to two orders of magnitude higher than the  $K_d$  determined in solution by ITC. These results show again that immobilization of the aptamer can have a significant influence on the aptamer performance. QCM was also combined with SELEX by Hu et al.<sup>184</sup> to monitor the QCM frequency in real-time throughout each selection round and consequently determine the  $K_d$  values of selected aptamer candidates for acrylamide.

## 2.3 Structural studies

Aptamers can adopt a wide range of structural motifs, such as loops, hairpins, pseudoknots and G-quadruplexes. These structural elements define the aptamer structure, which is crucial for target binding. Understanding the structural properties and conformational changes upon binding of a target is therefore a fundamental step in the understanding of how an aptamer works and further prove its selectivity toward the ligand. In this frame, we describe the main analytical techniques to study aptamer structure which can be divided in two main sections: high-resolution techniques where an atomic resolution is reached (section 2.3.1) and low-resolution techniques which provide general information on the size and shape of the aptamer (section 2.3.2).

### 2.3.1 High-resolution techniques

There are only three techniques which can provide atomic resolution structures: NMR spectroscopy, X-ray crystallography and electron microscopy (EM). NMR spectroscopy, commonly used for aptamers in complex with small molecules, and X-ray crystallography, mainly used for aptamer-protein complexes, are discussed in more detail in section 2.3.1.1 and 2.3.1.2, respectively. Finally, in the category of EM, especially cryo-EM is interesting since molecules are frozen but hydrated at cryogenic temperatures.<sup>185</sup> Therefore, cryo-EM allows imaging of samples in their native state. Despite its great potential, cryo-EM has not been used to determine aptamer structure so far.

### 2.3.1.1 NMR spectroscopy

NMR spectroscopy has been used since the 1990s to study the 3D structure of aptamers and aptamer-target complexes. The use of NMR spectroscopy is limited to relatively small biomolecules (< 40 kilodaltons (kDa)) due to broadening and overlap of NMR signals when molecules become too complex. Secondary and tertiary structure determination of free-form aptamers is difficult since they often have an undefined, heterogeneous form in their unbound state. However, NMR spectroscopy is an excellent tool to study the structures of aptamer in their bound state. Currently, over one hundred aptamer-target structures have been determined by NMR spectroscopy.<sup>56</sup>

Structure determination of aptamers is often difficult due to overlap of signals, but even when the structure cannot be determined, important information on aptamers can be obtained. The imino proton region of guanosine, thymidine and uridine (10 to 15 ppm) provides information about the base pairing in aptamers, as was demonstrated by Minagawa et al.<sup>170</sup> and by Philip Johnson's group.<sup>113,186,187</sup> The first used the imino proton signals of an aptamer against salivary  $\alpha$ -amylase measured at different temperatures to obtain information on the thermal stability of the aptamer. The disappearance of signals from 40 °C onwards indicated disruption of the base pairs and the consequent unfolding of the aptamer. Neves et al.<sup>113</sup> showed that the imino signals can indicate how well-structured certain aptamers are. They did so by using a set of cocaine-binding aptamers with different stem lengths. Aptamers with many sharp peaks in the imino region were found to be rigidly structured while fewer and broad peaks are attributed to loosely structured and dynamic aptamers. Similar conclusions were drawn by analyzing the exchange rate of imino protons of two of these cocaine-binding aptamers. The exchange rate values were higher for the more dynamic aptamers compared to the rigidly structured one.<sup>186</sup> Upon binding of the target, the exchange rate values were reduced indicating a more stable and less solvent accessible structure. Interestingly, base pairs which were already preformed also experience a reduction in dynamics upon binding.<sup>187</sup> Verdonck et al.<sup>188</sup> studied a duplex with imidazole-tethered thymidines. These thymidines can interact with a nucleotide in the opposite strand and form a so-called pK<sub>a</sub>-motif, which increases the thermal stability of the duplex.<sup>189</sup> Using a combination of MD simulations and nuclear Overhauser spectroscopy, the authors confirmed the formation of pK<sub>a</sub>-motifs in the duplex. Furthermore, they applied the same principle to a L-argininamide-binding aptamer and found the motif occurs and stabilises the aptamer while maintaining the binding capacity.

By comparison of the NMR signals in the absence and presence of a target, conformational changes upon target binding can be monitored. Oguro et al.<sup>190</sup> showed this for a spermine-binding aptamer which has a stem-loop structure. The terminal side of the structure is loose while the loop side forms a stable structure, and the binding of spermine induced a conformational change. More recently, structural changes of a tetramethylrhodamine-binding aptamer upon binding of the target were monitored.<sup>191</sup> The authors found the aptamer undergoes extensive structural changes and forms a stable three-way junction upon binding. Slavkovic et al.<sup>192</sup> used a combination of thermal stability, ITC and NMR experiments to determine why the ATP-binding aptamer binds two copies of the target cooperatively. By investigating the aptamer and two related constructs, a population shift mechanism was discovered which results in a cooperative binding mechanism.

Besides the commonly used <sup>1</sup>H NMR, also fluorine-19 (<sup>19</sup>F) NMR, first reported by Marshall et al.<sup>193</sup> in 1977, can be used to analyze structural features of nucleic acids. <sup>19</sup>F NMR has several advantages compared to <sup>1</sup>H NMR:<sup>194</sup> *i*) the <sup>19</sup>F nucleus is highly sensitive to changes in the environment and is therefore ideal to study conformational changes; *ii*) <sup>19</sup>F is absent in natural compounds and incorporation of a <sup>19</sup>F probe in nucleic acids, either nucleotide-based within the sequence<sup>195</sup> or at the end of the sequence,<sup>196</sup> generates spectra which are easy to interpret. Ishizuka et al.<sup>197</sup> used <sup>19</sup>F NMR to investigate the thrombin-binding aptamer with G-quadruplex structure (Figure 17). Several aptamer variants with a single <sup>19</sup>F probe incorporated at each thymine position were used to: *i*) monitor structural changes in function of temperature and *ii*) determine thermodynamic parameters of the G-quadruplex. Moreover, the binding of thrombin to the aptamer was followed by considering the changes in chemical shift.

NMR was also used to obtain structural information on nucleic acids in living cells.<sup>198,199</sup> Recently, Broft et al.<sup>200</sup> studied a riboswitch using in-cell NMR and observed binding of 2'-deoxyguanosine to the aptamer domain of the riboswitch. This technique holds great potential to investigate structure-function relationships of aptamers within cells to monitor aptamer treatment.

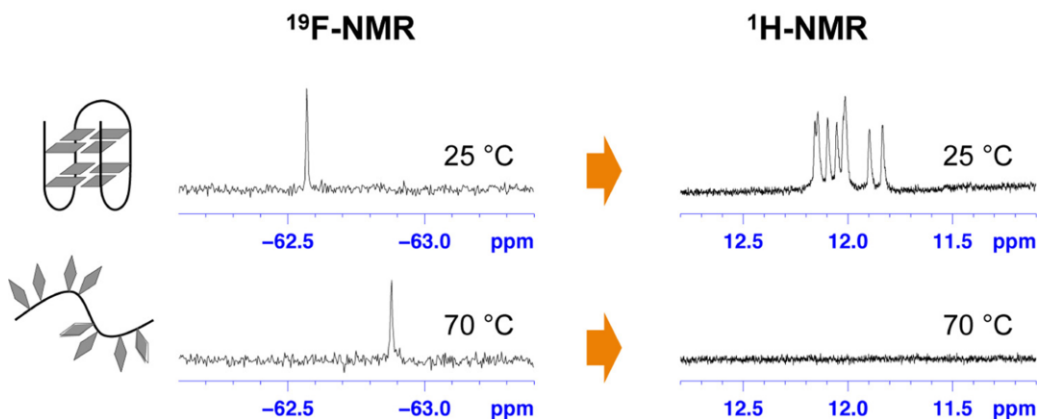


Figure 17.  $^{19}\text{F}$  NMR and  $^1\text{H}$  NMR spectra of the thrombin-binding aptamer with an  $^{19}\text{F}$ -labelled nucleotide at the T10 position at 25 or 70 °C. The quadruplex is unfolded at 70 °C which results in a change of chemical shift in  $^{19}\text{F}$  NMR and a disappearance of the signals in  $^1\text{H}$  NMR. Reprinted with permission from Ishizuka et al.<sup>197</sup> Copyright (2017) American Chemical Society.

### 2.3.1.2 X-ray crystallography

X-ray crystallography is mostly used to investigate aptamers in complex with relatively large molecules, such as proteins (a detailed overview of the use of X-ray crystallography to study aptamer-protein interactions was provided by Gelinas et al.<sup>201</sup>). A crystal structure provides detailed information on the interactions between the two binding partners. It is, however, often difficult to obtain well-diffracting crystals since the co-crystallization depends on many factors such as the purity of the compounds, the conformation of the aptamer and the ratio between the aptamer and its target. Therefore, finding the conditions which provide suitable diffracting crystals is usually a time-consuming process of trial and error.<sup>57</sup> Dynamic and conformationally flexible molecules are difficult to crystallize as was recently shown by Schmidt et al.<sup>202</sup> The authors studied an aptamer against the flexible peptide ghrelin and were not able to crystallize the aptamer or peptide alone due to the many conformational changes they undergo. The crystal structure of the aptamer-ghrelin complex was, however, determined since this complex is more rigid compared to the two components alone.

Regular X-ray crystallography provides static information of a molecule, but Stagno et al.<sup>203</sup> used serial femtosecond crystallography (SFX) with an X-ray free-electron laser to determine transient states of the adenine riboswitch aptamer domain. During SFX experiments, snapshots of static structures are recorded and over time this reveals conformational changes of processes in the picosecond to millisecond timescale. Upon

binding of adenine, structures of four states of the adenine riboswitch aptamer domain were determined. Later, Ding et al.<sup>204</sup> used SFX in combination with NMR to determine the conformational flexibility of the same riboswitch aptamer domain in both the free and bound form. This technique holds great potential to obtain high resolution data on conformational changes of aptamers and their complexes.

## 2.3.2 Low resolution techniques

Several techniques can provide structural information on the aptamer conformation without providing a full atomic resolution structure. These so-called low-resolution techniques provide general information on the size and shape of the aptamer or provide information on secondary structure elements. The two frequently used techniques providing this type of information are CD spectroscopy and small-angle X-ray scattering (SAXS).

### 2.3.2.1 Circular dichroism spectroscopy

CD spectroscopy is a widely used technique to study the secondary structure of aptamers and their conformational changes upon binding. Various secondary structural elements have distinguished CD spectra with specific maxima and minima in ellipticity in function of the wavelength. The main advantages of CD spectroscopy are that it is relatively inexpensive, fast and has a high sensitivity.<sup>205</sup> As CD spectroscopy only determines the global features of macromolecules, it is often used in combination with other techniques.

CD spectroscopy is frequently applied to study aptamers with a G-quadruplex structure. Zhang et al.<sup>206</sup> studied the PW17 aptamer in which G-quadruplex formation is induced by the presence of potassium ions (Figure 18). It was shown that at low K<sup>+</sup> concentrations the aptamer is loose and unstable and upon increasing the K<sup>+</sup> concentration the aptamer folded into a parallel G-quadruplex. Wiedman et al.<sup>207</sup> determined a G-quadruplex structure of an aptamer against posaconazole, an antifungal drug. They found that the G-quadruplex structure is essential for binding the target and that Mg<sup>2+</sup> enhances the folding of the G-quadruplex. CD spectroscopy was also used in combination with online predicting tools for an aptamer against the antibody rituximab.<sup>208</sup> Six different aptamers were studied, and it was found that two

aptamers fold into a G-quadruplex, while the other four adopt a structure similar to B-DNA helices. More recently, Aljohani et al.<sup>209</sup> used the change in the intensity of the ellipticity as a measure of the conformational change and strength of the binding. They studied an aptamer against dabigatran etexilate, an anti-coagulant, together with a truncated form and found that upon addition of the target the truncated form has a more sensitive response. Therefore, they stated the truncated form is a better binder than the native aptamer.

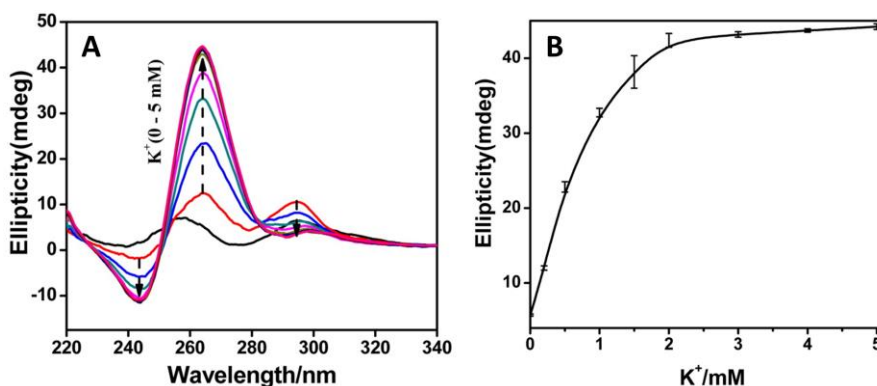


Figure 18. A) CD spectra of the PW17 aptamer with G-quadruplex structure. Spectra are recorded with  $K^+$  concentrations from 0.02 mM to 5 mM from bottom to top. B) The CD intensity at 264 nm is plotted in function of the  $K^+$  concentration. The CD spectroscopy results show the G-quadruplex formation is induced by the presence of  $K^+$  and that from 2 mM  $K^+$  onwards a stable structure is formed. Reprinted with permission from Zhang et al.<sup>206</sup> Copyright (2016) American Chemical Society.

CD spectroscopy can also be used to investigate the structural stability of aptamers. Yang et al.<sup>94</sup> reported CD-melting curves of a thrombin-binding aptamer in the free form and bound to the natural product jatrorrhizine. It was found that this target increases the thermal stability, and thus the conformational stability, of the G-quadruplex structure.

### 2.3.2.2 Small-angle X-ray scattering

SAXS is often used as a complementary method and allows to investigate the spatial molecule structure and conformational changes induced by either varying conditions (e.g. temperature and pH) or target binding.<sup>210</sup> From SAXS results, a spatial distribution of the electron density of the aptamer can be built to obtain the general aptamer shape (Figure 19).

The structure of two aptamers against the interleukin-6 receptor were investigated using SAXS and were found to have an elongated shape and existed as a dimer in solution.<sup>211,212</sup> Recently, Schmidt et al.<sup>202</sup> studied an aptamer against the peptide ghrelin with non-natural L-nucleotides which are resistant to nucleases. SAXS experiments showed the aptamer undergoes a conformational change and becomes more compact upon binding of the target. Moreover, the experiments allowed to derive the molecular weight and suggested the aptamer exists as a dimer in solution, while presenting a 1:1 stoichiometry aptamer-ghrelin. Tomilin et al.<sup>213</sup> proposed a four-step process to obtain a 3D structure of a thrombin-binding aptamer. From SAXS results, a structural envelope was built. Using MD simulations, a 3D model was built based on the primary and secondary structure of the aptamer and in a final step this model was compared with the experimental SAXS data to further refine the model.

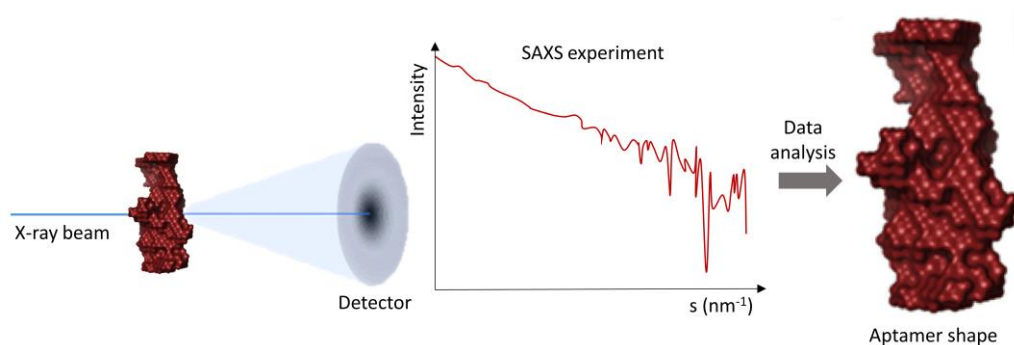


Figure 19. The general working principle to obtain information on the aptamer shape using SAXS. SAXS experiments are performed on an aptamer in solution and consequently a structural envelope is built from these SAXS results.

## 2.4 Conclusions

This chapter aimed to describe the main analytical tools for aptamer characterization, including their limits and potential, and to answer the need for a more critical evaluation of aptamer performance which was recently emphasized in the literature. By grouping the analytical techniques presented in respect of the information they provide, we aim to help researchers to identify the most suitable characterization protocol for the desired application. Therefore, it is fundamental to distinguish kinetic and thermodynamic studies from structural ones. The examples presented per section underline the consequences that the choice of a certain analytical protocol can have

and how misleading the data interpretation can be, with further implications in the following applications (i.e. non-functioning aptamers applied in aptasensors).

The techniques discussed in this review are compared in Figure 20 concerning the type of information provided. Several techniques provide quantitative or semi-quantitative kinetic and/or thermodynamic information on the binding event (e.g. binding affinity and/or stoichiometry), while they do not provide any structural information. Only two techniques, i.e. native (IM-)MS and SERS, provide information on the binding event and structure of the aptamer-target complex. Both techniques only provide qualitative information on the binding (e.g. ranking of binding affinities) and low-resolution structural information (e.g. general shape). Low-resolution structural information can also be obtained by CD and SAXS but these do not provide any information on the binding event. Finally, high-resolution structural information (e.g. a structure at atomic resolution) can be obtained by NMR spectroscopy or X-ray crystallography.

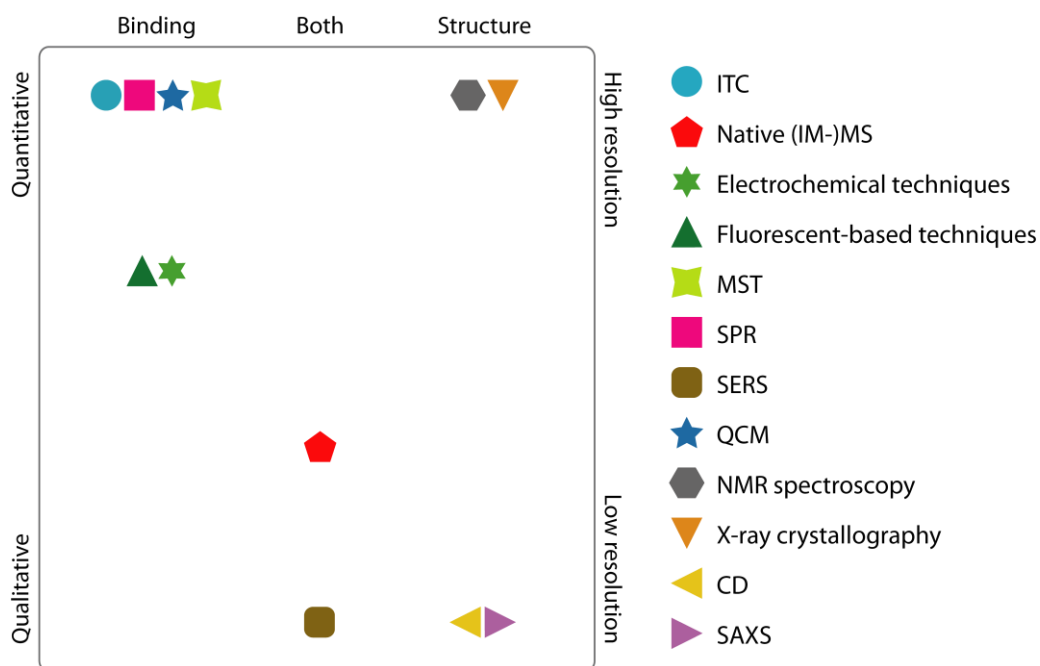


Figure 20. Overview of the information on aptamer-target complexes obtained using each of the discussed techniques. The information concerns the binding, the structure or both. Binding information can be the quantitative, semi-quantitative or qualitative while for structural information the level of resolution is considered (high or low).

These general observations lead to the conclusion that multi-analytical approaches are recommended to thoroughly characterize aptamers and aptamer-target complexes. In

this context, the design of the analytical protocol plays a key-role and the choice of the analytical tools require an extensive knowledge and continuous updates of techniques, instrumentation and software. The critical selection of the analytical tools needs to take into account the final application of the aptamer since certain techniques can report different affinities of a given aptamer. Indeed, the examples showed that introducing a label to the aptamer or immobilizing the aptamer can alter the aptamer behavior (i.e. testing the aptamer complex in solution or at a confined surface). Therefore, a rational choice between label-free, labelled or immobilized approaches is recommended.

Apart from the accurate evaluation of the applicability and performance of the described analytical techniques, several other parameters should be taken into account when designing the characterization protocol, such as costs, speed, amount of sample and user-friendliness (Figure 21). The costs include the instrument costs, its maintenance and the protocol-related costs (e.g. sample preparation). The speed ranges from minutes to hours for an analysis and is important to consider, especially for screening purposes for which you preferably have a fast technique. The amount of sample includes both the concentration (nM to mM-range) and volume ( $\mu$ L-range) required to perform an analysis. Finally, the user-friendliness of the techniques is evaluated. This parameter does not only include the easiness of performing the experiment but also following procedures such as data analysis and interpretation.

It is worth noticing that the rising interest in an in-depth characterization of aptamer-target complexes is leading to the development of new analytical tools often already known for other applications. One of the examples is kinetic ITC for studying the kinetics of aptamer-target binding or on a structural side, cryo-EM. Despite the variety of tools already available it is fundamental to be able to map the gaps of these techniques in terms of information provided and limits of applicability. Certain multi-analytical approaches cannot be afforded/applied in routine studies for the development of aptamers for medical treatments, etc. There is still the urgent need to design, or redesign, new analytical tools able to provide high performance and rapid analysis at an affordable cost.

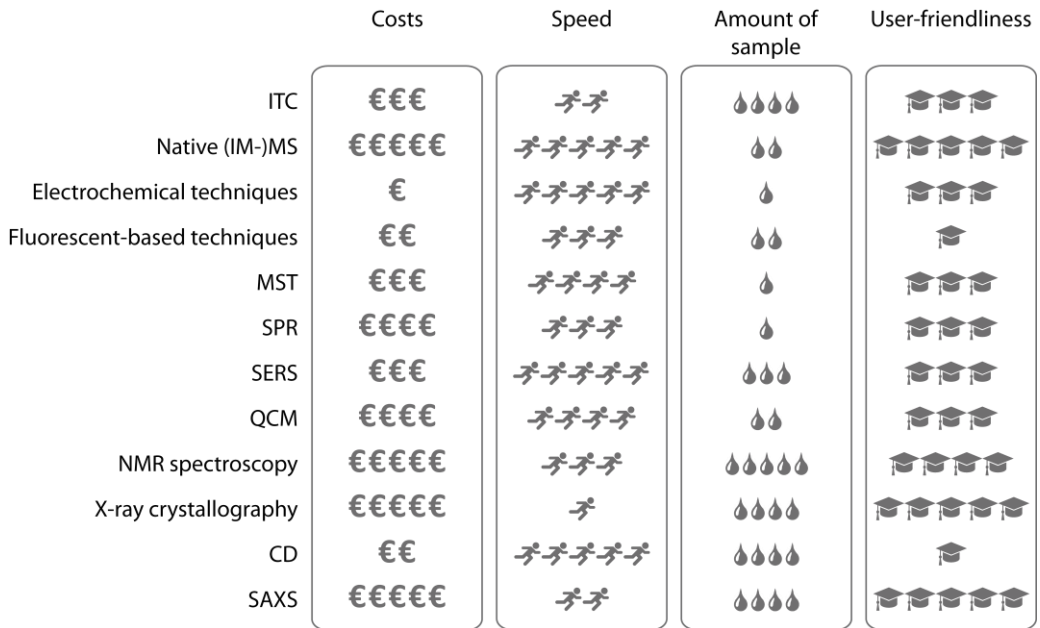


Figure 21. Comparison of the discussed techniques in terms of costs, speed, amount of sample required and user-friendliness.

# |3

## Mapping the structure and stability of aptamers

### **Section 3.3.1** - Is CID structure-sensitive for aptamers?

Part of this work was performed by Maria Stavrou under my supervision (Erasmus student at UA)

### **Section 3.3.2** - Probing the conformational stability of aptamers with CIU

Collaboration with Stefano Piccolo and Valérie Gabelica

At European Institute of Chemistry and Biology (IECB), Pessac, France

### **Section 3.3.3** - Can ETD provide structural information of aptamers?

Collaboration with Tom Vennekens and Thomas De Vijlder

At Janssen Pharmaceutical Companies of Johnson & Johnson, Beerse, Belgium



## Abstract

In this chapter the use of native mass spectrometry in combination with collision-induced dissociation (CID), collision-induced unfolding and electron transfer dissociation (ETD) for determining the higher-order structure of oligonucleotides was evaluated. A set of related cocaine-binding aptamers, displaying a range of folding properties, was used as a model system. First, CID was explored to verify whether unpaired nucleobases fragment more easily than nucleobases involved in a base pair. Second, the difference in gas-phase stabilities of aptamers with different stem lengths was studied and compared with the solution behavior of these aptamers. Finally, the possibility to fragment aptamers using ETD was studied, since this radical-based fragmentation technique might provide structural information of aptamers as is the case for proteins.

### 3.1. Introduction

Throughout this chapter, different fragmentation methods are explored to evaluate their potential to obtain information on the higher-order structure and conformational stability of aptamers. Several cocaine-binding aptamers were used throughout this study. The cocaine-binding aptamers were first synthesized around 20 years ago<sup>214,215</sup> and are currently one of the best characterized class of aptamers for small molecules. The structure of these aptamers consists of three stems built around a three-way junction (Figure 24). Although all cocaine-binding aptamers are closely related, they exhibit different conformational dynamics (i.e. concerning structural rigidity) and are therefore an ideal system for a comparative MS analysis.

CID is commonly used to fragment denatured oligonucleotides and to obtain information on their sequence and possible modifications (e.g. methylation).<sup>59,216–219</sup> CID typically provides many different fragments, as shown in Figure 22, which allows sequencing of the oligonucleotide. Here, we use structured oligonucleotides, i.e. aptamers, to investigate the potential of CID to map unpaired nucleotides in aptamers measured in native conditions, and thereby obtaining higher-order structural information. Our hypothesis is that fragmentation is more likely to occur at or near more exposed and unpaired nucleotides/nucleobases, which are not engaged in hydrogen bonding, meaning that the corresponding fragments produced by collisional activation would be more abundant.

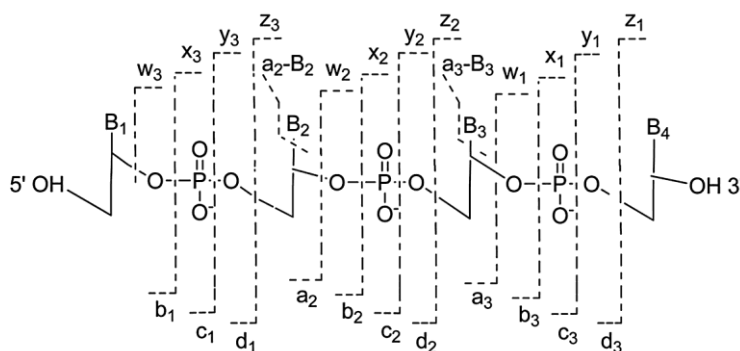


Figure 22. Scheme of the oligonucleotide fragmentation nomenclature.<sup>220</sup>

In a next step, CIU experiments were performed on aptamers with different stem lengths to probe their gas-phase stabilities and check whether their structural characteristics that are present in solution, i.e. unstructured vs. structured, can be

detected and investigated in the gas-phase by sampling their unfolding behavior. The expectation is that aptamers with fewer electrostatic interactions, particularly hydrogen bonds, are less structured and display a lower energy threshold for unfolding of the aptamer.

Finally, the radical-based activation technique ETD was briefly explored to fragment positively charged aptamers and to investigate whether higher-order structural information could be obtained. In ETD, electrons are transferred from an electron donor to a multiply charged cation, which results in the formation of charge-reduced species.<sup>221</sup> The primary reaction products are radical cations that are usually unstable and can undergo dissociation, although sometimes fragments can also remain weakly bound to each other. If the conditions during the experiments are gentle enough to maintain the noncovalent interactions, as during native MS, it is expected that the ETD reaction only takes place at the exposed surface of the analyte, where fragmentation sites are accessible. Therefore, ETD can, similar to proteins,<sup>222,223</sup> preferentially fragment more exposed sites and therefore release fragments of unpaired residues more easily. Smith and Brodbelt<sup>224</sup> performed ETD on positively charged oligonucleotides consisting of 6 nucleotides and found that they generate multiple ETD product ions as shown in Figure 23.

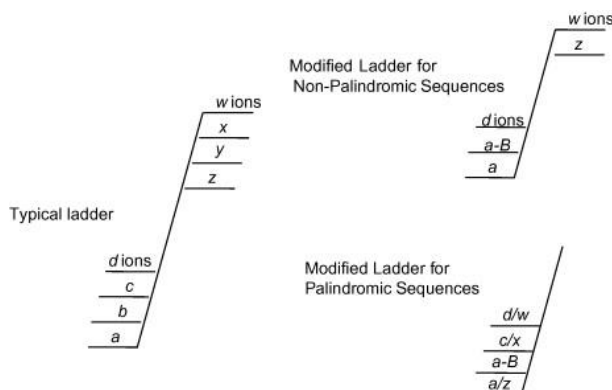


Figure 23. The ETD product ions observed for non-palindromic and palindromic sequences for six-mers by Smith and Brodbelt.<sup>224</sup>

## 3.2 Materials and methods

### 3.2.1 Sample preparation

#### 3.2.1.1 CID and ETD experiments

Aptamers and dsDNA sequences (as depicted in Figure 24 and Figure 28, respectively) were purchased from Eurogentec (Belgium) purified with a differential precipitation method. Ammonium acetate solution (7.5 M, molecular biology grade) was purchased from Sigma-Aldrich (Bornem, Belgium). All solutions were prepared using deionized water which had a conductivity of  $\leq 0.1 \mu\text{S}/\text{cm}$  after purification using a Silex I B system from Eurowater (Nazareth-Eke, Belgium). All aptamers were buffer exchanged to 300 mM ammonium acetate pH 6.8 using Micro Bio-spin columns (Bio-gelP6, Bio-rad). Samples of 10  $\mu\text{M}$  were prepared in 300 mM ammonium acetate pH 6.8.

#### 3.2.1.2 CIU experiments

Aptamers (OR7-A, OR8-A, MN19-A, MN4 and OR11) were obtained from Integrated DNA Technologies (Leuven, Belgium) and dissolved in RNase-free water (Ambion™, ThermoFischer Scientific, France). Samples were desalted using Amicon Ultra centrifugal filters with a molecular weight cut-off of 3 kDa. Three consecutive steps of a buffer exchange to 0.5 M trimethylammonium acetate (3 times, 13000 rpm, 30 min), 500 mM ammonium acetate (2 times, 13000 rpm, 30 min) and RNase-free water (5 times, 13000 rpm, 30 min) were performed. The concentrations of the aptamers was afterwards verified using a Nanodrop2000 (Thermo Scientific). Final samples were prepared by diluting the aptamers to 10  $\mu\text{M}$  in the desired buffer: 25 mM ammonium acetate.

### 3.2.2 MS protocol

#### 3.2.2.1 CID experiments

The MS analyses were performed on a Synapt G2 HDMS Q-TOF instrument (Waters, Manchester, UK). Approximately 3-5  $\mu\text{l}$  of sample was introduced into the mass

spectrometer, using nESI with gold-coated borosilicate glass tapered-tip capillaries made in-house. Experiments were performed in the positive ionization mode. The following settings were used: spray capillary voltage 1.5-1.7 kV, source temperature 30 °C, sampling cone 25 V, extraction cone 1 V, trap collision energy 5-50 V (as indicated in the text), transfer collision energy 0 V, trap DC bias 45 V, IMS wave height 22 V and IMS wave velocity 500 m/s. The backing pressure was set to 2.7 mbar, the source pressure to  $2.2 \cdot 10^{-3}$  mbar, the trap pressure to  $2.3 \cdot 10^{-2}$  mbar, the IMS pressure to 3.0 mbar, the transfer pressure to  $2.4 \cdot 10^{-2}$  mbar. All data were analyzed using MassLynx v4.2 (Waters).

### 3.2.2.2 CIU experiments

The MS analyses were performed on an Agilent 6560 instrument (Agilent, United States) in the negative ionization mode. The samples were ionized using ESI with a flow rate of 3  $\mu$ L/min. The IM drift tube was filled with helium at 3.89 Torr. The following settings were used: drying gas 5 L/min, nebulizer pressure 13 psig, capillary voltage -3.5 kV, fragmentor -300 V to -600 V (in steps of 10 V, as indicated in the text), high pressure funnel RF -160  $V_{p-p}$ , trap funnel delta -140 V, trap funnel RF -160  $V_{p-p}$ , trap entrance grid delta -2 V. All data were analyzed using IM-MS Browser B.08.00 and CIU plots were made using Sigmaplot 12.5. CCS values were extracted from the deprotonated 7- charge state (no mass selection) from the full width at half maximum of the peak without salt adducts. As an example: for the MN19-A aptamer this corresponds to an m/z-window from 1591.5 to 1592.5 m/z.

### 3.2.2.3 ETD experiments

The ETD experiments were performed on a Fusion Lumos instrument (ThermoFisher Scientific). The samples were ionized using ESI in the positive ionization mode with a flow rate of 10  $\mu$ L/min. The following settings were used: spray voltage 3.5 kV, sheath gas 30 arb. unit, auxiliary gas 4.3 arb. unit, sweep gas 0 arb. unit, ETD reaction time 10-100 ms, maximum injection time 100 ms, and AGC target  $5 \cdot 10^4$ . Fluoroanthene (ThermoFisher Scientific) was used as ETD reagent. All data were analyzed using Xcalibur.

## 3.3 Results and discussion

### 3.3.1 Is CID structure-sensitive for aptamers?

To investigate whether CID can provide higher-order structural information of aptamers by, for example, releasing the unpaired nucleotides more easily, two closely related cocaine-binding aptamers (MN19 and MN4) were used (Figure 24). The structure of both aptamers consists of three stems built around a three-way junction. The key difference between these aptamers is the length of stem 1. In the MN19 aptamer stem 2 and 3 are already folded without a target while stem 1 is not formed and only folds upon binding of the target. Therefore, this aptamer is in the literature described as a loosely folded structure.<sup>52,225</sup> In contrast, the MN4 aptamer has a longer stem 1 which is already formed in the absence of the target and is, thus, described as structurally rigid.<sup>52</sup> As a control multiple dsDNA (Figure 28) strands with mismatches were used.

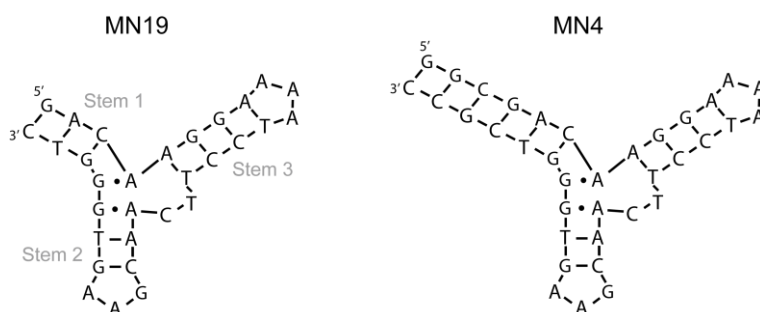


Figure 24. Secondary structures of the MN19 and MN4 cocaine-binding aptamers. Watson-Crick base pairs are indicated with dashes and non-Watson-Crick base pairs are shown as dots.

In Figure 25, the mass spectrum of the MN19 aptamer acquired in the positive ionization mode is characterized by a highly intense 5+ charge state and a low-intensity 4+ charge state. The experimentally determined mass of MN19 was found to be  $9274 \pm 3$  Da and corresponds well with the theoretical mass of 9273.1 Da. The mass spectrum of the MN4 aptamer shows 6+ and 5+ charge states from which an experimental mass of  $11129 \pm 3$  Da was determined. Again, this corresponds well with the theoretical mass of 11128.3 Da. The broadness of the peaks is due to  $\text{NH}_4^+$  and  $\text{Na}^+$  adducts that are not fully resolved in this experiment.

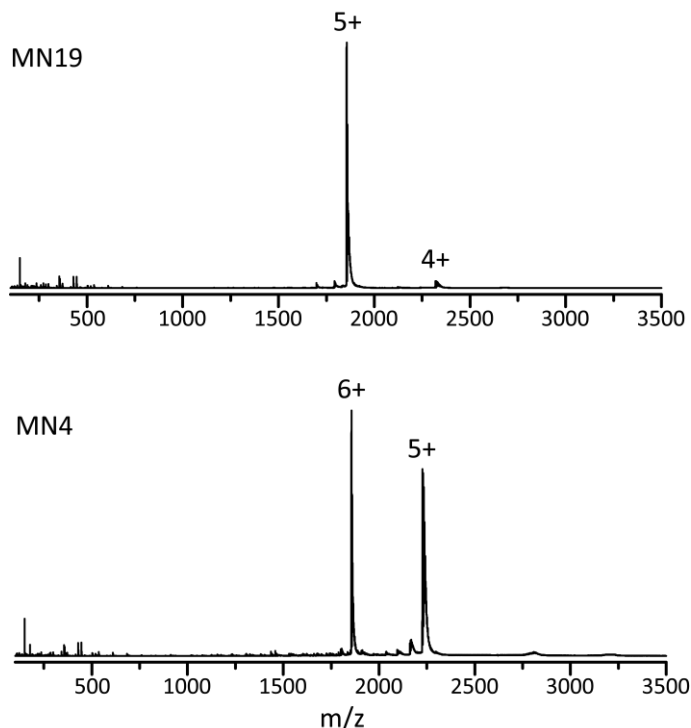


Figure 25. Native MS of the MN19 and MN4 cocaine-binding aptamers in 300 mM ammonium acetate in the positive ionization mode.

### 3.3.1.1 The loosely structured MN19 aptamer

Prior to increasing the trap collision energy, the 5+ charge state of the MN19 aptamer, at 1855 m/z, was selected (product ion scan shown in Figure 26A, top). Since fragmentation is expected and new peaks will appear, this will aid the data interpretation. By raising the acceleration voltage to 40 V, multiple new peaks are observed in the spectrum (Figure 26A, middle). In the low m/z-range, three peaks are observed at 112.1 m/z, 136.1 m/z and 152.1 m/z. These peaks can be assigned to the nucleobases cytosine, adenine and guanine, respectively, which indicates the glycosidic bond between the nucleobase and the sugar moiety is broken. The fact that these bases are observed indicates that positively charged nucleobases are lost upon increasing the trap collision energy. Interestingly, thymine is not observed (theoretical m/z of 127.1) meaning that either no thymine is released from the aptamer or that thymine is released as a neutral species. The loss of thymine as a neutral nucleobase is likely as the proton affinity of thymine is much lower than for the other nucleobases and protonation of thymine is strongly disfavored.<sup>226</sup>

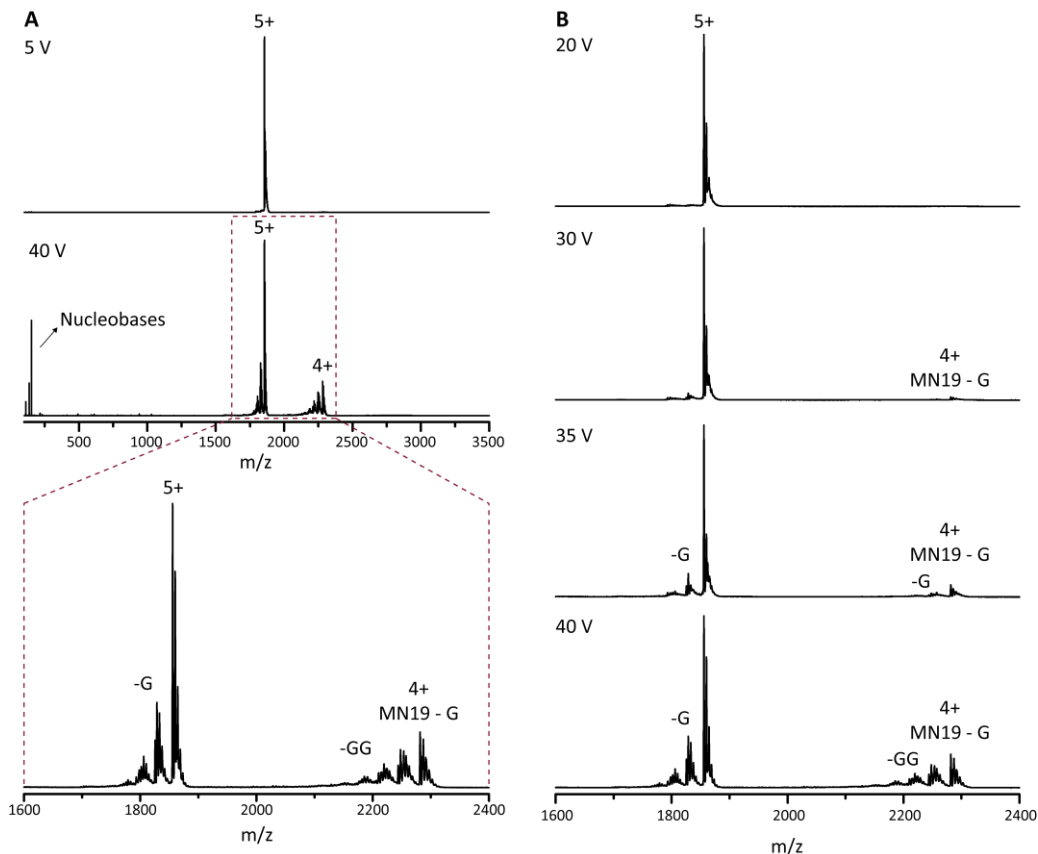


Figure 26. A) Product ion spectra of the MN19 cocaine-binding aptamer acquired in 300 mM ammonium acetate. The 5+ charge state, at 1855 m/z, was selected (top) and fragmented using a trap collision energy of 40 V (middle). A zoom of the region with fragments is shown in the bottom spectrum. B) Product ion spectra of the MN19 cocaine-binding aptamer acquired in 300 mM ammonium acetate with a trap collision energy varying from 20 to 40 V.

By zooming in on the 5+ charge state at 40 V collision energy, one can clearly observe new peaks in front of the selected peak at 1855 m/z (Figure 26A, bottom). The mass difference in between these peaks may reveal which nucleobases are lost and are, thus, possibly unpaired in the aptamer structure. First, a mass difference of 151 Da, corresponding to guanine, is observed. The second nucleobase loss at the 5+ charge state could not be assigned to a specific nucleobase due to low intensity. Information on further nucleobase losses was, however, obtained by looking at the 4+ charge state which arises due to the loss of a charged nucleobase, more specifically guanine. Further assignment of the peaks, revealed the loss of two more guanines. Therefore, are in total three guanine nucleobases released from the aptamer upon increasing the collision energy.

More detailed information on which nucleobase is lost at which energy is provided in Figure 26B. The acceleration voltage was step-wise increased up to 40 V. Only from 30 V onwards, the loss of nucleobases is observed. At 30 V, there is a low intensity peak corresponding to the first neutral nucleobase loss at the 5+ charge state, although it cannot be assigned to a specific nucleobase yet. Moreover, a 4+ charge state of the MN19 aptamer minus one guanine is observed due to the loss of a charged guanine. Increasing the energy further enhances the signal of the product ions and makes it possible to assign more and more losses of guanine. These results indicate a gradual release of the nucleobases.

By looking at the proposed MN19 aptamer structure (Figure 24), one can see that only one guanine is unpaired in the loop of stem 2. However, since MN19 is loosely structured, stem 1 is not formed in absence of the target and therefore two more guanines are unpaired. This could explain the loss of the three guanine nucleobases, although the question arises why the other unpaired nucleobases are not observed at the 5+ and 4+ charge states.

### 3.3.1.2 The structured MN4 aptamer

To investigate this in more detail, the same experiments were performed with the structurally rigid MN4 aptamer. This aptamer has stem 1 already formed in absence of the target and has therefore fewer unpaired nucleobases which should make the assignment easier.

For this aptamer, the 6+ charge state was selected first and fragmented afterwards (Figure 27A). Again, the nucleobases cytosine, adenine and guanine are observed in the low  $m/z$ -range. Moreover, due to the loss of charged nucleobases, both 5+ and 4+ charge states are observed. The 5+ charge state corresponds to the MN4 aptamer minus one charged guanine and the 4+ charge state to the MN4 aptamer minus two charged guanines. Furthermore, the mass differences observed within one charge state are used for a further assignment of the nucleobase losses. For the 6+ charge state, only one nucleobase loss could be assigned. The first nucleobase lost is again a guanine. For the 5+ charge state, it was possible to assign multiple peaks and the order of nucleobase release was found to be guanine, guanine and adenine. Similar observations are made for the 4+ charge state, where both a guanine and an adenine are lost in addition to the two guanines already lost to generate the 4+ charge state. By

selecting and fragmenting the 5+ charge state of the aptamer, very little fragmentation was observed. The only information obtained is the loss of a guanine.

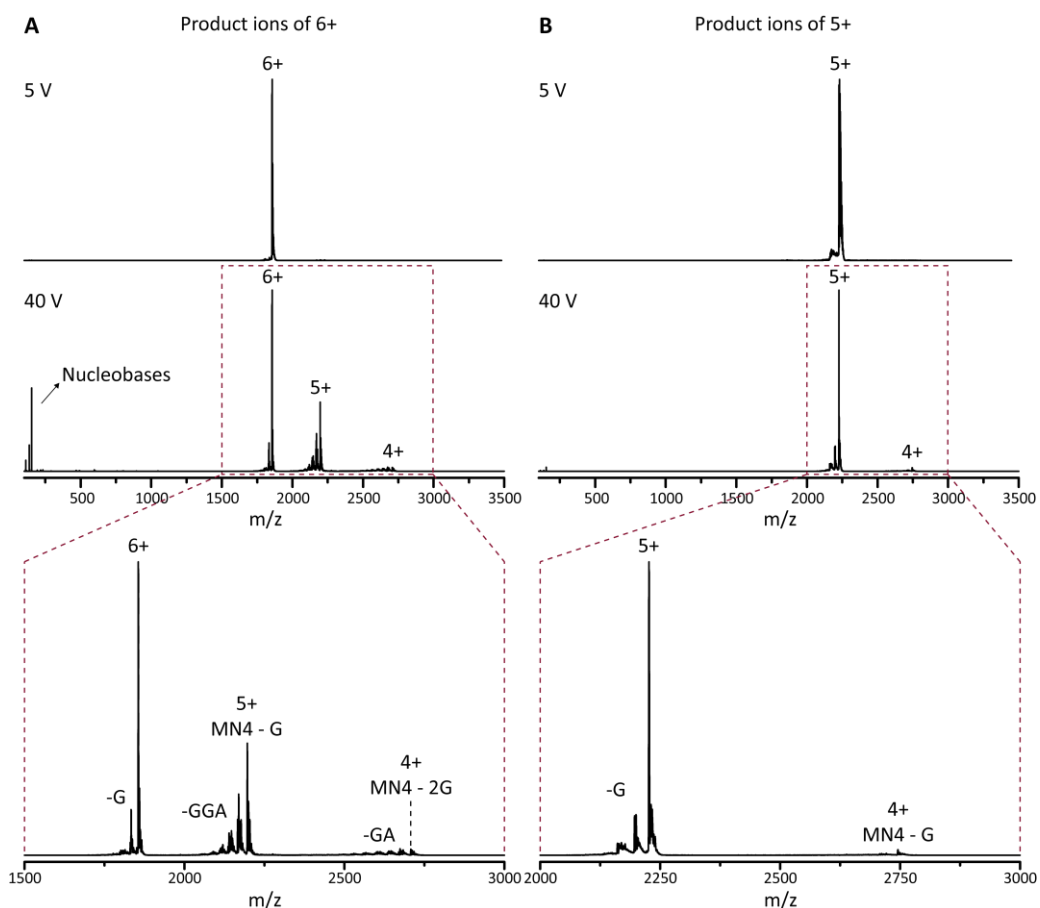


Figure 27. Product ion spectra of the MN4 cocaine-binding aptamer acquired in 300 mM ammonium acetate. A) The 6+ charge state, at 1855 m/z, and B) 5+ charge state, at 2226 m/z, were selected (top) and fragmented using a trap collision energy of 40 V (middle). A zoom of the regions with fragments are shown in the bottom spectra.

By combining the information of all charge states, we can conclude that three guanines and one adenine are released from the aptamer upon increasing the collision energy. In the structure of the MN4 aptamer (Figure 24) there is, however, only one unpaired guanine while there are five unpaired adenines and also an unpaired cytosine and thymine. Therefore, the CID experiments performed on the aptamers do not seem to yield direct structural information concerning paired or unpaired nucleotides.

### 3.3.1.3 Double-stranded DNA

Aptamers are, however, complicated systems and the exact structures are often not well understood. Therefore, CID experiments were performed on simpler systems which are better characterized. Six different dsDNA sequences of equal length, of which three sequences have one mismatch and two sequences have two mismatches, were subjected to fragmentation (Figure 28). The hypothesis is that mismatched nucleobases are unpaired (or paired more weakly in case of non-Watson Crick base pairs) and are therefore more easily released when the applied energy is increased.

dsDNA 1	AAA CAG TCG CTG CAT CTA AGA CCA G TTT GTC AGC GAC GTA GAT TCT GGT C
dsDNA 2	AAA CAG TCG <b>ATG</b> CAT CTA AGA CCA G TTT GTC AGC <b>GAC</b> GTA GAT TCT GGT C
dsDNA 3	AAA CAG TCG CTG CAT <b>CGA</b> AGA CCA G TTT GTC AGC GAC GTA <b>GAT</b> TCT GGT C
dsDNA 4	AAA CAG TCG <b>ATG</b> CAT <b>CGA</b> AGA CCA G TTT GTC AGC <b>GAC</b> GTA <b>GAT</b> TCT GGT C
dsDNA 5	AAA CAG TCG <b>ATG</b> CAT <b>CCA</b> AGA CCA G TTT GTC AGC <b>GAC</b> GTA <b>GAT</b> TCT GGT C
dsDNA 6	AAA CAG TCG CTG CAT <b>CCA</b> AGA CCA G TTT GTC AGC GAC GTA <b>GAT</b> TCT GGT C

Figure 28. dsDNA sequences used for CID fragmentation. Watson-Crick base pairs are indicated in black and mismatches in blue.

The 7+ charge state of each dsDNA was selected and fragmented using a trap collision energy of 50 V (Figure 29). As observed for the aptamers, lower charge states (6+ and 5+) appear due to the loss of charged nucleobases. Once again, only cytosine, adenine and guanine are observed in the low m/z-range. The nature of the released nucleobases was again determined based on the mass differences between the peaks of the 7+, 6+ and 5+ charge states. Interestingly, only guanine losses were observed for all dsDNA sequences used, independent of the presence and nature of the mismatches. For all dsDNA sequences, except dsDNA 4, the loss of up to four guanine losses could be assigned. For dsDNA 4, the loss of only three guanine losses were assigned.

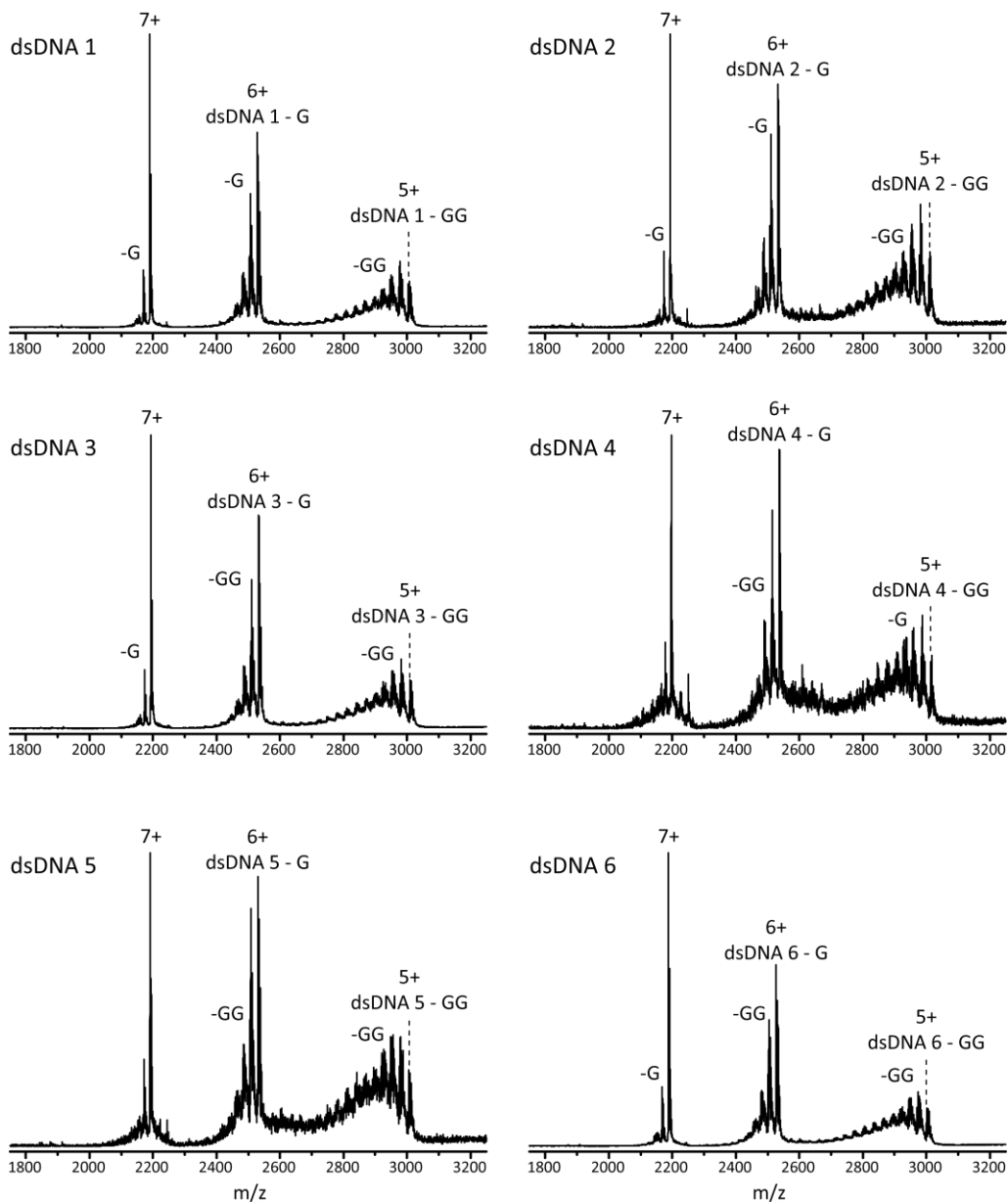


Figure 29. Product ion spectra of the six different dsDNA sequences (shown in Figure 28) acquired in 300 mM ammonium acetate. The 7+ charge state was selected and fragmented using a trap collision energy of 50 V.

None of the dsDNA sequences have, however, three or four unpaired guanines indicating that not only unpaired nucleobases are lost during the CID process. Therefore, the CID experiments performed on the dsDNA do not seem to yield direct structural information concerning paired or unpaired nucleotides. The fact that mainly

guanine losses were observed for both the aptamers and the dsDNA corresponds well with the observations of Ickert et al.<sup>219</sup> The authors investigated multiple dsDNA oligonucleotides and found that glycosidic bond was broken and the bases were lost in the following order: guanine > adenine >> cytosine >>> thymine. Interestingly, the glycosidic bond of the purines (i.e. guanine and adenine) spontaneously hydrolyzes faster than the glycosidic bond of the pyrimidines (i.e. cytosine and thymine) in nature.<sup>227</sup> This implies that the glycosidic bond of purines has a lower stability in general. Furthermore, the gas-phase decomposition process mirrors the stability in solution or in the environment.

### 3.3.2 Probing the conformational stability of aptamers with CIU

In a next step it was investigated whether CIU can provide information on the conformational dynamics and unfolding stability of aptamers. Again, closely related cocaine-binding aptamers were used for this study. Five aptamers with different lengths of stem 1 were selected: OR7, OR8, MN19, MN4 and OR11 with one, two, three, six and seven base pairs in stem 1, respectively. Previously, Neves et al.<sup>228</sup> determined using ITC and NMR spectroscopy that cocaine-binding aptamers with less than three base pairs are completely unstructured and have no base pairs formed, meaning the short stem 1 compromises the folding of the complete aptamer. Aptamers with three base pairs are partially structured with only stem 1 unstructured, while these with more than three base pairs are structured. Thus, OR7, OR8 and MN19 are expected to be (partially) unstructured while MN4 and OR11 should be structured.

As shown in Figure 25 for the MN19 and MN4 aptamer, the charge state distribution varies due to the difference in number of nucleotides of these aptamers. To avoid different charge state distributions and have similar masses for all aptamers, the three shortest aptamers were modified by adding deoxyadenosines to both the 3' and 5'-end to obtain the same number of nucleotides (36) as the MN4 aptamer (Figure 30). Deoxyadenosines were chosen since these form one of the weakest homo base pairs mismatches (GG > TT ≥ AA > CC).<sup>229,230</sup> Since guanines and cytosines can form secondary structures like G-quadruplexes and i-motifs, respectively, these nucleobases were not considered for the extension.

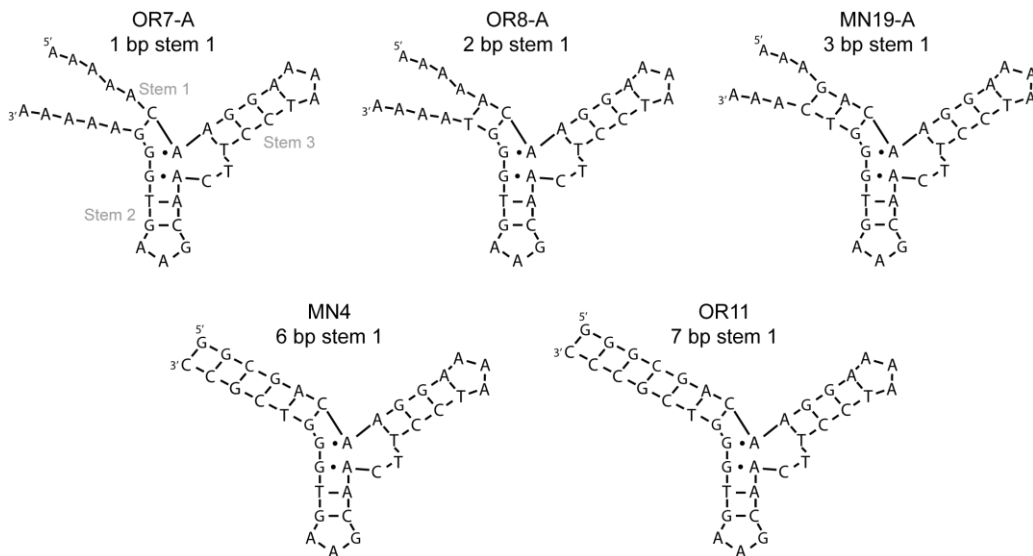


Figure 30. Secondary structures of the cocaine-binding aptamers used for the CIU experiments. Watson-Crick base pairs are indicated with dashes and non-Watson-Crick base pairs are shown as dots.

The native MS spectra of the five cocaine-binding aptamers (with deoxyadenosine extensions) are shown in Figure 31. The 7-, 6- and 5- charge states are observed for all aptamers. Moreover, a second charge state distribution of higher charge states (up to 13-) is observed for the OR7-A, OR8-A and MN19-A aptamers. This can be explained by the (partially) unstructured nature of these aptamers in 25 mM ammonium acetate as reported in the literature.<sup>113,228</sup> The MN4 and OR11 aptamers lack this second charge state distribution, which matches the expectation that they should be more structured.

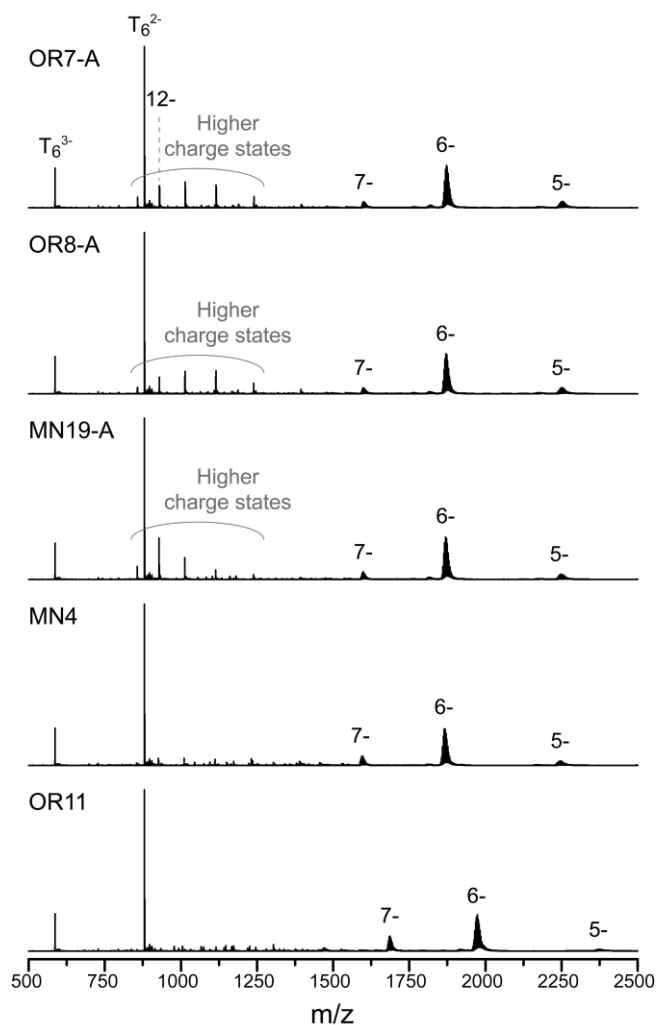


Figure 31. Native MS spectra of OR7-A, OR8-A, MN19-A, MN4 and OR11 (from top to bottom) acquired in 25 mM ammonium acetate in the negative ionization mode. The samples were spiked with  $T_6$  for standardizing the intensity scale.

Increasing the fragmentor voltage, and thereby collisionally activating the ion, during the MS analysis leads to removal of  $NH_4^+$  adducts as shown for the 7- charge state of the MN19-A aptamer in Figure 32. For the following CIU experiments, only the peak of the deprotonated MN19-A aptamer without any adducts was used to extract CCS values (more details are provided in section 3.2.2.2). The number of adducts could otherwise have an effect on the voltage required to unfold the aptamer which makes comparison between aptamers difficult.

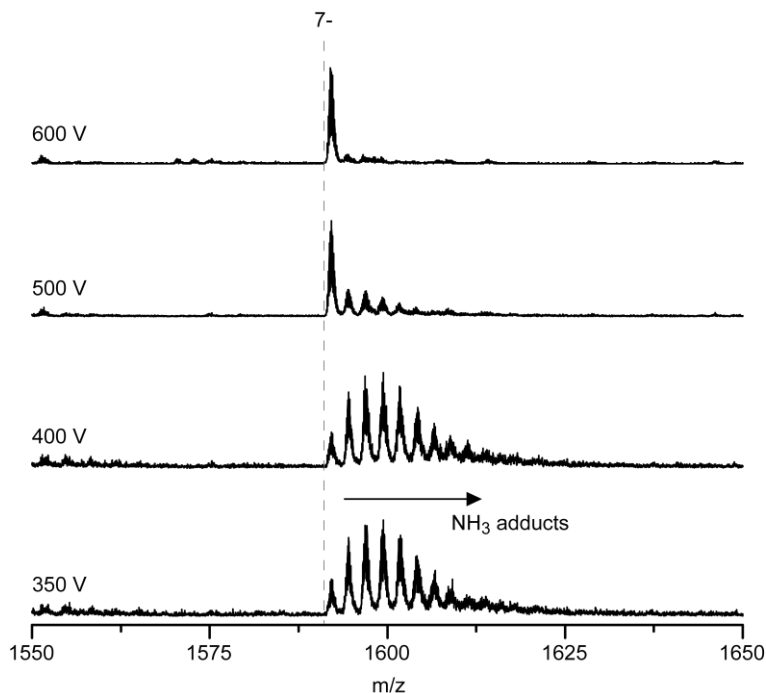


Figure 32. Zoom of the 7- charge state of the MN19-A aptamer in 25 mM ammonium acetate upon increasing the fragmentor voltage from 350 V (bottom) to 600 V (top).

The CIU plots in Figure 33 show that the gas-phase stabilities of the aptamers depend on their stem length since they have a different unfolding threshold. OR7-A and OR8-A, with only one and two base pairs in stem 1, respectively, unfold at 475 V. The MN19-A aptamer, which has three base pairs in stem 1 and is partially folded in solution, unfolds at 490 V. The aptamers which are structurally rigid in solution and have six and seven base pairs (MN4 and OR11, respectively) unfold at even higher fragmentor voltages: 510 V and 565 V, respectively. These results show that the number of base pairs in stem 1 corresponds well with the relative gas-phase stabilities of these aptamers: the higher the number of base pairs, the higher the threshold for unfolding and the more stable the aptamer is. It can be noticed that the CCS distributions of the unfolded state are broad and slightly different for all aptamers, except MN4, but no clear trends that could explain these differences were observed.

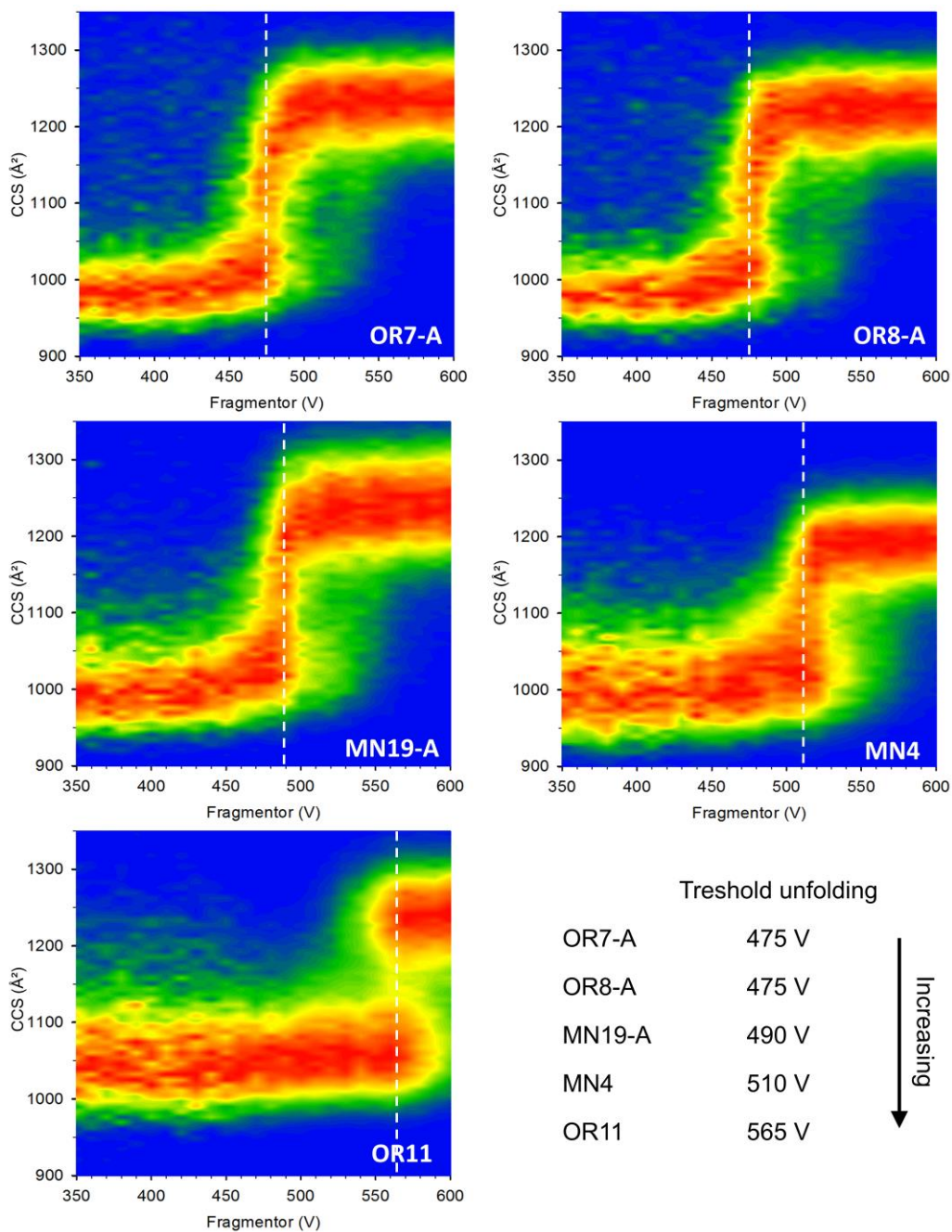


Figure 33. CIU plots of the OR7-A, OR8-A, MN19-A, MN4 and OR11 aptamer acquired in 25 mM ammonium acetate. The CCS, extracted from the 7- charge state, is plotted in function of the fragmentor voltage and the intensity is shown using a color scale (red is 100 % and blue 0 %). Dotted white lines indicate the threshold for unfolding. CCS values were extracted from the deprotonated peak, without  $\text{NH}_4^+$  adducts.

It is important to point out that the OR7-A and OR8-A aptamers can still undergo unfolding in the gas-phase although they are fully unfolded in solution. This can be explained by several factors. First, fully unfolded does not necessarily mean completely extended since unfolded structures can still be relatively compact. Second, the 7-charge state was selected for these experiments which is a fairly compact state and not one of the highest charge states which are probably more extended. Finally, aptamers can undergo some compaction in the gas-phase, as was reported in the literature for dsDNA.<sup>91</sup> Applying collisional activation to this compact state can thus fully unfold the aptamers in the gas-phase.

In conclusion, the key characteristics of the aptamers related to the number of base pairs in stem 1 (unstructured, partially structured and structured) can be monitored and detected in the gas-phase using CIU. It was found that fewer hydrogen bonds in stem 1 of the cocaine-binding aptamers and the less structured nature of certain aptamers makes them easier to unfold.

### 3.3.3 Can ETD provide structural information of aptamers?

The MN19 cocaine-binding aptamer was used to investigate whether ETD can provide higher-order structural information of aptamers by preferentially fragmenting accessible sites. It was found that during ETD experiments of the MN19 aptamer, charge reduction takes place, indicating there is an efficient transfer of the electrons to the DNA. There is, however, no fragmentation visible. One possible explanation could be that the noncovalent interactions between the fragments are keeping the fragments together. Therefore, CID was applied after the ETD reaction, but only typical CID fragments could be assigned and no ETD fragments. This indicates that although the electrons are transferred to the oligonucleotides, no fragmentation occurs. Most likely, this can be attributed to the stabilization of the unpaired electrons by  $\pi$ - $\pi$  stacking interactions of neighboring nucleobases as described by Hari et al.<sup>231</sup> Also Smith and Brodbelt<sup>224</sup> previously identified limited backbone cleavages in oligonucleotides as a result of ETD, especially when the length of the oligonucleotide increases. In conclusion, positive ionization mode ETD could not be used to obtain structural information of aptamers.

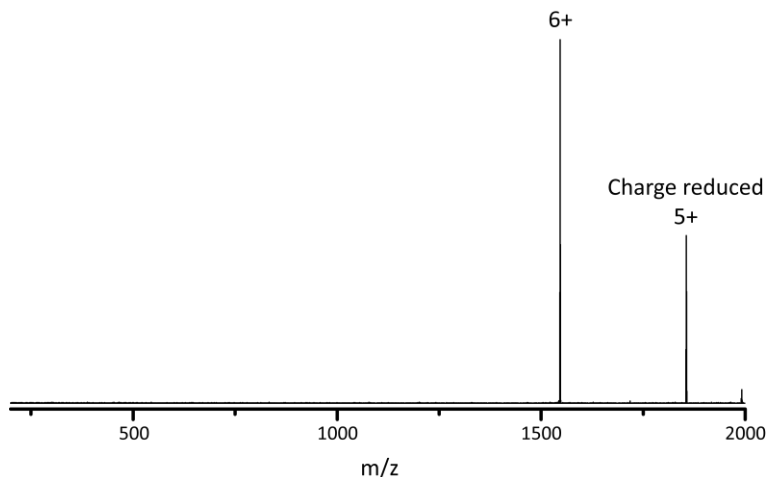


Figure 34. Native ETD of the MN19 acquired in 300 mM ammonium acetate. The 6+ charge state (1546.45 m/z) was selected prior to the ETD reaction.

### 3.4 Conclusions

Although CID, CIU and ETD have shown significant promise for the characterization of protein structure and/or stability, the obtained results show that CID and ETD sequencing cannot contribute to the characterization of the higher-order structure of aptamers. By using CID under native conditions, the preferential release of guanine, and to a lesser extent adenine and cytosine, residues was observed independent of the structure (paired vs. unpaired nucleotides). ETD did not yield sequence or higher-order structure information since the expected fragmentation, as typically observed for proteins, was not observed for the aptamers. Most likely, this can be attributed to the stabilization of the unpaired electrons by  $\pi$ - $\pi$  stacking between the nucleobases.

However, CIU did show great promise to analyze the conformational dynamics and gas-phase stabilities of aptamers. More rigid cocaine-binding aptamers were found to unfold at higher collisional energies than (partially) unstructured aptamers and have therefore higher gas-phase stabilities. Although there are indications that the aptamers are compacted in the gas-phase,<sup>91</sup> the observed trend of gas-phase stabilities corresponds well with the known solution behavior of the aptamers.

These findings show that certain techniques, which are now commonly used for the characterization of proteins, do not always provide immediate results for aptamers, or

maybe even other biomolecules in general. It is, however, worthwhile exploring these techniques further for oligonucleotides.

# |4

Dynamic structure and stability of nucleosomes investigated by native ion mobility-mass spectrometry and fragmentation approaches

**Elise Daems, Ahmad Ali-Ahmad, Konstantin Barylyuk, Esther M. Martin, Mats de Jong, Karolien De Wael, Nikolina Sekulić, and Frank Sobott**

*Manuscript in preparation*



## Abstract

Nucleosomes are protein-DNA complexes that play an important role in allowing access to the genetic information during the DNA transcription process. The shape and dynamics of nucleosomes can be influenced by minor changes in the protein or DNA sequences. Moreover, these changes can alter the properties of nucleosomes and therefore attract other protein complexes to reach the final chromatin structure. Understanding how the nucleosome structure is affected by the histones and DNA is, thus, important to understand how epigenetics works. In this chapter, native ion mobility-mass spectrometry (IM-MS) is used to analyze whether changes in nucleosome composition, i.e. a different histone variant or DNA sequence, influence the dynamic behavior of the nucleosome. More specifically, we focused on the H3 histone and its variant centromere protein A for the protein part and the superpositioning 601 sequence and a naturally occurring AT-rich sequence present in centromeres for the DNA part. In total, four types of nucleosomes were assembled and characterized using native MS to map the contribution of the histone and DNA modifications on the conformational dynamics of nucleosomes.

## 4.1. Introduction

Within eukaryotic cells, long lengths of DNA are compacted into heterogeneous assemblies of proteins and DNA known as chromatin. The fundamental subunit of chromatin is a nucleosome. Nucleosomes consist of 145-147 base pairs of DNA wrapped around protein complexes that are made up of eight subunits called histones. A histone octamer contains two copies each of H2A, H2B, H3, and H4 which are assembled as H2A/H2B dimers and an (H3/H4)<sub>2</sub> tetramer.<sup>232</sup> Each histone has a structured region that interacts with the DNA, and flexible histone tails that extend away from the nucleosome core.<sup>233</sup> Posttranslational modifications of histone tails (and to a lesser extent the histone core) play a crucial role in the regulation of chromatin structure that in turns controls gene expression.<sup>234</sup> Also, different histone variants further expand the diversity of nucleosomes across genomes.<sup>235</sup> Finally, certain DNA sequences are more amenable to nucleosome formation than others.<sup>236</sup> As a result, different chromatin architectures that are governing the accessibility of DNA, could be primarily initiated directly at the nucleosome level – through histones and DNA on which it assembles. Small changes in protein and DNA sequence are affecting the shape and dynamics of nucleosomes which is reflected directly in different properties of assembled nucleosome arrays that are then attracting other protein complexes to reach the final chromatin state. Thus, understanding how the nucleosome structure is affected by histones and DNA is central to understanding how epigenetics works.

Actually, since the first crystal structure of a nucleosome was reported in 1997,<sup>237</sup> which revealed the nucleosome structure at atomic resolution, it took some time to start appreciating the dynamic nature of nucleosomes. Numerous subsequent nucleosome structures were mostly identical, leading to the impression that nucleosomes are very rigid. However, similar crystallization conditions were probably always favoring the same crystal packing resulting in extremely similar final structures. In-solution techniques, like fluorescent resonance energy transfer and SAXS, started to give a glimpse on the dynamic nature of nucleosomes that is influenced by histone modifications, histone variants and the DNA sequence.<sup>238,239</sup> Recently, with the fast development of cryo-EM, it became obvious, at high-resolution, that even canonical nucleosomes on a super-positioning DNA sequence adopt several different conformations.<sup>240,241</sup> However, even with cryo-EM only a limited amount of nucleosome conformations can be captured during freezing without falling apart. In order to thoroughly analyze conformational assemblies of a nucleosome differing in

histone variant or DNA sequence, we need a technique that is inclusive, robust and highly sensitive to conformational and stability features.

Native MS can offer this, but only a few examples of native MS studies of nucleosomes are published in the literature. Saikusa et al. found that both histone multimers<sup>242</sup> and the whole nucleosome<sup>243</sup> have structural variety in which the histone tails have different degrees of compaction. Mayanagi et al.<sup>244</sup> later used native MS to determine the stoichiometry of an octasome in complex with a histone chaperone.

We applied native MS to investigate how histone variants and different DNA sequences affect the conformational dynamics and stability of the nucleosome using native MS techniques. In particular, we focused on histone H3 and its variant CENP-A, which epigenetically marks centromeres. The core histones are among the most conserved proteins in all organisms. Not only are they conserved across evolution, but also within variants of core histones within the same species.<sup>245</sup> For the human histone H3, four known variants (H3.1, H3.2, H3.3 and H3.1t) exist which differ by only a few amino acids. In contrast, the centromere-specific variant of human H3, CENP-A, shares only 62 % identity with H3.1 in the histone core domain, while tails are completely dissimilar. The CENP-A nucleosome alone is able to recruit the full functional centromere complex (reviewed by Sekulić et al.<sup>246</sup>). We reasoned that the high sequence divergence between H3 and CENP-A, and unique features of CENP-A nucleosomes that were proposed based on cryo-EM structures, hydrogen deuterium exchange and MNase digestions (reviewed by Ali-Ahmad and Sekulić<sup>247</sup>) would provide a good system to study. Furthermore, we also wanted to test the effect of the sequence on nucleosome dynamics and stability. Here, we focus on the well-characterized super-positioning 601 sequence<sup>248</sup> and the naturally occurring AT-rich DNA sequence present in centromeres on the human X chromosome (further referred as the NAS sequence).<sup>249</sup>

Using CENP-A and H3 histones and 601 and NAS sequences, we assembled 4 types of nucleosomes: the H3 nucleosome on the 601 sequence (H3<sup>601</sup>), the H3 nucleosome on the NAS sequence (H3<sup>NAS</sup>), the CENP-A nucleosome on the 601 sequence (CENP-A<sup>601</sup>), and the CENP-A nucleosome on the NAS sequence (CENP-A<sup>NAS</sup>) (see Figure 35). Next, native IM-MS was used to explore whether changes in nucleosome structure, contributed by a specific histone and DNA composition, influence the dynamic behavior of nucleosomes.

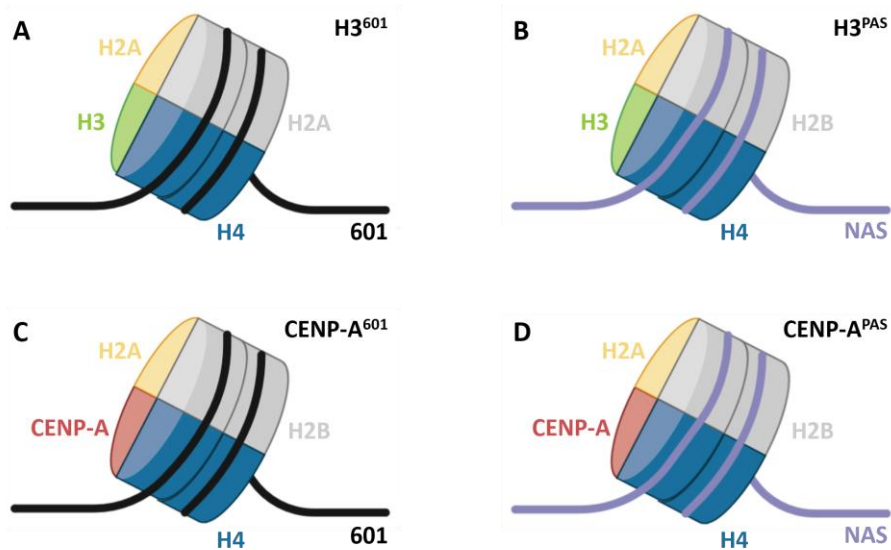


Figure 35. Schematic representations of A) the H3 nucleosome on the 601 sequence ( $H3^{601}$ ), B) the H3 nucleosome on the NAS sequence ( $H3^{NAS}$ ), C) the CENP-A nucleosome on the 601 sequence ( $CENP-A^{601}$ ), and D) the CENP-A nucleosome on the NAS sequence ( $CENP-A^{NAS}$ ).

## 4.2 Materials and methods

### 4.2.1 Sample preparation

Human histones were recombinantly expressed in *E. coli* pLysS cells and purified as previously described by Ali-Ahmad et al.<sup>250</sup> Briefly, soluble CENP-A/H4 tetramers were expressed using bicistronic construct cloned in pET28 vector and purified using hydroxyapatite beads and cation exchange chromatography. H3, H4, H2A and H2B histones were individually expressed in inclusion bodies and purified in denaturing conditions using size exclusion and cation exchange chromatography. H3/H4 tetramers and H2A/H2B dimers were assembled by mixing the histones at equimolar ratios in denaturing conditions, followed by three rounds of dialysis in refolding buffer (20 mM Tris, 2 M NaCl, 0.5 mM ethylenediaminetetraacetic acid (EDTA), and 5 mM 2-mercaptoethanol) and a size exclusion chromatography. 147 bp  $\alpha$ -satellite (Bunick) DNA and 145 bp 601 DNA were amplified in *E. coli* HB101 cells using plasmids with eight copies and six copies, respectively. The DNA was extracted and purified using the same protocol described by Dyer et al.<sup>251</sup> Purified plasmids were digested with EcoRV and purified using anion exchange chromatography.

Human CENP-A and H3 nucleosomes were assembled by mixing the histone tetramer (CENP-A/H4 or H3/H4), the histone dimer H2A/H2B and the DNA at a 1/2/1 molar ratio in high salt buffer (20 mM Tris, 2 M NaCl, 0.5 mM EDTA, and 2 mM dithiothreitol). The salt was then gradually dialyzed out overnight to reach 0 mM. The nucleosome quality was checked using native-PAGE gel electrophoresis. Prior to the MS experiments, the nucleosomes were dialyzed against 100 mM aqueous ammonium acetate (pH 6.9) and stored for a short time at 4 °C until used.

## 4.2.2 Native MS

Native MS experiments were carried out on a Synapt G1 (Waters) operating in the positive ionization mode. Aliquots of 3-5  $\mu\text{L}$  were loaded into platinum-coated capillaries prepared in-house and infused into the mass spectrometer. For the source settings, a spray capillary voltage of 1.1-1.4 kV was applied with a sample cone voltage of 40 V and an extraction cone voltage of 2 V. The trap DC bias was set to 20 V, and the trap and transfer collision energy were set to 10 V and 12 V, respectively. The IMS wave height and wave velocity were set at 8 V and 300 m/s, respectively. For the CID experiments, the trap collision energy was varied from 15 V to 180 V and a ramped IMS wave velocity was used from 0 V to 30 V. The following pressures were used within the instrument: trap  $4.8 \cdot 10^{-2}$  mbar, IM  $3.5 \cdot 10^{-1}$  mbar, backing 5.5 mbar. During all MS measurements, the quadrupole transmission window was set to 100 to 32000 m/z and the MS profile function was used to focus on the region between 500 and 8000 m/z.

## 4.2.3 Data analysis

Data were acquired and processed using MassLynx v4.2 and DriftScope (Waters). Estimation of experimental CCS values was carried out through the previously reported calibration procedure using measurements of native proteins under the same conditions.<sup>73,252</sup> The arrival times were obtained in nitrogen but calibrated using CCS values in helium to compare them to theoretical CCS values (obtained in helium), as described by Bush et al.<sup>252</sup> These theoretical CCS values were calculated using Ion Mobility Projection Approximation Calculation Tool (IMPACT).<sup>253</sup>

For the stability assays, the peaks were detected using a custom MATLAB R2019a script with the *'findpeaks'* function<sup>254</sup> allowing fast identification using a consistent approach.

Moreover, the peak positions, peak widths, and peak prominences were determined using this custom script. The peak prominence is used instead of the peak height since the peak prominence accounts for the altering baseline. The peak area was used to determine the relative abundance of all species. The 50 % survival (CID50) value of each nucleosome was determined by fitting the decreasing linear part of the stability plots (from 110 V onwards for the H3<sup>601</sup> and H3<sup>NAS</sup> nucleosomes and from 120 V onwards for the CENP-A<sup>601</sup> and CENP-A<sup>NAS</sup> nucleosomes). Errors on the values were calculated using the correlation coefficient of each fitting.

## 4.3 Results and discussion

### 4.3.1 Nucleosomes are mainly compact folded entities, but a small fraction exists in the extended form

A typical mass spectrum of the H3<sup>601</sup> nucleosome is shown in Figure 36A with intense charge states from 25+ to 30+ centered around 7500 m/z. From these peaks, an experimental mass of  $209.9 \pm 1.7$  kDa was determined which corresponds well with the theoretical mass of the assembled nucleosome of 208427.6 Da (Table 2). The small mass difference is related to adducts with buffer and cations such as Na<sup>+</sup> and K<sup>+</sup>, common contaminations in native MS. Moreover, a less abundant charge state distribution, with an experimental mass of  $209.7 \pm 1.3$  kDa, is centered around 5000 m/z which matches the mass of the intact nucleosome but is much more highly charged (46+ to 41+). Higher charge states generally indicate unfolding or extension of the structure<sup>255</sup> and therefore we assign these peaks to the extended nucleosome (this is also evident from the IM analysis described further). Other charge states for the nucleosome are also observed between 5500 and 7000 m/z but these overlap with another charge state distribution. This last distribution (17+ to 15+) has an experimentally determined mass of  $91.9 \pm 1.6$  kDa and can be ascribed to the free 89.5 kDa 601 DNA sequence of which a small proportion is detected. Finally, some low-intensity peaks between 10000 and 11500 m/z can be observed. These peaks (42+ to 37+) correspond to an experimental mass of  $423 \pm 6$  kDa and are related to dinucleosomes. Although minor amounts of nonspecific oligomers can be an MS artifact, it is also possible that small amounts of nucleosomes interact with each other in solution forming pairs of nucleosomes, as they would in chromatin. Similar behavior was observed by cryo-EM.<sup>256</sup>

A typical mobilogram in which the third dimension, i.e. the arrival time, is added, is shown in Figure 36B. IM data provides a more detailed view on conformation and can even highlight coexisting conformational states within one charge state. On examination of this IM plot, four different populations can be observed. Not surprisingly, the compact folded nucleosomes and traces of free DNA are dominating the spectrum, as these are also the most intense in the mass spectrum. However, also clear signals for dinucleosomes and the extended nucleosome form are observed.

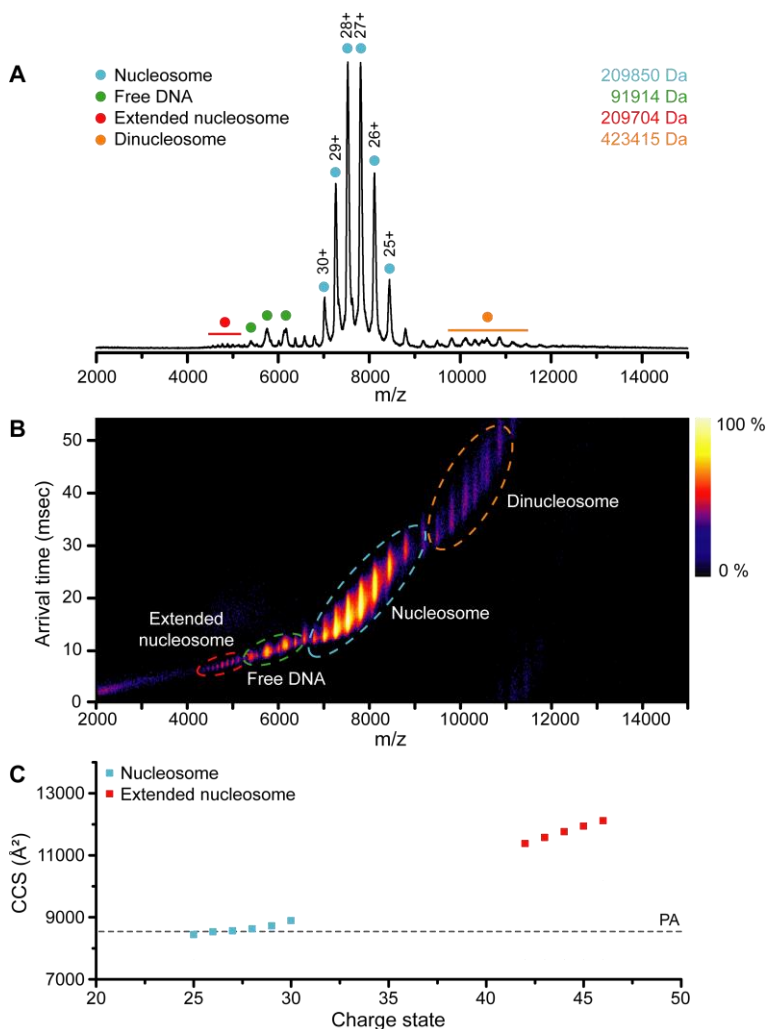


Figure 36. A) Native MS spectrum of the H3<sup>601</sup> nucleosome with the experimentally determined mass in the top right corner. B) The corresponding mobilogram showing the arrival time (y-axis) as a function of the m/z-ratio (x-axis) and intensity (low intensity in blue and high intensity in yellow). C) Experimentally determined CCS values in function of the charge state. The dotted line indicates the theoretical CCS obtained using the projection approximation (PA) approach in IMPACT.

Table 2. Theoretical and experimentally determined masses and sequences of the histones and DNA sequences. Also, the theoretical and experimentally determined masses of the four nucleosomes used in this study are provided.

	Theoretical mass (Da)	Experimental mass (Da)	Sequence
Tagged H2A	19347.1	19354	MHHHHHHSSGLVPRGSGMKETAALKFERQHMDSPDL GTLELVFQGPLGMSGRGKQGGKARAKAKSRSSRAGLQ FPVGRVHRLLRKGNYAERVGAGAPVYMAAVLEYLTAEI LELAGNAARDNKKTRIIPRHLQLAIRNDEELNKLKGVTI AQGGVLPNIQAVLLPKKTESHKAKGK
H2B	13775.7	13777	PEPAKSAPAPKKGSKKAVTKAQKDKGKKRKRSRKESYSV YVYKVLKQVHPDTGISSKAMGIMNSFVNDIFERIAGEAS RLAHYNKRSTITSREIQTAVRLLLPGELAKHAVSEGKAV TKYTSSK
H3	15117.5	15115	ARTKQTARKSTGGKAPRKQLATKAARKSAPATGGVKKP HRYRPGTVALREIRRYQKSTELLIRKLPFQRLVREIAQDFK TDLRFQSSAVMALQEACEAYLVGLFEDTNLCAIHAKRVT IMPKDIQLARRIRGEA
CENP-A	15990.3	15990	MGPRRRSRKPEAPRRRSPSPTPTPGPSRRGPSLGASSH QHSRRRQGWLKEIRKLQKSTHLLIRKLPFSRLAREICVKF TRGVDFNWQAQALLALQEAAEAFVHLFEDAYLLTLHA GRVTLFPKDVQLARRIRGLEELG
H4	11236.0	11235	SGRGKGGKGLGKGGAKRHRKVLDRDNIQGITKPAIRRLA RRGGVKRISGLIYEETRGLVKVFLENVIRDAVITYTEHAKR KTVTAMDVVYALKRQGRPLYGFGG
601 DNA	89478.0		ATCAGAATCCCGGTGCCGAGGCCGCTCAATTGGTCGT AGACAGCTCTAGCACCGCTTAAACGCACGTACGCGCT GTCCCCCGCTTTTAAACGCCAAGGGGATTACTCCCT AGTCTCCAGGCACGTGTCAGATATATACATCGAT
NAS DNA	90249.8		ATCAAATATCCACCTGCAGATTCTACCAAAGTGTATT TGGAAACTGCTCCATCAAAGGCATGTTACAGTCTGT GAGTGAAACTCCATCATCAAAGAATATTCTGAGAA TGCTTCCGTTTGCCTTTTATATGAACTTCTCGAT
H3 <sup>601</sup>	208427.6	209850	
H3 <sup>NAS</sup>	209198.4	211013	
CENP-A <sup>601</sup>	210174.2	2119937	
CENP-A <sup>NAS</sup>	210946.0	213867	

In the next step, we used the measured arrival times of the different charge states to determine the experimental CCS values of nucleosome ions and compare them with theoretical CCS values predicted using 3D structural models of the nucleosomes. In this work, the projection approximation (PA) approach<sup>257,258</sup> was used to determine the theoretical CCS. This approach calculates the CCS value by rotating the structure through all possible orientations and finding the average ‘shadow’ of the ion.<sup>259</sup> The PA

algorithm is, however, known to underestimate the CCS but this does not pose a significant drawback when examining macromolecules such as proteins and their complexes.<sup>253,260</sup> The experimental CCS values for the native nucleosome are depicted in Figure 36C and range from  $8446 \pm 11 \text{ \AA}^2$  to  $8896 \pm 11 \text{ \AA}^2$  for the 25+ and 30+ charge state, respectively. The errors associated with the experimentally determined CCS values were estimated based on the arrival time resolution of the measurement. By comparing these values with the theoretical CCS of the H3<sup>601</sup> nucleosome obtained using the PA approach ( $8547 \pm 39 \text{ \AA}^2$ ), we found that this CCS corresponds well with the 27+ charge state of the nucleosome ( $8569 \pm 11 \text{ \AA}^2$ ). Furthermore, the experimental CCS for the more highly charged nucleosome is determined and ranges between  $11374 \pm 11 \text{ \AA}^2$  and  $12109 \pm 11 \text{ \AA}^2$  for the 42+ and 46+ charge state, respectively (Figure 36C). This CCS value is approximately 42 % larger than the CCS of the native nucleosome.

We reasoned that the extended conformation of the nucleosome could be ascribed to extended histone tails, or unwrapped DNA, or both. An atomistic model with altered conformations of the histone tails compared to the H3<sup>601</sup> nucleosome was examined and compared with the experimental data. The effect of the tails' extension was described previously by Saikusa et al. for both histone multimers (the H2A/H2B dimer and the (H3/H4)<sub>2</sub> tetramer) and a complete nucleosome.<sup>242,243</sup> The CCS of the model in which the nucleosome has unfolded and, thus, fully extended tails was found to be  $10116 \pm 39 \text{ \AA}^2$ , which is too low compared to the experimentally determined CCS values of the extended nucleosome ( $11374$  to  $12109 \text{ \AA}^2$  from the 42+ to 46+ charge state). This structure in which the histone tails are unfolded does therefore not fully justify the extended nucleosome observed in the mass spectrum. One other possibility which might explain or contribute to the extended nucleosome form is the unwrapping of the DNA as described by Bilokapic et al.<sup>240</sup> in cryo-EM studies.

Thus, our native IM-MS data indicate that canonical nucleosomes on well-positioning DNA are mainly compact globular entities that can interact with each other forming dinucleosomes. A small amount of nucleosomes exists in the extended form, which probably reflects nucleosome breathing by terminal DNA unwrapping and unfolding of the histone tails. Our results are in agreement with cryo-EM and other solutions studies<sup>240,256</sup> and give confidence that native IM-MS techniques can be used to analyze nucleosome conformations in vitro.

### 4.3.2 Both histone variant CENP-A and $\alpha$ -satellite sequence contribute to a less compact nucleosome form

Next, we investigated whether the presence of a different histone variant or a different DNA sequence affects the conformation and dynamics of nucleosomes. In particular, we focused on centromeric chromatin that is epigenetically specified by the histone H3 variant, CENP-A, and repetitive so-called NAS sequences which are usually associated with centromeres. Four different nucleosome types were assembled (H3<sup>601</sup>, CENP-A<sup>601</sup>, H3<sup>NAS</sup>, and CENP-A<sup>NAS</sup>) as shown in Figure 35. As is the case for the H3<sup>601</sup> nucleosome, all these nucleosome variants exhibit a similar, intense charge state distribution from 30+ to 25+ between 7000 and 9000 m/z corresponding to the intact nucleosome (Figure 37). All experimentally determined masses correspond well with the theoretical mass of each nucleosome reported in Table 2. Furthermore, low-intensity charge state distributions are observed for the free DNA (18+ to 15+) and the dinucleosomes, for all four nucleosomes. Similar to the H3<sup>601</sup> nucleosome, the data for CENP-A<sup>601</sup> and H3<sup>NAS</sup> nucleosomes also show the presence of high charge states of the extended intact nucleosome (46+ to 41+). The peaks corresponding to the extended form are absent for the CENP-A<sup>NAS</sup> nucleosome.

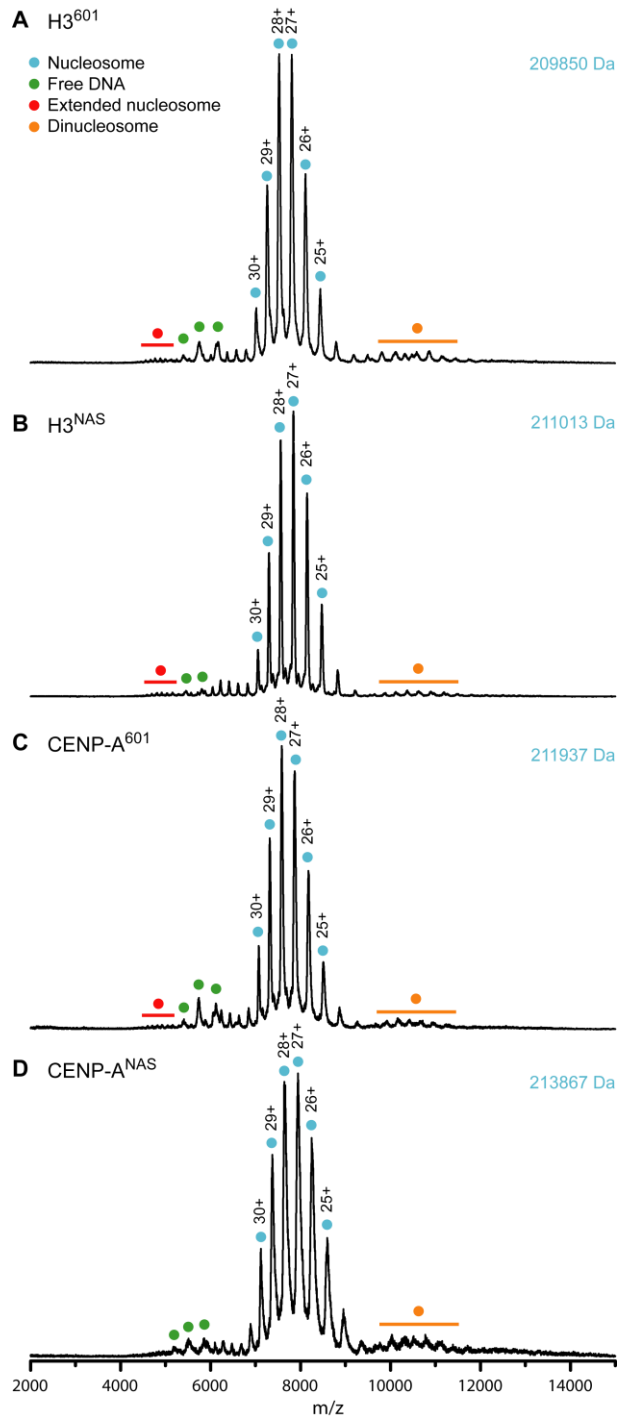


Figure 37. Native MS spectra of A) the  $H3^{601}$  nucleosome; B)  $H3^{NAS}$  nucleosome; C)  $CENP-A^{601}$  nucleosome and D)  $CENP-A^{NAS}$  nucleosome. Experimentally determined masses for the nucleosomes are indicated in the top right corner of each panel.

By examining the CCS values of the different nucleosomes across all charge states, small variations between the CCS values are observed as is shown in Figure 38A. This variation is small for the lowest charge states 25+ and 26+, but becomes more prominent for the higher charge states of the native compact nucleosome. This is expected since increasing numbers of charges cause some repulsion and slight extension of the structure without dramatically changing the conformation. The slope of the CCS increase with charge state differs for the H3 vs. CENP-A nucleosomes. One possible explanation for this could be that the tails of both nucleosome variants behave in different ways when taking up more charges since the tails of H3 and CENP-A are completely dissimilar. The differences in CCS values across the nucleosomes persist for the extended nucleosome form. There is, however, no difference in slope of the CCS increase for the H3 and CENP-A nucleosomes in this case. This might be explained by the fact that the tails are already unfolded and can therefore not behave differently.

In all cases, the CCS values of the H3<sup>601</sup> and the H3<sup>NAS</sup> nucleosomes correspond closely to each other. The same observation is made for CENP-A<sup>601</sup> and CENP-A<sup>NAS</sup> nucleosomes. By considering the 27+ charge state, which is the most abundant and has an experimental CCS matching well with the theoretical CCS of the H3<sup>601</sup> nucleosome (Figure 36C), this was investigated in more detail (Figure 38B).

The H3<sup>601</sup> nucleosome has the smallest experimental CCS ( $8569 \pm 11 \text{ \AA}^2$ ) compared to the other nucleosomes. Replacing the H3 histone in this nucleosome with CENP-A results in a CCS increase by approximately  $111 \text{ \AA}^2$  to  $8680 \pm 11 \text{ \AA}^2$ . The same trend is observed for the nucleosomes with the NAS sequence; the H3<sup>NAS</sup> nucleosome has a CCS of  $8614 \pm 11 \text{ \AA}^2$  and substituting H3 by CENP-A results in a  $109 \text{ \AA}^2$  increase to  $8723 \pm 11 \text{ \AA}^2$ . The increase in CCS values of  $111 \text{ \AA}^2$  and  $109 \text{ \AA}^2$  is considered significant since the error associated with the experimental CCS values, estimated based on the arrival time resolution of the measurement, is only  $\pm 11 \text{ \AA}^2$ . Moreover, differences of  $\geq 2 \%$  in arrival times, which corresponds to  $\pm 15 \text{ \AA}^2$  on the CCS values reported here, are commonly accepted as significant.<sup>71</sup> Therefore, CENP-A nucleosomes have a significantly larger CCS than H3 nucleosomes independent of the type of DNA wrapped around the histone core. CENP-A nucleosomes can therefore be considered as more open and dynamic structures. Similar observations were made in the literature. The CENP-A nucleosome was found to have a slightly different conformation in solution<sup>261,262</sup> and to be more dynamic than H3 nucleosomes due to weaker binding of the DNA ends to the nucleosome core particle.<sup>263,264</sup>

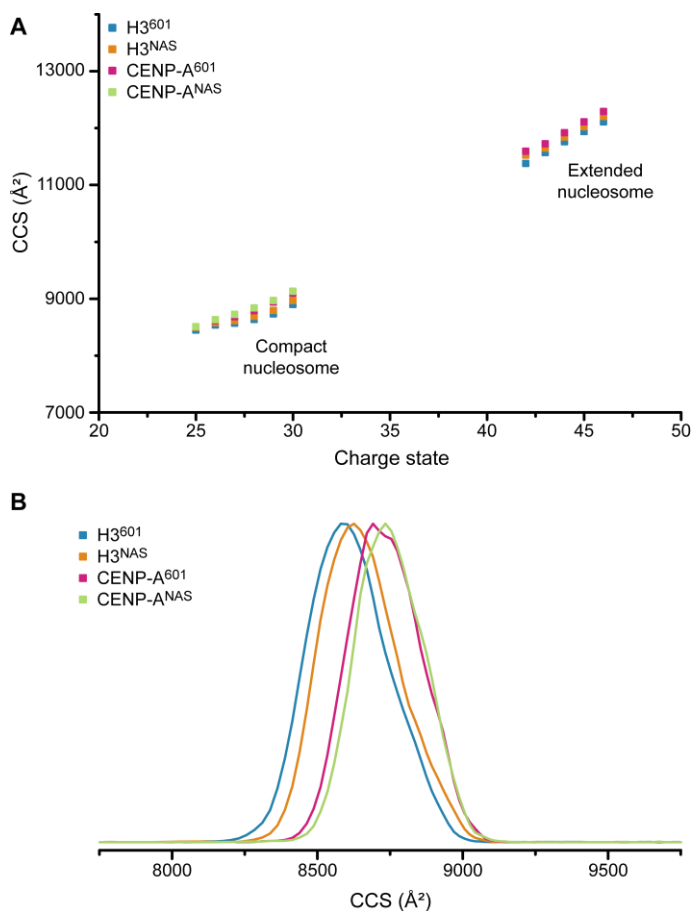


Figure 38. A) Experimentally determined CCS values in function of the charge state of the four nucleosomes used in this study. B) Extracted arrival times of the 27+ charge state of the four nucleosomes used in this study.

The effect of the type of DNA is smaller than between histone variants, but again consistently observed. Displacing the 601 DNA sequence by the NAS sequence induces an increase in the experimental CCS values for both the H3 and CENP-A nucleosomes. The CCS shift between the H3<sup>601</sup> and H3<sup>NAS</sup> nucleosome is characterized by an increase of 45 Å<sup>2</sup>, while the shift between CENP-A<sup>601</sup> and CENP-A<sup>NAS</sup> is 43 Å<sup>2</sup>. Again, these differences can be considered significant, which means that the nucleosomes with the 601 DNA sequence are slightly more compact than those with the NAS sequence. Furthermore, this implies the 601 sequence is wrapped more tightly around the histone core than the NAS sequence. These results match well with what is known in the literature. The 601 DNA sequence is considered a strong positioning sequence which is tightly wrapped around the histones,<sup>248,265</sup> while the NAS sequence has a different conformation, i.e. a bulge in super-helical location 1 and 2.<sup>266</sup> Therefore the latter

sequence is more loosely bound around the histone complex, corresponding to the CCS increase observed in our study.

The IM-MS results above indicate that both the histone variant CENP-A and the NAS sequence contribute to a less compact nucleosome form. These observations are in agreement with X-ray crystallography,<sup>264,265</sup> cryo-EM,<sup>266,267</sup> and hydrogen deuterium exchange (HDX) MS<sup>263</sup> data. This shows that IM-MS allows the detection of small changes in conformation and dynamic behavior of nucleosomes as a result of adjustments to their composition.

### 4.3.3 Both the histone variant CENP-A and the NAS sequence increase the stability of the nucleosome in collision-induced dissociation

HDX-MS experiments revealed that both CENP-A/H4 tetramers<sup>268</sup> and the CENP-A nucleosome core<sup>269</sup> are more rigid than their canonical counterparts. To verify whether the observed rigidity translates into a higher stability and to probe the intrinsic stability of the nucleosomes as a function of their composition, CID experiments were conducted at variable collision energy offsets. Figure 39 shows the influence of increased collision energy, from 30 V to 150 V (Figure 39A and B, respectively), on the H3<sup>601</sup> nucleosome. Increasing the energy applied to the nucleosome results in the appearance of new peaks below 2000 m/z and above 12000 m/z. Simultaneously, the intensity of the intact nucleosome, dinucleosome, and free DNA decreases. The signals between 500 and 2000 m/z can be assigned to the single histones present in the nucleosome (Figure 39C). Since collisionally activated complexes predominantly eject monomers in CID,<sup>270</sup> one does not observe the H2A/H2B dimer and (H3/H4)<sub>2</sub> tetramer as they exist in solution.<sup>232</sup> The remaining complex after the loss of a histone subunit is observed in the range between 12000 and 18000 m/z. Assignment of these residual complexes to a specific species (e.g. a heptasome) was not possible due to low signal intensities. The free DNA fully fragments at these collision energies into small pieces, with the nucleobases observed between 110 and 155 m/z.

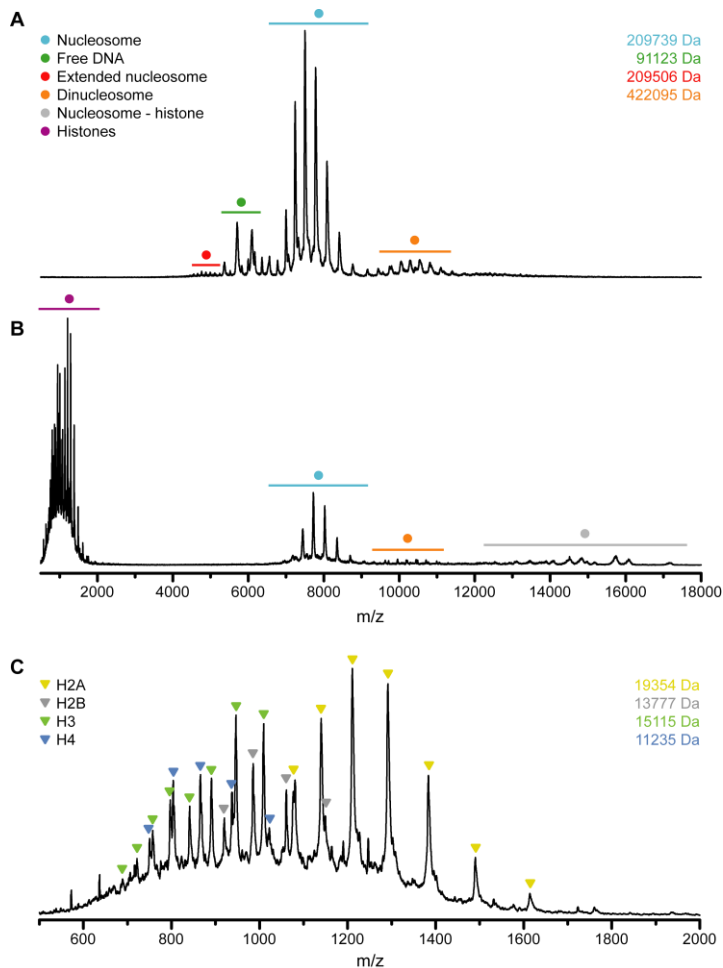


Figure 39. MS spectra of the H3<sup>601</sup> nucleosome at a trap collision energy of A) 30 V and B) 150 V. C) A zoom of the histone region at a trap collision energy of 150 V. Experimentally determined masses are shown in the top right corner of each panel.

We systematically varied the collision energy voltage offset in the range from 30 to 180 V and monitored the relative MS signal intensities of the intact nucleosome and CID product ions for the four types of nucleosome complexes. The collision energy required to dissociate 50 % of the intact nucleosome (later referred to as CID50) and the dissociation pathways provide information on the relative stability of the different nucleosome assemblies (Figure 40). The H3 nucleosomes stay intact until 90-100 V and afterwards dissociation starts until only a small amount of the intact nucleosome (8 % and 14 % for H3<sup>601</sup> and H3<sup>NAS</sup> nucleosomes, respectively) remains at 180 V, the highest energy used. The histones H2A and H3 are the first ones to be ejected from the H3 nucleosomes around 90-100 V, while H2B and H4 remain bound to the H3 nucleosomes at these energies. These latter histones are ejected from 110-120 V onwards. This

implies H2A and H3 are the less tightly bound histones, while H2B and H4 are the most tightly bound in the nucleosome core during CID. Although the histone ejection pattern is similar for both H3 nucleosomes, the type of DNA does influence the stability of the nucleosome slightly. To be able to compare the stability of the nucleosomes, the CID50 values of all nucleosomes were calculated. The CID50 values of the H3<sup>601</sup> and H3<sup>NAS</sup> nucleosome were determined at  $144 \pm 2$  V and  $147.0 \pm 0.4$  V, respectively (Figure 40A and B). The same trend was observed for the CENP-A<sup>601</sup> and CENP-A<sup>NAS</sup> nucleosomes which have a CID50 value of  $153.6 \pm 0.5$  V and  $157.9 \pm 0.5$  V, respectively (Figure 40C and D). These results indicate a stabilization of the core nucleosome by the NAS sequence.

Next, the effect of the histone variant on the stability and rigidity of the nucleosome was investigated. The CENP-A nucleosomes have a different histone ejection pattern than the H3 nucleosomes. First of all, the ejection of the histones occurs at higher energies, around 110 V, for the CENP-A nucleosomes compared to the H3 nucleosomes (from 90-100 V onwards). More importantly, the loss of the histone variant itself dramatically influences the pattern. While the H3 histone was easily lost around 90-100 V, the CENP-A histone remains bound to the nucleosome core. Even at the highest collision energy of 180 V, there is only 2 % free CENP-A detected (Figure 40C and D). This could be explained by the stronger association between CENP-A and H4 in comparison with H3 and H4, with more hydrophobic interactions holding CENP-A/H4 together.<sup>261</sup> Moreover, the CID50 value of the CENP-A nucleosomes is consistently higher than that of the H3 nucleosomes (Figure 40) indicating the overall stability of the nucleosome is increased by the presence of CENP-A, independent on the type of DNA wrapped around the nucleosome core.

In conclusion, the CENP-A<sup>NAS</sup> nucleosome is the most stable towards dissociation in this study. The increased stability can be attributed to both the histone variant (CENP-A) and the DNA sequence (NAS sequence). The question remains, however, why some histones are ejected more easily than others. Several hypotheses are presented. First, the less tightly bound histone, i.e. the histone which has less interactions with other histones and the DNA, can be ejected at the lowest collision energies. This hypothesis holds true to explain the observation that H3 is ejected at lower collision energies than CENP-A histone since CENP-A has more hydrophobic interactions with H4 than H3 with H4.<sup>261</sup> Second, more exposed histones can be prone to being ejected at lower collision energies. For example, nucleosome gapping, in which the nucleosomal DNA opens up like a clam shell,<sup>271</sup> exposes histone H2A more. This could explain why H2A is lost more

easily than the other histones. The final hypothesis is that the internal fold stability of the histones themselves plays a role. Since asymmetric dissociation takes place during CID in which a subunit first unfolds, takes up charges and is then ejected, the subunit with the lowest fold stability could be more prone to being ejected from the nucleosome.

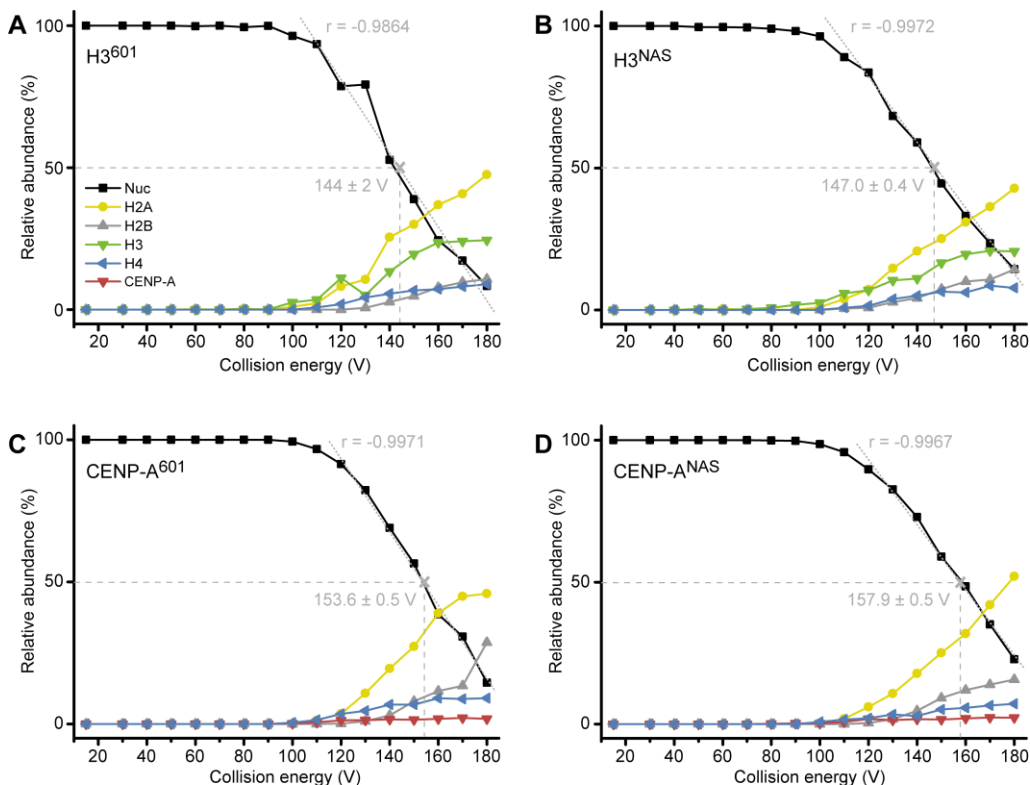


Figure 40. Stability and dissociation pathways of intact nucleosomes in CID as a function of the nucleosome composition: A) the H3<sup>601</sup> nucleosome; B) H3<sup>NAS</sup> nucleosome; C) CENP-A<sup>601</sup> nucleosome and D) CENP-A<sup>NAS</sup> nucleosome. The relative abundance of the nucleosome and each histone are plotted in function of the trap collision energy. The grey dotted lines indicate the fitting used to calculate the CIU50 value of each nucleosome.

## 4.4 Conclusions

We reported the use of native IM-MS to reveal the influence of changes in nucleosome structure on the conformation and stability of the nucleosome. We focused on the effect of a different histone variant, in particular histone H3 vs. its centromeric variant

CENP-A, and the effect of the DNA sequence, i.e. the super-positioning 601 sequence vs. the AT-rich NAS sequence.

Native IM-MS experiments showed that nucleosomes are mainly observed in a compact conformation while a small portion exists in an extended form. Most likely, this extended form arises due to a combination of histone tails unfolding and terminal DNA unwrapping. Moreover, the nucleosomes were found to interact with each other forming dinucleosomes. By determining the experimental CCS of all nucleosomes, we found that both the CENP-A histone and the NAS DNA sequence contribute to a less compact nucleosome form. The CENP-A<sup>NAS</sup> nucleosome was found to be the most open and dynamic nucleosome studied here. This is in agreement with the literature. Native IM-MS is, thus, able to detect small changes in the conformation and behavior of nucleosomes with small alterations in their structure. Therefore, native IM-MS allows to detect features that are difficult to detect with structural methods such as X-ray crystallography and cryo-EM, since these techniques only capture a limited amount of conformations.

Finally, the intrinsic unfolding and dissociation stability of the nucleosomes as a function of their composition was studied by performing CID experiments. These experiments showed that nucleosomes with the histone CENP-A and the NAS DNA sequence are more stable than nucleosomes containing either the H3 histone or the 601 DNA sequence. Moreover, the H3 histone follows a completely different dissociation trajectory than its variant CENP-A. H3 is ejected at relatively low collision energies while CENP-A remains bound to the nucleosome core. The exact contributions of why certain histones are released at lower energies than others are not understood yet and more information is needed to understand this in-depth. Currently, MD simulations are ongoing to obtain more insights in the conformational dynamics of the nucleosomes and to investigate the dissociation ability of the histones in more detail.

# |5

Native mass spectrometry for the design and selection of protein bioreceptors for perfluorinated compounds

**Elise Daems\*, Giulia Moro\*, Herald Berghmans, Ligia M. Moretto, Silvia Dewilde, Alessandro Angelini, Frank Sobott, and Karolien De Wael**

*Adapted from Analyst, 146, 2065-2073 (2021)*

**\* Contributed equally**



## Abstract

Biosensing platforms are answering the increasing demand for analytical tools for environmental monitoring of small molecules, such as per- and polyfluoroalkyl substances (PFAS). By transferring toxicological findings in bioreceptor design we can develop innovative pathways for biosensor design. Indeed, toxicological studies provide fundamental information about PFAS-biomolecule complexes that can help evaluate the applicability of the latter as bioreceptors. The toolbox of native mass spectrometry (MS) can support this evaluation, as shown by the two case studies reported in this work. The analysis of model proteins' (i.e. albumin, hemoglobin, cytochrome c and neuroglobin) interactions with well-known PFAS, such as perfluorooctanoic acid (PFOA) and perfluorooctanesulfonic acid (PFOS), demonstrated the potential of this native MS screening approach. In the first case study, untreated and delipidated albumin were compared in presence and absence of PFOA confirming that the delipidation step increases albumin affinity for PFOA without affecting protein stability. In the second case study, the applicability of our methodology to identify potential bioreceptors for PFOS/PFOA was extended to other proteins. Structurally related hemoglobin and neuroglobin revealed a 1:1 complex, whereas no binding was observed for cytochrome c. These studies have value as a proof-of-concept for a general application of native MS to identify bioreceptors for toxic compounds.

## 5.1. Introduction

Biosensing platforms are answering the increasing demand for analytical tools for environmental monitoring.<sup>272–274</sup> A key step in the development of biosensors is the selection of the bioreceptor or biorecognition element, a biomolecule (e.g. protein or nucleic acid) which enables the specific recognition of the analyte and undergoes biochemical changes that can be further translated into a detectable signal.<sup>275</sup> The possibility to combine a protein bioreceptor within a biosensing platform depends mainly on the affinity and specificity of the recognition, the compatibility with the matrix of interest (e.g. waste water, biological fluids, etc.), the production costs and the physicochemical stability in the required working conditions.<sup>276</sup> These criteria should be carefully evaluated while screening new bioreceptors for small molecules, such as PFAS.

PFAS, a class of more than 3,000 manmade chemicals, represent a global issue due to their persistent, bioaccumulative and toxic behavior, which has adverse effects on the ecosystem and human health.<sup>277–279</sup> In the last two decades, improved regulatory plans and phase-out initiatives supported by in-depth toxicological and environmental studies limited the usage of PFAS, such as perfluorooctanoic acid (PFOA) and perfluorooctanesulfonic acid (PFOS).<sup>280–283</sup> However, Barceló and Ruan<sup>284</sup> pointed out that *“this is not the end of the story”* since novel fluorinated compounds are continuously entering the market to replace the old ones, following the trend predicted by Wang and co-workers.<sup>285</sup> The monitoring of long-chain and new generation PFAS through fluorescence-based, optical and electrochemical sensors is giving promising results.<sup>286–289</sup> However, examples of biosensing platforms are still limited.<sup>290</sup> Transposing toxicological studies, particularly the ones focused on PFAS-protein interactions, to bioreceptor design is of great importance to develop new sensing platforms. Indeed, toxicological studies provide fundamental information about PFAS-protein complexes by clarifying binding site distributions, affinity constants, stoichiometries, etc. Liu et al. offered a complete overview of the analytical techniques in use for the characterization of these compounds giving emphasis to their limits and potential.<sup>291</sup> For instance, PFOA and PFOS affinity towards serum proteins such as albumin and Hb was extensively characterized by multi-analytical approaches based on fluorescence spectroscopy, MS, CD spectroscopy, ITC, X-ray crystallography, and molecular docking.<sup>292–295</sup> Multi-analytical studies confirmed the strong affinity of PFOA for hSA: PFOA's carboxylate head and fluorinated C<sub>8</sub> tail mimic the structure of fatty acids promoting PFOA binding into hSA's hydrophobic pockets.<sup>296,297</sup> Similarly to fatty

acids, hSA-PFOA interactions are noncovalent, mainly hydrophobic, and influenced by protein conformation and environmental conditions (such as pH).<sup>298</sup> These findings suggest the possibility to use hSA as a bioreceptor.<sup>290</sup> Also other proteins were found to be good candidates: in 2016, Wang et al. described how PFOS influences the stability and conformation of Hb, providing key information about its half-life in blood. PFOS was found to interact with the protein, leading to a significant conformational change and exposure of the heme group.<sup>292</sup>

In this context, native MS offers a rich toolbox to support bioreceptor screening studies. Here, we describe two case studies dedicated to PFAS-protein complexes to show the potential of native MS in bioreceptor screening. PFOA/PFOS were used as model analytes and albumin, cyt c and NGB as possible bioreceptors. In the first case study we assessed the applicability of hSA isolated and purified from blood as a bioreceptor for PFOA (Figure 41A). Considering the fatty acid-mimicking nature of PFOA, untreated and delipidated hSA were first compared. Although the delipidation step improved PFOA affinity by removing residual fatty acids present in the hSA isolated from blood, it could also lead to a lower stability of the protein itself. Native MS was applied to characterize the hSA-PFOA complexes, while the complex stability was probed by CIU.

Since the interactions of Hb with PFAS have been previously studied, we probe the use of other hemoproteins such as NGB and cyt c (Figure 41B and C) in the second case study. Cyt c is a 12 kDa, water-soluble protein and can be considered as a model protein, easy to combine with sensing platforms such as electrochemical ones.<sup>299–301</sup> However, its interaction with PFAS is unclear and its applicability in PFAS biosensing was never tested. NGB is a 17 kDa globin with a 3/3 fold expressed in the central and peripheral nervous system, cerebrospinal fluid, retina and endocrine tissues.<sup>302,303</sup> In contrast to cyt c, NGB was not applied in biosensing so far. Therefore, the possibility to include cyt c and NGB in a PFAS bioreceptor library was screened by native MS. Through these case studies we aim to demonstrate the use of native MS as a complementary method for the design and characterization of bioreceptors.

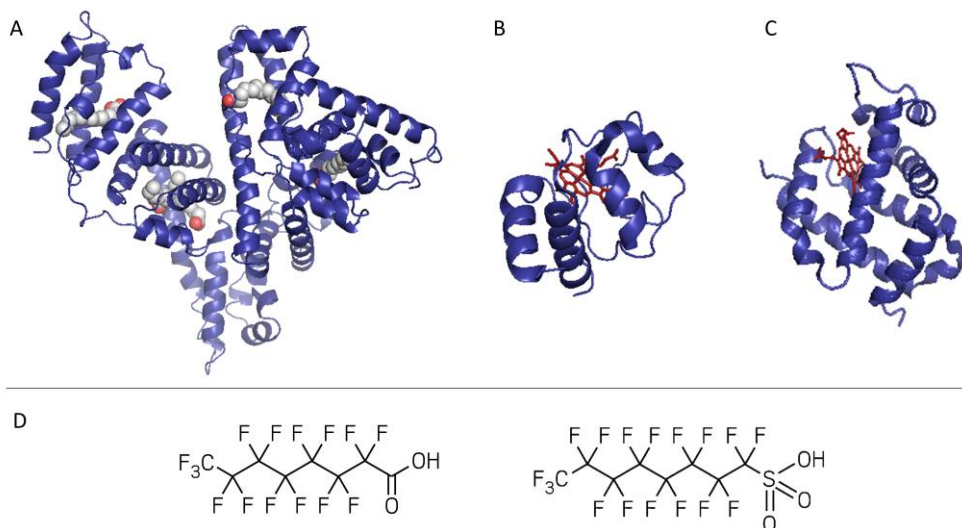


Figure 41. Summary of the proteins tested as bioreceptors: (A) hSA in complex with myristic acid, (B) cyt c, and (C) NGB. The heme group is shown in red. The proteins were screened against PFOA and/or PFOS (D from the left to the right). PDB Data Bank ID are reported in Table 3.

## 5.2. Materials and methods

### 5.2.1. Materials

Perfluorooctanoic acid ( $\geq 96\%$ ), perfluorooctane sulfonic acid potassium salt ( $\geq 98\%$ ), human hemoglobin and cytochrome c from human heart were purchased from Sigma-Aldrich (Belgium). Human serum albumin was isolated from blood and purified as previously described by Chen et al.<sup>304</sup> Recombinant human neuroglobin was expressed and purified as reported previously.<sup>305</sup> The 100 mM ammonium acetate solution pH 6.8 was prepared using ammonium acetate ( $> 98\%$ ) purchased by Sigma-Aldrich (Belgium). All other reagents were of analytical grade and solutions were prepared using double distilled deionised water.

### 5.2.2. Sample preparation

Prior to use, untreated hSA, delipidated hSA and Hb were dialysed overnight in 100 mM ammonium acetate pH 6.8 using Slide-a-Lyzer Mini dialysis units with a molecular weight cut-off of 3.5 kDa (Thermo Fisher Scientific, Belgium). The denatured samples

were directly prepared in 50/50 acetonitrile/MilliQ water with 0.1 % formic acid. The concentrations of the protein solutions were verified using a Nanodrop2000 (Thermo Fisher Scientific) using the parameters in Table 3. The average of three triplicate measurements was considered. NGB and cyt c were buffer exchanged to 100 mM ammonium acetate pH 6.8 using Micro Bio-spin columns (Bio-gelP6, Bio-rad). Samples of 10  $\mu$ M protein with the desired concentration of PFOA/PFOS were prepared in 100 mM ammonium acetate pH 6.8. Once prepared the protein:PFOA/PFOS solutions were kept for maximum 5 h in the fridge at 4 °C. No incubation time with the target was needed before running the measurements.

*Table 3. Used parameters for Nanodrop2000 measurements and PDB ID reference used in Figure 41.*

<b>Protein</b>	<b>Wavelength (nm)</b>	<b>Molecular weight (Da)</b>	<b>Extinction coefficient (mol<sup>-1</sup>cm<sup>-1</sup>L)</b>	<b>Protein data bank ID</b>
hSA	280	66531	34445	1BJ5
Hb (oxyhemoglobin)	414	64458	524280	1NQP
NGB	410	17501	12200	1OJ6

### 5.2.3. Native MS

A sample volume of approximately 2-4  $\mu$ L protein solution was required for each measurement and introduced into the mass spectrometer using nESI with in-house made gold-coated borosilicate capillaries. Two different instruments were used in this work. The hSA measurements were performed on a Q-TOF2 instrument (MSVision) that is modified for the transmission of high-mass macromolecular assemblies.<sup>306</sup> The spray capillary voltage ranged between 1.2 and 1.8 kV, the source temperature was set to 30 °C and the sample and extractor cone were set to 25 V and 10 V, respectively. The collision energy was fixed to 50 V. Gas pressures were 10 mbar and  $1 \cdot 10^{-2}$  mbar for the backing and collision gas, respectively. The measurements of the other proteins and the CIU experiments of hSA were performed on a Synapt G2 HDMS instrument (Waters) with N<sub>2</sub> gas (purity 99.9999 %, Messer) in the IM cell and the following instrument settings were used: spray capillary voltage 1.2-1.9 kV, source temperature 30 °C, sampling cone 25 V, extraction cone 1 V, trap collision energy 5 V (for the CIU experiments this was varied from 10 to 150 V), transfer collision energy 0 V, trap DC bias 45 V, IMS wave height 35 V and IMS wave velocity 700 m/s. The backing pressure was set to 3.9 mbar, the source pressure to  $2.8 \cdot 10^{-3}$  mbar, the trap pressure to  $2.4 \cdot 10^{-2}$  mbar, the IMS pressure to 3.0 mbar, and the transfer pressure to  $2.5 \cdot 10^{-2}$  mbar.

## 5.2.4. Data processing

All data were analyzed using MassLynx v4.2 (Waters) and Driftscope v2.3 (Waters). The Gaussian peak deconvolution algorithm within OriginPro 2018 was used to separate main and shoulder peaks and bound and unbound states. Afterwards, the intensity of these peaks was used to estimate the abundance of each species. The  $K_d$  of untreated hSA-PFOA complex was estimated from a single point measurement, as described by Göth et al., for all charge states and the mean  $K_d$  was reported.<sup>307</sup> Arrival times were extracted from the 15+ charge state (no mass selection) from the full width at half maximum of the whole peak, including salt adducts and complexes (where appropriate). This corresponds to an  $m/z$ -window from 4435 to 4455  $m/z$  and 4435 to 4520  $m/z$  for the unbound and bound hSA, respectively. Experimental  $^{TW}CCS_{N_2}$ <sup>71</sup> values were calculated using a previously reported method relying on a calibration with other native proteins under the same experimental conditions.<sup>252</sup> During the calibration procedure, a linear fitting was applied according to Thalassinos et al.<sup>75</sup> The CIUSuite 2 software (v2.2) developed by Polasky et al. was used to generate the CIU plots and analyze these data.<sup>308</sup>

## 5.3. Results and discussion

### 5.3.1. Testing hSA's applicability as PFOA-bioreceptor

In this first case study, the possibility of improving hSA-PFOA binding affinity and stoichiometry was tested by comparing untreated and delipidated hSA. To assess the stability of the delipidated hSA-PFOA complex, the CIU threshold and pattern were compared with the untreated hSA-PFOA.

Toxicological studies showed high affinity of PFOA for hSA fatty acids binding sites.<sup>296–298</sup> To facilitate access to hSA cavities, a delipidation pretreatment of hSA was included, as previously reported.<sup>304</sup> The removal of endogenous fatty acids is expected to lead to better reproducibility of the interaction and a higher sensitivity. To verify these hypotheses, we determined the number of binding sites and compared the affinity of delipidated hSA and untreated hSA towards PFOA. In Figure 42A, the mass spectrum of untreated hSA shows the presence of the protein monomer (charge states 18+ to 12+), nonspecific dimer (charge states 23+ to 20+) and nonspecific trimer (charge states 28+

to 26+). The experimentally determined mass of hSA was found to be  $66.7 \pm 0.3$  kDa, which corresponds well with the mass of mature albumin which is subjected to cleavage of the signal peptide and the propeptide resulting in 585 amino acids (66.5 kDa).<sup>309</sup> Moreover, a small amount of the complete hSA consisting of 609 amino acids (including propeptide and signal peptide) can be observed as the minor charge state distribution in between the main peaks, with an experimentally determined mass of  $68.9 \pm 0.9$  kDa. Analysis of the monomer revealed the presence of a shoulder to the main peak with an intensity of 52 % compared to the main peak (Figure 42B). This is not observed upon denaturing of the protein (Figure 43) and the intensity of the shoulder decreases to 31 % upon applying higher collision energies (Figure 44). Therefore, this feature is noncovalent in nature and can possibly be ascribed to the presence of long- or short-chain fatty acids.<sup>310,311</sup> Upon addition of PFOA (10-fold excess), a 1:1 stoichiometry complex was formed as indicated by the appearance of the second peak in Figure 42C. Over all charge states present, ca. 49 % of the untreated hSA is present in its unbound state and 51 % has one PFOA bound. The  $K_d$  was estimated to be  $90 \pm 5$   $\mu$ M. This value is in agreement with the previously reported  $K_d$  of  $100 \pm 90$   $\mu$ M by Beesoon et al. for the hSA-PFOA complex.<sup>312</sup> The observed stoichiometry is lower compared to other values reported in the literature in which bovine serum albumin and rat serum albumin were used.<sup>296,298</sup> The exact concentration, type and state of the protein used can influence the stoichiometry.

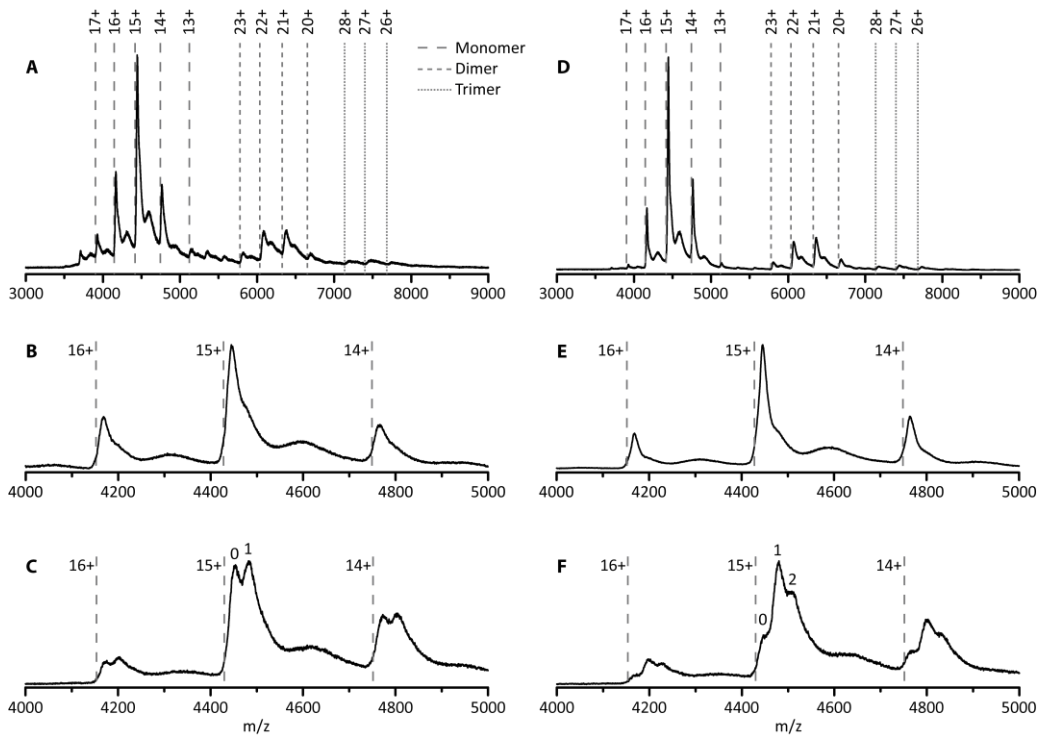


Figure 42. Native MS spectra of untreated (A, B, C) and delipidated (D, E, F) hSA. The full MS spectra of hSA are given (A and D), together with a zoom of the monomer region (B and E) and spectra of hSA in complex with PFOA at a 1:10 protein:ligand ratio (C and F). The dashed lines indicate the theoretical  $m/z$ -values of the monomer, dimer and trimer of hSA.

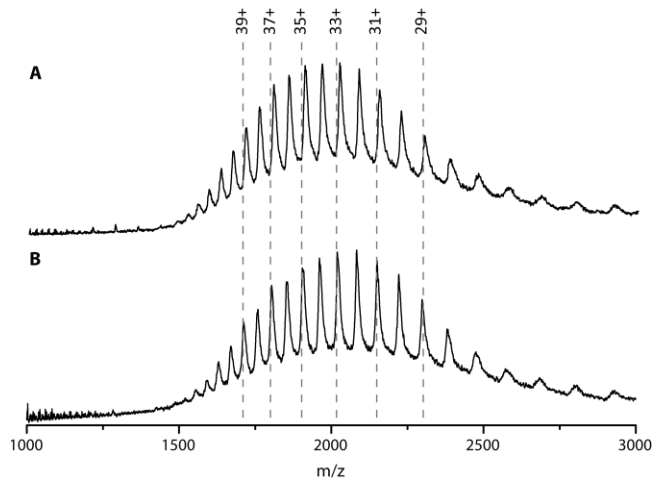


Figure 43. Denatured MS spectra of untreated (A) and delipidated (B) hSA recorded in 50/50 acetonitrile/MilliQ with 0.1 % formic acid. The dashed lines indicate the theoretical  $m/z$ -values of hSA calculated from the theoretical mass of 66531 Da.

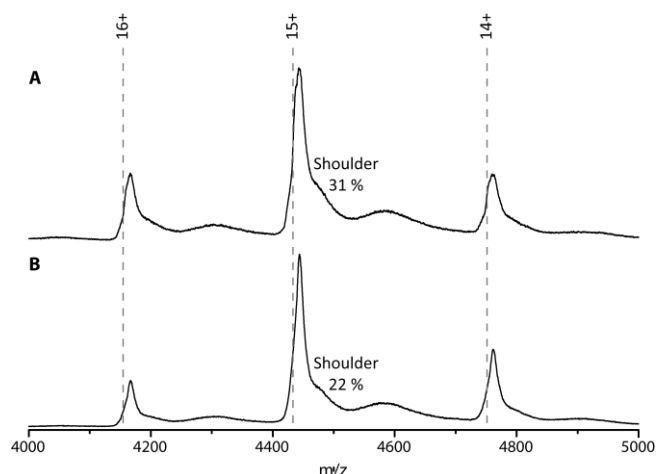


Figure 44. MS spectra of untreated (A) and delipidated (B) hSA recorded at 100 V trap collision energy. The dashed lines indicate the theoretical  $m/z$ -values of hSA.

The same experiments were performed with the delipidated hSA and an experimental mass of  $66.6 \pm 0.2$  kDa was obtained. Again, a shoulder is observed on the main peak, but with a lower intensity of only 31 % compared to 52 % for the untreated hSA, suggesting the delipidation process removed the noncovalent feature (most likely fatty acids) at least partially (Figure 42E). Addition of 10-fold excess of PFOA to delipidated hSA yielded a complex with different stoichiometry (1:2, Figure 42F). Moreover, the intensity of the hSA peak without any PFOA bound is significantly lower for the delipidated hSA (20 %) than for the untreated hSA (49 %), suggesting a shift towards more complex formation. Approximately 45 % of the hSA has one PFOA bound, while 35 % has two PFOA molecules bound. The increase of the binding stoichiometry can be attributed to the delipidation step. As such, native MS confirmed that hSA delipidation is important to attain higher binding stoichiometries of the proposed bioreceptor.

### 5.3.2. Inspecting hSA conformational stability

To investigate whether the delipidation of hSA influences protein conformational stability and binding capacity, we performed CIU experiments on both untreated and delipidated protein. The gas-phase unfolding thresholds and pathways of untreated and delipidated hSA are compared.

From the plots in Figure 45A and C and the corresponding feature detection in Figure 46A and C, it is possible to observe that both proteins showed a similar  $^{TW}CCS_{N_2}$  (4469

$\pm 22 \text{ \AA}^2$  and  $4458 \pm 22 \text{ \AA}^2$  for the native untreated and delipidated hSA, respectively) up to a collision energy of 825 eV, which corresponds with an applied potential difference of 55 V. At higher energies a multi-step unfolding process started.<sup>313,314</sup> The first transition occurs between 60 and 70 V (Figure 47) and results in a state with a  $^{\text{TW}}\text{CCS}_{\text{N}_2}$  of  $5284 \pm 22 \text{ \AA}^2$  and  $5262 \pm 22 \text{ \AA}^2$  for the untreated and delipidated hSA, respectively (Figure 46). Eschweiler et al. assigned this second conformation to the unfolding of domain II.<sup>313</sup> The second transition takes place just above 100 V and generates a state with a  $^{\text{TW}}\text{CCS}_{\text{N}_2}$  of  $5563 \pm 22 \text{ \AA}^2$  and  $5551 \pm 22 \text{ \AA}^2$  for the untreated and delipidated hSA, respectively, which corresponds to the partial unfolding of domain III. A final unfolding step occurs between 120 and 130 V, which results in a state with a  $^{\text{TW}}\text{CCS}_{\text{N}_2}$  of  $5686 \pm 22 \text{ \AA}^2$  and  $5641 \pm 22 \text{ \AA}^2$  for the untreated and delipidated hSA, respectively. This final transition can be ascribed to the unfolding of domain I and the remainder of domain III.<sup>313</sup> The consistency of the unfolding patterns, with a relatively low root-mean-square deviation (RMSD) of 9.26 (Figure 48), suggested that the delipidation process did not affect the stability of hSA. No significant differences in the unfolding products nor changes in the threshold collision energies were observed. These preliminary results proved that the delipidation treatment did not affect the protein stability.

The CIU experiments were also extended to the hSA-PFOA complexes, to test whether the presence of ligands influenced the stability of the proteins, particularly the delipidated form. A 10-fold excess of PFOA to hSA was tested and the unfolding pathways of treated and untreated hSA are shown in Figure 45B and D. To extract the CCS, the full width at half maximum of the complete peak, which contains both the bound and the unbound state, was used since there is no complete separation of both states. The initial conformation has a  $^{\text{TW}}\text{CCS}_{\text{N}_2}$  of  $4480 \pm 22 \text{ \AA}^2$  (Figure 46) and unfolds between 60 and 70 V (Figure 47) to generate a state with a  $^{\text{TW}}\text{CCS}_{\text{N}_2}$  of  $5284 \pm 22 \text{ \AA}^2$  and  $5306 \pm 22 \text{ \AA}^2$  for untreated and delipidated hSA, respectively. The final state has a  $^{\text{TW}}\text{CCS}_{\text{N}_2}$  of  $5641 \pm 22 \text{ \AA}^2$ . This compares well with the fourth and final state of both proteins without PFOA indicating the third feature, corresponding to the partial unfolding of domain III, disappears in the unfolding process of the complex. In general, the unfolding pathways of the complexes were found to be comparable between the two proteins (RMSD of 7.90) as shown in Figure 48.

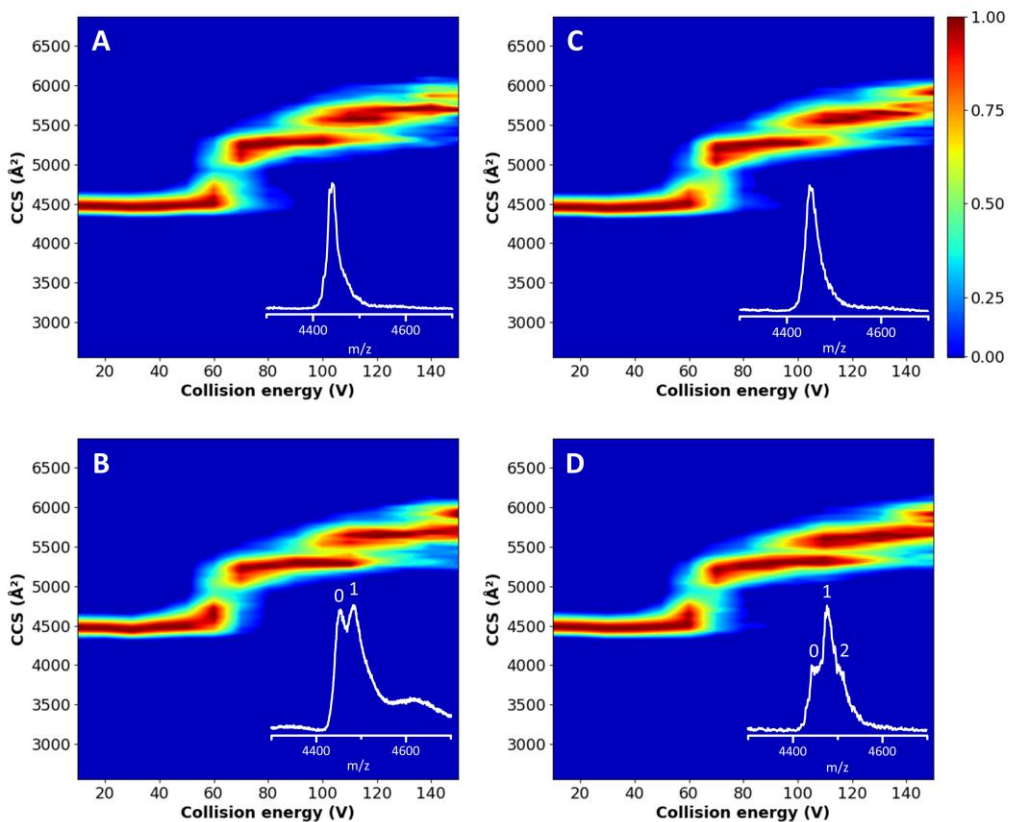


Figure 45. CIU plots of untreated (A) and delipidated (C) hSA and of the untreated (B) and delipidated (D) hSA in complex with PFOA (1:10 protein:PFOA ratio). The  $^{TW}CCS_{N_2}$  is plotted as function of the trap collision energy and the intensity is shown using a color scale (red is 100 % and blue 0 %). The insets show the peaks selected (15+ charge state) for extraction of the  $^{TW}CCS_{N_2}$  at a trap collision energy of 60 V. Arrival times were extracted from the whole peak, including salt adducts and complexes (where appropriate) as explained in more detail in section 5.2.4.

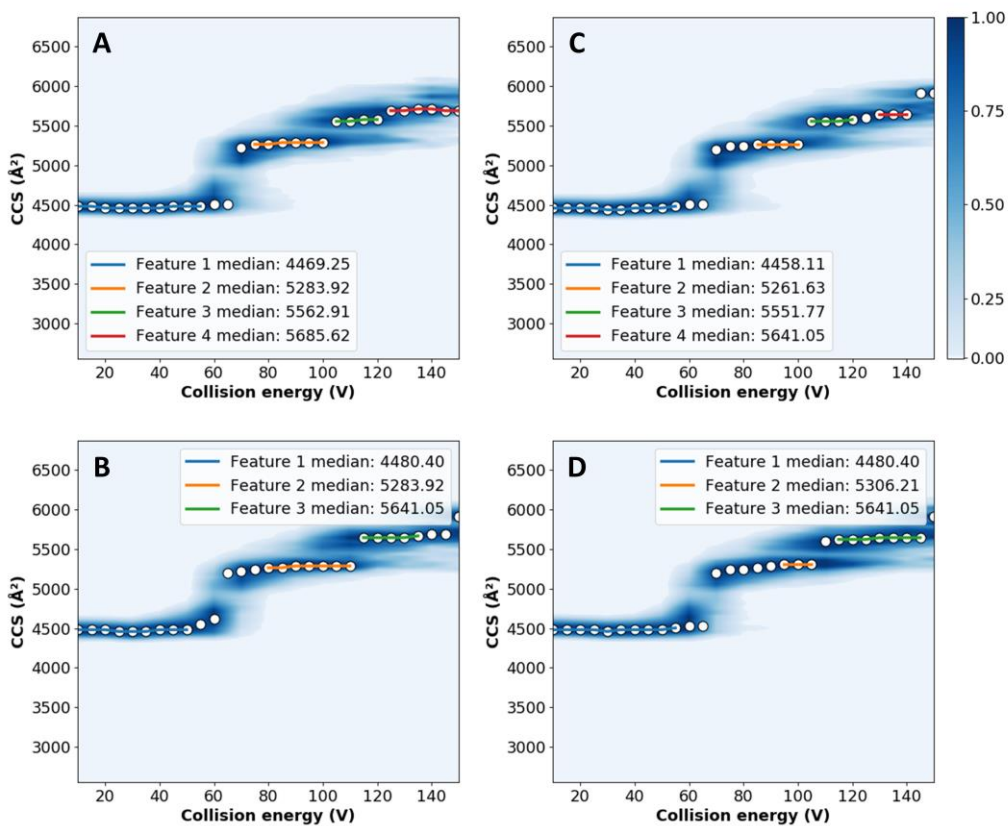


Figure 46. Feature detection performed using CIUsuite 2 on the CIU plots of untreated (A) and delipidated (B) hSA and of the untreated (C) and delipidated (D) hSA in complex with PFOA (10-fold excess) shown in Figure 45.

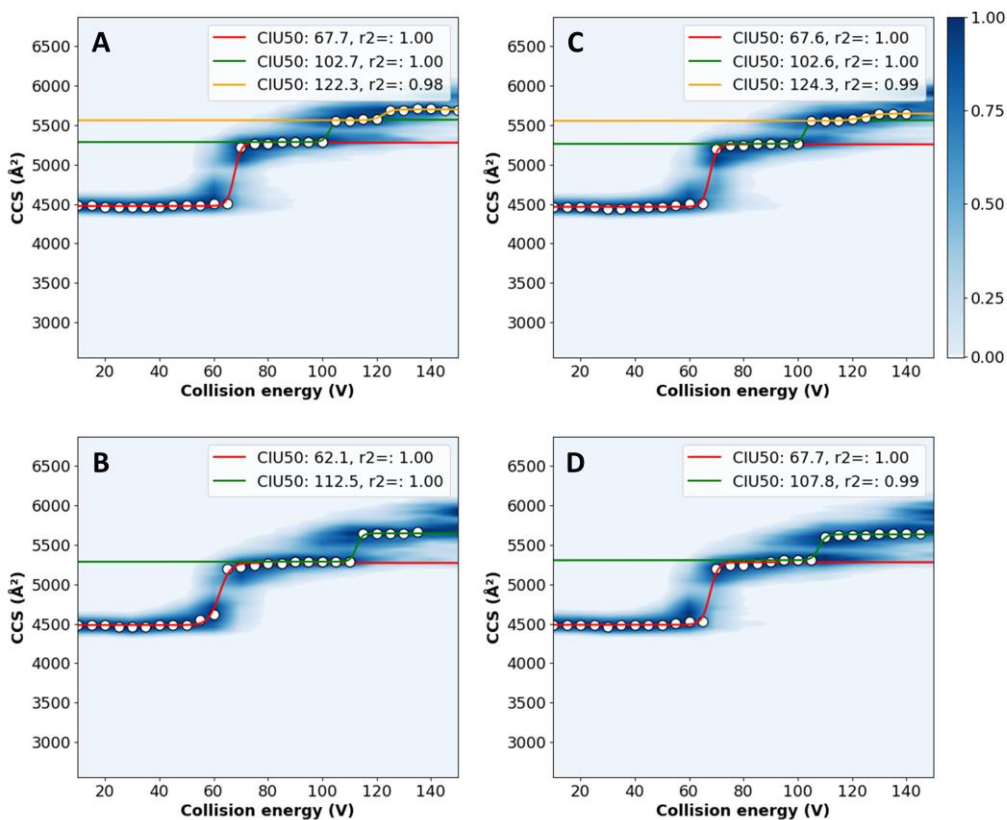


Figure 47. CIU50 analysis performed using CIUSuite 2 on the CIU plots of untreated (A) and delipidated (B) hSA and of the untreated (C) and delipidated (D) hSA in complex with PFOA (10-fold excess) shown in Figure 45.

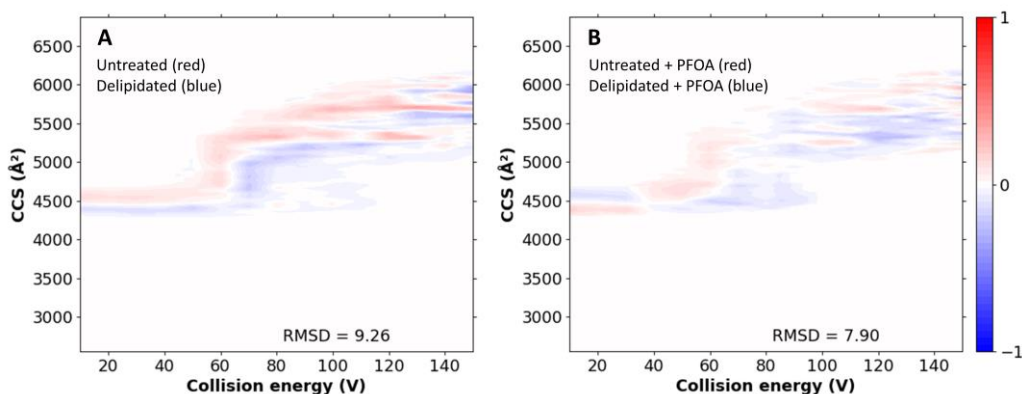


Figure 48. RMSD values and CIU difference plots, generated with CIUSuite, for comparison of the CIU data shown in Figure 45. The red/blue color code indicates the intensity differences between the CIU plots. Comparisons are made between untreated and delipidated hSA (A) untreated hSA in complex with PFOA and delipidated hSA in complex with PFOA (B).

Throughout all conformational transitions and up to the highest energy applied (Figure 49), PFOA remains bound to hSA (both untreated and delipidated) which illustrates that the strength of ligand binding is comparable to the protein's intramolecular interactions, i.e. conformational stability. This indicates that the binding site for PFOA is not significantly affected by the initial unfolding, and implies that the PFOA is most likely buried in the structure of domain I or III,<sup>313</sup> rather than binding peripherally to the surface. Since our experimental data shows that the transition corresponding to the partial unfolding of domain III is absent for the hSA-PFOA complexes (Figure 45B and D and Figure 46B and D), it is clear that the binding of PFOA influences the stability of domain III. This further implies PFOA is most likely bound in domain III rather than in domain I for both the untreated and delipidated hSA.

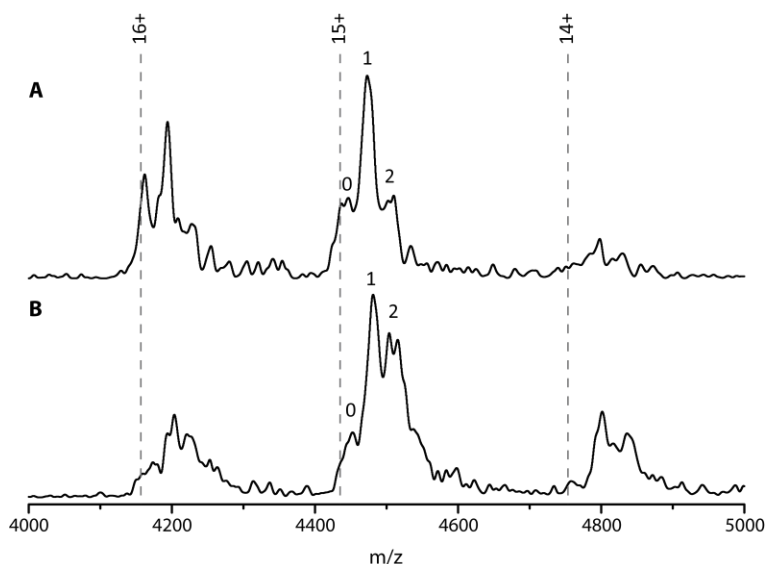


Figure 49. MS spectra of untreated (A) and delipidated (B) hSA in complex with PFOA at a 1:10 protein:ligand ratio recorded at 150 V trap collision energy on the Synapt G2 instrument. The dashed lines indicate the theoretical  $m/z$ -values of hSA.

This method provides a useful preliminary control to assess the applicability of a protein as bioreceptor under different working conditions. Since no differences in the unfolding paths and stabilities have been observed, our study supports the possibility to use delipidated hSA as a bioreceptor in different sensing platforms. This is also supported by previous work on the design of a proof-of-concept impedimetric sensor for PFOA, where delipidated hSA was immobilized on portable screen-printed electrodes modified with pyrrole carboxylic acid.<sup>273</sup> Then, PFOA-hSA complex formation was followed at a confined surface. Despite the limited sensitivity of the platform, this

sensing strategy is a first proof of the applicability of delipidated hSA as a bioreceptor for PFAS monitoring in water.

### 5.3.3. Probing hemoproteins as bioreceptors

In this second case study, we screened other possible bioreceptors for PFOA using Hb as a starting point. Hb is known to bind PFOS molecules.<sup>292</sup> The native mass spectrum of Hb (Figure 50A) shows that the protein is mainly present in its native tetrameric form (charge states 17+ to 14+). Upon adding a 10-fold excess of PFOS, a complex with a 1:1 stoichiometry is observed, proving the coherence of the native MS data with the literature (Figure 50C).<sup>292</sup> After verifying the formation of the Hb-PFOS complex, we studied the interaction of PFOA with Hb. Again, a 1:1 Hb-PFOA complex was observed after addition of a 10-fold excess of the target. The intensity of the peak corresponding to this complex (93 %) is higher than the Hb-PFOS complex (51 %) (Figure 50D). In both cases, the heme groups are not removed from the Hb upon binding of PFOA/PFOS, indicating there is no competition between the heme groups and PFOS or PFOA.

These findings are in agreement with the Hb-PFOS complex structure suggested by molecular modelling by Wang et al.<sup>292</sup> in which the target molecule was suggested to bind the domain proximal to the heme without any direct interactions with the prosthetic group. Therefore, Hb-PFOA/PFOS screening confirmed the formation of complexes and their stability (i.e. no loss of the heme group) as well as the consistency of MS data with the literature. Once we confirmed the capability of Hb to bind PFAS, it was possible to proceed with the screening of other hemoproteins, such as cyt c and NGB.

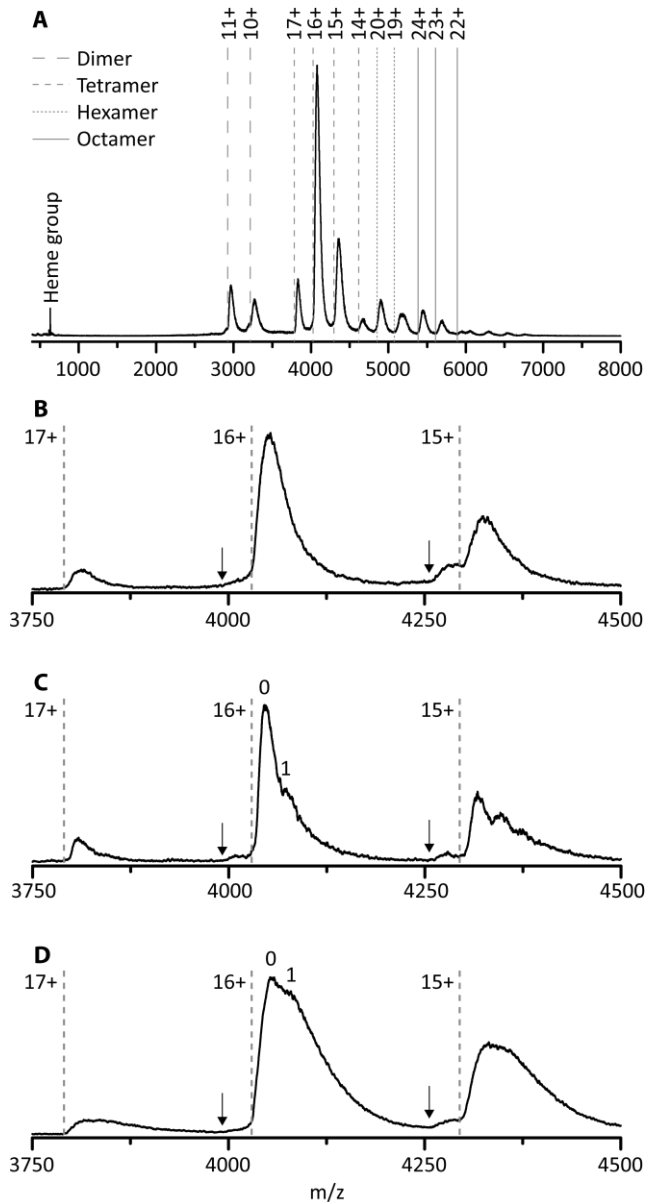


Figure 50. Native MS spectrum of Hb (A) together with a zoom of the tetramer region (B). Native MS spectrum of Hb in complex with PFOS (C) and PFOA (D) in a 1:10 protein:target ratio. The dashed lines indicate the theoretical  $m/z$ -values of Hb. The arrows indicate the theoretical  $m/z$ -value of Hb minus one heme group.

Cyt c was chosen because it is well-known to bind to lipid bilayers. To check whether cyt c can bind PFOA, native MS experiments were performed (Figure 51A). Cyt c shows two charge states (7+ and 6+) which are heavily adducted with sodium ions (a common contamination in native MS). Upon adding a 10-fold excess of PFOA, no new peaks

122

appeared indicating the lack of a cyt c-PFOA complex (Figure 51B). To verify this observation, the negatively charged PFOS was used as well, but again no complex was observed (Figure 52). This is unexpected since cyt c is well-known to interact with anionic phospholipids, such as cardiolipin.<sup>315</sup> Over the years, multiple binding sites for these anionic lipids were discovered and it was found that electrostatic forces play a key role in the cyt c-lipid interaction.<sup>316–319</sup> Since PFOA and PFOS mimic fatty acids and are negatively charged at neutral pH,<sup>320,321</sup> it was plausible that cyt c could interact with these PFAS and could work as a bioreceptor. One possible explanation for the absence of complex is that cyt c specifically binds cardiolipins and that the PFAS used here are structurally too different to interact with cyt c.

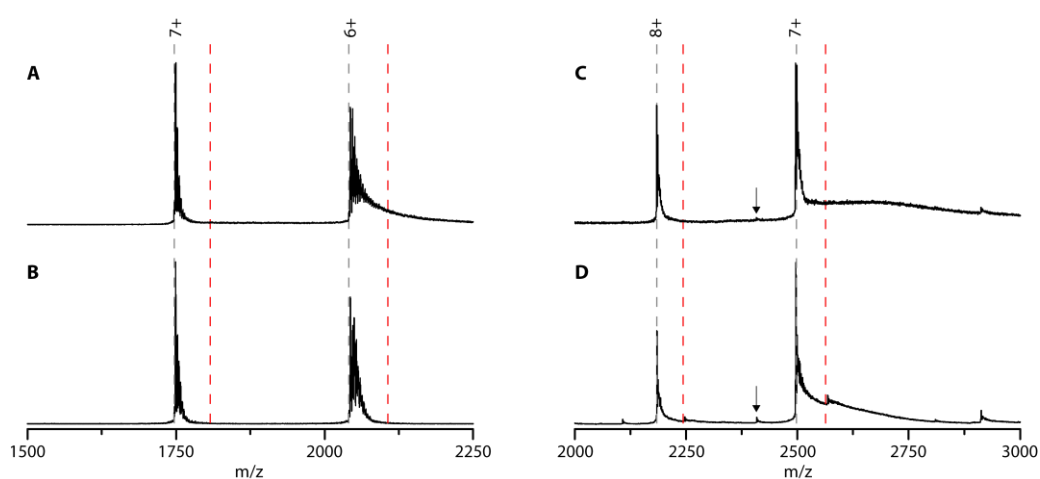


Figure 51. Native MS spectra of cyt c (A and B) and NGB (C and D) without (A and C) and in the presence of PFOA in a 1:10 protein:target ratio (B and D, respectively). The dashed lines indicate the theoretical  $m/z$ -values of the protein and 1:1 protein-PFOA complex in grey and red, respectively. The arrows indicate the theoretical  $m/z$ -value of NGB without heme group.

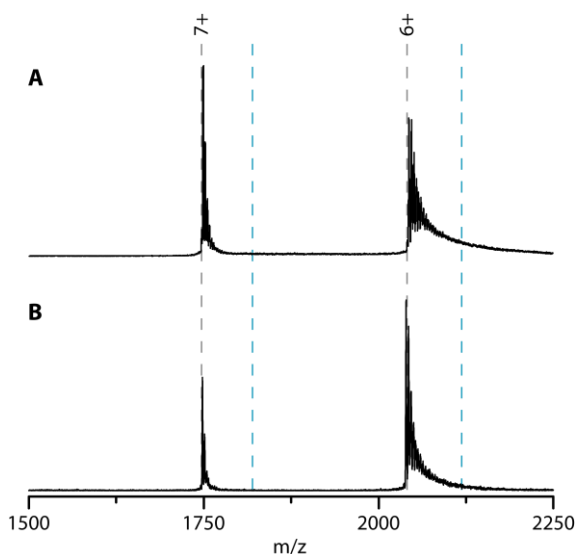


Figure 52. Native MS spectra of cyt c alone (A), and of cyt c in the presence of PFOS in a 1:10 protein:target ratio (B). The dashed lines indicate the theoretical m/z-values of the protein and 1:1 protein-PFOS complex in grey and blue, respectively.

Next, possible NGB-PFOA interactions were investigated. Since the ability of Hb to bind PFOA was confirmed using native MS, it is possible that another globin, NGB, could also bind to PFOA and work as a bioreceptor. To our knowledge, NGB-PFOA interactions were not investigated so far. The mass spectrum of NGB shown in Figure 51C is characterized by two prominent charge states (8+ and 7+). Upon adding a 10-fold excess of PFOA only low-intensity peaks corresponding to the 1:1 complex were observed (Figure 51D). Overall, 87 % of the NGB is present in its unbound state and only 13 % has one PFOA bound. This indicates NGB is only able to bind PFOA weakly and with a lower affinity than Hb. The most intense peaks correspond to NGB with heme group and the very low intensity peaks around 2110 and 2410 m/z that are present after addition of PFOA can be assigned to NGB without the heme group. This could suggest that PFOA is affecting the stability of NGB. Furthermore, there is no evidence of NGB without a heme group binding to PFOA.

Finally, the NGB-PFOS complex formation was investigated (Figure 53). The spectra showed that the amount of NGB-PFOS complex formed (7 %) is even lower than for NGB-PFOA and is therefore not investigated in more detail. From this screening, NGB is found to be a less suitable bioreceptor for PFAS compared to Hb.

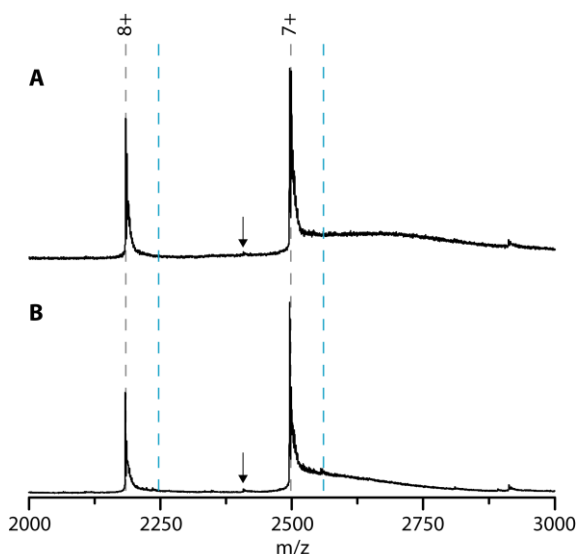


Figure 53. Native MS spectra of NGB alone (A), and of NGB in the presence of PFOS in a 1:10 protein:target ratio (B). The dashed lines indicate the theoretical  $m/z$ -values of the protein and 1:1 protein-PFOS complex in grey and blue, respectively. The arrows indicate the theoretical  $m/z$ -value of NGB without heme group.

## 5.4. Conclusions

The two case studies reported here underline the potential of applying native MS in the screening of biorecognition elements and implementation of bioreceptor libraries for environmental contaminants such as PFAS.

Native MS revealed the higher PFOA binding capacity of delipidated hSA in respect to the untreated hSA. Removal of fatty acids from the hydrophobic pockets facilitates binding of PFOA to the cavities. CIU experiments showed that fatty acid removal did not affect the conformational stability of the protein or the complex itself. PFOA appears to bind tightly to hSA-PFOA as the complex is retained even at high collision energies. This evidence correlates well with protein stability and implies that PFOA is buried in the protein structure.

Furthermore, it was shown that native MS can be used to screen other possible bioreceptors for PFAS. Hb, a protein known to bind PFOS, can also bind PFOA. Conversely, the structurally related NGB displays a lower binding affinity toward both compounds. Finally, cyt c, a well-known lipid-binding protein, does not show any binding.

These examples illustrate how native MS can contribute to the screening and characterization of possible bioreceptors. Although many challenges still remain, our approach has the potential to play an important role in the transfer of toxicological findings to the design of bioreceptors for innovative biosensing strategies. One of the major challenges will be the screening of short-chain PFAS which will possibly require a more extensive sample preparation and multiple desalting steps to enhance the peak separation in native MS. Future research efforts should be oriented toward testing novel proteins and assessing binding affinity and stoichiometry using different molar ratios.

# |6

Aptamer-ligand recognition studied by native ion mobility-mass spectrometry

**Elise Daems, Debbie Dewaele, Konstantin Barylyuk, Karolien De Wael, and Frank Sobott**

*Adapted from Talanta, 224, 121917 (2021)*



## Abstract

The range of applications for aptamers, small oligonucleotide-based receptors binding to their targets with high specificity and affinity, has been steadily expanding. Our understanding of the mechanisms governing aptamer-ligand recognition and binding is however lagging, stymieing the progress in the rational design of new aptamers and optimization of the known ones. Here we demonstrate the capabilities and limitations of native ion mobility-mass spectrometry (IM-MS) for the analysis of their higher-order structure and noncovalent interactions. A set of related cocaine-binding aptamers, displaying a range of folding properties and ligand binding affinities, was used as a case study in both positive and negative electrospray ionization modes. Using carefully controlled experimental conditions, we probed their conformational behavior and interactions with the high-affinity ligand quinine as a surrogate for cocaine. The ratios of bound and unbound aptamers in the mass spectra were used to rank them according to their apparent quinine-binding affinity, qualitatively matching the published ranking order. The arrival time differences between the free aptamer and aptamer-quinine complexes were consistent with a small ligand-induced conformational change, and found to inversely correlate with the affinity of binding. This IM-MS-based approach provides a fast and convenient way to study the molecular basis of aptamer-ligand recognition.

## 6.1. Introduction

Native MS, often in combination with IM spectrometry, has become an important technique for studies of the structure of biomolecular conformation and interactions.<sup>64,65</sup> Nevertheless, particularly flexible or disordered protein structures have been found to undergo some degree of gas-phase “collapse” even under gentle MS conditions, in cases where the free enthalpy barriers for these transitions were low.<sup>322</sup> Moreover, in contrast to G-quadruplexes which appear rigid, short DNA duplexes were found to compact over 20 % according to their CCS values and compared to canonical B helices.<sup>91</sup> The question therefore arises to what extent aptamers retain key characteristics of their structure in the gas-phase, preserving key aspects of their folding and ligand recognition.

In this study, we focus on a set of cocaine-binding aptamers, with a range of binding mechanisms from folding-upon-binding to preformed rigid binders, and their interactions with the ligand quinine.<sup>52,228</sup> Although originally selected to specifically recognize cocaine, cocaine-binding aptamers are known to bind also to other alkaloids and steroids, with up to 30-fold greater affinity toward quinine than cocaine. Reinstein et al. proposed that this higher affinity could be explained by the larger bicyclic aromatic ring in the quinine ligand, which probably provides an increase in stacking interactions with the DNA bases of the aptamer.<sup>52</sup> We demonstrate that counter-ions play an important role for stabilization of the higher-order structure of the aptamer, by analyzing aptamer samples prepared in solutions of different ionic strengths. Although the current paradigm postulates that the negative ionization mode is the “natural” one for the analysis of nucleic acids, we show that aptamers and ligand complexes can also be detected and analyzed in the positive mode with high sensitivity and specificity. By comparing the MS spectra of the set of aptamers, it becomes apparent that native MS is able to determine relative binding strengths and rank ligands according to their affinity. IM spectrometry allows observation of small conformational changes, which we find to relate to the mode of binding. In summary, we propose native IM-MS as a relatively fast and simple method to study aptamer-ligand interactions, with obvious applications in SELEX panels and aptamer development.

## 6.2. Materials and methods

### 6.2.1. Materials and sample preparation

All aptamers and the random control sequence derived from MN19 (AAA GTA ACT ACG GAC GGG ATA CCA GCA GTT) were purchased from Eurogentec (Belgium) purified with a differential precipitation purification method. Ammonium acetate solution (7.5 M, molecular biology grade) and quinine hydrochloride dihydrate ( $\geq 98.0\%$ ) were purchased from Sigma-Aldrich (Bornem, Belgium). All solutions were prepared using deionized water which had a conductivity of  $\leq 0.1\ \mu\text{S}/\text{cm}$  after purification using a Silex I B system from Eurowater (Nazareth-Eke, Belgium). All aptamers were dialyzed and buffer-exchanged overnight using Slide-a-Lyzer Mini dialysis units with a molecular weight cut-off of 3.5 kDa (Thermo Fisher Scientific) to 300 mM ammonium acetate pH 6.8 (no pH adjustment required), unless stated otherwise. The buffer was replaced twice during the dialysis. The concentrations of the dialyzed aptamers were verified using a Nanodrop2000 (Thermo Scientific). Extinction coefficients were calculated by the Nanodrop2000 software based on the oligonucleotide sequences. Quinine was solubilized in 300 mM ammonium acetate, after which aptamer-quinine complexes were prepared using a 1:1 aptamer-quinine molar ratio with a final concentration of 5-10  $\mu\text{M}$  and afterwards incubated for a few minutes (no re-annealing was done).

### 6.2.2. Native nESI IM-MS

Native nESI-IM-MS analyses were performed on a Synapt G2 HDMS Q-TOF instrument (Waters, Manchester, UK). Approximately 3-5  $\mu\text{l}$  of sample was introduced into the mass spectrometer, using nESI with in-house made gold-coated borosilicate glass tapered-tip capillaries. Experiments were performed in both the positive and the negative ionization mode. The instrument was carefully tuned to balance preservation of native structure with achieving sufficient declustering, in order to obtain well-resolved spectra. Figure 54 shows the effect of tuning three key parameters which control ion activation (internal energy) on the survival of aptamer-ligand complexes. The voltages employed here are shown to retain ca. 50 % of the noncovalent complex present. The following settings were used: spray capillary voltage 1.0-1.4 kV, source temperature 30 °C, sampling cone 25 V in positive and 20 V in negative ionization mode, extraction cone 1 V in positive and 5 V in negative ionization mode, trap collision energy

5 V, transfer collision energy 0 V, trap DC bias 45 V, IMS wave height 35 V and IMS wave velocity 800 m/s. The backing pressure was set to 2.75 mbar, the source pressure to  $2.34 \cdot 10^{-3}$  mbar in the positive ionization mode and  $1.51 \cdot 10^{-3}$  mbar in the negative ionization mode, the trap pressure to  $2.38 \cdot 10^{-2}$  mbar, the IMS pressure to 2.98 mbar, the transfer pressure to  $2.50 \cdot 10^{-2}$  mbar. An overview of these settings is provided in Table 4. All data were analyzed using MassLynx 4.1 and Driftscope (Waters). The relative abundances of all species were calculated by integrating the peak areas of each species. Arrival time profiles were extracted at the full width at half maximum (FWHM) of the peaks without adducts. An overview of all  $m/z$ -values used for extraction of the arrival times is shown in Table 5.

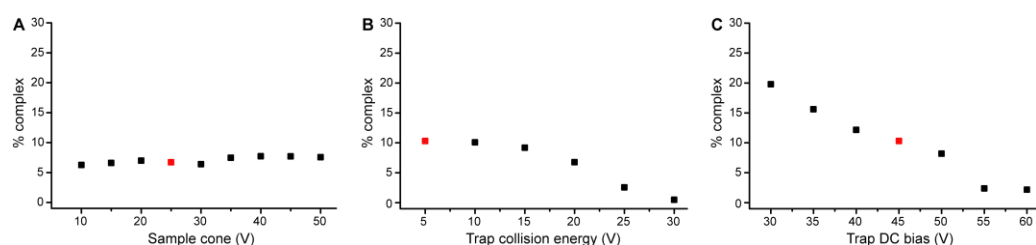


Figure 54. Synapt G2 instrument tuning showing the effect of three key parameters A) Sample cone; B) Trap collision energy and C) Trap DC bias, which control ion activation (internal energy) on the survival of the MN19-quinine complex. All spectra were recorded in 300 mM ammonium acetate with aptamer and ligand in a 1:1 ratio. The voltages employed here are shown to retain ca. 50 % of the noncovalent complex present, with the Trap DC Bias chosen for effective declustering but also causing some ligand loss.

Table 4. Instrumental parameters used for the native nESI IM-MS experiments.

Instrumental parameters	Positive ionization mode	Negative ionization mode
Spray capillary voltage	1.0-1.4 kV	1.0-1.4 kV
Source temperature	30 °C	30 °C
Sampling cone	25 V	20 V
Extraction cone	1 V	5 V
Trap collision energy	5 V	5 V
Transfer collision energy	0 V	0 V
Trap DC bias	45 V	45 V
IMS wave height	35 V	35 V
IMS wave velocity	800 m/s	800 m/s
Backing pressure	2.75 mbar	2.75 mbar
Source pressure	$2.34 \cdot 10^{-3}$ mbar	$1.51 \cdot 10^{-3}$ mbar
Trap pressure	$2.38 \cdot 10^{-2}$ mbar	$2.38 \cdot 10^{-2}$ mbar
IMS pressure	2.98 mbar	2.98 mbar
Transfer pressure	$2.50 \cdot 10^{-2}$ mbar	$2.50 \cdot 10^{-2}$ mbar

Table 5. The *m/z*-values selected for extraction of the arrival times of each aptamer and complex. The full width of half maximum (FWHM) of the peaks without adducts was used.

Aptamer	Charge state	<i>m/z</i>	<i>m/z</i> of complex
MN19	5+	1855.6	1920.5
MN19	5-	1853.6	1918.5
MNS-7.9	5+	1858.5	1923.5
MN4	6+	1855.7	1909.8
38-GC	6+	1958.6	2012.7

### 6.3. Results and discussion

In this study, we use a set of closely related DNA-based cocaine-binding aptamers as model compounds for the comparative native MS analysis. Four cocaine-binding aptamers were chosen: MN19, MNS-7.9, MN4 and 38-GC (Figure 55). Their structure contains three stems built around a three-way junction, which is the proposed binding pocket.<sup>215</sup> The second stem contains only Watson-Crick base pairs, whereas stems 1 and 3 contain non-canonical base pairs. When aligned, the sequences only differ in their terminal parts and at position 24 of the consensus sequence (Figure 56). The MNS-7.9 and MN19 aptamers consist of 30 nucleotide residues, with the only difference being the base pair at position 24 (compared to the consensus), where the C has been replaced with T. The MN19 aptamer has a  $K_d$  of 26.7  $\mu\text{M}$  for cocaine (obtained in 20 mM Tris (pH 7.4), 140 mM NaCl, and 5 mM KCl) and is reported as a loosely folded structure.<sup>52</sup> The MNS-7.9 aptamer has a corresponding  $K_d$  of 20  $\mu\text{M}$  (obtained in the same buffer as the  $K_d$  of MN19) and is described as structurally very flexible.<sup>215</sup> Roncancio et al. developed the 38-GC sequence (38 bases) by modifying the existing aptamer MNS-4.1, resulting in a higher affinity for cocaine binding ( $K_d$  value for cocaine: 2.6  $\mu\text{M}$  obtained in 10 mM Tris buffer (pH 7.4) with 0.01 mM  $\text{MgCl}_2$  and 5 % DMSO). They stabilized the 38-GC aptamer by *i*) replacing the non-canonical base pairs in MNS-4.1 with Watson-Crick base pairs and *ii*) by converting the G-T wobble pair in the stem 3 to a matched G-C base pair. As a result, the 38-GC aptamer is characterized by a rigid structure, which stably folds in the absence of ligand at room temperature.<sup>323</sup> The fourth aptamer MN4 consists of 36 bases, has a  $K_d$  value of 7  $\mu\text{M}$  for cocaine (obtained in the same buffer as the  $K_d$  of MN19 and MNS-7.9) and is described in the literature as structurally rigid.<sup>52,324,325</sup> Although all these aptamers were originally selected to specifically recognize cocaine, they bind quinine with a higher affinity.<sup>52</sup> Therefore, quinine was chosen as ligand in this study as a surrogate for cocaine.

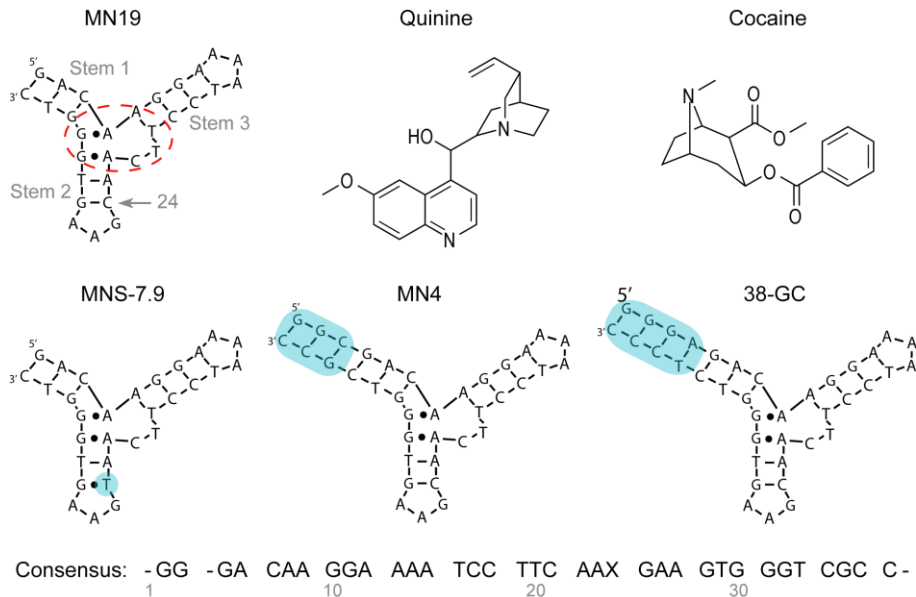


Figure 55. Secondary structures of the cocaine-binding aptamers used in this study, the consensus sequence where X stands for C or T (bottom), and chemical structures of the quinine and cocaine ligands (top right). Watson-Crick base pairs are indicated with dashes and non-Watson-Crick base pairs are shown as dots. The ligand binding site is indicated with a red dashed ellipse. Differences in aptamer sequence compared to the MN19 aptamer are indicated with a blue background.

MN19	GA CAA GGA AAA TCC TTC AAC	GAA GTG GGT C
MNS-7.9	GA CAA GGA AAA TCC TTC AAT	GAA GTG GGT C
38-GC	GGG AGA CAA GGA AAA TCC TTC AAC	GAA GTG GGT CTC CC
MN4	GG CGA CAA GGA AAA TCC TTC AAC	GAA GTG GGT CGC C
Consensus	-GG -GA CAA GGA AAA TCC TTC AAX	GAA GTG GGT CGC C-
	1 10 20 30	

Figure 56. Sequence alignment of the different cocaine-binding aptamers: MN19, MNS-7.9, 38-GC, and MN4. The area highlighted in grey indicates position 24 in the sequence with either a C or T.

### 6.3.1. Ionic strength in solution is crucial for preservation of the aptamer fold in the negative ionization mode

The presence of cations is an important factor for the structure and stability of oligonucleotides in general; they act as counter-ions to the negatively charged phosphate backbone. For example, high concentrations of monovalent cations (i.e. Na<sup>+</sup> and K<sup>+</sup>) stabilize DNA duplexes, resulting in higher melting temperatures.<sup>326</sup> Divalent Mg<sup>2+</sup>-ions are even more important *in vivo*, because not only do they stabilize the

structure but also facilitate the folding of duplexes into secondary and tertiary structures.<sup>327</sup> Such effects are also expected for aptamers,<sup>328</sup> and here we studied the effect of the ionic strength of the solution on the structure of aptamers. We tested several concentrations of ammonium acetate, which is commonly used in native IM-MS, (50 to 300 mM in water, pH 6.8) as well as pure water to probe the effect of the ionic strength on the charge state distribution of the MN19 aptamer in both negative and positive ionization mode. In native MS of proteins, the amount of charging observed due to multiple (de-)protonation events correlates well with the extent of the exposed surface area, which in turn depends on the compactness of the structure.<sup>329</sup>

In the negative ionization mode, the charge states we observed ranged from 18- to 7- in water (Figure 57A). Increasing the ionic strength to 50 mM ammonium acetate resulted in a shift to lower values (12- to 5-), and from 100 mM onwards only 6-, 5-, and 4- ions were observed. These observations highlight that the presence of ions, here ammonium and acetate, plays an important role for the charge state distribution of ssDNA aptamers (Figure 58A). The presence of highly charged species, represented by the 14- charge state, would indicate an extended form of the aptamer in the absence of counter-ions. In 50 mM ammonium acetate, this extended state disappears while an intermediate state, represented by the 6- charge state, shows up together with the compact state centered on the 5- charge state. From 100 mM onwards, this narrow distribution around 5- persists, implying compact structures of the aptamers.<sup>330</sup> In the positive ionization mode, only the 5+ and 4+ charge states of aptamer ions, representing compact structures, were present in the spectra throughout the whole range of ionic strengths (Figure 57B). In contrast to the negative ionization mode, no highly charged species were present at low ionic strength (Figure 58B). This has also been previously observed for i-motifs.<sup>331</sup>

The interesting observation, that the aptamer only appears highly charged without buffer in the negative ionization mode, is explained by the lack of counter-ions, which would otherwise reduce the net charge in the highly acidic phosphate backbone. Coulombic repulsion destabilizes the structure in solution, as is well known for DNA,<sup>332</sup> but would also prevent refolding or compaction of the desolvated and highly charged i.e. extended ions in the gas-phase.<sup>91</sup> This is further supported by the findings of Sharawy et al., who performed MD simulations of negatively charged electrospray nanodroplets containing a dsDNA.<sup>333</sup> In the positive ionization mode, adduct formation during ESI diminishes this charge density in the backbone so that the oligonucleotides are more likely to be released as compact molecules. At the same time, high positive

charge states cannot be reached without sufficient ammonium ions present which can protonate the oligonucleotide (via adduct formation, with volatile ammonia lost during ESI).

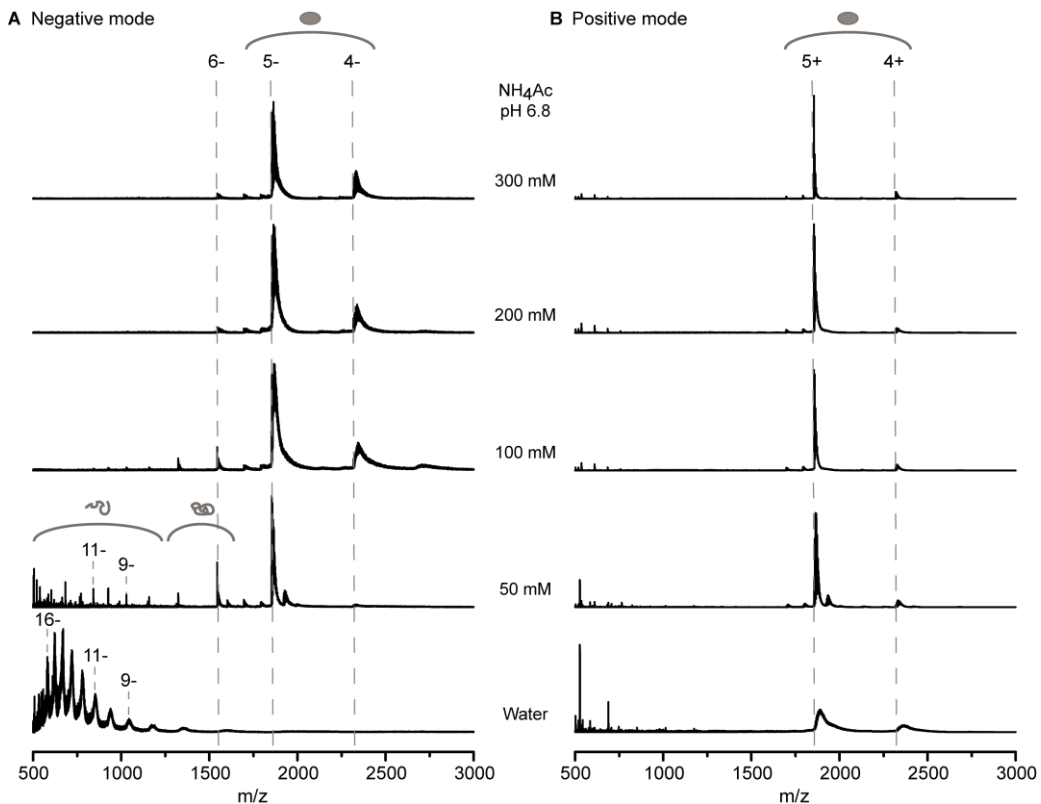


Figure 57. Native MS of the MN19 cocaine-binding aptamer in water, 50, 100, 200, and 300 mM ammonium acetate (NH<sub>4</sub>Ac) in A) the negative and B) the positive ionization mode. Dashed lines indicate the theoretical peak positions of multiple charge states of the aptamer.

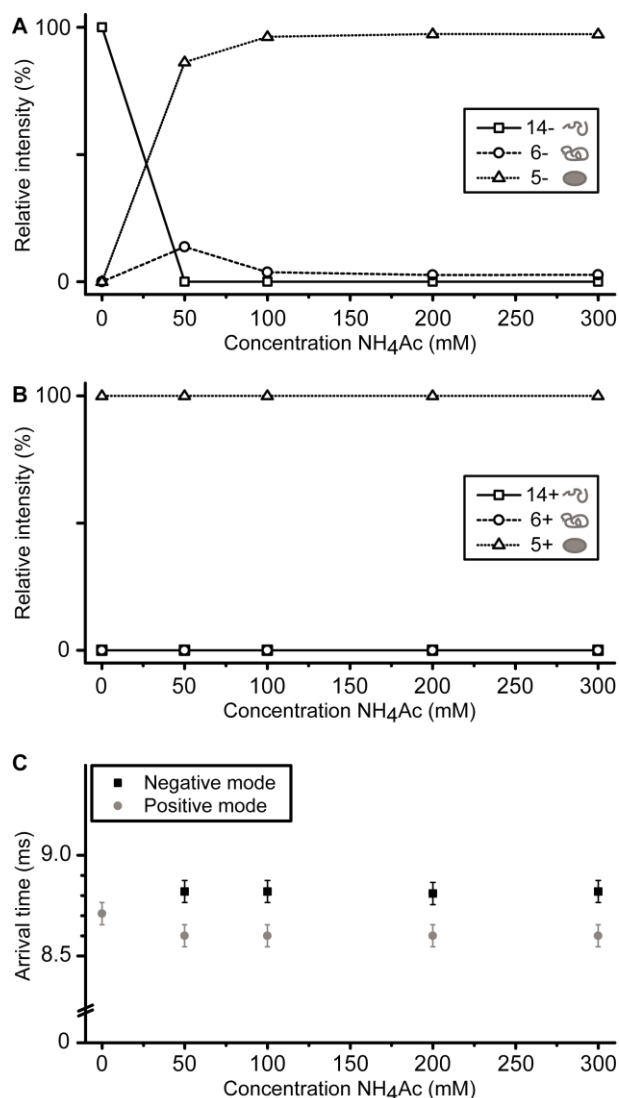


Figure 58. Native MS of the MN19 cocaine-binding aptamer in water, 50, 100, 200, and 300 mM ammonium acetate (NH<sub>4</sub>Ac) in A) the negative and B) the positive ionization mode. The relative intensity of the three distributions (extended, intermediate and compact state which are represented by the 14-, 6- and 5- charge state) is shown (see Figure S-3 for corresponding spectra). C) Extracted arrival times of the 5-/5+ charge state of the MN19 cocaine-binding aptamer in different concentrations of ammonium acetate. No signal was observed for the 5- charge state in pure water. The error bars represent the measurement uncertainty due to the arrival time resolution of the instrument.

When using IM spectrometry, the arrival time (or derived CCS) can provide detailed insights into the structure of an aptamer in the gas-phase.<sup>330</sup> We compared the arrival times for the 5- and 5+ “compact” charge state over the range of ionic strengths (Figure 58C). The error of all arrival times is limited by the time resolution of the measurement

and can be estimated as  $\pm 0.055$  ms. Assuming this level of accuracy, we observed only minor deviation in the measured arrival times of the 5- and 5+ aptamer ions electrosprayed from solutions with different ionic strengths, suggesting that there were no major structural differences for this particular charge state. A consistent, albeit small difference is seen between the negative and the positive ionization mode, with the positive form appearing slightly more compact (lower arrival times). The same is true for the 4- and 4+ charge state (Figure 59). These small differences may be linked to asymmetries in the instrument settings for negative and positive ions, and can also be caused by slightly different long-range interactions of the analyte ions with the drift gas, but their origin cannot be conclusively determined within the scope of the present work. Importantly, while the appearance and extent of the charge state distributions was found to depend on the ionic strength and ionization mode used, no significant differences were observed in the arrival time of a specific charge state.

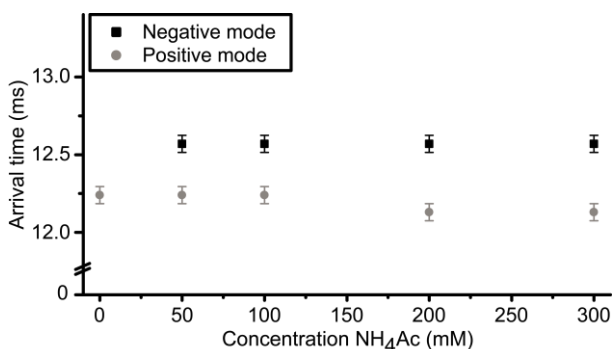


Figure 59. Extracted arrival times of the 4-/4+ charge state of the MN19 cocaine-binding aptamer at different ionic strength (water, 50, 100, 200, and 300 mM ammonium acetate).

The MS and IM data in this study are in agreement with previous observations in literature where the use of  $\geq 100$  mM ammonium acetate was considered to be a “native” buffer for ESI MS.<sup>91</sup> But more importantly, this also corroborates the fact that cations are of great significance for the structure and stability of DNA, including aptamers.<sup>326,327,334</sup>

### 6.3.2. Native IM-MS detects MN19-quinine complexes and indicates a conformational change upon ligand binding

In order to investigate ligand binding to the cocaine-binding aptamers, quinine was chosen because of its higher affinity than cocaine (see above), meaning that quinine

138

concentrations are more amenable to the native MS analysis. The  $K_d$  of MN19 aptamer complexes was previously determined to be  $0.7 \pm 0.2 \mu\text{M}$  for quinine and  $26.7 \pm 0.7 \mu\text{M}$  for cocaine using ITC.<sup>52</sup> These values are averages of 2-5 individual ITC experiments and the reported error is the standard deviation.

A 300 mM ammonium acetate solution was selected here for the IM-MS experiments, since an ionic strength of at least 100 mM was found to be necessary to preserve the folded structure (see above), and fewer non-volatile adducts are present at higher buffer concentration. The addition of quinine to MN19 at 1:1 molar ratio resulted in the formation of ligand-aptamer complexes that were detected in both negative and positive ionization mode, albeit at different relative signal intensities (Figure 60). In the negative ionization mode, 41 % of the aptamer is complexed, while in the positive mode only 18 % of the aptamer binds to quinine. These results demonstrate an effect of the ionization mode on the preservation of noncovalent complexes of oligonucleotides and ligands upon transfer from the solution to the gas-phase. A higher amount of a ligand bound to DNA in the negative ionization mode than in the positive ionization mode was also observed before by Rosu et al.<sup>335</sup> We attribute the observed difference in the relative intensity of the complex signal to a varying gas-phase stability in both ionization modes. More specifically, we believe the charge localization, which is different in both ionization modes, causes partial complex dissociation in the positive ionization mode. In the negative mode, the charges are localized mostly on the phosphate groups of the sugar phosphodiester backbone, whereas positive charges are expected on the nucleobases with the phosphate backbone largely neutralized.<sup>336</sup> The ligand itself can also become charged; the  $pK_a$  values of the quinuclidinyl and quinolone group of quinine at 20 °C are 4.1 and 8.5, respectively. Hence, quinine is positively charged at neutral pH in solution,<sup>337</sup> causing repulsion with the positive charges near the nucleobase interaction site and weakening the interaction in the positive, but not in the negative ionization mode.

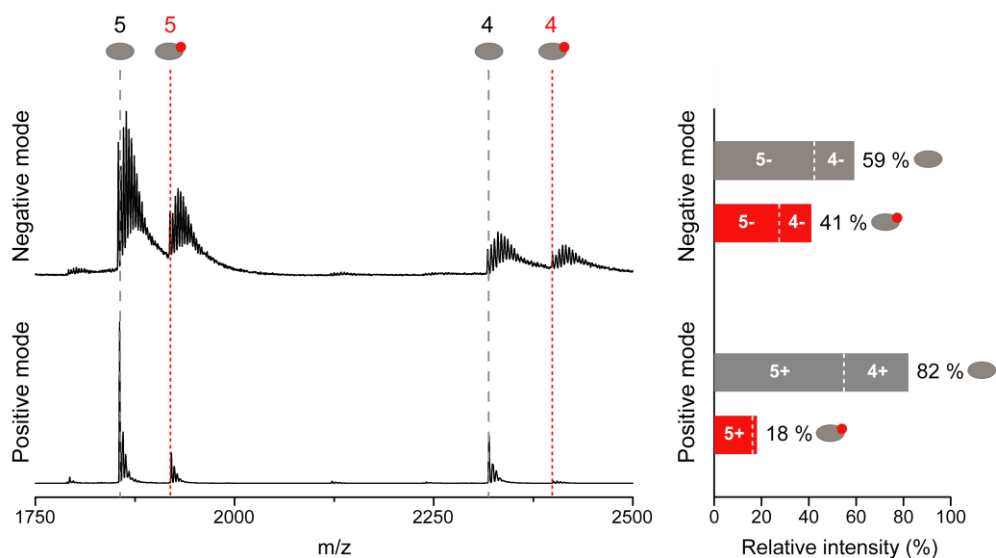


Figure 60. Native IM-MS measurements in the negative and positive ionization mode of the MN19 cocaine-binding aptamer incubated with quinine at a 1:1 molar ratio in 300 mM ammonium acetate. Lines indicate the theoretical peaks of the apo form (grey, dashed) and complex (red, dotted) for the 5-/ and 4-/ charge state. Percentages of the aptamer and the complex signals are represented in the bar graph in grey (top) and red (bottom), respectively.

In general, the amount of complex detected was lower than expected, given the  $K_d$  values in the nM range previously reported. For example, over 88 % of MN19 ( $K_d = 0.7 \mu\text{M}$ ) is expected to bind quinine at a concentration of both aptamer and ligand equal to  $5 \mu\text{M}$ , whereas only up to 41 % (or 18 % in the positive ionization mode) of the aptamer showed complexation in our experiments. A likely explanation for this difference lies in the instrument tuning parameters which were chosen here to achieve good peak resolution. Particularly the used Trap DC bias voltage has a slight activating effect, accounting for roughly 50 % ligand loss (see Figure 54). A possible additional effect is due to the contribution of hydrophobic interactions to ligand binding. Hydrophobic interactions are known to be absent in the gas-phase (as they rely on the tendency of water to sequester nonpolar solutes), thereby shifting the balance of attractive forces which keep ligands bound, and potentially leading to a weakening of the complex upon transfer from solution to the gas-phase.<sup>95,96</sup> This is in contrast to electrostatic interactions which are strengthened in the absence of water in the gas-phase. The observation that we can detect ligand binding, but not in a quantitative manner, indicates that the binding is not purely charge-driven.<sup>338</sup> Finally, also the exact buffer and concentration (here 300 mM ammonium acetate), as well as the temperature (in our case room temperature), can influence the affinity of the aptamer compared to other methods.

In order to investigate the effect of ligand binding on the structure of an aptamer, we used IM spectrometry again. The extracted arrival times of the 5- and 5+ charge state of the MN19 aptamer and the corresponding aptamer-quinine complex are shown in Figure 61. Upon addition of quinine, shifts towards higher arrival times of 5.0 % and 6.4 % respectively in the negative and positive ionization modes are observed. Based on the arrival time resolution alone, an error of 0.055 ms or 0.25 % is expected but accuracies of  $\leq 2\%$  are commonly accepted for this instrumental setup.<sup>71</sup> This means that the detected differences are similar in both polarities, and significant: the binding of the ligand has an observable effect on the structure of the aptamer in the gas-phase. The additional size of the ligand alone, if it were to bind peripherally (i.e. add to the overall volume), compared to the size of the aptamer would not explain the observed difference in arrival time. For the MN19 aptamer there is a 3.4 % mass increase upon binding to quinine; assuming a proportional volume increase, an estimate can be made that the additional molecular volume would only correspond to a 2.3 % increase in arrival time (which correlates with the cross section, i.e. scales with volume<sup>2/3</sup>; and less if the ligand were to bind inside a pocket). This is significantly less than the observed 6.4 % (or 5.0 %) increase, which we therefore expect to be caused by a conformational change of the aptamer upon binding.

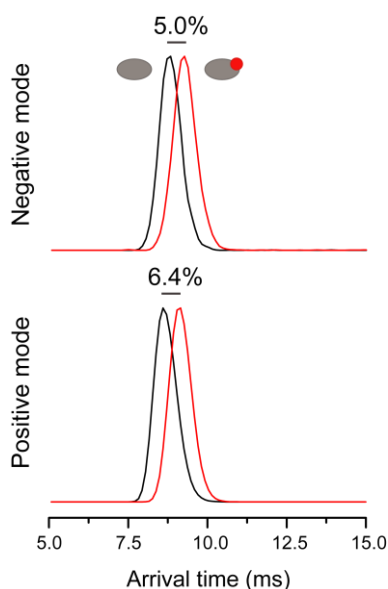


Figure 61. Extracted arrival times of the 5-/5+ charge state of the MN19 cocaine-binding aptamer (black) and its complex with quinine (red) in the negative and positive ionization mode.

Two extreme cases for binding mechanisms can be considered: folding-upon-binding and binding to preformed aptamers (conformational selection) (Figure 62). Folding-

upon-binding would correspond to a significant conformational change of the global 3D structure upon binding of the ligand, but no corresponding shift in the charge state distribution of the aptamer peaks is seen (data not shown). The observed, relatively small change in arrival time does also not support this model. Binding of the ligand to a preformed, completely rigid aptamer on the other hand is also rather unlikely, since this would not result in an observable arrival time increase beyond the small amount due to the volume of the ligand itself. The observation of a significant, but relatively small change in arrival time suggests that the aptamer broadly retained its fold and only more subtle conformational changes occurred. Interestingly also to observe that the arrival time was found to increase upon ligand binding.

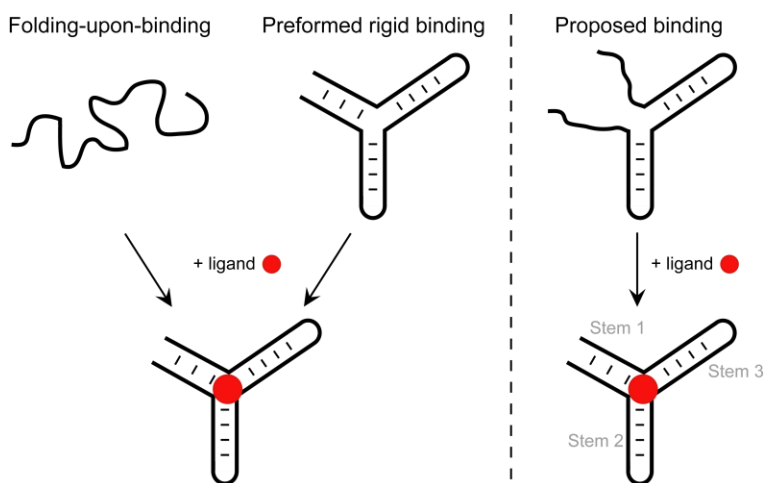


Figure 62. Schematic representation of binding modes for cocaine-binding aptamers with the ligand quinine (red circle). Binding of the ligand might occur via two extreme mechanisms: folding-upon binding of the aptamer and binding to preformed rigid aptamers. Most likely is a scenario in which stem 1 is formed upon binding (proposed binding) as suggested in the literature.<sup>113,225</sup>

These findings can be interpreted in the context of the literature. For the MN19 aptamer with 3 base pairs in stem 1, the three-way junction was proposed as the binding site.<sup>52,215</sup> Moreover, Cekan et al. suggested a binding model based on EPR and fluorescence data, where stem 2 and 3 are already folded without a ligand while stem 1 is not formed and only folds upon binding of the ligand.<sup>225</sup> This model was later confirmed by Neves et al. for the MN19 aptamer specifically using NMR spectroscopy.<sup>113</sup> These findings are reflected in our IM-MS data of the aptamer and complex, which corroborate that the aptamer-ligand complex formation occurs with a small conformational change. Specifically it seems that binding is accompanied by a slight extension of the structure, as evidenced by the increase in arrival time. This

observation might at first appear counter-intuitive because the MN19 aptamer goes from a partially unfolded, possibly larger, structure to a rigid, possibly more compact structure upon binding of the ligand. An unfolded stem 1 does, however, not necessarily mean that it takes up more space (in 3D). The stem can be “coiled up” before binding the ligand and stiffens to extend the general structure upon complexation with the ligand.

### 6.3.3. Native IM-MS captures trends in ligand affinity and conformational dynamics of increasingly more rigid cocaine-binding aptamers

The IM-MS approach was extended in the positive ionization mode to a panel of cocaine-binding aptamers (MN19, MNS-7.9, MN4 and 38-GC) to test the ability of the method to differentiate between closely related aptamer structures, and how their relative ligand binding affinities differ. These aptamers exhibit a range of binding properties; it was previously shown that mainly stem 1 determines the binding behavior.<sup>228</sup> For example, the MN4 aptamer, which has a long stem 1 (6 base pairs), has been described with a well-defined structure in its free and bound forms. By contrast, the MN19 aptamer, which has a shortened stem 1 (3 base pairs), has a rather loose and unstructured conformation and only becomes structured after ligand binding.<sup>52,228</sup>

A randomized sequence, with the same composition as the MN19 aptamer, was used as a control. Upon adding quinine (1:1 ratio) to this sequence, no complex was formed proving that there is no nonspecific binding under the conditions used (Figure 63A and Figure 64). The addition of quinine to the cocaine-binding sequences resulted in ligand-aptamer complexes. Importantly, the amount of complex formed differed for all cocaine-binding aptamers, reflecting their differences in binding affinity, albeit not in a quantitative fashion (see discussion above for MN19). The affinity to quinine has been determined previously by ITC only for some of the aptamers studied here (see Table 6). Nevertheless, it was shown before by comparing multiple aptamers that the relative affinity towards cocaine is a measure for the relative affinity towards quinine and vice versa.<sup>52,113</sup> In native IM-MS, the relative complex signal intensity upon adding quinine at a 1:1 molar ratio varies systematically between the different aptamers (Figure 63). The MN19 aptamer, which has the highest  $K_d$  value among them, binds the least quinine (22 %). On the other hand, the aptamer with the lowest  $K_d$  (38-GC) binds the most

quinine (43 %). In general, there is a clear trend in the signal intensity of the complex in agreement with the expected trend in the solution-phase binding affinity. These results show that native ESI-MS can be used to determine relative, albeit not absolute binding strengths of aptamers correctly, based on the intensity ratio of complex and aptamer signals, confirming previously reported data in the literature.<sup>52,113,215,323</sup>

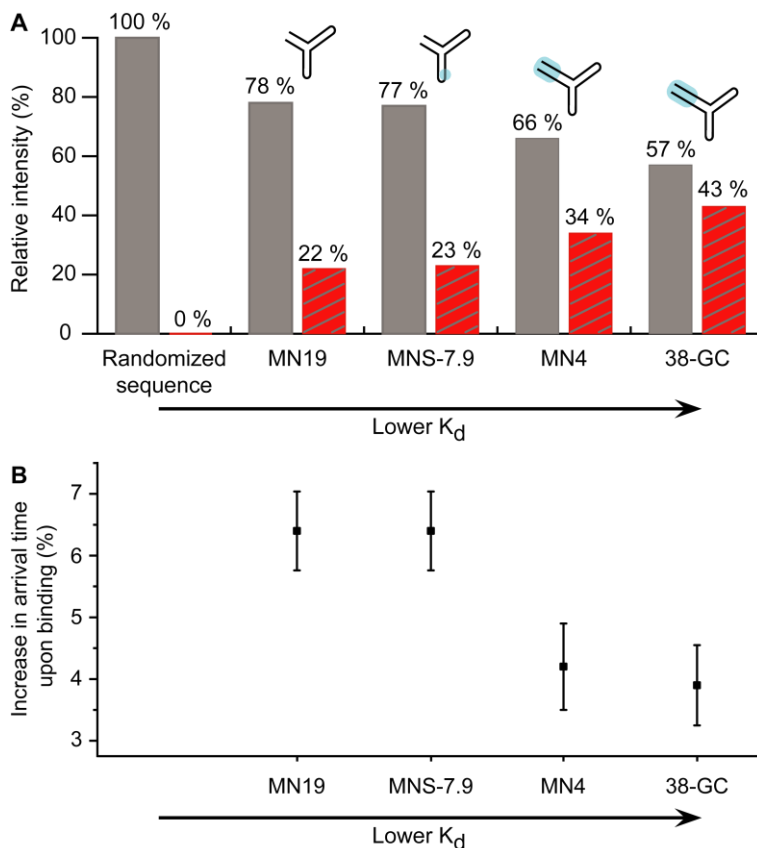


Figure 63. A) Native IM-MS measurements in the positive ionization mode of four cocaine-binding aptamers (MN19, MNS-7.9, MN4, and 38-GC) and a randomized sequence incubated with quinine at a 1:1 molar ratio in 300 mM ammonium acetate. The abundance of the apo form (grey filled area) and complex (red hatched area) are indicated for all aptamers. B) The percentage increase in arrival time upon complexation for the four cocaine-binding aptamers (MN19, MNS-7.9, MN4 and 38-GC).

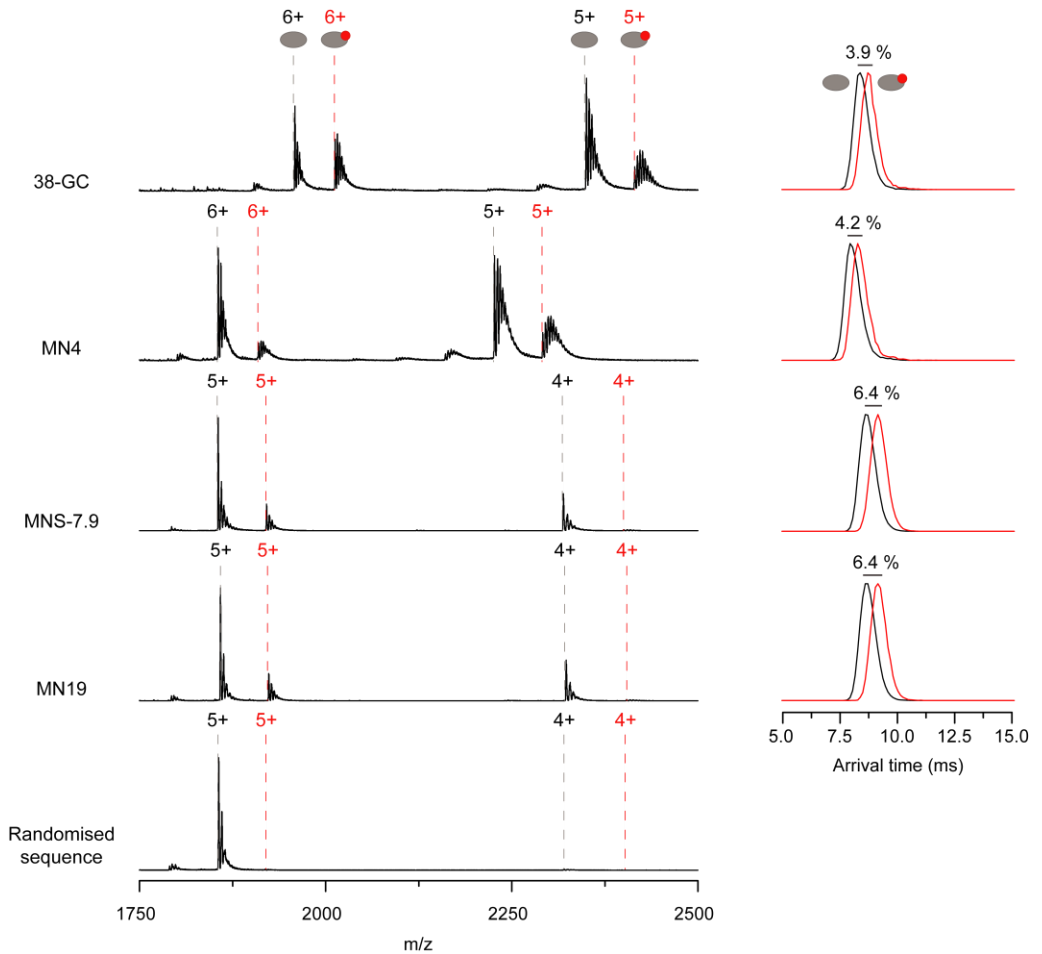


Figure 64. Native IM-MS measurements in the positive ionization mode of a randomized sequence and four cocaine-binding aptamers (MN19, MNS-7.9, MN4, and 38-GC) incubated with quinine at a 1:1 molar ratio at 300 mM ammonium acetate. Dashed lines indicate the theoretical peaks of the apo form (black) and the complex (red) for all aptamers. Arrival times (of the 5+ charge state for MN19 and MNS-7.9 and the 6+ charge state for MN4 and 38-GC) were extracted for the aptamers (black) and the complexes (red).

Table 6. Previously reported  $K_d$  values of the cocaine-binding aptamers used in this study.

Aptamer	$K_d$ quinine ( $\mu\text{M}$ )	$K_d$ cocaine ( $\mu\text{M}$ )	Buffer	Reference
MN19	$0.7 \pm 0.2$	$26.7 \pm 0.7$	20 mM Tris (pH 7.4), 140 mM NaCl, and 5 mM KCl	52
MNS-7.9	/	20	20 mM Tris (pH 7.4), 140 mM NaCl, and 5 mM KCl	215
MN4	$0.23 \pm 0.03$	$7 \pm 1$	20 mM Tris (pH 7.4), 140 mM NaCl, and 5 mM KCl	52
38-GC	/	$2.6 \pm 1$	10 mM Tris buffer (pH 7.4) with 0.01 mM $\text{MgCl}_2$ and 5 % DMSO	323

In a next step, we investigated the influence of ligand binding on aptamer structure. Upon addition of quinine, arrival time increases ranging from 3.9 % to 6.4 % were observed for the different aptamers (Figure 63B). As for the MN19 aptamer, these changes in arrival time cannot be assigned to the additional size of the ligand compared to the size of the aptamers alone, which would only account for a maximum of 2.0 - 2.3 % increase in arrival time for peripheral binding (and less for occluded binding). The same interpretation of the arrival time shifts can be followed for all aptamers: The relatively small increase in arrival time upon binding, and the observation that no charge state shifts occur, suggests that complex formation did not result in a dramatic conformational change of the global 3D structure (which folding-upon-binding would cause). The aptamers seemed to broadly retain their fold and only more subtle conformational changes occurred, which are most likely due to the behavior of stem 1. There are some interesting differences however between the aptamers (Figure 63B). With increasing length of stem 1 from MN19 to MN4 and 38-GC, the arrival time differences upon complexation showed a downward trend from 6.4 % to 4.2 % and 3.9 %, respectively, while at the same time binding affinity increased (lower  $K_d$ ). We propose that the more preformed, “rigid” binding e.g. seen in MN4 leads to less structural rearrangement upon complexation (as evidenced by the smaller arrival time changes) accompanied by a higher binding affinity (Figure 63A), whereas the more adaptive binding suggested for MN19 requires more reorganization and comes with a lower ligand affinity, possibly due to an entropic penalty.<sup>52</sup> The key difference between these aptamers is the length of stem 1, but without detailed structural models we can only speculate why ligand binding leads to a slight size increase of the overall structure. The results obtained with IM-MS are broadly consistent with data in literature obtained with NMR and SAXS by Reinstein et al. and Neves et al.<sup>52,228</sup>

## 6.4. Conclusion

We reported here the use of native IM-MS to analyze cocaine-binding aptamers in the negative and positive ionization mode; specifically, their higher-order structure and noncovalent interactions. The data showed that counter-ions play an important role in stabilizing the folded form of the aptamers in the negative ionization mode upon transfer from the solution to the gas-phase. This is due to the negatively charged phosphate backbone which leads to significant intramolecular charge repulsion, both in solution and in the gas-phase, and reflects the key role cations are known to have in stabilizing oligonucleotide higher-order structure in solution. Positive charges on the other hand are due to protonation during ESI and differently distributed throughout the molecule, and only low-charged compact states are detected in the spectra. The use of buffers with an ionic strength of 100 mM ammonium acetate or higher was previously reported as “native” solution conditions in native MS.

Moreover, it was demonstrated that aptamer-ligand complexes can be detected and analyzed in the positive ionization mode native IM-MS, despite the previously claimed superiority of the negative ionization mode for the analysis of nucleic acids. Advantages of being able to work in the positive ionization mode are for example that IM calibrants are more readily available, and that protein-oligonucleotide complexes are usually studied in the same ionization mode. Native MS can also determine relative binding affinities of a set of cocaine-binding aptamers by using the ratio of the bound and unbound peak in the mass spectra; the ranking order thus obtained matches known complex stabilities ( $K_d$  values). The approach has proven to be sensitive towards small structural alterations of the aptamer, and since a randomized sequence did not show any binding, we conclude that there are only selective interactions occurring under the conditions used in this study. The fact that less complex was observed than expected from the reported solution-phase binding affinity is largely explained by the chosen instrument tuning settings.

IM data gave insight into structural differences between the aptamers upon ligand binding. Each charge state appeared to have a defined arrival time irrespective of ionization polarity and ionic strength of the solution (although certain charge states were absent without sufficient counter-ions), within the error margin of the overall experiment ( $\leq 2\%$ ). IM experiments allowed determination of subtle conformational changes within one charge state, when comparing the structure of different aptamers and also detecting structural effects of ligand binding. The magnitude of the change

was found to correlate with the binding mode, with the more pre-formed and rigid aptamers such as the long-stem MN4 showing higher binding affinity but a smaller arrival time increase. It is important to note though that dsDNA is expected to undergo compaction during transfer from the solution to the gas-phase,<sup>91,333</sup> and this can reasonably be expected to also occur in aptamers. We did therefore not attempt to determine the actual CCS values, although this will be of great interest in a future study, but carefully observed arrival time shifts, i.e. relative differences, under identical experimental conditions. These shifts gave nevertheless an insightful qualitative, arguably semi-quantitative, picture of structural differences between aptamers and upon ligand binding, allowing us to infer tenets of the binding mechanism and the structural reorganization which accompanies ligand recognition.

We showed that native MS combined with IM can contribute to the understanding of the higher-order structure of aptamers and their complexes. Although this structural MS method stands strong in itself, combining it with other structural and computational approaches holds considerable promise towards a deeper understanding of oligonucleotide higher-order structure and function. This perspective will be worthwhile exploring in future oligonucleotide-oriented research.

Do aptamers always bind? The need for a multifaceted analytical approach when demonstrating binding affinity between aptamer and low molecular weight compounds

**Fabio Bottari\***, **Elise Daems\***, **Anne-Mare de Vries\***, **Pieter Van Wielendaele**, **Stanislav Trashin**, **Ronny Blust**, **Frank Sobott**, **Annemieke Madder**, **José C. Martins**, and **Karolien De Wael**

*Adapted from Journal of the American Chemical Society, 142, 46, 19622-19630 (2020)*

**\* Contributed equally**



## Abstract

In this chapter, we compare different analytical methodologies to validate or disprove the binding capabilities of aptamer sequences. This was prompted by the lack of a universally accepted and robust quality control protocol for the characterization of aptamer performances coupled with the observation of independent yet inconsistent data sets in the literature. As an example, we chose three aptamers with a reported affinity in the nanomolar range for ampicillin, a  $\beta$ -lactam antibiotic, used as biorecognition elements in several detection strategies described in the literature. Application of a well-known colorimetric assay based on aggregation of gold nanoparticles (AuNPs) yielded conflicting results with respect to the original report. Therefore, ampicillin binding was evaluated in solution using isothermal titration calorimetry (ITC), native nano-electrospray ionization mass spectrometry (nESI-MS) and  $^1\text{H}$  nuclear magnetic resonance (NMR) spectroscopy. By coupling the thermodynamic data obtained with ITC with the structural information on the binding event given by native nESI-MS, and  $^1\text{H}$  NMR we could verify that none of the ampicillin aptamers show any specific binding with their intended target. The effect of AuNPs on the binding event was studied by both ITC and  $^1\text{H}$  NMR, again without providing positive evidence of ampicillin binding. To validate the performance of our analytical approach, we investigated two well-characterized aptamers for cocaine/quinine (MN4), chosen for its nanomolar range affinity, and L-argininamide (1OLD) to show the versatility of our approach. The results clearly indicate the need for a multifaceted analytical approach, to unequivocally establish the actual detection potential and performance of aptamers aimed at small organic molecules.

## 7.1. Introduction

While aptamers appear promising tools for analytical chemists and biologists alike, and their potential for commercialization is broadly recognized, many challenges remain to be faced before this can be achieved. A variety of factors have been put forward to explain why aptamers have not yet penetrated the market:<sup>339</sup> one of the main reasons can be identified as the so-called “thrombin problem”. Indeed, rather than developing assays for more clinically relevant targets, hundreds of investigators continue to focus their attention on perfecting thrombin-binding aptamers or designing clever detection strategies for this target. The same can be said to a lesser extent for cocaine-binding aptamers in the field of small organic molecule analysis.

We strongly believe that the lack of a universally accepted and reliable quality control protocol for the characterization of aptamer performances is one of the main obstacles toward successful valorization and should therefore be tackled first. Only very few aptamers for small molecules were extensively characterized and their affinity validated. The few exceptions such as cocaine-binding aptamers<sup>214</sup> have become the gold standard. In general, novel aptamers are only characterized by the group that selected them in the first place and are used uncritically afterward in other applications by different groups. Caution toward (the affinity of) the aptamers in each new application (with different experimental settings) has considerably diminished over time.

In this chapter, we focus on ampicillin aptamers. Ampicillin is a  $\beta$ -lactam antibiotic that belongs to the family of penicillins and is one of the most frequently used antibiotics for both human and veterinary medicine. Residues in the environment and the food chain may cause allergic reactions in hypertensive individuals, interfere with fermentation processes, but, most importantly, increase antimicrobial resistance (AMR).<sup>340</sup> As surveillance is one of the main suggested interventions to tackle AMR,<sup>341</sup> the development of reliable sensors for antibiotics is a research topic of significant impact. In 2012, Song et al.<sup>342</sup> selected three different aptamer sequences for ampicillin (AMP4, AMP17, and AMP18) using FluMag-SELEX in which the ampicillin was covalently immobilized on magnetic beads.<sup>24</sup> Furthermore, they used them in a colorimetric detection strategy (Figure 65) based on gold nanoparticle (AuNP) aggregation to detect the antibiotic in the low nanomolar range, both in aqueous solution and in milk samples. A fluorescence-colorimetry assay was used to calculate the  $K_d$  values. This was the very first example of an aptamer against a  $\beta$ -lactam antibiotic described in the

literature. More specifically, the authors reported that the selected aptamers are capable of recognizing the side chain of ampicillin (1-phenylethylamine), assuring a high selectivity against structurally related compounds. In the last eight years, these aptamers have been used by other research groups around the world, in different analytical approaches and sensor configurations. The latter mostly include electrochemical transduction, with very good results in terms of both figures of merit and real sample analysis (for a complete overview, see Table 9 in Appendix). The affinity constant, the selectivity, and the specificity reported in the original paper were always taken for granted, and no further studies on their binding mechanism have appeared.

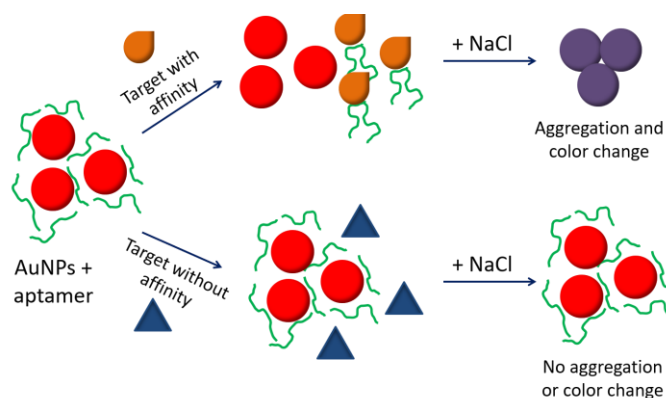


Figure 65. Schematic representation of the colorimetric AuNPs assay.

Therefore, we undertook a systematic study of the ampicillin aptamer binding interactions, using different state-of-the-art analytical techniques which do not require immobilization: ITC, native nESI-MS, and  $^1\text{H}$  NMR. These techniques were previously used for aptamer characterization,<sup>56,93,343,344</sup> but rarely combined, although they provide complementary results. A single ITC experiment delivers information about the  $K_d$ , thermodynamics, and stoichiometry of the interaction.<sup>344–346</sup> Native nESI-MS provides information about the stoichiometry (provided that the affinity is in the low  $\mu\text{M}$  to nM range), and allows identification and characterization of individual species. Moreover, multiple species, which are, e.g. coexisting in equilibrium, can be detected separately rather than as an average or a selected, prominent state.<sup>64,87,93</sup> Solution-state  $^1\text{H}$  NMR reveals the behavior of compounds on a molecular level and allows delineation of the location of the intermolecular interaction surface involved in the aptamer-target interactions.<sup>228,347–349</sup> By combining ITC, native nESI-MS, and  $^1\text{H}$  NMR, one can obtain a complete overview of the binding affinity, selectivity, and mechanism between aptamers and small molecule targets without immobilizing them to a substrate.<sup>53,93,228,349</sup>

In this way, it is possible to validate or disprove the binding affinity and mechanism of aptamer sequences for small organic molecules, beyond reasonable doubt. Therewith, we hope to prevent a proliferation of publications which suggest aptamer sequences and applications without a proper validation of the aptamer-target affinity.

## 7.2. Materials and methods

### 7.2.1. Aptamers and reagents

Ampicillin aptamers, the MN4 (quinine/cocaine binding) aptamer, the 1OLD (L-argininamide binding) aptamer and random ssDNA sequence (N36) were all purchased from Eurogentec (Belgium). In Table 7, the specifications of the five different sequences can be found. Ampicillin sodium salt, nafcillin sodium salt, quinine hydrochloride dihydrate, L-argininamide dihydrochloride and ammonium acetate solution (7.5 M) were obtained from Sigma-Aldrich. Cephalexin monohydrate and chloramphenicol were obtained from TCI (Europe). All other chemicals were reagent grade and used without further purification. Milli-Q water was obtained with a Millipore Milli-Q Academic system.

Table 7. Acronym, sequence, length and previously reported  $K_d$  of the ampicillin aptamers (AMP4, AMP17, and AMP18), MN4 (quinine binding) aptamer and random ssDNA sequence (N36) used in the study.

Acronym	Sequence	Length (bp)	Target	$K_d$ (nM)
AMP4	5'-CAC-GGC-ATG-GTG-GGC-GTC-GTG-3'	21	Ampicillin	9.4 <sup>342</sup>
AMP17	5' GCG-GGC-GGT-TGT-ATA-GCG-G-3'	19	Ampicillin	13.4 <sup>342</sup>
AMP18	5'-TTA-GTT-GGG-GTT-CAG-TTG-G-3'	19	Ampicillin	9.8 <sup>342</sup>
MN4	5'-GGC-GAC-AAG-GAA-AAT-CCT-TCA-ACG-AAG-TGG-GTC-GCC-3'	36	Quinine	100 <sup>a 350</sup>
1OLD	5'-GAT-CGA-AAC-GTA-GCG-CCT-TCG-ATC-3'	24	L-argininamide	165·10 <sup>3</sup> <sub>351</sub>
N36	5'-NNN-NNN-NNN-NNN-NNN-NNN-NNN-NNN-NNN-NNN-NNN-3'	36	-	-

<sup>a</sup> $K_d$  value of binding with quinine.

### 7.2.2. AuNPs synthesis

Gold nanoparticles were prepared according to Storhoff et al.<sup>352</sup> All glassware was cleaned in aqua regia (3 parts HCl, 1 part HNO<sub>3</sub>), rinsed with MilliQ, and then oven dried prior to use. An aqueous solution of 1 mM HAuCl<sub>4</sub> was brought to boiling under stirring, and then 10 mL of a 38.8 mM trisodium citrate (Na<sub>3</sub>C<sub>6</sub>H<sub>5</sub>O<sub>7</sub>) solution was added quickly, which resulted in a color change from pale yellow to deep red. After the color change, the solution was left to boil for additional 15 min and then allowed to cool down to room temperature. The resulting NPs were filtrated under vacuum to remove aggregates and impurities. The size and concentration of the nanoparticles was estimated according to Haiss et al.<sup>353</sup> AuNPs with a diameter of 13 nm and a concentration of 20.4 nM were obtained.

### 7.2.3. AuNPs colorimetric assay

The colorimetric AuNPs assay was performed according to Song et al.<sup>342</sup> A solution of AuNPs (≈4 nM) was incubated with 100 nM of the selected ampicillin aptamers in 10 mM phosphate buffer pH 8 for 1 h with tilting and rotation. A 100 nM solution of the chosen target in 10 mM phosphate buffer pH 8 was then added to the vial and incubated for 1 h. Subsequently, 100 mM of NaCl was added to the solution to promote the eventual aggregation of the nanoparticles and the color change (from red to purple) linked to the binding event. UV-Vis spectra were recorded after each step. The results were reported in terms of the ratio between the absorbance at 520 and 620 nm ( $A_{520}/A_{620}$ ). UV-Vis spectra were acquired between 400 and 800 nm with a Cary100 Conc spectrophotometer (Agilent Technologies) operated by Cary Win UV 4.20 software and with a NanoPhotometer N60 (Implen) operated by NanoPhotometer NPOS software.

### 7.2.4. ITC protocol

ITC experiments were performed on a MicroCal PEAQ-ITC instrument (Malvern Panalytical) operated by MicroCal PEAQ-ITC control software. Data analysis was performed with the MicroCal PEAQ-ITC Analysis software. Since many different parameters have been tested a summary is reported in Table 8 for ease of reference. For the control experiments only one set of parameters was used. For the MN4

aptamer: 50  $\mu\text{M}$  quinine was titrated in 5  $\mu\text{M}$  of aptamer. The assay buffer was a 0.1 M Tris buffer with 5 mM KCl at pH 7.4. A total of 16 injection was performed with a volume of 2.5  $\mu\text{L}$  (initial delay 180 s, spacing 150 s and reference power 5  $\mu\text{cal/s}$ ). For the 1OLD aptamer: 7.5 mM L-argininamide was titrated in 150  $\mu\text{M}$  of aptamer at 25  $^{\circ}\text{C}$ . The assay buffer was a 10 mM phosphate buffer containing 100 mM NaCl at pH 7.5. A total of 20 injections was performed with the volume of the first 11 injections set at 1  $\mu\text{L}$  and of the last 9 set at 3  $\mu\text{L}$  with a spacing of 150 s and reference power of 5  $\mu\text{cal/s}$ . The reference cell was filled with degassed ultrapure water. The aptamer solutions were always put in the sample cell, after a two minutes pre-equilibration time with assay buffer. The target solution was administered in the injection syringe. The instrument temperature was set to the run temperature before loading and kept constant during the complete run. In order to determine the dilution heats, control titrations were performed consisting of injection of the ligand into the sample cell filled only with buffer. Thermograms for the binding of quinine to MN4 and L-argininamide to 1OLD were analyzed using the 'one set of sites' binding model, by including the corresponding control titration.

Table 8. Instrumental and analytical parameters of the ITC experiments.

<b>Instrumental parameters</b>	
Total number of injections	13; 19; 25
Cell temperature	20; 25; 30; 37; 40 °C
Reference power	2; 5; 10 $\mu$ cal/s
Initial delay	180 s
Stirring speed	750 rpm
Injection volume	1; 2; 3 $\mu$ L
Spacing	150 s
<b>Analytical parameters</b>	
Aptamers	AMP4; AMP17; AMP18
Targets	Ampicillin; Cephalexin
Buffers	0.1 M Phosphate buffer, 100 mM NaCl
	10 mM Phosphate buffer, 100 mM NaCl
	0.1 M Tris buffer, 5 mM KCl
	10 mM Tris Buffer, 5 mM KCl
pHs	2; 5; 6; 7; 7.4; 7.6; 8
Molar ratios	1/2; 1/5; 1/10
Concentration range	Aptamer: 1 – 25 $\mu$ M
	Target: 50 $\mu$ M – 1 mM
Annealing <sup>a</sup>	Yes/No
Sonication <sup>b</sup>	Yes/No

<sup>a</sup>Annealing<sup>53</sup> = 3 min at 90 °C, followed by 1 min at 4°C, then 1 min at RT before injection.

<sup>b</sup>Sonication = all solutions were sonicated in an ultrasonic bath for 10 min to remove air bubbles.

#### 7.2.4.1. ITC with AuNPs

Prior to the ITC experiments, AuNPs were dialyzed overnight against MilliQ water with a dialysis cellulose membrane (Dialysis tubing cellulose membrane, avg. flat width 10 mm, Sigma Aldrich). ITC measurements were performed in MilliQ at 25 °C, with 26 injections of 1.5  $\mu$ L of 1 mM ampicillin solution, with 1  $\mu$ M of AMP17 in the cell (reference power 5  $\mu$ cal/s, 180 s initial delay and 150 s spacing). Different titrations were performed without aptamer and without nanoparticles, to assess the heat exchange contribution of all interactions.

### 7.2.5. Native nESI-MS protocol

Prior to native MS analysis, the aptamers were buffer exchanged into 150 mM aqueous ammonium acetate (pH 6.8) using Micro-Biospin P-6 columns (Bio-rad Laboratories, USA), in order to desalt the samples and to provide a volatile electrospray buffer of appropriate ionic strength. Solutions of 5 to 10  $\mu\text{M}$  aptamer with a five-fold excess of ampicillin, quinine or L-argininamide were prepared for binding to the AMP17, MN4 or 1OLD aptamer respectively, and 3-5  $\mu\text{L}$  of each sample was injected into the mass spectrometer using in-house prepared, gold-coated borosilicate nESI emitters. The experiments were performed on a Synapt G2 HDMS (Waters, Manchester, UK) in positive ionization mode using careful tuning to maintain fragile noncovalent interactions during ionization and inside the instrument. Experiments were performed in sensitivity and mobility mode. The spray capillary voltage ranged between 1.3-1.5 kV and the sampling cone voltage was 25-50 V. The trap and transfer collision energy were set at 5 V and 0 V, respectively and the trap DC bias was fixed to 35 V. The IMS wave velocity was set to 800 m/s and the IMS wave height to 35 V. Gas pressures were 2.57 mbar and  $2.16 \cdot 10^{-3}$  mbar for the backing and source gas, respectively. All data was analyzed using MassLynx 4.1 (Waters).

### 7.2.6. $^1\text{H}$ NMR protocol<sup>354</sup>

NMR spectra were recorded at 25 or 5  $^{\circ}\text{C}$  on a Bruker Avance II spectrometer operating at a  $^1\text{H}$  frequency of 700.13 MHz, under Topspin 3.1pl7 and using a 5 mm triple channel Prodigy  $\text{N}_2$ -cryocooled probe with a Z-gradient of 6.56 G/mm. Standard pulse sequences from the Bruker library were used throughout. Samples for reference spectra consisted of 550  $\mu\text{L}$  of 1 mM solutions of AMP17 and ampicillin or 1OLD and L-Argininamide in  $\text{D}_2\text{O}$ , buffered at pH 7 using aliquots of acid or base (DCl or NaOD). All 1D  $^1\text{H}$  spectra were recorded using a spectral width of 20 ppm and consisted of 128 to 256 scans of 64K TD points each preceded by a 2.0 s relaxation delay. Processing consisted of one order zero-filling prior to multiplication and Fourier transformation. Chemical shifts are referenced against internal DSS (4,4-dimethyl-4-silapentane-1-sulfonic acid). An additional experiment involved  $^1\text{H}$ - $\{^{13}\text{C}\}$  HMBC for assignment of the ampicillin and L-argininamide resonances. Titrations were executed by adding aliquots from a solution containing 8 mM ampicillin or L-argininamide and 0.4 mM AMP17 or 1OLD, to a 0.4 mM solution of AMP17 or 1OLD, thus keeping the aptamer concentration constant throughout the titration. Final aptamer:target ratios varied from 1:0 to 1:10.

In addition, for the AMP17 aptamer pulsed-field-gradient (PFG) NMR was performed to detect aptamer-ligand interactions by monitoring the diffusion coefficient of the ampicillin resonances.

## 7.3. Results and discussion

### 7.3.1. Colorimetric AuNPs assay

To test the specificity of the aptamers, the colorimetric AuNPs assay employed by Song et al. was repeated. In this type of assay, ssDNA is first adsorbed on the gold surface to protect the nanoparticles against aggregation in the presence of an electrolyte salt.<sup>355,356</sup> An explicative scheme of the assay is depicted in Figure 65. Colorimetric assays based on citrate-capped AuNPs are widely used as an analytical tool to investigate aptamer-target interactions.<sup>357,358</sup> It supposedly provides a fast approach to test aptamer performances and binding capabilities. The assay used by Song et al. was replicated to allow for a direct comparison with the original results. Along with ampicillin, cephalexin was tested, since it has the same side-chain as ampicillin, for which the aptamer should be selective, according to the conclusion of the original article. The protocol was applied to ampicillin, cephalexin, and two other antibiotics for which no affinity is expected, i.e., nafcillin and chloramphenicol. In addition, a random ssDNA sequence (N36) was tested in similar conditions.

The results for the colorimetric test are reported in terms of the ratio between the absorbance of the UV-vis band at 520 and 620 nm, respectively. The band at 520 nm corresponds to the amount of dispersed particles, while the one at 620 nm corresponds to that of aggregated particles. As both dispersed and aggregated nanoparticles are present in solution at the outset, and binding of the aptamer to its target induces aptamer release, more aggregation of AuNPs will occur upon subsequent addition of salt; thus, the absorbance will increase at 620 nm (aggregated AuNPs) in intensity, while that at 520 nm (dispersed AuNPs) should decrease. This change is typically monitored by a decrease in the  $A_{520}/A_{620}$  ratio (Figure 72 in Appendix) which is considered more reliable and sensitive than the change in individual absorbance alone.<sup>358</sup> The original paper reports an arbitrarily chosen ratio of 2 as a threshold between positive (binding, ratio < 2) and negative (nonbinding, ratio > 2) results. In the article of Song et al., only the assay with the aptamer and the specific target ampicillin showed an  $A_{520}/A_{620}$  ratio below 2, with AMP17 demonstrating the best performances. Therefore, we first

repeated the measurements with AMP17 in our study (Figure 66). The histogram shows that the ratio for all the considered combinations (including nafcillin and chloramphenicol for which no binding is expected) is lower than 2, so all have to be considered as positive results, according to the original protocol. It was observed that for ampicillin and cephalixin the  $A_{520}/A_{620}$  ratio is lower than the ratio obtained with nafcillin and chloramphenicol. This observation is consistent with the report of Song et al., as the aptamer should specifically recognize the side chain of ampicillin and cephalixin. For this reason, a more efficient binding can be expected for those two targets. However, the standard deviations (three repeated measurements) are relatively large; the differences in  $A_{520}/A_{620}$  between targets remain small and below the threshold value of 2 in all cases. Our results are therefore not entirely consistent with the ones reported before, and prompted us to investigate the interaction via other techniques to establish whether the results of AuNPs assay is linked (or not) to the binding event.

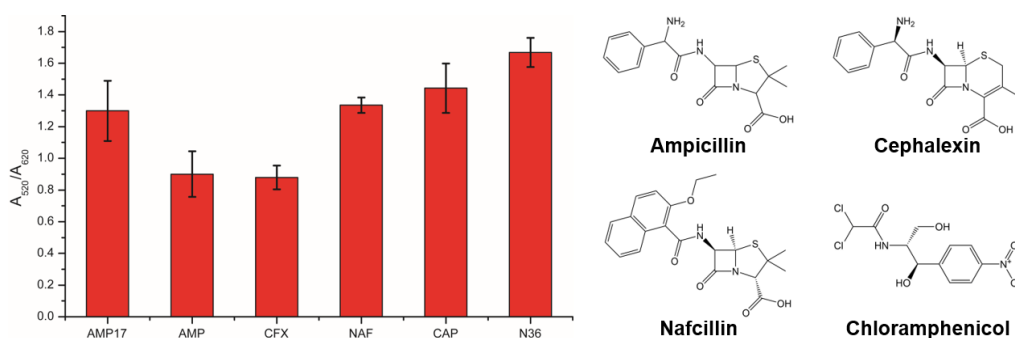


Figure 66. Absorbance ratio ( $A_{520}/A_{620}$ ) for the AuNPs solutions with 100 nM of AMP17 in the absence of an antibiotic (AMP17) and with 100 nM of various antibiotics in the presence of 100 mM NaCl: ampicillin (AMP), cephalixin (CFX), nafcillin (NAF), and chloramphenicol (CAP); Negative control with a random 36 bp ssDNA (N36) in the presence of 100 nM ampicillin and 100 mM NaCl. Inset: structures of ampicillin, cephalixin, nafcillin, and chloramphenicol.

### 7.3.2. Aptamer binding in solution

The AuNP assay can be considered a label- and immobilization-free assay, since the aptamer only interacts with the AuNPs via electrostatic interactions. Therefore, other techniques which do not involve labeling and immobilization were selected to characterize the behavior of the aptamer in the same conditions. ITC measurements were carried out while varying different parameters such as buffer composition, pH, and target to aptamer molar ratio. First of all, the titration was performed in the

conditions reported for the original AuNPs assay, i.e., 10 mM phosphate buffer pH 8 with the AMP17 aptamer in a concentration of 5  $\mu$ M titrated with 50  $\mu$ M of ampicillin. Given the reported  $K_d$  value (13.4 nM), the thermogram should show a clear exothermic binding trend. However, no heat exchange that could be linked to specific binding was observed, even when changing the aptamer (AMP4 and AMP18). Trying to understand if the buffer composition used during the SELEX process (Tris instead of phosphate) could influence the affinity of the aptamers for ampicillin, we also tested buffers more similar to the binding buffer of SELEX. Moreover, the buffer ionic strength was varied by adding NaCl and KCl. In addition, the possible effect of the pH on the interaction between ampicillin and the aptamer was taken into consideration. Since ampicillin is a zwitterion, with  $pK_a$  of 3.2 and 7.4,<sup>359</sup> several buffers with pHs above and below the  $pK_a$  of ampicillin were tested (see Table 8 for a complete overview of all tested parameter combinations). However, none of the considered combinations allowed us to observe a binding response. Figure 67 shows two sets of thermograms comparing different aptamers (Figure 67A) and different buffers (Figure 67B). The only visible heat exchange in the thermograms is linked to the injection heat.

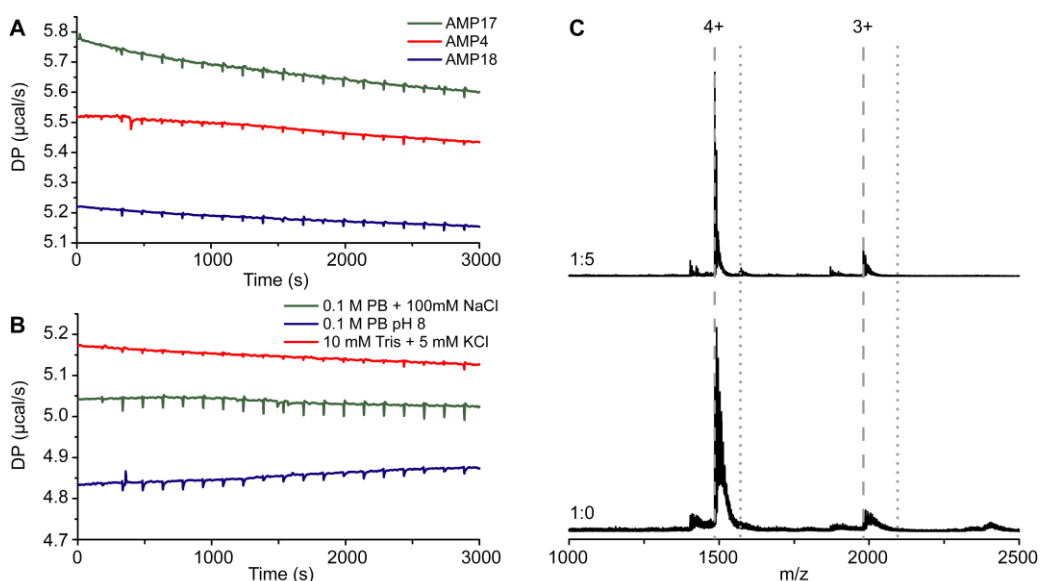


Figure 67. Different thermograms for the (absent) interaction of ampicillin aptamers with their target (ampicillin); A) 20  $\mu$ M of AMP17 (blue), AMP4 (green), and AMP18 (red) in 0.1 M phosphate buffer (PB) pH 8 at 25  $^{\circ}$ C, titrated with 280  $\mu$ M of ampicillin; B) 20  $\mu$ M AMP17 at 25  $^{\circ}$ C in 0.1 M phosphate buffer pH 8 with 100 mM NaCl (green), 0.1 M phosphate buffer pH 8 (blue), 0.1 M Tris buffer pH 7.4 with 5 mM KCl (red), titrated with 280  $\mu$ M of ampicillin; C) Native nESI-MS of the ampicillin-binding aptamer AMP17 without ampicillin and with ampicillin incubated at a 1:5 aptamer:ampicillin ratio in 150 mM ammonium acetate buffer pH 6.8. Theoretical  $m/z$ -values of the apo form (dashed lines) and the 1:1 stoichiometry of the complex (dotted lines) are indicated for the 4<sup>+</sup> and 3<sup>+</sup> charge states.

As the heat exchanged as a result of binding may be smaller than expected and therefore not easily detected by our ITC protocols, native nESI-MS experiments were performed to further investigate the aptamer-ampicillin interaction. Figure 67C shows the mass spectrum of the aptamer before and after addition of the ligand at a 1:5 aptamer:ampicillin ratio. The aptamer is detected at charge states 4+ ( $m/z = 1486.2$ ) and 3+ ( $m/z = 1981.3$ ) with some nonspecifically bound sodium ions. Sodium ions are a rather common contamination in MS due to impurities of the chemicals and solvents used, but they can also originate from the borosilicate needles used for nESI. For a 1:1 binding stoichiometry, the aptamer-ampicillin complex should occur at  $m/z = 1573.5$  and  $m/z = 2097.4$  for the 4+ and 3+ charge state, respectively. However, no high-intensity peaks are visible at these  $m/z$  values (dotted lines in Figure 67C). Assuming specific binding of ampicillin to the aptamer taking place according to the previously reported  $K_d$  of 13.4 nM,<sup>342</sup> these peaks should be present with high intensity. A small, broad peak at the theoretical value for the 4+ complex is most likely due to nonspecific binding or very weak interactions. Thus, similar to the performed ITC experiments, the nESI-MS results do not support the occurrence of a specific aptamer-target interaction under the conditions used. However, one could assume that the absence of the complex might be due to the fact that only aptamers which show a  $K_d$  in the low  $\mu\text{M}$  to nM range can be observed using native nESI-MS, which means that binding can still occur in the high  $\mu\text{M}$  to mM range.<sup>64</sup>

To investigate the possibility of a lower affinity complexation we turned to  $^1\text{H}$  NMR spectroscopy, as this allows us to also monitor specific intermolecular interactions with  $K_d$  values well into the millimolar range. Typically, the presence of a specific interaction may be inferred by monitoring the changes in the  $^1\text{H}$  NMR fingerprint as the target is titrated into a solution of the aptamer.<sup>360,361</sup> A low affinity interaction will typically manifest itself through the presence of a set of resonances for each species with concentration-dependent chemical shifts due to fast exchange conditions on the NMR time scale.<sup>361,362</sup> In favorable cases, monitoring these enables  $K_d$  determination. Alternatively, chemical exchange may be slow on the NMR time scale, leading to a separate set of resonances for the free and complexed species in solution and immediately indicating the presence of complex formation. The titration of a 0.4 mM solution of the AMP17 aptamer with ampicillin up to a 10-fold excess of the latter is shown in Figure 68A. If the  $K_d$  value reported before for AMP17<sup>342</sup> is in the nanomolar range, this should lead to full complexation and clear perturbations of the  $^1\text{H}$  NMR spectra. While the full assignment of all resonances in the spectra is not required for monitoring purposes, the resonances of ampicillin could be completely assigned (Figure

73A in Appendix), while only partial assignment of the aptamer sequence was obtained (Figure 73B in Appendix). As can be seen from Figure 68A, each spectrum recorded when titrating ampicillin to the AMP17 solution leads to a single set of resonances for each species, with constant chemical shifts that are in all cases completely identical to those of the individual species in the pure solutions, suggesting lack of interaction. In the literature, several examples exist of aptamer-NMR studies where changes that occur in the imino region of the aptamer, including the appearance of additional imino signals, are used as a sensitive indicator of binding and associated change in tertiary structure upon binding.<sup>186,363,364</sup> Here again, no change can be seen and line-widths also appear unaffected, all indicative of a lack of mutual interaction (Figure 74 in Appendix). Finally, the same conclusion follows from monitoring the molecular translational diffusion coefficients of the aptamer and the ampicillin target using PFG-NMR spectroscopy. Assuming rapid exchange on the diffusion time-scale<sup>361</sup> and depending on whether ampicillin is mostly complexed or free in solution as the ampicillin to aptamer ratio increases, the self-diffusion coefficient will increase, reflecting the changing balance between the bound and free state. Within error, however, the self-diffusion coefficients remain constant during the titration, and similar to that of the pure solutions (Figure 68B). To conclude, all NMR data indicates the absence of complexation in the millimolar concentration range, and therefore, any eventual specific binding event must lie above the millimolar  $K_d$  range. This is the final independent indication that the aptamer does not bind the target. Together with the lack of any interaction from ITC and native nESI-MS, we must conclude that there are no grounds to believe that complexation occurs within the low nM to high mM range.

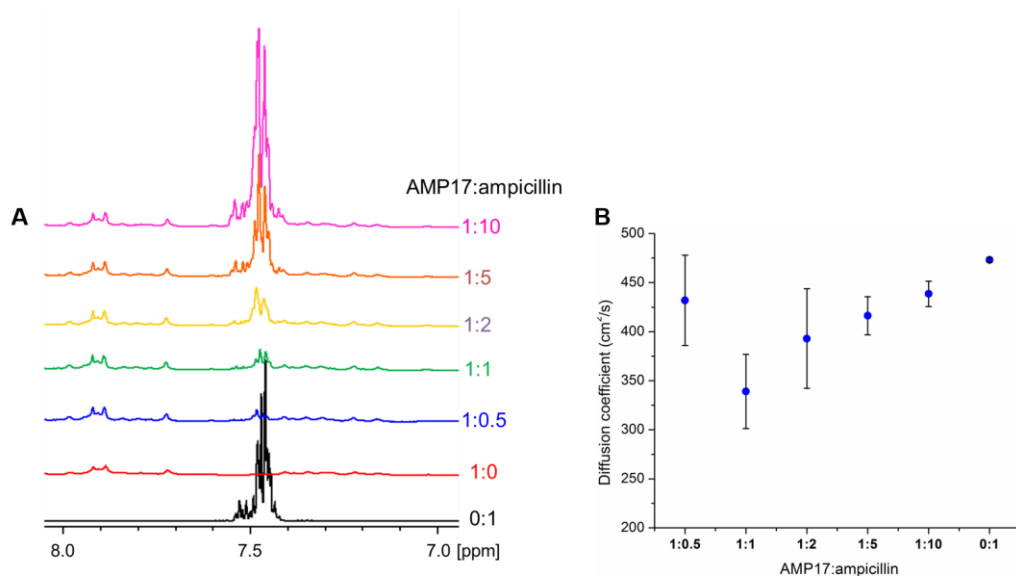


Figure 68. Impact of the titration of ampicillin in the presence of the AMP17 aptamer monitored by  $^1\text{H}$  NMR spectroscopy. A) Stacked plot of the 1D  $^1\text{H}$  NMR spectra of (from bottom to top) pure ampicillin (black), AMP17 (red), and mixtures of AMP17:ampicillin with ratios varying from 1:0.5 to 1:10. A concentration of 0.4 mM AMP17 was used throughout. B) Diffusion coefficient for ampicillin measured with PFG-NMR spectroscopy for the various ratios reported in panel A. The lack of significant variations in either  $^1\text{H}$  NMR or diffusion data indicates the absence of complexation under the concentrations used (see text).

### 7.3.3. Validation of the multifaceted analytical approach

All the results presented thus far evidence the lack of any binding between AMP17 and its target ampicillin. To validate our approach with a positive control, the same set of experiments was performed with two other aptamers. First of all, the MN4 cocaine-binding aptamer which is one of the most studied and well-characterized for analytical applications, and it also binds strongly with quinine,<sup>53,365</sup> as evidenced by a lower  $K_d$  value (ca. 100 nM compared to 5.5  $\mu\text{M}$  for cocaine), bringing it close to the value reported for the ampicillin binding aptamers (nM range). Therefore, the quinine/MN4 system provides a suitable positive control for the combined analytical approach. The native nESI-MS experiments performed in a 1:5 MN4:quinine ratio clearly demonstrate the binding of the MN4 aptamer to quinine. In Figure 69A, the MN4 is detected at charge states 6+ ( $m/z = 1855.7$ ), 5+ ( $m/z = 2226.7$ ), and 4+ ( $m/z = 2783.1$ ) with some nonspecifically bound sodium. After addition of the ligand, new peaks that correspond to the 6+ ( $m/z = 1909.8$ ), 5+ ( $m/z = 2291.6$ ) and 4+ ( $m/z = 2864.2$ ) charge state of the complex are present. Moreover, the thermogram for the ITC titration of MN4 aptamer

with quinine in 0.1 M Tris buffer pH 7.4 with 5 mM KCl (Figure 69B) shows clear evidence of an exothermic binding process (Figure 69C) from which it is possible to calculate a  $K_d$  of  $171 \pm 45$  nM ( $n = 3$ ). This value is close to the one previously reported in the literature ( $\sim 100 \pm 40$  nM) using again ITC.<sup>53</sup>  $^1\text{H}$  NMR for the cocaine-binding aptamer was already extensively reported before and the tertiary structure of the aptamer and binding mechanism were already validated.<sup>52,186</sup> These experiments indicate that our analytical approach works well to observe aptamer-target binding in the nanomolar range.

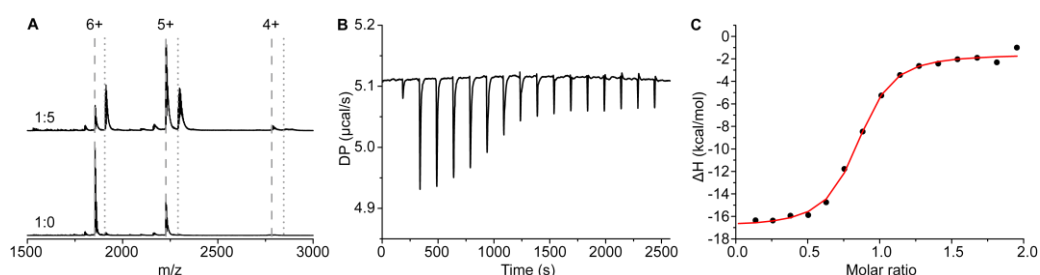


Figure 69. A) Native nESI-MS of the MN4 aptamer with and without quinine incubated at a 1:5 aptamer:quinine ratio in 150 mM AmAc (pH 6.8). Theoretical peaks of the apo form (dashed lines) and complex (dotted lines) are indicated for the 6+, 5+, and 4+ charge states. B) Thermogram for the ITC titration of  $5 \mu\text{M}$  of MN4 aptamer with  $50 \mu\text{M}$  of quinine in 0.1 M Tris buffer pH 7.4 with 5 mM KCl. C) Binding curve of the ITC titration for MN4 and quinine, the red line represent the fitting with the "one set of binding sites" model.

In order to check whether our approach can be extended to affinity studies in the micromolar range (to avoid missing a possible binding of ampicillin with the given aptamers in the  $\mu\text{M}$ -range), the 1OLD L-argininamide aptamer was chosen as a second positive control. The ITC data (Figure 70A and B) clearly show binding of L-argininamide to the 1OLD aptamer. A  $K_d$  of  $176 \pm 15 \mu\text{M}$  was determined, which is in good agreement with the one reported in the literature ( $K_d = 165 \mu\text{M}$ ).<sup>351</sup> The titration of L-argininamide into a 1OLD solution followed by 1D  $^1\text{H}$  NMR shows the appearance of new signals in the imino region, as visualized in Figure 70C. From the assignment, it becomes apparent that the interaction between the aptamer and L-argininamide zips up the hairpin, as base pairs 6●19 and 7●18 show up. In addition, the loop becomes structured around the target.<sup>366</sup> The native nESI-MS experiments using a 1:5 1OLD:L-argininamide ratio show only a small amount of (likely nonspecific) complex formation between the aptamer and target (Figure 76 in Appendix), which in accordance with the fact that complexes with a  $K_d$  in the micromolar range cannot be observed using this technique. Using both the MN4 and the 1OLD aptamer as a positive control, it is clearly

demonstrated that the multifaceted approach allows one to determine aptamer-target interactions, in the both nanomolar and micromolar ranges.

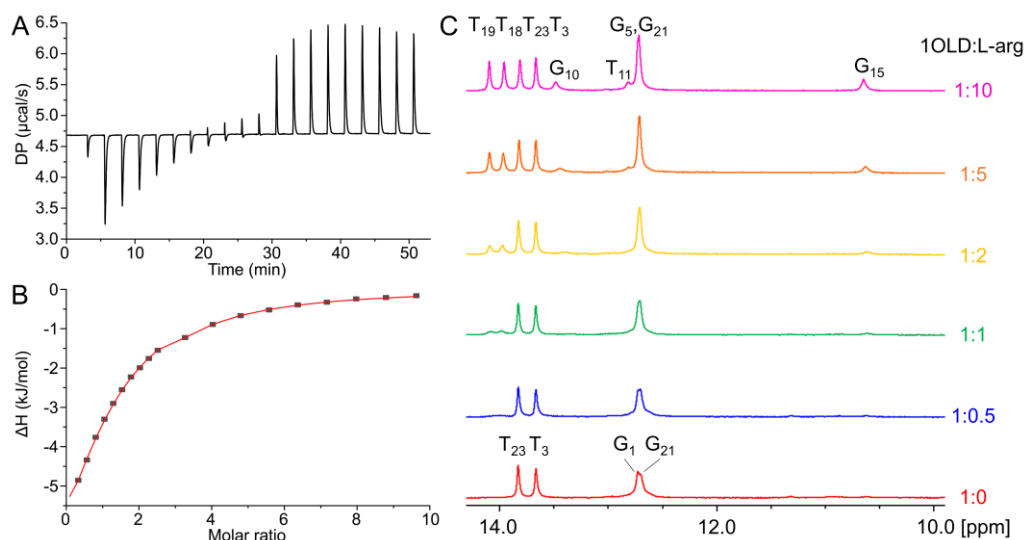


Figure 70. A) ITC thermogram and B) ITC binding curve of the 1OLD L-argininamide binding aptamer. C) Stacked plot of the imino region of six  $1\text{D } ^1\text{H NMR}$  spectra of (from bottom to top) 1OLD (red) and mixtures of 1OLD:L-argininamide (L-arg) with ratios varying from 1:0.5 to 1:10. A concentration of 0.4 mM 1OLD was used throughout.

### 7.3.4. Effect of AuNPs on ampicillin-binding aptamers

To explain the discrepancy between our findings and the results reported by Song et al., it is possible to consider a beneficial effect of the AuNPs on the binding event between AMP17 and the target. Indeed, both assays used in the original paper were performed in the presence of AuNPs. However, this hypothesis was considered as many different interactions are known to take place between DNA and AuNPs.<sup>355</sup> Moreover, McKeague et al. observed that  $K_d$  values obtained using the AuNP assay were significantly improved compared to the previously reported values, indicating that the presence of AuNPs may enhance the binding capabilities of an aptamer.<sup>105</sup>

To test this hypothesis, ITC titrations were performed with AuNPs and aptamers using the same AuNPs concentration (4 nM) as reported by Song et al.<sup>367,368</sup> Two titrations were performed to assess all possible heat exchange contributions: the first one with

AuNPs, AMP17, and the ampicillin target, the second one with AuNPs and ampicillin alone.

Figure 71 illustrates the heat generated ( $\Delta Q$ ) at each injection for the titration of the AMP17/AuNPs solution with ampicillin (full dots) compared to the titration with only ampicillin and AuNPs (empty squares). The graph shows that the detected heat exchange mainly stems from the interaction of the antibiotic with the AuNPs, while AMP17 does not contribute to the generated heat. From the raw titration data (Figure 77A and B in Appendix) a clear heat exchange can be observed, with intense peaks at the beginning that tend toward saturation at the end of the titration, as expected for an exothermic binding event. This indicates that ampicillin has a strong affinity for the AuNPs. Native nESI-MS experiments could not be performed due to the presence of the AuNPs which cannot be transferred to the gas-phase. Therefore the absence of a specific interaction between AMP17 and its target ampicillin, in the presence of AuNPs, was verified again using  $^1\text{H}$  NMR. The spectra of the aptamer with and without nanoparticles (Figure 78A in Appendix) show no relevant differences apart from a slight broadening of the peaks; in addition the titration with ampicillin (Figure 78B in Appendix) does not indicate binding between AMP17 aptamer and the target in the presence of AuNPs. As observed before when considering the diffusion coefficient measurements for the antibiotic in the absence of AuNPs (see Figure 68B), also when titrating ampicillin into AMP17 in the presence of AuNPs, the diffusion coefficient values remain constant within the experimental error associated with 6 repeated measurements for ampicillin (Figure 78C in Appendix). All these data reaffirm the absence of binding between the aptamer and ampicillin even in the presence of AuNPs in solution, and this cannot explain the discrepancy between our findings and the previously reported results. Finally, there are several papers which reported that immobilization of aptamers influences (even enhances) their affinity, but for none of these aptamers was a complete elimination of affinity in solution reported.<sup>369–373</sup>

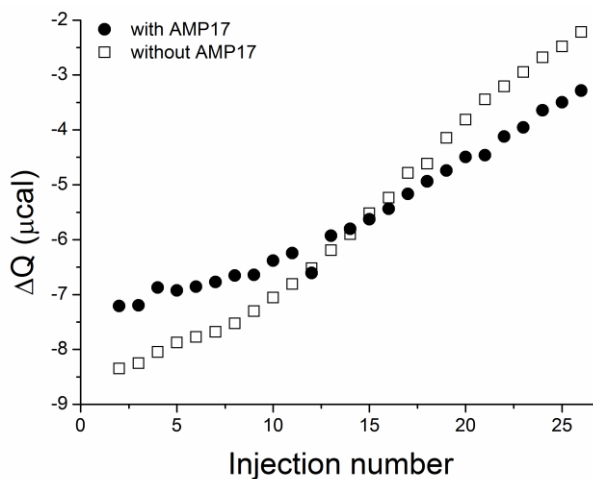


Figure 71.  $\Delta Q$  for each injection for the titration with AMP 17 aptamer (full dots) and without AMP17 aptamer (empty squares) in the ITC cell.

## 7.4. Conclusions

In line with the increasing awareness within the aptamer community, we clearly illustrated the need to address and validate the aptamer-target interaction using a multifaceted analytical approach before “applying” aptamer sequences in other studies. More specifically, researchers should avoid relying exclusively on fast and easy-to-perform assays as analytical approaches to validate binding affinity, since the risk to misinterpret the real performance of a specific aptamer is particularly high. For the majority of reported data collected in this way, the exact experimental conditions play a critical role and are often not entirely clear from the description of the work, thus difficult to replicate or adapt to a different analytical application. Therefore, extrapolating the performances of a given aptamer sequence to different experimental conditions may lead to conflicting or poorly reproducible results. The fact that no one technique is generally applicable to characterize all aptamers and the need for multiple characterization strategies was also identified by McKeague et al., who compared multiple techniques and found that the sensitivity of each technique affects the apparent  $K_d$  of a given aptamer.<sup>105</sup> Here, we offer a validation strategy to verify the performance and improve the reliability of aptamers for analytical applications. As for the aptamers used in the present study the question is still open; without completely ruling out the possibility that they do indeed bind ampicillin, it is obvious that their binding mechanism is poorly understood or superficially evaluated. This need for

critical evaluation of aptamer performances was firmly identified and discussed on the occasion of the Aptamers 2019 meeting in Oxford, UK. Guidelines for standardization in aptamer selection, characterization, and application are slowly finding their way into the interdisciplinary oriented aptamer community. With the present study, we aim to contribute to these endeavors and provide the research community with the tools to adopt a robust analytical multifaceted approach to validate aptamer-target interactions prior to applying them.

## 7.5. Appendix

Table 9. Summary of analytical parameters for biosensors based on AMP aptamers

Analytical approach	Aptamer	Linear range	LOD	Selectivity	Real samples	Reference
Dual colorimetric detection with AuNPs	AMP4 (9.4 nM <sup>a</sup> ) AMP17 (13.4 nM <sup>a</sup> ) AMP18 (9.8 nM <sup>a</sup> )	0.1 to 140 nM	0.1 nM	Benzylpenicillin, Amoxicillin, Other non $\beta$ -lactam antibiotics	Milk	342
Microfluidic impedimetric biosensor	AMP17	10 pM to 1 $\mu$ M	10 pM	Nonspecific ssDNA sequence	Milk	374, 375
Electrochemical aptasensor based on quadratic recycling amplification	AMP17	5 pM to 10 nM	1.09 pM	Amoxicillin, Benzylpenicillin, Penicillin	Milk	376
Electrochemical aptasensor based on dual recycling amplification	AMP17	0.2 to 40 nM	4 pM	Amoxicillin, Benzylpenicillin, Penicillin, Lincomycin	Milk	377
Signaling probe displacement electrochemical aptasensor	AMP17	100 pM to 1 mM	10 pM	Kanamycin A, Tetracycline, Streptomycin, Sulfadimethoxine	no	378
Fluorescent AuNPs aptasensors with nicking enzyme	AMP17	0.1 to 100 nM	0.07 nM	Amoxicillin, Benzylpenicillin, Sulfadimethoxine, Chloramphenicol	River water	379
Probe displacement electrochemical aptasensor	AMP18	0.2 to 15000 $\mu$ M	30 nM	Levofloxacin, Amoxicillin, Trimethoprim, Sulfamethoxazole, Nitrofurantoin	Urine Tap water Milk Saliva	380
Reusable signal-off electrochemical aptasensor	AMP18	5 to 5000 $\mu$ M (ACV) 100 to 5000 $\mu$ M (SWV)	1 $\mu$ M (ACV) 30 $\mu$ M (SWV)	Levofloxacin, Amoxicillin, Trimethoprim, Sulfamethoxazole, Nitrofurantoin	Milk Saliva Calf serum	381
Electrochemical-SPR aptasensor	AMP4	2.5 to 1000 $\mu$ M	1 $\mu$ M	Penicillin G, Penicillin V, Oxacillin, Cephalexin	River water	382

ACV = alternate current voltammetry, SWV = square wave voltammetry

Analytical approach	Aptamer	Linear range	LOD	Selectivity	Real samples	Reference
Metal-organic framework impedimetric biosensor	AMP18	0.001 to 2000 pg/mL	$0.2 \cdot 10^{-3}$ pg/mL	Doxorubicin, Penicillin, Trombamyacin, Streptomycin, Kanamycin, Cefazolin	Serum River water Milk	<sup>383</sup>
Electrochemical aptasensor with endonuclease digestion amplification	AMP17	0.1 to 100 nM	32 pM	Chloramphenicol, Florfenicol, Tobramycin, Thiamphenicol, Penicillin, Streptomycin, Melamine, Tetracycline, Kanamycin, Oxytetracycline, Amoxicillin, Lincomycin	Milk Tap water	<sup>384</sup>
Metal-organic framework AuNPs (MOF) colorimetric sensing platform	AMP17	50 to 100 nM	13 nM	Amoxicillin, Tetracycline, Chloramphenicol, Sulfadimidine, Kanamycin, Oxytetracycline,	no	<sup>385</sup>
Metal-organic framework impedimetric aptasensor	AMP18	0.01 pg/mL to 2 ng/mL	6 fg/ml	Tetracycline, Kanamycin, Tobramycin, Na <sup>+</sup> , K <sup>+</sup> , Streptomycin, Oxytetracycline	Diluted human serum	<sup>386</sup>
Ladder-shaped DNA based electrochemical aptasensor	AMP17	7 pM to 100 nM	1 pM	Amoxicillin, Levofloxacin, Chloramphenicol, Kanamycin, Tetracycline	Milk	<sup>387</sup>
Dual AuNPs colorimetric assay	AMP17	1 to 600 nM 1 to 400 nM	0.1 nM 0.5 nM	Amoxicillin, Penicillin, Lincomycin, Benzylpenicillin	Milk	<sup>388</sup>
Exonuclease III-powered DNA walking machine electrochemical aptasensor	AMP17	1 pM to 10 nM	0.7 pM	Kanamycin, Chloramphenicol, Oxytetracycline, Terramycin, Carbenicillin	Milk	<sup>389</sup>
DNase I-assisted cyclic enzymatic signal amplification graphene oxide aptasensor	AMP17	10 ng/mL to 500 ng/mL	2.4 ng/ml	Chloramphenicol, Penicillin, Carbenicillin, Amoxicillin	Milk	<sup>390</sup>

<sup>a</sup> $K_d$  determined with fluorescence titration;  $K_d$  was not determined in all other publications.

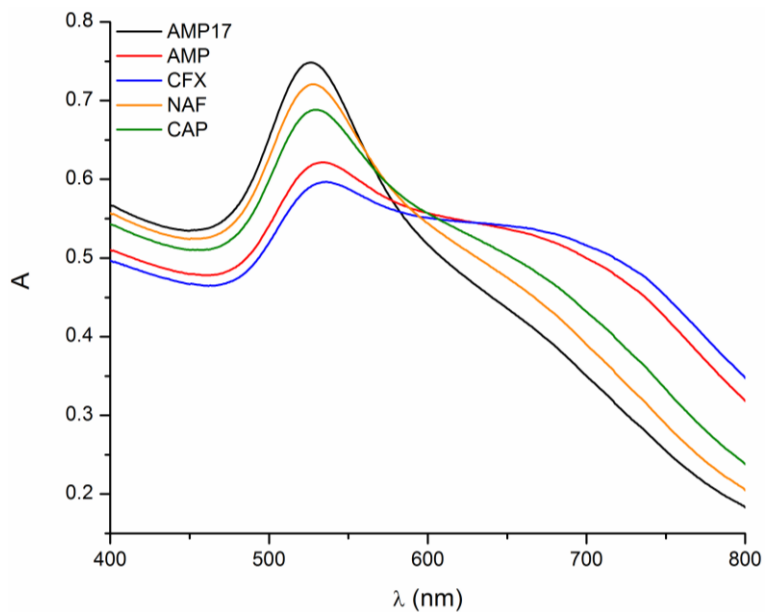


Figure 72. UV Vis spectra for the AuNPs solutions with AMP17 in the absence of an antibiotic (black) and with 100 nM of various antibiotics in the presence of 100 mM NaCl: ampicillin (red), cephalexin (blue), nafcillin (orange) and chloramphenicol (green).

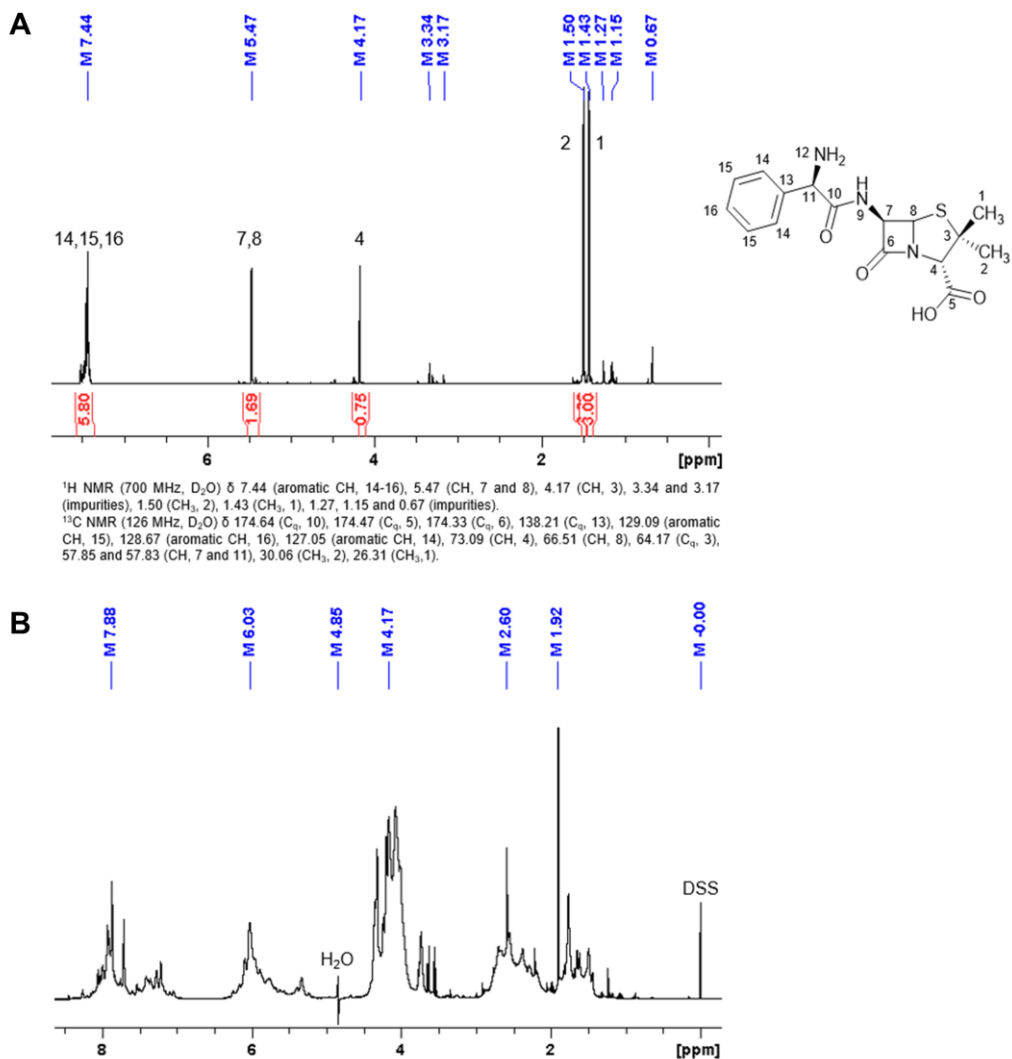


Figure 73. A) 1D <sup>1</sup>H spectrum of pure ampicillin in D<sub>2</sub>O with integration regions and values (red) indicating the number of hydrogen atoms and their assignment (black labels) match the labelled positions in the depicted structure (right). B) 1D <sup>1</sup>H spectrum of pure AMP17 in D<sub>2</sub>O.

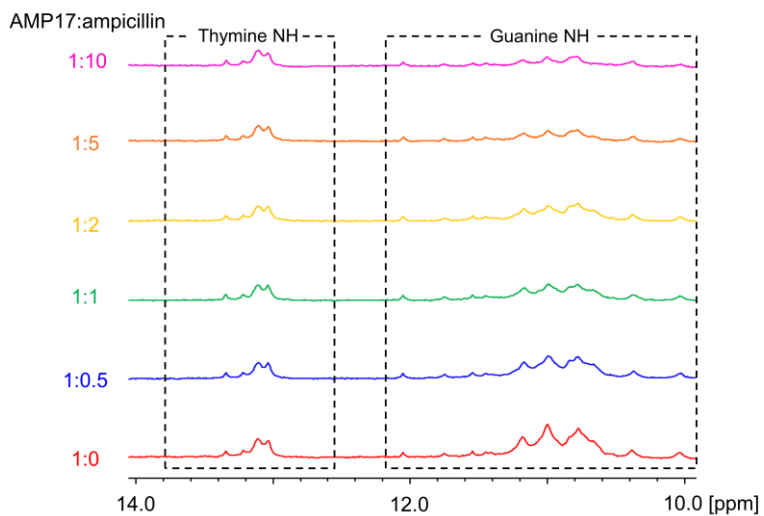


Figure 74. Overlay of the imino region of the AMP17 aptamer during titration with ampicillin, ratios are indicated (0.4 mM AMP17, H<sub>2</sub>O/D<sub>2</sub>O 90:10, pH 7, 700 MHz).

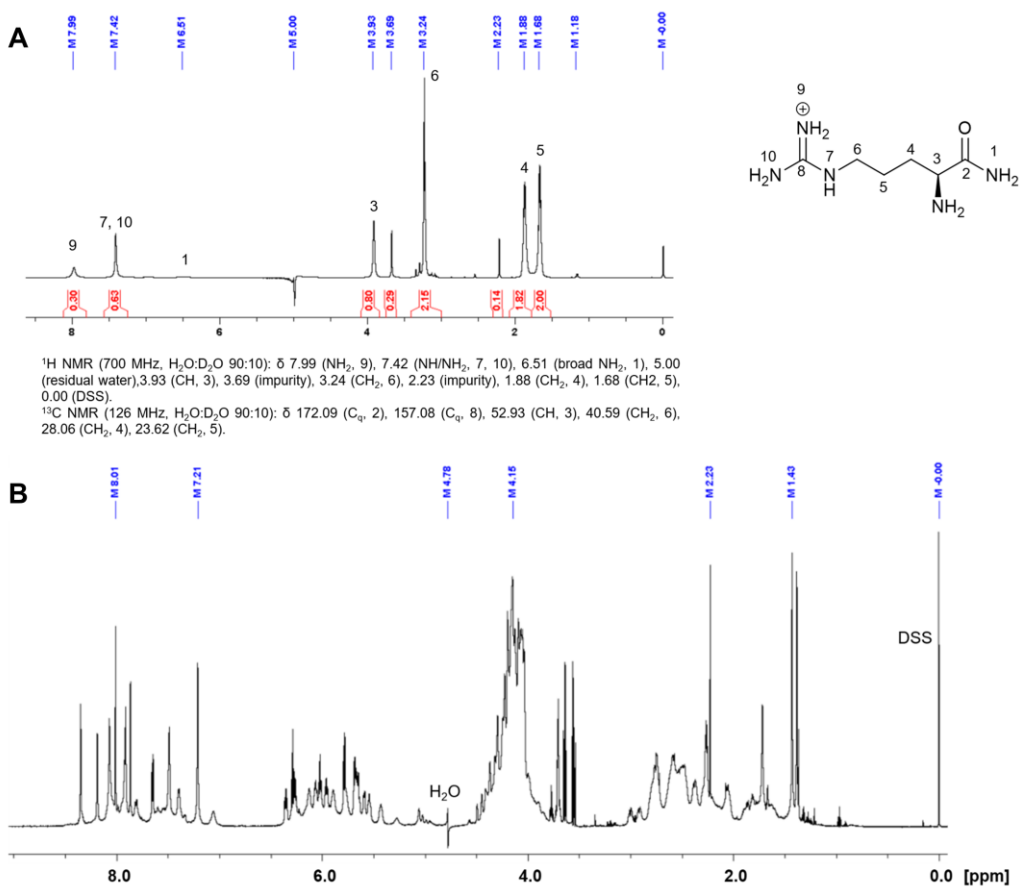


Figure 75. (A) 1D <sup>1</sup>H spectrum of pure L-argininamide in H<sub>2</sub>O:D<sub>2</sub>O 90:10 with integration regions and values (red) indicating the number of hydrogen atoms and their assignment (black labels) match the labelled positions in the depicted structure (right). (B) 1D <sup>1</sup>H spectrum of pure 10LD in D<sub>2</sub>O.

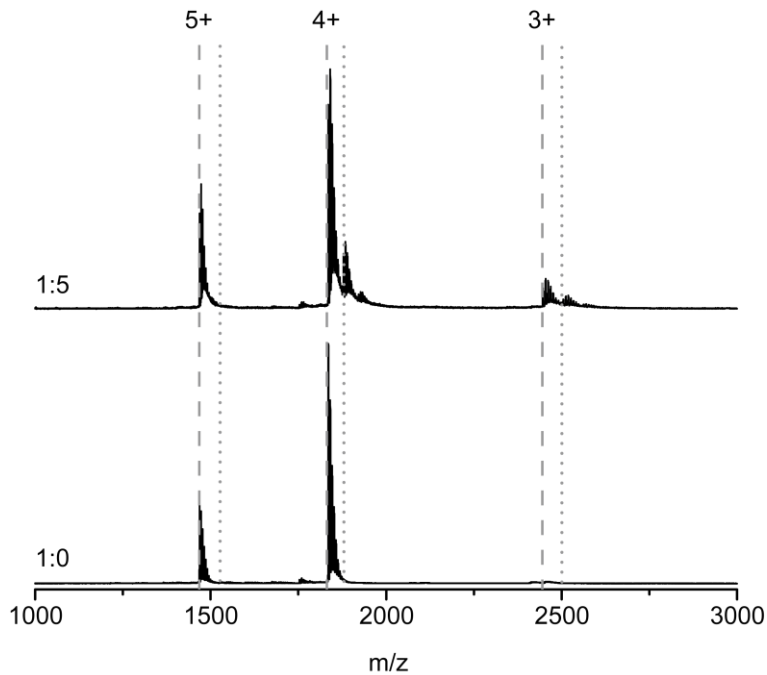


Figure 76. Native nESI-MS of the 10LD aptamer with and without L-argininamide incubated at a 1:5 aptamer:L-argininamide ratio in 150 mM AmAc (pH 6.8). Theoretical peaks of the apo form (dashed lines) and complex (dotted lines) are indicated for the 5+, 4+ and 3+ charge state.

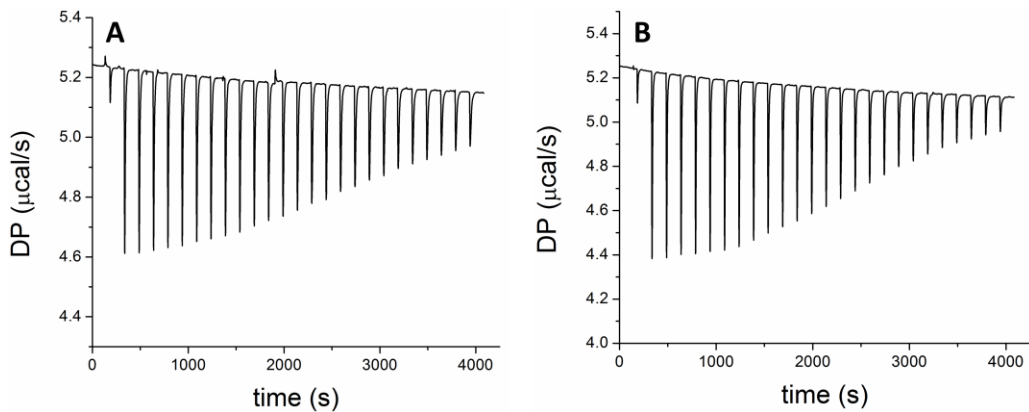


Figure 77. Thermograms of the titrations with AuNPs; A) 1  $\mu\text{M}$  AMP17 in the presence of 4 nM AuNPs, titrated with 1 mM AMP in MilliQ water, B) titration of 4 nM AuNPs with 1 mM AMP in MilliQ water.

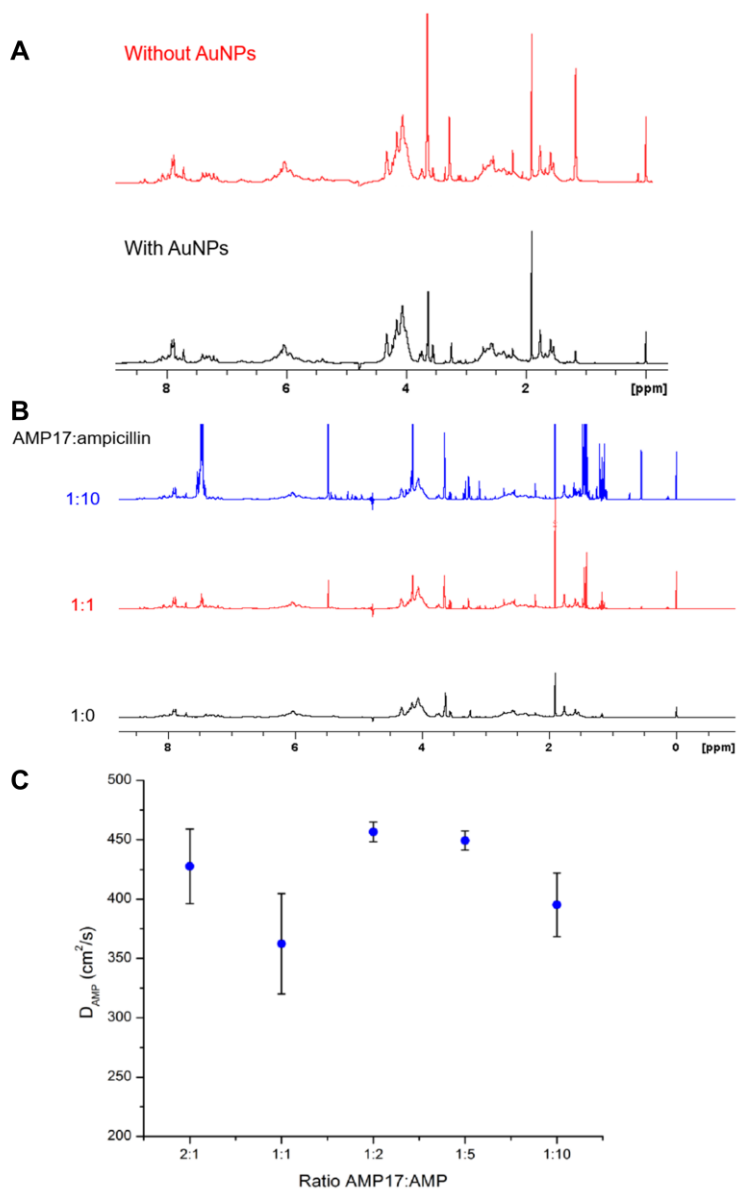


Figure 78. A) Overlay of 1D <sup>1</sup>H spectra of AMP17 with (black) and without (red) AuNPs; B) Overlay of the titration experiment, AMP17:ampicillin ratios are indicated, in the presence of AuNPs; C) Diffusion coefficient of ampicillin upon titration into a solution of AMP17 in presence of AuNPs.



Proof-of-concept electrochemiluminescent assay  
for the aptamer-based detection of small molecules

**Rocio Cánovas\*, Elise Daems\*, Rui Campos\*, Frank Sobott, and  
Karolien De Wael**

*Adapted from submission to Biosensors and Bioelectronics*

**\* Contributed equally**



## Abstract

This work presents a proof-of-concept assay for the quantification of small molecules based on aptamer recognition and electrochemiluminescence readout. The testosterone-binding aptamer (TESS.1) was used to demonstrate the novel methodology. The analytical capability of the electrochemiluminescence (ECL) array towards testosterone detection was studied using different incubation protocols. Concurrently, and to improve the analytical performance, the optimal concentration of the TESS.1 aptamer was investigated. Subsequently, the selectivity of the proposed array was assessed by performing negative control experiments with a randomized single-stranded DNA sequence and two other steroids i.e. deoxycholic acid and hydrocortisone. In parallel, complementary analytical techniques were employed to confirm the suggested mechanism: *i)* native nano-electrospray ionization mass spectrometry was used to determine the stoichiometry of binding, and for the characterization of aptamer-target interactions; and, *ii)* isothermal titration calorimetry was carried out to elucidate the binding affinity of TESS.1 for testosterone. The combination of these techniques provided a better understanding of the aptamer performance, the binding mechanism, affinity and selectivity. This research will pave the way for the development of new aptamer-based biosensor assays coupled with ECL sensing for the detection of relevant small molecules.

## 8.1. Introduction

In the last decades, electrochemical methods using aptamers as biorecognition elements for the detection of different small molecules, such as neomycin B, aflatoxin B1, tetracycline, cocaine, bisphenol A, ochratoxin A, estradiol, dopamine and ATP, have been developed.<sup>160,391,392</sup> Nevertheless, ECL, a type of chemiluminescence reaction triggered by electrochemical methods, is gaining momentum.<sup>393–395</sup> ECL has attracted considerable attention because of several appealing features, such as: *i*) absence of a background optical signal; *ii*) precise control of reaction kinetics offered by controlling the applied potential; *iii*) compatibility with solution-phase and thin-film configurations; *iv*) separation of excitation source (electronics) and detection readout (optical) improving the sensitivity and *v*) possibility of integrating nanomaterials (nanoparticles and nanotubes) for enhancing the intensity of the signal. Together, these characteristics make ECL attractive as a highly sensitive and selective analytical methodology.<sup>396</sup> Hence, ECL aptasensors are promising because they combine the advantages of both electrochemical and chemiluminescence biosensors, i.e. high sensitivity, low background, cost-effectiveness, and ease of control.<sup>393,397</sup>

Different examples of ECL aptamer-based electrodes (no assays) for small molecule recognition can be found in the literature.<sup>398–407</sup> The detection principle usually involves the use of luminophores as ruthenium complex, luminol-hydrogen peroxide based reactions and/or quenchers. The use of nanomaterials such as AuNPs is often suggested as excellent labels since AuNPs can enhance the affinity (up to 3 orders of magnitude).<sup>408</sup> Noteworthy, all approaches are based on single or, in one case, dual detection while none of them are able to measure several targets at the same time. Thus, the proof-of-concept presented herein offers the possibility of achieving the next goal by introducing an aptamer-based assay for the simultaneous detection of multiple small molecules.

Indeed, the technology of this type of assay, employing a 96-well plate with electrochemical capabilities and ECL reader, enables the multiple detection of biomarkers in different formats. To the best of our knowledge, the combination of such devices with aptamers for the ECL detection of small molecules has not been reported yet. Interestingly, some examples have incorporated the ECL device in the past years, but none of them for small molecule recognition.<sup>409,410</sup> For example, Duo and co-workers recently developed a slow off-rate modified aptamer (SOMAmer)-based approach using ECL for the quantification of a protein, glypican-3.<sup>411</sup>

Herein, we present a proof-of-concept ECL assay for the high-affinity detection of small molecules by aptamers, using the testosterone-binding aptamer (TESS.1) as a case of study. Moreover, the aptamer performance, the binding mechanism, affinity and selectivity was unraveled thanks to the combination of analytical techniques such as ITC<sup>412</sup> and native nESI-MS.<sup>58</sup> First, the immobilization and incubation protocols and the concentration of the TESS.1 aptamer were optimized proving the analytical capability of the ECL assay towards testosterone detection. Different negative control experiments were carried out using a randomized ssDNA sequence and two other steroids i.e. deoxycholic acid (DCA) and hydrocortisone (HC). In parallel: *i*) native nESI-MS experiments were performed to determine the stoichiometry of binding, and for the identification and characterization of species; and *ii*) ITC was used to elucidate the  $K_d$  of TESS.1 for testosterone. This unique approach opens new perspectives and insights in the use of aptamers coupled with ECL sensing for the accurate and highly sensitive detection of a wide range of small molecules simultaneously.

## 8.2 Materials and methods

### 8.2.1 Reagents

Sodium chloride and magnesium chloride were acquired from Fisher Scientific; potassium chloride and deoxycholic acid (98.5 %) were purchased from Acros Organics; sodium phosphate dibasic, sodium phosphate monobasic, potassium phosphate dibasic and potassium phosphate monobasic salts, Tween 20 and testosterone ( $\geq 99.0$  %) were purchased from Sigma Aldrich; and hydrocortisone ( $> 98.0$  %) from TCI.

The initial testosterone, deoxycholic acid and hydrocortisone stocks were prepared in absolute ethanol ( $\geq 99.8$  %) from Fisher Scientific in a concentration of 50 mM and the following dilutions of the target were performed using hybridization buffer. The rest of solutions and buffers were prepared in  $18.2 \text{ M}\Omega \text{ cm}^{-1}$  doubly deionized water (Sartorius, Arium® Ultrapure Water Systems). The pH was measured using a 913 pH meter from Metrohm (The Netherlands).

Hybridization buffer containing 10 mM phosphate buffer, 150 mM sodium chloride and 100 mM magnesium chloride and washing buffer (PBS-T) with 137 mM sodium chloride, 2.7 mM potassium chloride, 10 mM sodium phosphate dibasic, 1.8 mM potassium phosphate monobasic and 0.05 % of Tween 20 were prepared in ultrapure

water and the pH was adjusted to 7.0. The surfactant Tween 20 was added to increase the ECL efficiency. The enhancement mechanism involves adsorption of the surfactant on the electrode surface which facilitates the hydrophobic analytes to be closer to the surface.<sup>396</sup>

## 8.2.2 DNA sequences

All DNA sequences were purchased from Eurogentec (Belgium). The randomized DNA sequence was derived from TESS.1 and designed using the OligoAnalyzer Tool of Integrated DNA Technologies. The part complementary to the capture probe was preserved while the other nucleotides of the TESS.1 aptamer were scrambled. DNA sequences without modifications were used for the ITC and native MS experiments, while the oligonucleotides carried some modification for the ECL experiments. An overview is provided in Table 10. The capture probe was ordered with a biotin modification at the 3' end, whereas the TESS.1 aptamer and randomized sequence carry a DIG modification at their 3' end.

Table 10. DNA sequences utilized in this work.

	Sequence of oligonucleotides	Modifications
Capture probe	5'- GTC TGC CCG AGA G -3'	Biotin on 3'
Aptamer TESS.1	5'- CTC TCG GGA CGA CCG GAT GTC CGG GGT ACG GTG GTT GCA GTT CGT CGT CCC -3'	DIG on 3'
Randomized TESS.1	5'- CTC TCG GGA CGA <u>CTG ACG GGC ACT CAG TTG</u> <u>TGT TGG GGT CTC GCC CGG TGG</u> -3'	DIG on 3'
Short version of TESS.1 (TESS.1short)	5'- GGG ATG TCC GGG GTA CGG TGG TTG CAG TTC -3'	-
Stem 1	5'- CTC TCG GGA CGA CCG G -3'	-
Stem 2	5'- TTC GTC GTC CC -3'	-

The bases underlined in the randomized TESS.1 are those whose position is different when compared to TESS.1. The nucleotides from stems 1 and 2 in common with the aptamers are highlighted in blue and green, respectively.

## 8.2.3 Electrochemiluminescence measurements

The difference between the protocols tested lies in the order of incubations of the three components (i.e. capture probe, aptamer and target), providing relevant information about their interactions. Briefly, the first protocol (P1) consists of the following steps: *i*) incubation of the capture probe in the well while the aptamer is incubated separately with the testosterone in an Eppendorf; *ii*) addition and incubation of the mixture of aptamer and testosterone in the well. The second protocol (P2) includes: *i*) hybridization of the capture probe with the aptamer in an Eppendorf; *ii*) incubation of this mixture in the well; *iii*) incubation with testosterone. The third protocol (P3) follows a simpler procedure where: *i*) the capture probe, aptamer and testosterone are incubated in an Eppendorf; *ii*) the complex mixture is added and incubated in the well. Finally, all protocols were followed by an incubation with the antibody anti-DIG before the reading of the ECL signal. Detailed information about each protocol is specified in section 8.2.3.1.

Functionalized anti-DIG (Goat polyclonal anti-digoxigenin antibody (AbCam, ab76907)) conjugated with tris(2,2'-bipyridyl)ruthenium(II) ( $\text{Ru}(\text{bpy})_3^{2+}$ ) labels from the MSD Gold Sulfo-Tag NHS-Ester conjugation kit (Meso Scale Diagnostics, Cat. R31AA-1) and MSD GOLD Read Buffer (R92TG-1) were used. The antibody carries multiple  $\text{Ru}(\text{bpy})_3^{2+}$  labels which emit light upon electrochemical stimulation due to the reaction between the amine groups of the antibody with the ester on the  $\text{Ru}(\text{bpy})_3^{2+}$  labels. The ECL measurements were performed in a MESO QuickPlex SQ 120 controlled by the Methodical Mind reader software. The plates used were MSD GOLD™ 96-well Small Spot Streptavidin SECTOR Plate (L45SA-1). From the ECL measurements, the  $K_d$  of the aptamer-testosterone complex was estimated according to a method described by Chambers and Sauer.<sup>413</sup>

### 8.2.3.1 Detailed information protocols

Herein, the detailed information of the three protocols mentioned in section 8.2.3 is profoundly described. All protocols were tested using two concentrations of testosterone (5  $\mu\text{M}$  and 0  $\mu\text{M}$  as blank), one fixed concentration of capture probe (200 nM) and four concentrations of TESS.1 aptamer (400 nM, 200 nM, 100 nM and 0 nM) to be optimized in parallel. Therefore, different stocks were prepared in order to make the corresponding mixtures.

First of all, the 96 well plate was initially washed once with 150  $\mu\text{L}$  PBS-T and tap dried. Afterwards, for the first protocol (P1) (Figure 79): *i*) incubation of the 25  $\mu\text{L}$  capture probe in the well (always sealing the plate with parafilm to avoid evaporation) while 55  $\mu\text{L}$  of the aptamer (400 nM, 200 nM, 100 nM or buffer as 0 nM) is incubated with 55  $\mu\text{L}$  of testosterone (5  $\mu\text{M}$  or buffer) in an Eppendorf during 1 hour (all incubations were performed in a shaker at 550 rpm and RT); *ii*) discard the capture from the plate, washed 3 times with PBS-T and tap dried; *iii*) addition of 50  $\mu\text{L}$  of the mixture of aptamer and testosterone to the well plate and incubation another hour with shaking; *iv*) discard the mixture from the plate, washed 3 times with PBS-T and tap dried; *v*) incubation with 25  $\mu\text{L}$  of 1  $\mu\text{g mL}^{-1}$  functionalized anti-DIG conjugated with  $\text{Ru}(\text{bpy})_3^{2+}$  labels, 1 hour with shaking; *vi*) discard the solution from the plate, washed 3 times with PBS-T and tap dried; *vii*) add 150  $\mu\text{L}$  of MSD GOLD Read Buffer to each well; and, *viii*) immediately read the ECL signal in the Meso Scale Diagnostics device.

In the case of the protocol 2 (P2) (Figure 79): *i*) hybridization of 55  $\mu\text{L}$  of TESS.1 aptamer (400 nM, 200 nM, 100 nM or buffer) with the capture probe (55  $\mu\text{L}$ ) in an Eppendorf allowing the reaction during 1 hour under shaking at 550 rpm, RT; *ii*) add 50  $\mu\text{L}$  of each master mix into the wells, seal and incubated during 1 hour (shaking); *iii*) discard the solution from the plate, washed 3 times with PBS-T and tap dried; *iv*) add 25  $\mu\text{L}$  of testosterone (5  $\mu\text{M}$  or buffer), seal and let it incubate for 1 hour under shaking; *v*) discard the solution from the plate, washed 3 times with PBS-T and tap dried; *vi*) incubation with 25  $\mu\text{L}$  of 1  $\mu\text{g mL}^{-1}$  functionalized anti-DIG conjugated with  $\text{Ru}(\text{bpy})_3^{2+}$  labels, 1 hour with shaking; *vii*) discard the solution from the plate, washed 3 times with PBS-T and tap dried; *viii*) add 150  $\mu\text{L}$  of MSD GOLD Read Buffer to each well; and, *x*) immediately read.

Finally, for the protocol 3 (P3) (Figure 79): *i*) mix in an Eppendorf 35  $\mu\text{L}$  of capture, 35  $\mu\text{L}$  of aptamer and 35  $\mu\text{L}$  of testosterone (using the corresponding combination from each stock) allowing the reaction to take place during 1 hour, shaking 550 rpm at RT as usual; *ii*) discard the master mix from the plate, washed 3 times with PBS-T and tap dried; *iii*) add 50  $\mu\text{L}$  of each master mix into the wells, seal the plate and incubate with shaking; *iv*) discard the solution from the plate, washed 3 times with PBS-T and tap dried; *v*) add 25  $\mu\text{L}$  of 1  $\mu\text{g mL}^{-1}$  functionalized anti-DIG conjugated with  $\text{Ru}(\text{bpy})_3^{2+}$  labels, 1 hour with shaking; *vi*) discard the solution from the plate, washed 3 times with PBS-T and tap dried; *vii*) add 150  $\mu\text{L}$  of MSD GOLD Read Buffer to each well; and, *viii*) immediately read.

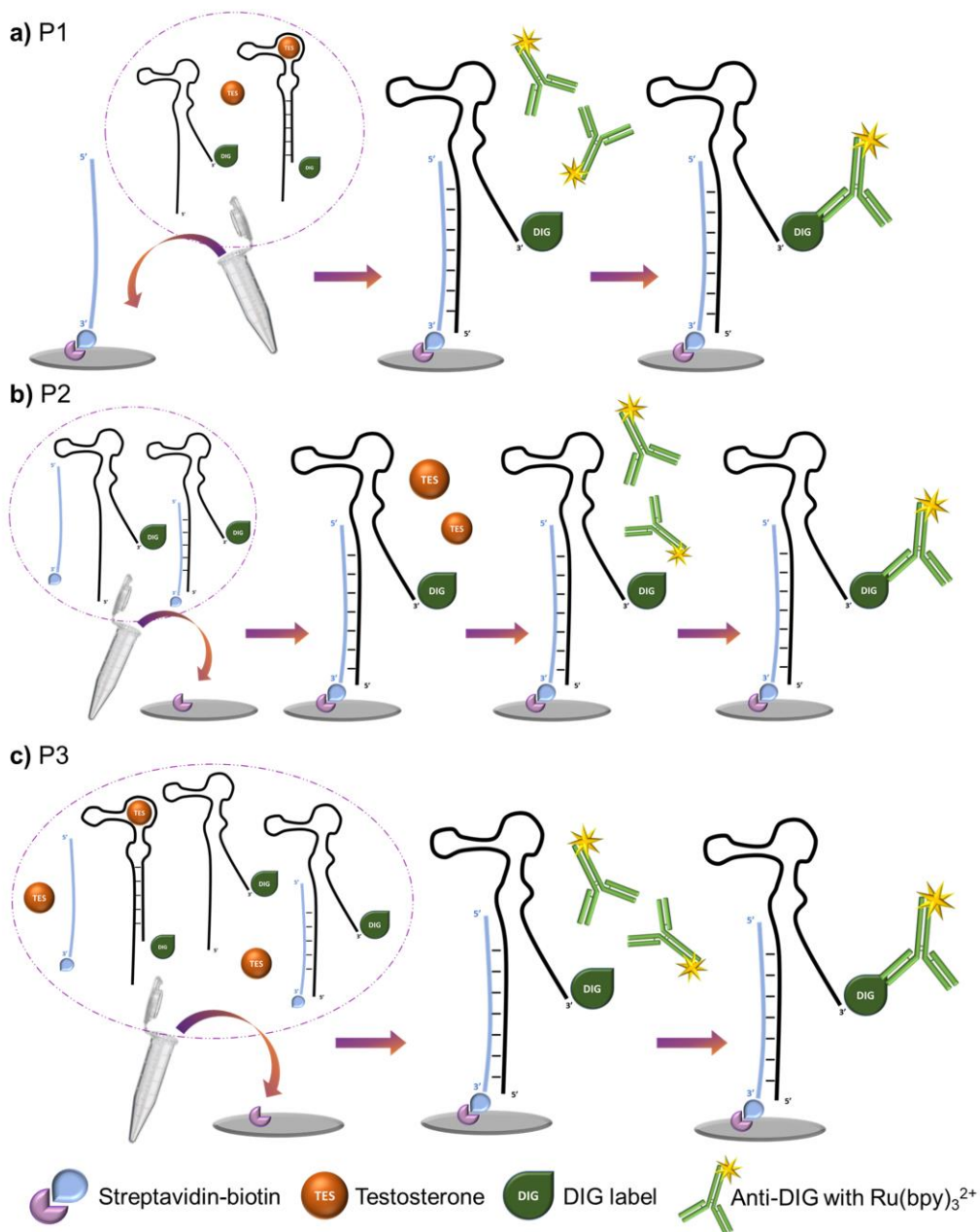


Figure 79. Schematic representation of the three different protocols tested a) protocol 1 (P1), b) protocol 2 (P2) and c) protocol 3 (P3). Capture probe is portrayed as a blue line and the TESS.1 aptamer is represented by the black structure.

## 8.2.4 Isothermal Titration Calorimetry

ITC experiments were performed on a MicroCal PEAQ-ITC instrument (Malvern Panalytical operated by MicroCal PEAQ-ITC control software). The binding experiments were performed using 150  $\mu\text{M}$  of target which was titrated in 10  $\mu\text{M}$  of aptamer solution. The assay buffer was a 10 mM phosphate buffer with 150 mM NaCl and 150 mM  $\text{MgCl}_2$  at pH 7.0 and was degassed prior to use. The experiment consisted of 15 injections of 2.7  $\mu\text{L}$  with a spacing of 150 s. The first injection was 0.4  $\mu\text{L}$  to account for diffusion (initial delay 180 s). To correct for the dilution heat of the titrant, control titrations were performed consisting of injection of the target into the sample cell filled only with buffer. The reference power was set to 5  $\mu\text{cal/s}$  and all titrations were performed at 25  $^\circ\text{C}$ . Data analysis was performed with the MicroCal PEAC-ITC Analysis software using a one-site binding model.

## 8.2.5 Native nESI-MS

Prior to native nESI-MS analysis, the aptamers and randomized DNA sequence were dialyzed into 300 mM aqueous ammonium acetate (pH 6.8) using Slide-a-Lyzer Mini dialysis units with a molecular weight cut-off of 3.5 kDa (Thermo Fisher Scientific), in order to desalt the samples and to provide a volatile electrospray buffer of appropriate ionic strength. The capture probe, stem 1 and stem 2 were not dialyzed due to its low molecular weight (3975.6 Da, 4923.2 Da and 3259.2 Da, respectively). The concentrations of the dialyzed aptamers were verified using a Nanodrop2000 (Thermo Scientific). Extinction coefficients were calculated by the Nanodrop2000 software based on the oligonucleotide sequences. Aptamer-target complexes were prepared using a 1:10 aptamer-target ratio with a final concentration of 10  $\mu\text{M}$  aptamer. For the experiments involving the capture probe, 15  $\mu\text{M}$  aptamer and 15  $\mu\text{M}$  capture probe were incubated together for 30 minutes. Afterwards a 10 fold excess of the target was added and incubated for 30 minutes to obtain a final concentration of 10  $\mu\text{M}$  aptamer. For the experiments with the stems of the aptamer equimolar ratios of all species were used.

Native nESI-MS analyses were performed on a Synapt G2 HDMS Q-TOF instrument (Waters, Manchester, UK) in the positive ionization mode. Approximately 2-4  $\mu\text{L}$  of sample was introduced into the mass spectrometer, using nESI with gold-coated borosilicate glass tapered-tip capillaries made in-house. The instrument was carefully

tuned to preserve the native structure and noncovalent interactions. The spray capillary voltage ranged between 1.2-1.6 kV and the sampling cone voltage was 20 V. The trap and transfer collision energy were set at 5 V and 0 V, respectively and the trap DC bias was fixed to 40 V. The IMS wave velocity was set to 800 m/s and the IMS wave height to 35 V. Gas pressures were 2.57 mbar and  $2.2 \cdot 10^{-3}$  mbar for the backing and source gas, respectively. All data was analyzed using MassLynx v4.2 (Waters). The abundance of all bound and unbound states was estimated based on the peak area.

### 8.3 Results and discussion

Yang and co-workers developed a fluorescence-based aptasensor, without electrochemical initiation and in solution-phase, for testosterone, which comprises two DNA strands: *i*) a TESS.1 labelled aptamer with fluorescein (F) together with *ii*) a partially complementary oligonucleotide sequence carrying a quencher (D) (see Figure 80a). Upon addition of the target, a high-affinity binding of TESS.1 to testosterone occurs, which leads to dissociation of the double helix between TESS.1 and its complementary strand and results in a fluorescent signal.<sup>10</sup> Our ECL assay is inspired by the same principle of competitive binding, but with different modifications on the TESS.1 aptamer, i.e. our aptamer does not have a quencher neither fluorescein attached. In this case, the TESS.1 carries the digoxigenin (DIG) label, to which the  $\text{Ru}(\text{bpy})_3^{2+}$ -labelled anti-DIG will bind (Figure 80b). Hence, the aptamer, which is not immobilized, will be washed away in presence of the target. Therefore, the signal of the label is only observed when the aptamer is not bound to testosterone, and decreases upon adding more target (Figure 80c). Besides, our TESS.1 complementary ssDNA, named capture probe in this manuscript, is not in solution but is instead immobilized on the surface of the working electrode (in the 96-well plate to allow assay based detections). Following the same principle as Yang et al., the capture probe only hybridizes with the aptamer when it is not bound to the target (Figure 80c.i). In this work, the ECL detection technology uses an anti-DIG antibody as co-reactant<sup>414</sup> which has high affinity and specificity for the DIG label.<sup>415</sup> Concurrently, the antibody carries multiple  $\text{Ru}(\text{bpy})_3^{2+}$  labels which emit light upon electrochemical stimulation whereas signal amplification is provided by tripropylamine (TPrA) present in the reading buffer. Considering that the aptamer does not bind to the capture probe upon binding of testosterone, the ECL signal decreases upon increasing concentration of the target (Figure 80c.iii).

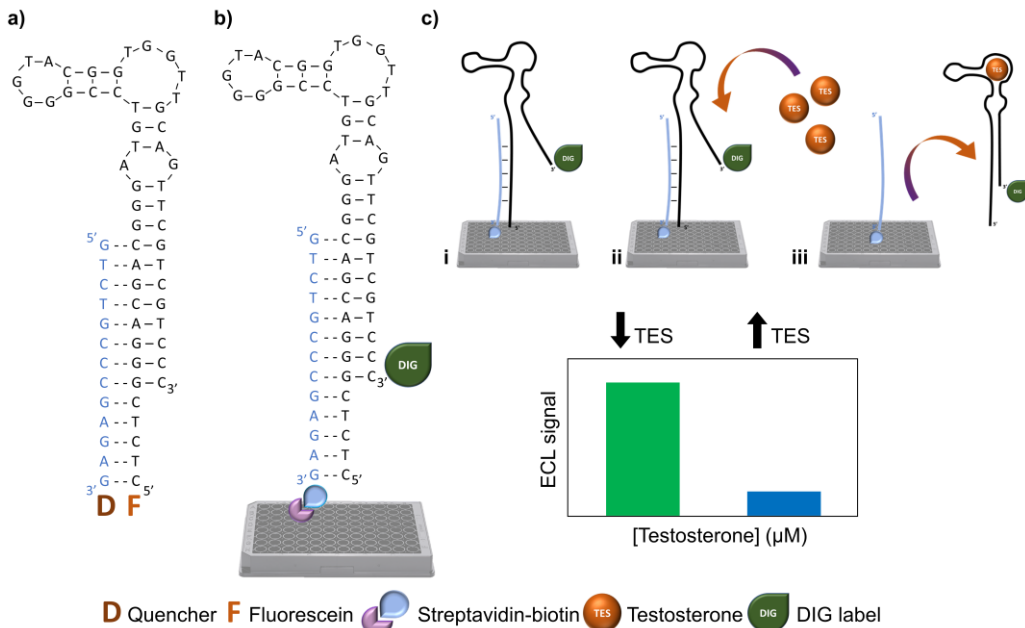


Figure 80. Competitive binding principle. TESS.1 aptamer used by a) Yang et al. and b) in the present work. c) Schematic representation showing: i. the hybridization between the capture probe (blue sequence attached to the 96-well plate) with the aptamer (black sequence); ii. the subsequent addition of testosterone, iii. how the aptamer leaves the capture probe after binding with the target; and the ECL signal produced depending on the lower and higher concentrations of testosterone.

### 8.3.1 Characterization of the TESS.1 aptamer

Firstly, to investigate whether the aptamer preferentially binds to the capture probe rather than closing its stem, native nESI-MS experiments with only the stems and capture probe were performed (Figure 81). When measuring a mixture of stem 1 (complementary to the capture probe) and stem 2 (complementary to stem 1), a duplex of these stems is noticed and only low intensity peaks for the stems alone can be identified (Figure 81, top). The mixture of the capture probe and stem 1 also forms a duplex (Figure 81, middle). After combining all three species in an equimolar mixture, a clear signal for the capture-stem 1 duplex is observed while only a low intensity peak for the stem 1-stem 2 duplex is detected (Figure 81, bottom). Thereby, native nESI-MS proved the aptamer preferentially binds to the capture probe rather than closing the stems to stabilize the aptamer structure. This can be also supported by the higher number of complementary base pairs between the capture probe-stem 1 in comparison with stem 1-stem 2.

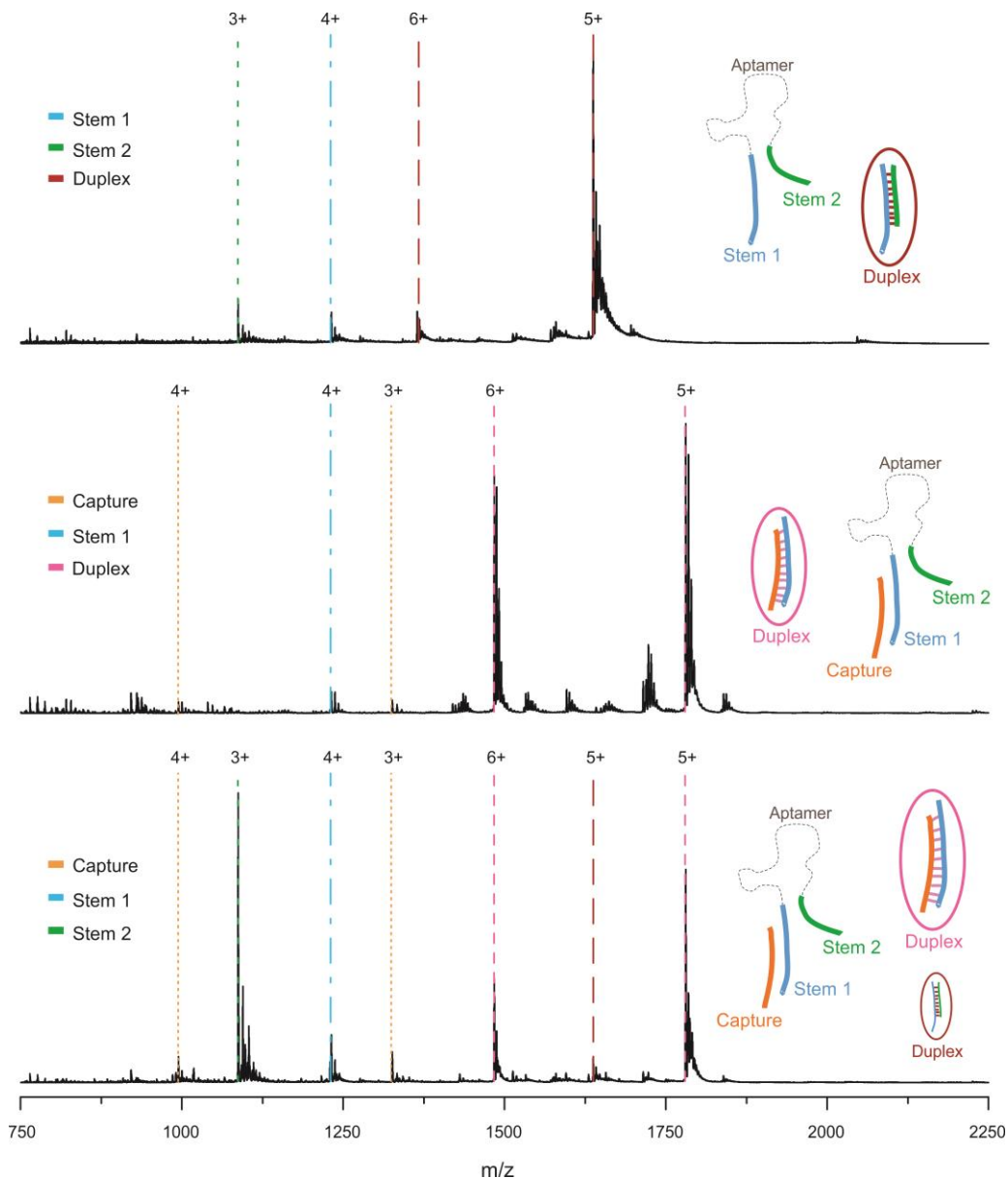


Figure 81. Native MS spectra of stem 1 (complementary to the capture probe) and stem 2 (complementary to the stem 1) (top), capture and stem 1 (middle) and stem 1, stem 2 and the capture (bottom) in equimolar ratios. The lines represent the theoretical  $m/z$ -values for each species and complex.

As it was previously mentioned, the proposed principle assumes that the aptamer cannot form a duplex with the capture probe upon binding to testosterone. This hypothesis was confirmed using native nESI-MS in which an aptamer-capture complex was disrupted upon addition of testosterone and an aptamer-testosterone complex was formed (Figure 82). In absence of testosterone, a clear signal for the aptamer-

capture complex is observed (Figure 82, bottom). Simultaneously, there is some free aptamer and free capture detected. Upon addition of testosterone, the aptamer-capture interaction was disrupted and an aptamer-testosterone complex was formed (Figure 82, top).

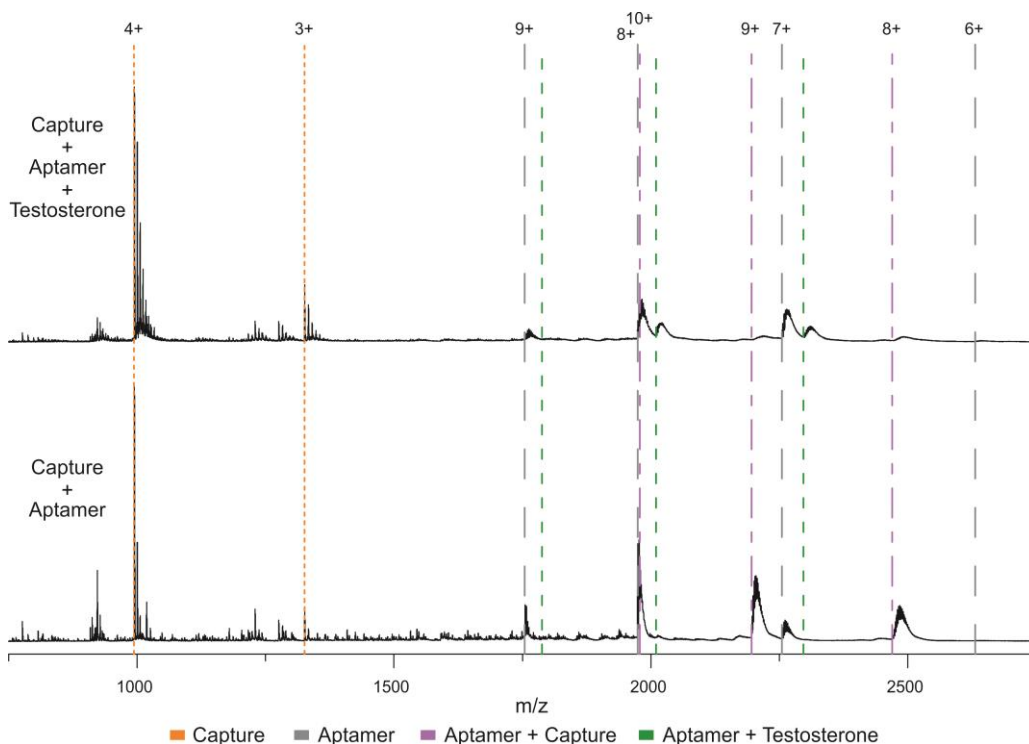


Figure 82. Native MS spectrum of the aptamer and capture in a 1:1 ratio (bottom) and the same mixture with testosterone added in a 1:10 ratio (top). The dotted orange lines, dashed grey lines, dotted green lines and dashed-dotted purple lines represent the theoretical  $m/z$ -values of the capture probe, aptamer, aptamer-testosterone complex and aptamer-capture probe complex, respectively.

In order to validate the binding between the TESS.1 aptamer and testosterone, ITC and native MS experiments were carried out (see SM for more details). The thermogram for the ITC titration of TESS.1 with testosterone (Figure 83a) shows a clear exothermic binding process (Figure 83b). From these results (Table 11) it is possible to calculate a  $K_d$  of  $240 \pm 29$  nM, which is slightly higher than the previously reported value of  $\sim 80$  nM by Yang et al.<sup>10</sup>

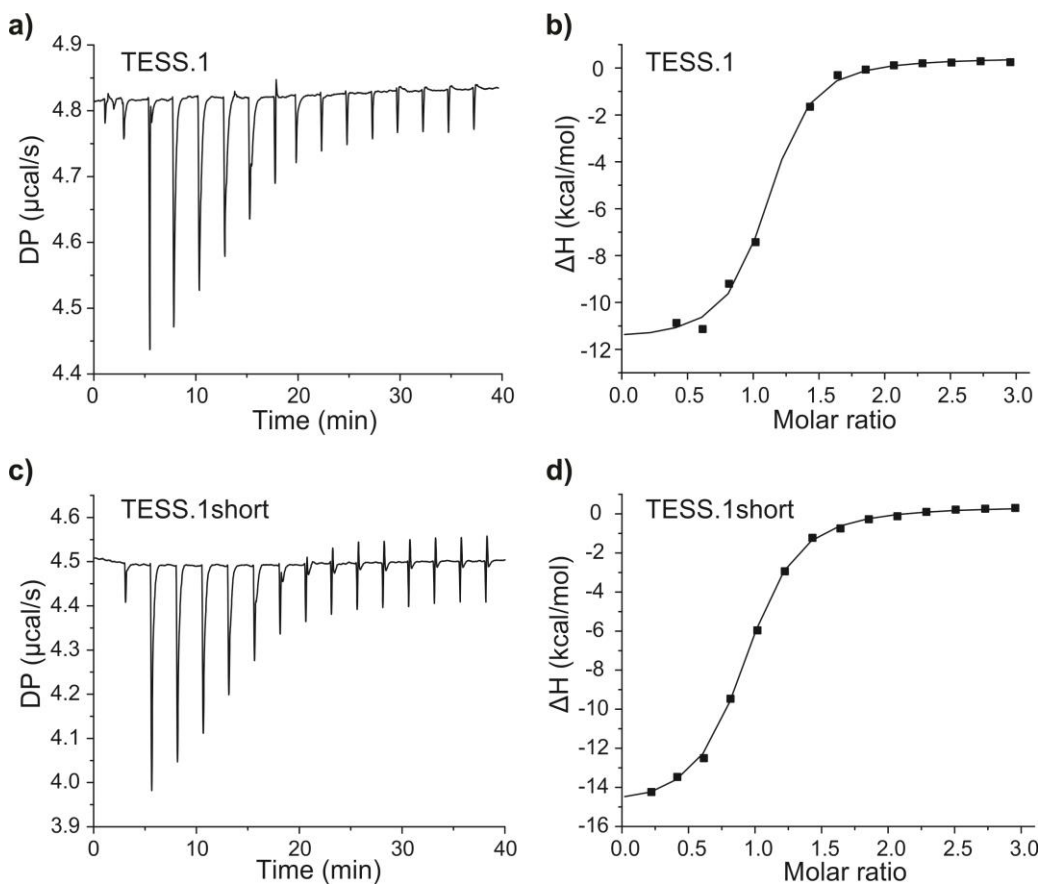


Figure 83. a) Thermogram and b) binding curve of the ITC titration of 10  $\mu\text{M}$  of the TESS.1 aptamer with 150  $\mu\text{M}$  of testosterone. c) Thermogram and d) binding curve of the ITC titration of 10  $\mu\text{M}$  of the TESS.1short aptamer with 150  $\mu\text{M}$  of testosterone. The line in the binding curve represents the fitting with the “one set of binding sites” model.

Table 11. Parameters determined by ITC.

ITC parameter	TESS.1	TESS.1short
$K_d$ (nM)	$240 \pm 29$	$489 \pm 58$
Stoichiometry	$1.15 \pm 0.09$	$0.93 \pm 0.07$
$\Delta G$ (kcal/mol)	$-9.04 \pm 0.07$	$-8.61 \pm 0.07$
$\Delta H$ (kcal/mol)	$-11 \pm 1$	$-15.7 \pm 0.6$
$-\Delta S$ (kcal/mol)	$2 \pm 1$	$7.1 \pm 0.6$

To investigate whether the stems of TESS.1 facilitate the binding of testosterone, native MS experiments were performed with the full length TESS.1 aptamer and a shorter variant, called TESS.1short, which is only eight bp shorter. Figure 84a displays the native MS spectrum of the full length aptamer and Figure 84b portrays the results acquired with the shorter version of the aptamer. A clear complex between the full length TESS.1

aptamer and testosterone was identified as it can be seen in Figure 84a. In this case, 40 % of the aptamer forms a complex with testosterone. On the other hand, TESS.1short only shows a low intensity peak corresponding to the complex (13 % of the aptamer is present as complex, green dashed lines in Figure 84b). Therefore, ITC experiments were performed to determine the  $K_d$  between TESS.1short aptamer and testosterone. Again, a clear exothermic binding process was observed from which the  $K_d$  was calculated to be  $489 \pm 58$  nM (Table 11, Figure 83c and d). Table 11 summarizes the parameters determined via ITC demonstrating slight differences between TESS.1 and TESS.1short from a thermodynamic point of view, where the entropy of TESS.1short is higher than TESS.1, showing more unfavorable conformational changes and in consequence, less affinity.<sup>344</sup> These results suggest that even though the TESS.1short aptamer still contains the binding region, the stems of TESS.1 are a crucial structural part for the folding of the aptamer into its binding-competent state. Hence, the presence of the stems clearly enhances the affinity of the aptamer towards testosterone. Since stem 1 and stem 2 of TESS.1 hybridize upon binding of the target, stem 1 is no longer available to interact with the capture probe, as shown in Figure 82.

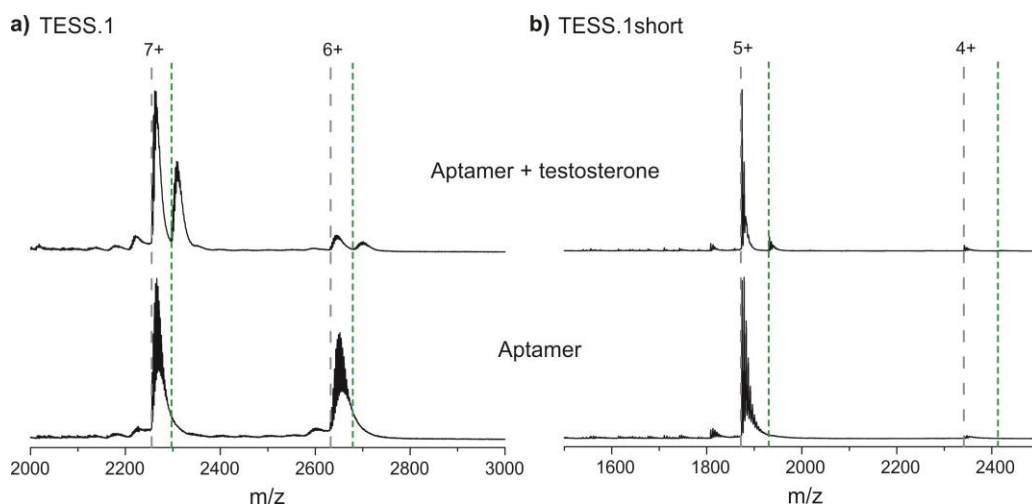


Figure 84. Native MS spectrum of the a) TESS.1 aptamer and b) TESS.1short aptamer. The bottom spectra are the aptamers alone while the top spectrum shows the aptamer after testosterone addition in a 1:10 ratio. The dashed grey and dotted green lines represent theoretical  $m/z$ -values of the aptamer and aptamer-testosterone complex, respectively.

### 8.3.2 Optimization of the incubation protocol for ECL detection

Different incubation protocols were tested in order to obtain the optimal analytical performance of the ECL assay and to study the interactions among the capture probe, the aptamer TESS.1 and the target (testosterone). Figure 79 portrays the schematic representation of the three followed protocols. All of them were tested using: *i*) one fixed concentration of capture probe (200 nM) since the full saturation of the surface was pursued, *ii*) two concentrations of testosterone (5  $\mu$ M and 0  $\mu$ M as blank) to measure the effectiveness of the binding with the aptamer, and *iii*) four concentrations of TESS.1 aptamer (400 nM, 200 nM, 100 nM and 0 nM) to be optimized in parallel. An equimolar interaction between aptamer and capture probe was expected but higher and lower concentrations were tested in order to verify and optimize the entire protocol.

Figure 85 summarizes the results obtained for the optimization of the protocol and concentration of the TESS.1 aptamer. The best protocol and optimal concentration of TESS.1 are defined by the highest difference in ECL counts between 0  $\mu$ M and 5  $\mu$ M of the target. The highest difference was obtained following P1 when using concentrations of 400 nM and 200 nM of TESS.1 aptamer, as can be seen in Figure 85a and b, showing 47 % and 61 % of the ECL counts, respectively. Comparing these percentages with P3, P3 exhibits a decrease in the percentage of ECL signal with 24 % and 22 %. Surprisingly, P2 showed negligible differences between both concentrations of testosterone (maximum 7 %). At first insight, the affinity between the capture probe and the aptamer seems higher than the affinity between testosterone and TESS.1, resulting in a situation very difficult for the target to dehybridize the aptamer/capture duplex. However, the native MS results demonstrated that testosterone always binds to the aptamer regardless of the protocol used (Figure 82). On the other hand, these results could likely be explained by different factors: *i*) this is the only protocol where testosterone was added to the 96-well plate instead of incubating it first with the aptamer in an Eppendorf (Figure 79); and/or, *ii*) the aforementioned absorption of the detergent Tween 20 on the electrode surface could play a critical role forming micelles, that encapsulate the testosterone, which is practically insoluble in water, banning its interaction with the aptamer.

Figure 85c (100 nM concentration of aptamer) exhibited low ECL signals (one order of magnitude below 400 nM data) and small differences (< 15 %) between testosterone concentrations. As expected, Figure 85d displays similar results for all protocols since

they are blank samples with no aptamer (concentration 0 nM). The ECL response observed in these blank samples is the usual ECL low background signal due to no external energy source being used.<sup>416</sup> Therefore, no interferences associated to luminescent impurity, auto fluorescence and scattering of light are present. In other works, the background ECL signal has been attributed to the electro-oxidation reaction between dissolved oxygen and two different products of TPA (present in the reading buffer).<sup>417</sup> Considering the obtained results, the concentration of 200 nM for the TESS.1 aptamer and P1 were chosen as the optimal conditions for the following experiments.

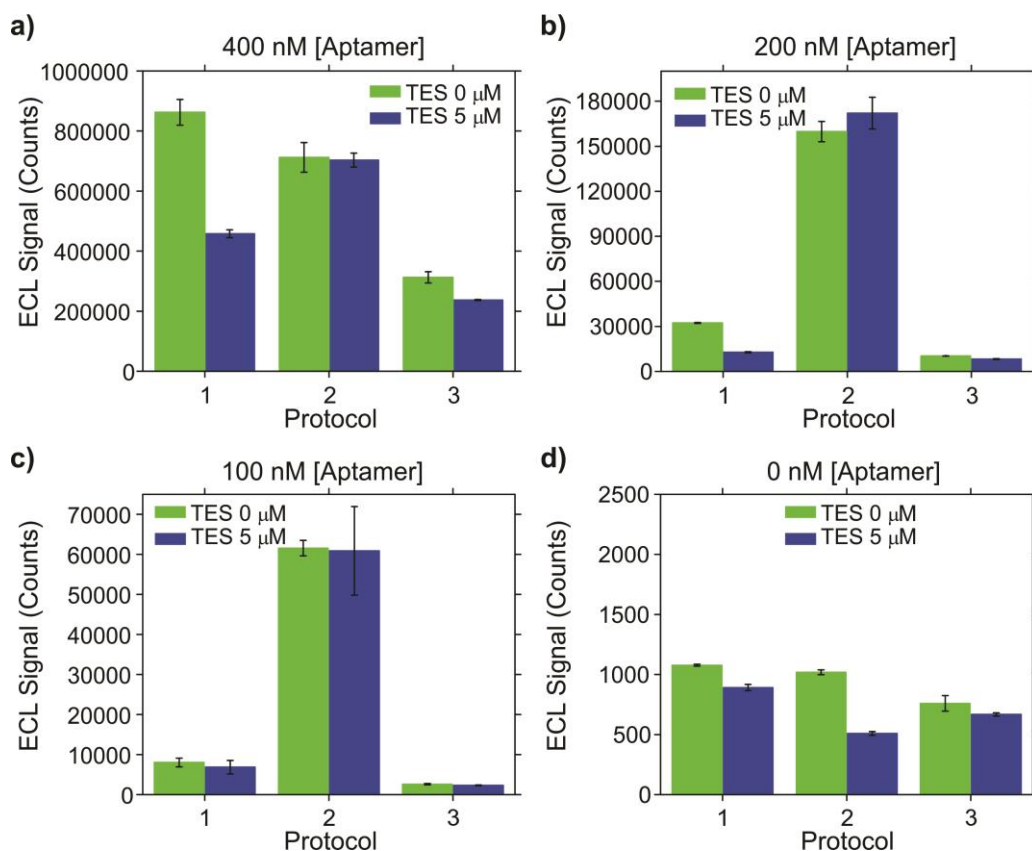


Figure 85. Parallel optimization of the ECL incubation protocol and the concentrations of the aptamer a) 400 nM, b) 200 nM, c) 100 nM and d) 0 nM, comparing the results with (5 μM) and without (0 μM) testosterone.

### 8.3.3 ECL detection of testosterone

**TESS.1 aptamer.** Following the optimizations in section 8.3.2., experiments with multiple concentrations of testosterone were performed to gain better insight in the binding of testosterone to its aptamer. Figure 86 (bottom curve, black squares) shows data of the TESS.1 aptamer in the presence of testosterone in a concentration range from 0 to 25  $\mu\text{M}$ . After the incubation of the aptamer with the different concentrations of testosterone, only the free aptamer will hybridize to the capture probe. The ECL signal already decreases with 14 % upon addition of the lowest concentration of testosterone used (0.39  $\mu\text{M}$ ). This decrease is due to the lower availability of the free TESS.1 aptamer to hybridize with the capture probe in presence of the target. The ECL response decreases until 3.13  $\mu\text{M}$  to 79 % of the initial value indicating an increasing amount of testosterone is binding to its aptamer in this range. From 3.13  $\mu\text{M}$  onwards the signal is almost constant which suggests saturation of the aptamer. A similar trend of the testosterone curve is observed in the results reported by Yang and co-workers.

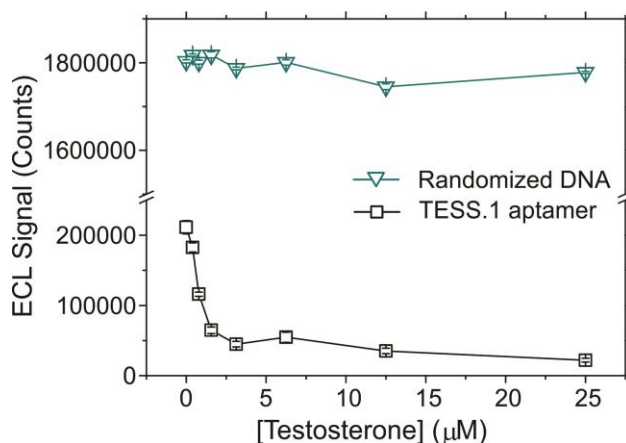


Figure 86. ECL data of testosterone (from 0 to 25  $\mu\text{M}$  with a total of 8 concentrations, two fold dilutions) in combination with the TESS.1 aptamer and randomized ssDNA sequence in the optimal concentration of 200 nM and following protocol 1.

From the ECL experiments, the  $K_d$  was estimated to be around of 0.97  $\mu\text{M}$ , which is slightly higher than the  $K_d$  determined by ITC, although it remains in the same range. It is important to consider that the presence of the capture probe (not present during ITC measurements) can likely influence within the increment of the value.

**Specificity of the ECL approach: randomized ssDNA.** To investigate whether the decrease in signal can be ascribed to specific binding, the same experiments were

performed using a randomized ssDNA sequence instead of TESS.1 as shown in Figure 86 (upper curve). It is relevant to highlight herein that the randomized sequence kept the part complementary to the capture probe to allow hybridization whereas the rest of the sequence was scrambled (see Table 10 for more details). Native MS experiments with the randomized ssDNA were carried out to confirm and demonstrate that no binding occurs between this sequence and the target (see Figure 87). In this case, the ECL signal at each concentration of testosterone is in the same range with a maximum deviation of 3 % compared to the blank. Important to notice is that the signal of the randomized sequence is much more intense than the one of the TESS.1 aptamer (Figure 86). This is most likely due to two factors: *i*) the randomized ssDNA is attached to the capture probe through the preserved region of the sequence and, *ii*) the scrambled part was designed to avoid the complementarity showed by TESS.1 between the stem 1 and the stem 2. As a result, this unfolded structure of the randomized sequence promotes a further position of the DIG label and therefore also the anti-DIG antibody with the  $\text{Ru}(\text{bpy})_3^{2+}$  labels with respect the surface of the electrode. In consequence, the labels were closer to the light source during the generation and reading of the ECL signal, offering the highest values ( $\sim 1.8 \cdot 10^6$  counts, Figure 86 upper curve). The increase of the ECL response due to the higher distance between the ruthenium complex and the surface of the electrode has already been explained and demonstrated in the literature.<sup>418</sup>

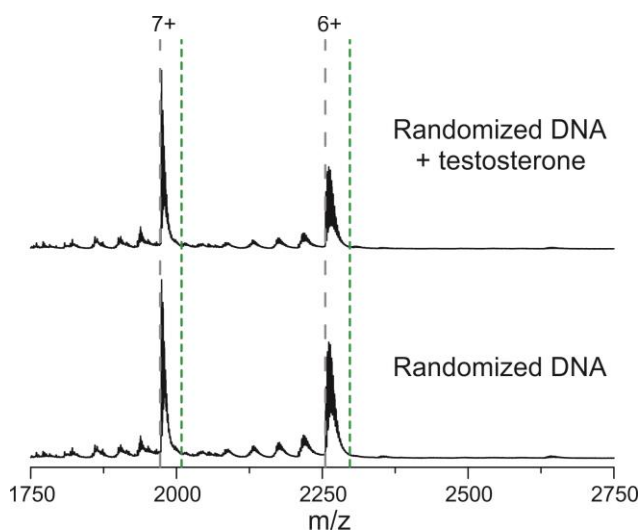


Figure 87. Native MS spectrum of the randomized DNA sequence. The bottom spectrum is the aptamer alone while the top spectrum shows the aptamer after addition of testosterone in a 1:10 ratio. The dashed grey and dotted green lines represent theoretical  $m/z$ -values of the aptamer and aptamer-testosterone complex, respectively.

### 8.3.4 Selectivity of the TESS.1 aptamer and the developed ECL approach

DCA and HC steroids were selected, after preliminary native MS experiments, as negative controls to replace testosterone in order to confirm the selectivity of the aptamer. Hence, the native MS results showed no interactions between DCA and the TESS.1 aptamer as can be seen in Figure 88, middle (red dashed lines). In addition, negligible binding between HC and the aptamer was observed during the native MS experiments (Figure 88, top, blue dashed lines). Figure 89 displays the normalized data of the ECL experiments of TESS.1 in presence of testosterone, DCA, or HC and the randomized ssDNA in presence of testosterone (the raw data for DCA and HC can be found in Figure 90). The raw data was normalized for the purpose of facilitating the comparison between the experiments. With the same intention, the inset shows the results on a different scale to enable a better distinction.

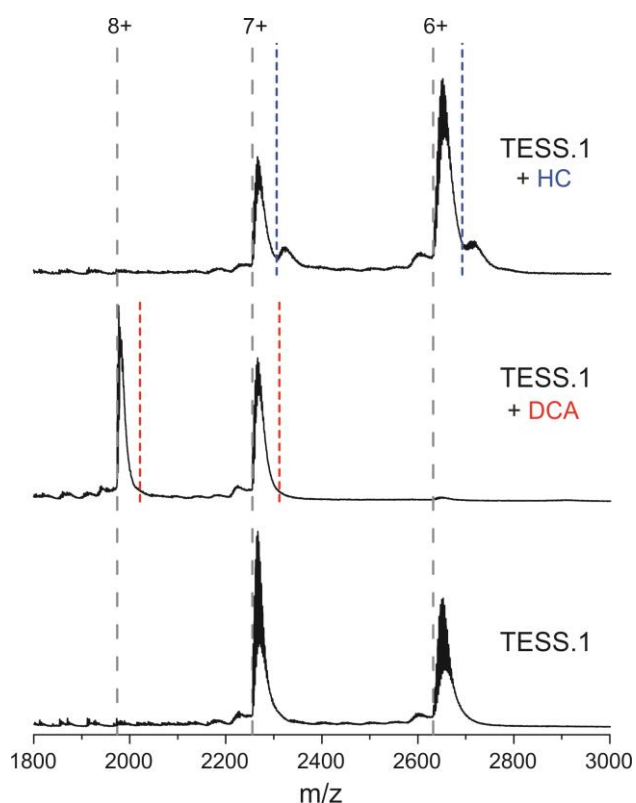


Figure 88. Native MS spectrum showing (from the bottom): the TESS.1 aptamer alone followed by the negative controls DCA and HC added in a 1:10 ratio to the aptamer. Theoretical  $m/z$ -values of the aptamer, aptamer-DCA complex and aptamer-HC complex are indicated with a dashed grey, dotted red and dotted blue line, respectively.

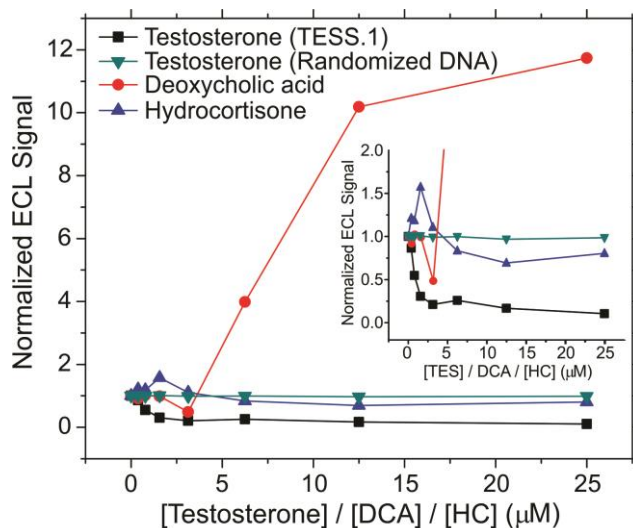


Figure 89. Normalized ECL data to compare testosterone (with the TESS.1 aptamer in black squares and with the randomized ssDNA in green triangles), DCA (red circles) and HC (blue triangles) responses. Inset: same data but in a different scale to enable a better comparison between the curves.

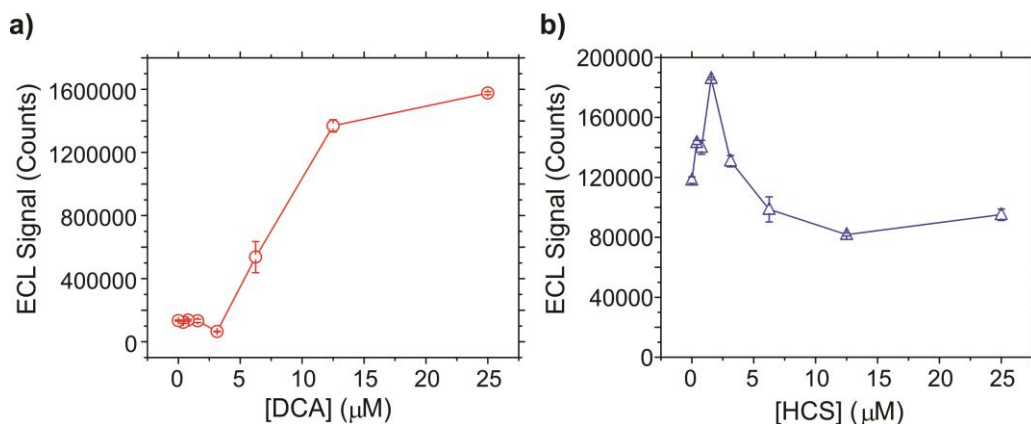


Figure 90. ECL data of the negative controls (from 0 to 25 μM with a total of 8 concentrations, two fold dilutions) a) DCA and b) HC using the TESS.1 aptamer in the optimal concentration of 200 nM and following protocol 1.

As it is depicted in Figure 89, in presence of DCA the ECL signal becomes much more intense from 6.25 μM onwards to reach 10 times over its initial value. The amount of counts measured at 25 μM testosterone (Figure 90a) is in the same order of magnitude as the ECL signal observed for the unstructured randomized ssDNA ( $\sim 1.6 \cdot 10^6$  and  $\sim 1.8 \cdot 10^6$  ECL counts, respectively). This indicates the presence of DCA might unfold the aptamer structure which brings the  $\text{Ru}(\text{bpy})_3^{2+}$  labels further away from the electrode surface and closer to the light source, leading to a higher amount of counts as it was previously discussed in section 8.3.3.<sup>418</sup> This hypothesis was confirmed by the shift of

charge states towards more positive charges observed during the native MS experiments (Figure 88, middle) which usually mean a more unfolded structure due to higher repulsion of charges. Finally, the addition of increasing concentration of HC to the TESS.1 aptamer first leads to a small increase of the ECL signal but afterwards decreases to 31 % of its initial value (Figure 89 and Figure 90). It is important to remark that the trend of this last part is similar to the one of the binding of testosterone to TESS.1, but with less intensity difference indicating only low-affinity binding. Besides, this is also supported by the native MS data in which a small amount of complex between TESS.1 and HC was detected (Figure 88, top).

## 8.4 Conclusions

A novel ECL assay based on aptamer recognition towards testosterone as model for small molecules was introduced. In parallel, a characterization of the aptamer-target interaction was validated using a multifaceted approach with analytical techniques such as ITC and native nESI-MS. The optimization of the incubation protocol as well as the concentration of the TESS.1 aptamer was carried out proving the analytical capability of the ECL assay towards testosterone detection in a selective manner. The best analytical performance of the ECL assay was obtained following a previous incubation of the TESS.1 aptamer (concentration of 200 nM) together with the target before adding them to the 96-well plate where the capture probe was immobilized. Currently, NMR experiments are ongoing to validate the hypothesis that DCA can unfold the aptamer structure and therefore increase the ECL signal. Although aptamer-based ECL sensors emerged only over one decade ago, they have already found broad applications in both fundamental research and biomedical diagnostics applications. The present work aims to open a new avenue for the development of reliable and robust ECL biosensor assays for biochemical analysis, promoting a deeper understanding of the potential of biosensors based on aptamers for the accurate detection of numerous biomolecules relevant in biomedical applications.



# 19

## Conclusions and outlook



Aptamers are promising tools in many analytical and biomedical applications. The global aptamer market is estimated to have a value of \$ 207.7 million in 2020, but it is predicted to more than double to \$ 448.8 million by the end of 2025.<sup>419</sup> Despite this fast growth in the aptamer world, there is still a lack of a thorough understanding of the relationship between the sequence, the higher-order structure and the specific interactions of aptamers. In this PhD thesis, I evaluated the ability of MS-based techniques, mainly native MS, to contribute to the characterization of the higher-order structure of aptamers and their interactions. Furthermore, the use of native MS (in combination with other analytical techniques) was explored to thoroughly understand the aptamer-target interactions in designed applications, which is critical for the aptamer performance.

First, CID and ETD, which are commonly used for sequencing purposes, were explored for their ability to obtain higher-order structural information of aptamers. Unfortunately neither of these techniques were found to be deliver structural data for aptamers under native conditions, other than sequence information which is routinely obtained by using CID. However, the conformational dynamics and gas-phase stabilities of aptamers could be analyzed by CIU experiments. More collisional activation is required to unfold more structured aptamers than (partially) unstructured aptamers. The unfolding thresholds correlate well with the stability of these aptamers in solution (structured vs. partially unstructured vs. fully unstructured).

In a next step, the ability of native MS to contribute to the screening and characterization of bioreceptors was identified. Although this was shown for proteins in this PhD thesis, the approach can easily be extended to aptamers as we showed aptamer-target interactions can be characterized by MS (given that the  $K_d$  is in the low- $\mu\text{M}$  to nM range). Moreover, this is not only possible in the negative ionization mode, which is often claimed to be superior for the analysis of oligonucleotides, but also in the positive ionization mode. It was found that native MS can determine relative binding affinities of aptamers which only differ slightly in sequence and structure. Furthermore, combining native MS with IM gave insight into subtle conformational changes upon binding, by monitoring the ions' arrival time. The magnitude of the change was found to correlate with the binding mode and binding affinity, as rigid aptamers undergo smaller conformational changes upon binding the target and bind the target with higher affinity than unstructured, flexible aptamers.

Besides several reports of non-working aptamers in the literature, the problem of misinterpretation of the real aptamer performance was identified by studying ampicillin aptamers using a multi-analytical approach (ITC, native MS and  $^1\text{H}$  NMR). This indicates once again the need for a comprehensive biophysical evaluation and characterization of aptamer-target interactions. We believe that a multi-analytical approach is required, since no single technique is generally capable to characterize all aptamers and offering a robust approach to validate aptamer-target interactions. Such a multi-analytical approach, combining native MS and ITC, was also used in the development of an aptamer-based ECL sensing approach for testosterone. To thoroughly understand the mechanistic details of the developed ECL sensing assay, the interactions between aptamer, target and capture probe needed to be fully understood. This work opened a new avenue for the development of reliable and robust ECL biosensor assays for biochemical analysis.

In general, I hope to contribute to raising awareness in the aptamer community that a critical approach of aptamer characterization is required before “applying” aptamer sequences in other studies and/or applications. The work on the ampicillin aptamers was first published online in November 2020 and received immediate attention on Twitter from prominent researchers in the field (e.g. Juewen Liu and Philip Johnson), received a recommendation on Faculty Opinions and is already cited by three independent groups that acknowledge the fact that some aptamers do not work as intended. Experimental conditions play a critical role and can influence the performance of a given aptamer. Therefore, it is important to identify the most suitable characterization protocol for the desired (analytical) application. However, it is of general interest for the entire aptamer research field that standardized strategies, by preference multidisciplinary approaches, could be used to obtain all relevant information on aptamers and their interactions. This allows to obtain the same type of information for all studied aptamers and objectively decide which aptamer is most suitable for a certain purpose or application.

Besides aiming for a better characterization of aptamers and their interactions, it is important to understand why certain sequences that do not bind a certain target, or only with a very low affinity, are retained during the SELEX process. The reasons for this are currently unknown, but should be identified to avoid the selection of new non-binding sequences in the future.

Next to the (native) MS-based approaches described throughout this PhD thesis, there are several other MS-based methods which hold great potential to contribute to the characterization of the higher-order structure of aptamers and aptamer-target interactions. These are occasionally used for the characterization of proteins and do not always provide immediate results for aptamers. One example is HDX MS which was recently explored for oligonucleotides for the first time by Largy and Gabelica<sup>420</sup> using G-quadruplexes as model systems. It was found that the exchange rates depend on the secondary structure of the G-quadruplexes. Therefore, HDX MS is a promising approach to study aptamers in the future. Other promising approaches include ultraviolet photodissociation MS, negative ETD, and electron photodetachment MS.<sup>421</sup> For the latter, Dababrata et al.<sup>422</sup> showed that it is possible to locate binding sites of cations and targets in G-quadruplexes. The challenge remains however to use this approach for oligonucleotides consisting of more than 20 nucleotides. Finally, hydroxyl footprinting in combination with MS can be explored since more exposed sites are most likely easier to oxidize and therefore this approach can provide structural information.

Although all these structural MS methods stand strong in themselves, the combination with other structural and computational approaches can contribute to a better understanding of the higher-order structure of aptamers and their interactions. Recently, several approaches have been developed to make the MD simulations of DNA more realistic,<sup>423</sup> but MD simulations of RNA remain a challenge for now.

Native IM-MS holds significant potential to support research and address problems in other oligonucleotide-related fields and not only aptamer characterization. First, native (IM-)MS could be used in combination with the SELEX process in order to quickly screen and characterize the aptamer-target interactions, as is now often done with more time-consuming techniques such as ITC or SPR. Second, native IM-MS is not limited to the characterization of aptamers and their interactions with targets, but can also be employed to study therapeutic DNA/RNA and interactions between these oligonucleotides. Moreover, DNA nanostructures (e.g. nanopores, cages and tetrahedrons) and their interactions can be investigated.

Once aptamers are thoroughly characterized, they have significant promise to be used in several application fields: sensing, therapeutics, diagnostics and targeted drug delivery. One example could be the development of pH-sensitive aptamers, which release their target in certain cells, e.g. cancer cells which typically have a different pH compared to healthy cells for targeted drug delivery. Well-characterized aptamers can

also be used in the development of commercial sensing strategies for e.g. environmental contaminants such as antibiotics to contribute to the fight against antimicrobial resistance.

## Bibliography

1. Cox, M. M., Doudna, J. A. & O'Donnell, M. *Molecular Biology: Principles and Practice*. (W.H. Freeman and Company, 2012).
2. Campbell, N. A. & Reece, J. B. *Biology*. (Pearson Education, 2008).
3. Kellis, M., Wold, B., Snyder, M. P., Bernstein, B. E. & Kundaje, A. Defining functional DNA elements in the human genome. *PNAS* **111**, 6131–6138 (2014).
4. Wilson, R. C. & Doudna, J. A. Molecular mechanisms of RNA interference. *Annu. Rev. Biophys.* **42**, 217–239 (2013).
5. Kole, R., Krainer, A. R. & Altman, S. RNA therapeutics: beyond RNA interference and antisense oligonucleotides. *Nat. Rev. Drug Discov.* **11**, 125–140 (2012).
6. Dunn, M. R., Jimenez, R. M. & Chaput, J. C. Analysis of aptamer discovery and technology. *Nat. Rev. Chem.* **1**, (2017).
7. Carothers, J. M., Goler, J. A., Kapoor, Y., Lara, L. & Keasling, J. D. Selecting RNA aptamers for synthetic biology: investigating magnesium dependence and predicting binding affinity. *Nucleic Acids Res.* **38**, 2736–2747 (2010).
8. Li, L. *et al.* Nucleic acid aptamers for molecular diagnostics and therapeutics: Advances and perspectives. *Angew. Chemie - Int. Ed.* **60**, 2221–2231 (2021).
9. Keefe, A. D., Pai, S. & Ellington, A. Aptamers as therapeutics. *Nat. Rev. Drug Discov.* **9**, 537–550 (2010).
10. Yang, K. A. *et al.* High-affinity nucleic-acid-based receptors for steroids. *ACS Chem. Biol.* **12**, 3103–3112 (2017).
11. Lee, K. H. & Zeng, H. A general double library SELEX strategy for aptamer selection using unmodified nonimmobilized targets. *Anal. Bioanal. Chem.* **409**, 5081–5089 (2017).
12. Amaya-González, S. *et al.* Affinity of aptamers binding 33-mer gliadin peptide and gluten proteins: Influence of immobilization and labeling tags. *Anal. Chim. Acta* **873**, 63–70 (2015).
13. Chakravarthy, M. *et al.* Development of DNA aptamers targeting low-molecular-weight amyloid- $\beta$  peptide aggregates: In vitro. *Chem. Commun.* **54**, 4593–4596 (2018).
14. Klingler, C. *et al.* DNA aptamers against the DUX4 protein reveal novel therapeutic implications for FSHD. *FASEB J.* **34**, 4573–4590 (2020).
15. Bock, L. C., Griffin, L. C., Latham, J. A., Vermaas, E. H. & Toole, J. J. Selection of single-stranded DNA molecules that bind and inhibit human thrombin. *Nature* **355**, 564–566 (1992).
16. Wang, G. *et al.* Selection and characterization of DNA aptamer against glucagon receptor by cell-SELEX. *Sci. Rep.* **7**, 17179 (2017).
17. Gopinath, S. C. B., Sakamaki, Y., Kawasaki, K. & Kumar, P. K. R. An efficient RNA aptamer against human influenza B virus hemagglutinin. *J. Biochem.* **139**, 837–846 (2006).
18. Tuerk, C. & Gold, L. Systematic evolution of ligands by exponential enrichment: RNA ligands to bacteriophage T4 DNA polymerase. *Science* **249**, 505–510 (1990).
19. Ellington, A. D. & Szostak, J. W. In vitro selection of RNA molecules that bind specific ligands. *Nature* **346**, 818–822 (1990).
20. Green, R., Ellington, A. D. & Szostak, J. W. In vitro genetic analysis of the Tetrahymena self-splicing intron. *Nature* **347**, 406–408 (1990).
21. Zhuo, Z. *et al.* Recent advances in SELEX technology and aptamer applications in biomedicine. *Int. J. Mol. Sci.* **18**, 1–19 (2017).
22. Tian, H., Duan, N., Wu, S. & Wang, Z. Selection and application of ssDNA aptamers against spermine based on Capture-SELEX. *Anal. Chim. Acta* **1081**, 168–175 (2019).
23. Spiga, F. M., Maietta, P. & Guiducci, C. More DNA-aptamers for small drugs: A capture-SELEX coupled with surface plasmon resonance and high-throughput sequencing. *ACS Comb. Sci.* **17**, 326–333 (2015).
24. Stoltenburg, R., Reinemann, C. & Strehlitz, B. FluMag-SELEX as an advantageous method for DNA aptamer selection. *Anal. Bioanal. Chem.* **383**, 83–91 (2005).

25. Stoltenburg, R., Nikolaus, N. & Strehlitz, B. Capture-SELEX: Selection of DNA aptamers for aminoglycoside antibiotics. *J. Anal. Methods Chem.* **2012**, 415697 (2012).
26. Park, J. W., Tatavarty, R., Kim, D. W., Jung, H. T. & Gu, M. B. Immobilization-free screening of aptamers assisted by graphene oxide. *Chem. Commun.* **48**, 2071–2073 (2012).
27. Drolet, D. W., Moon-McDermott, L. & Romig, T. S. An enzyme-linked oligonucleotide assay. *Nat. Biotechnol.* **14**, 121–1025 (1996).
28. Davis, K. A., Abrams, B., Lin, Y. & Jayasena, S. D. Use of a high affinity DNA ligand in flow cytometry. *Nucleic Acids Res.* **24**, 702–706 (1996).
29. Wang, L. *et al.* Recent advances in the development of electrochemical aptasensors for detection of heavy metals in food. *Biosens. Bioelectron.* **147**, 111777 (2020).
30. Mehlhorn, A., Rahimi, P. & Joseph, Y. Aptamer-based biosensors for antibiotic detection: A review. *Biosensors* **8**, 54 (2018).
31. Zhang, K. *et al.* Application of multiplexed aptasensors in food contaminants detection. *ACS Sensors* **5**, 3721–3738 (2020).
32. Hassani, S. *et al.* Novel label-free electrochemical aptasensor for determination of Diazinon using gold nanoparticles-modified screen-printed gold electrode. *Biosens. Bioelectron.* **120**, 122–128 (2018).
33. Wang, Y. *et al.* Electrochemical aptasensor based on gold modified graphene nanocomposite with different morphologies for ultrasensitive detection of Pb<sup>2+</sup>. *Sensors Actuators, B Chem.* **288**, 325–331 (2019).
34. Lee, E.-H., Lee, S. K., Kim, M. J. & Lee, S.-W. Simple and rapid detection of bisphenol A using a gold nanoparticle-based colorimetric aptasensor. *Food Chem.* **287**, 205–213 (2019).
35. Wu, Y. Y., Huang, P. & Wu, F. Y. A label-free colorimetric aptasensor based on controllable aggregation of AuNPs for the detection of multiplex antibiotics. *Food Chem.* **304**, 125377 (2020).
36. Hai, X. man *et al.* A fluorescence aptasensor based on two-dimensional sheet metal-organic frameworks for monitoring adenosine triphosphate. *Anal. Chim. Acta* **998**, 60–66 (2018).
37. Wang, Y. *et al.* A novel label-free fluorescence aptasensor for dopamine detection based on an Exonuclease III- and SYBR Green I- aided amplification strategy. *Sensors Actuators, B Chem.* **305**, 127348 (2020).
38. Wang, R. *et al.* A nanowell-based QCM aptasensor for rapid and sensitive detection of avian influenza virus. *Sensors Actuators, B Chem.* **240**, 934–940 (2017).
39. Yuan, M. *et al.* Aptasensor for lead(II) based on the use of a quartz crystal microbalance modified with gold nanoparticles. *Microchim. Acta* **184**, 1397–1403 (2017).
40. Ng, E. W. M. *et al.* Pegaptanib, a targeted anti-VEGF aptamer for ocular vascular disease. *Nat. Rev. Drug Discov.* **5**, 123–132 (2006).
41. Kaur, H., Bruno, J. G., Kumar, A. & Sharma, T. K. Aptamers in the therapeutics and diagnostics pipelines. *Theranostics* **8**, 4016–4032 (2018).
42. Bruno, J. G. & Kiel, J. L. In vitro selection of DNA aptamers to anthrax spores with electrochemiluminescence detection. *Biosens. Bioelectron.* **14**, 457–464 (1999).
43. Kulabhusan, P. K., Hussain, B. & Yüce, M. Current perspectives on aptamers as diagnostic tools and therapeutic agents. *Pharmaceutics* **12**, 646 (2020).
44. Li, X. *et al.* Evolution of DNA aptamers through in vitro metastatic-cell-based systematic evolution of ligands by exponential enrichment for metastatic cancer recognition and imaging. *Anal. Chem.* **87**, 4941–4948 (2015).
45. Kruspe, S., Mittelberger, F., Szameit, K. & Hahn, U. Aptamers as drug delivery vehicles. *ChemMedChem* **9**, 1998–2011 (2014).
46. Trinh, T. Le *et al.* A synthetic aptamer-drug adduct for targeted liver cancer therapy. *PLoS One* **10**, e0136673 (2015).
47. Esposito, C. L. *et al.* A combined microRNA-based targeted therapeutic approach to eradicate glioblastoma stem-like cells. *J. Control. Release* **238**, 43–57 (2016).
48. Liang, C. *et al.* Aptamer-functionalized lipid nanoparticles targeting osteoblasts as a novel RNA interference-based bone anabolic strategy. *Nat. Med.* **21**, 288–294 (2015).

49. Griffin, L. C., Tidmarsh, G. F., Bock, L. C., Toole, J. J. & Leung, L. L. K. In Vivo Anticoagulant Properties of a Novel Nucleotide-Based Thrombin Inhibitor and Demonstration of Regional Anticoagulation in Extracorporeal Circuits. *Blood* **81**, 3271–3276 (1993).
50. Ni, S. *et al.* Chemical Modifications of Nucleic Acid Aptamers for Therapeutic Purposes. *International Journal of Molecular Sciences* vol. 18 (2017).
51. Kovacevic, K. D., Gilbert, J. C. & Jilma, B. Pharmacokinetics, pharmacodynamics and safety of aptamers. *Adv. Drug Deliv. Rev.* **134**, 36–50 (2018).
52. Reinstein, O. *et al.* Quinine binding by the cocaine-binding aptamer. thermodynamic and hydrodynamic analysis of high-affinity binding of an off-target ligand. *Biochemistry* **52**, 8652–8662 (2013).
53. Slavkovic, S., Altunisik, M., Reinstein, O. & Johnson, P. E. Structure-affinity relationship of the cocaine-binding aptamer with quinine derivatives. *Bioorganic Med. Chem.* **23**, 2593–2597 (2015).
54. Zong, C. & Liu, J. The arsenic-binding aptamer cannot bind arsenic: critical evaluation of aptamer selection and binding. *Anal. Chem.* **91**, 10887–10893 (2019).
55. Tao, X. *et al.* Detection of chloramphenicol with an aptamer-based colorimetric assay: critical evaluation of specific and unspecific binding of analyte molecules. *Microchim. Acta* **187**, 668 (2020).
56. Sakamoto, T. NMR study of aptamers. *Aptamers* **1**, 13–18 (2017).
57. Ruigrok, V. J. B. *et al.* Characterization of aptamer-protein complexes by X-ray crystallography and alternative approaches. *Int. J. Mol. Sci.* **13**, 10537–10552 (2012).
58. Leney, A. C. & Heck, A. J. R. Native mass spectrometry: What is in the name? *J. Am. Soc. Mass Spectrom.* **28**, 5–13 (2017).
59. Schürch, S. Characterization of nucleic acids by tandem mass spectrometry - the second decade (2004-2013): From DNA to RNA and modified sequences. *Mass Spectrom. Rev.* **35**, 483–523 (2016).
60. Boeri Erba, E., Signor, L. & Petosa, C. Exploring the structure and dynamics of macromolecular complexes by native mass spectrometry. *J. Proteomics* **222**, 103799 (2020).
61. Barth, M. & Schmidt, C. Native mass spectrometry—A valuable tool in structural biology. *J. Mass Spectrom.* **55**, e4578 (2020).
62. Ishii, K., Zhou, M. & Uchiyama, S. Native mass spectrometry for understanding dynamic protein complex. *Biochim. Biophys. Acta - Gen. Subj.* **1862**, 275–286 (2018).
63. Marklund, E. G. & Benesch, J. L. Weighing-up protein dynamics: the combination of native mass spectrometry and molecular dynamics simulations. *Curr. Opin. Struct. Biol.* **54**, 50–58 (2019).
64. Boeri Erba, E. & Petosa, C. The emerging role of native mass spectrometry in characterizing the structure and dynamics of macromolecular complexes. *Protein Sci.* **24**, 1176–1192 (2015).
65. Sobott, F., Mccammon, M. G., Hernández, H. & Robinson, C. V. The flight of macromolecular complexes in a mass spectrometer. *Philos. Trans. R. Soc. A Math. Phys. Eng. Sci.* **363**, 379–391 (2005).
66. Xu, N., Chingin, K. & Chen, H. Ionic strength of electrospray droplets affects charging of DNA oligonucleotides. *J. Mass Spectrom.* **49**, 103–107 (2014).
67. Cech, N. B. & Enke, C. G. Practical implications of some recent studies in electrospray ionization fundamentals. *Mass Spectrom. Rev.* **20**, 362–387 (2001).
68. Konermann, L., Metwally, H., Duez, Q. & Peters, I. Charging and supercharging of proteins for mass spectrometry: Recent insights into the mechanisms of electrospray ionization. *Analyst* **144**, 6157–6171 (2019).
69. Wilm, M. & Mann, M. Analytical properties of the nano-electrospray ion source. *Anal. Chem.* **68**, 1–8 (1996).
70. Bohrer, B. C., Merenbloom, S. I., Koeniger, S. L., Hilderbrand, A. E. & Clemmer, D. E. Biomolecule analysis by ion mobility spectrometry. *Annu. Rev. Anal. Chem.* **1**, 293–327 (2008).
71. Gabelica, V. *et al.* Recommendations for reporting ion mobility mass spectrometry measurements. *Mass Spectrom. Rev.* **38**, 291–320 (2019).
72. Marchand, A., Livet, S., Rosu, F. & Gabelica, V. Drift tube ion mobility: How to reconstruct collision

- cross section distributions from arrival time distributions? *Anal. Chem.* **89**, 12674–12681 (2017).
73. Ruotolo, B. T., Benesch, J. L. P., Sandercock, A. M., Hyung, S. J. & Robinson, C. V. Ion mobility-mass spectrometry analysis of large protein complexes. *Nat. Protoc.* **3**, 1139–1152 (2008).
  74. Bush, M. F. *et al.* Collision cross sections of proteins and their complexes: A calibration framework and database for gas-phase structural biology. *Anal. Chem.* **82**, 9557–9565 (2010).
  75. Thalassinos, K. *et al.* Characterization of phosphorylated peptides using traveling wave-based and drift cell ion mobility mass spectrometry. *Anal. Chem.* **81**, 248–254 (2009).
  76. Benesch, J. L. & Robinson, C. V. Mass spectrometry of macromolecular assemblies: preservation and dissociation. *Curr. Opin. Struct. Biol.* **16**, 245–251 (2006).
  77. Benesch, J. L. P., Aquilina, J. A., Ruotolo, B. T., Sobott, F. & Robinson, C. V. Tandem mass spectrometry reveals the quaternary organization of macromolecular assemblies. *Chem. Biol.* **13**, 597–605 (2006).
  78. Jurchen, J. C. & Williams, E. R. Origin of asymmetric charge partitioning in the dissociation of gas-phase protein homodimers. *J. Am. Chem. Soc.* **125**, 2817–2826 (2003).
  79. Hyung, S. J., Robinson, C. V. & Ruotolo, B. T. Gas-phase unfolding and disassembly reveals stability differences in ligand-bound multiprotein complexes. *Chem. Biol.* **16**, 382–390 (2009).
  80. Dixit, S. M., Polasky, D. A. & Ruotolo, B. T. Collision induced unfolding of isolated proteins in the gas phase: past, present, and future. *Curr. Opin. Chem. Biol.* **42**, 93–100 (2018).
  81. Light-Wahl, K. J. *et al.* Observation of a small oligonucleotide duplex by electrospray ionization mass spectrometry. *J. Am. Chem. Soc.* **115**, 803–804 (1993).
  82. Gale, D. C., Light-Wahl, K. J., Goodlett, D. R. & Smith, R. D. Observation of duplex DNA-drug noncovalent complexes by electrospray ionization mass spectrometry. *J. Am. Chem. Soc.* **116**, 6027–6028 (1994).
  83. Gabelica, V., Galic, N., Rosu, F., Houssier, C. & De Pauw, E. Influence of response factors on determining equilibrium association constants of non-covalent complexes by electrospray ionization mass spectrometry. *J. Mass Spectrom.* **38**, 491–501 (2003).
  84. Gidden, J., Baker, E. S., Ferzoco, A. & Bowers, M. T. Structural motifs of DNA complexes in the gas phase. *Int. J. Mass Spectrom.* **240**, 183–193 (2005).
  85. Gabelica, V., Baker, E. S., Teulade-Fichou, M. P., De Pauw, E. & Bowers, M. T. Stabilization and structure of telomeric and c-myc region intramolecular G-quadruplexes: The role of central cations and small planar ligands. *J. Am. Chem. Soc.* **129**, 895–904 (2007).
  86. Ferreira, R., Marchand, A. & Gabelica, V. Mass spectrometry and ion mobility spectrometry of G-quadruplexes. A study of solvent effects on dimer formation and structural transitions in the telomeric DNA sequence d(TAGGGTTAGGGT). *Methods* **57**, 56–63 (2012).
  87. Balthasart, F., Plavec, J. & Gabelica, V. Ammonium ion binding to DNA G-quadruplexes: Do electrospray mass spectra faithfully reflect the solution-phase species? *J. Am. Soc. Mass Spectrom.* **24**, 1–8 (2013).
  88. Gabelica, V., Livet, S. & Rosu, F. Optimizing native ion mobility Q-TOF in helium and nitrogen for very fragile noncovalent structures. *J. Am. Soc. Mass Spectrom.* **29**, 2189–2198 (2018).
  89. Hommersom, B., Porta, T. & Heeren, R. M. A. Ion mobility spectrometry reveals intermediate states in temperature-resolved DNA unfolding. *Int. J. Mass Spectrom.* **419**, 52–55 (2017).
  90. Marchand, A., Rosu, F., Zenobi, R. & Gabelica, V. Thermal denaturation of DNA G-quadruplexes and their complexes with ligands: Thermodynamic analysis of the multiple states revealed by mass spectrometry. *J. Am. Chem. Soc.* **140**, 12553–12565 (2018).
  91. Porrini, M. *et al.* Compaction of duplex nucleic acids upon native electrospray mass spectrometry. *ACS Cent. Sci.* **3**, 454–461 (2017).
  92. Baker, E. S., Dupuis, N. F. & Bowers, M. T. DNA hairpin, pseudoknot, and cruciform stability in a solvent-free environment. *J. Phys. Chem. B* **113**, 1722–1727 (2009).
  93. Gülbakan, B. *et al.* Native electrospray ionization mass spectrometry reveals multiple facets of aptamer-ligand interactions: From mechanism to binding constants. *J. Am. Chem. Soc.* **140**, 7486–7497 (2018).
  94. Yang, P. *et al.* Evaluation of the binding of natural products with thrombin binding aptamer G-

- quadruplex using electrospray ionization mass spectrometry and spectroscopic methods. *Talanta* **200**, 424–431 (2019).
95. Sharon, M. & V. Robinson, C. A quantitative perspective on hydrophobic interactions in the gas-phase. *Curr. Proteomics* **8**, 47–58 (2011).
  96. Robinson, C. V *et al.* Probing the nature of non-covalent protein ligand interactions by mass spectrometry. *J. Am. Chem. Soc.* **118**, 8646–8653 (1996).
  97. Nimjee, S. M., White, R. R., Becker, R. C. & Sullenger, B. A. Aptamers as therapeutics. *Annu. Rev. Pharmacol. Toxicol.* **57**, 61–79 (2017).
  98. Wang, D. *et al.* Modularly engineered solid-phase synthesis of aptamer-functionalized small molecule drugs for targeted cancer therapy. *Adv. Ther.* **3**, 2000074 (2020).
  99. Jeon, J. *et al.* Homogeneous fluorescent aptasensor for active tuberculosis diagnosis by direct quantification of circulating TB7.7 based on aptamer beacon with graphene oxide. *Sensors Actuators, B Chem.* **317**, 128126 (2020).
  100. Chakraborty, S. *et al.* Aptamer-functionalized drug nanocarrier improves hepatocellular carcinoma toward normal by targeting neoplastic hepatocytes. *Mol. Ther. - Nucleic Acids* **20**, 34–49 (2020).
  101. Catuogno, S. *et al.* An anti-BCMA RNA aptamer for miRNA intracellular delivery. *Mol. Ther. - Nucleic Acids* **18**, 981–990 (2019).
  102. Jiang, Y. *et al.* Aptamer/AuNP biosensor for colorimetric profiling of exosomal proteins. *Angew. Chemie - Int. Ed.* **56**, 11916–11920 (2017).
  103. Jia, Y. *et al.* A metal-organic framework/aptamer system as a fluorescent biosensor for determination of aflatoxin B1 in food samples. *Talanta* **219**, 121342 (2020).
  104. Ilgu, M. & Nilsen-Hamilton, M. Aptamers in analytics. *Analyst* **141**, 1551–1558 (2016).
  105. McKeague, M. *et al.* Comprehensive analytical comparison of strategies used for small molecule aptamer evaluation. *Anal. Chem.* **87**, 8608–8612 (2015).
  106. Miranda-Castro, R., de-los-Santos-Álvarez, N. & Lobo-Castañón, M. J. Characterization of Aptamer–Ligand Complexes. *Aptamers for Analytical Applications* 127–172 (2018).
  107. Qin, Y., Yang, X., Zhang, J. & Cao, X. Target capturing performance of microfluidic channel surface immobilized aptamers: the effects of spacer lengths. *Biomed. Microdevices* **21**, 54 (2019).
  108. Wang, S., Dong, Y. & Liang, X. Development of a SPR aptasensor containing oriented aptamer for direct capture and detection of tetracycline in multiple honey samples. *Biosens. Bioelectron.* **109**, 1–7 (2018).
  109. Wiseman, T., Williston, S., Brandts, J. F. & Lin, L. N. Rapid measurement of binding constants and heats of binding using a new titration calorimeter. *Anal. Biochem.* **179**, 131–137 (1989).
  110. Freire, E., Mayorga, O. L. & Straume, M. Isothermal titration. *Anal. Chem.* **62**, 950–959 (1990).
  111. Challier, L. *et al.* Multianalytical study of the binding between a small chiral molecule and a DNA aptamer: Evidence for asymmetric steric effect upon 3'-versus 5'-end sequence modification. *Anal. Chem.* **88**, 11963–11971 (2016).
  112. Bayraç, C. & Öktem, H. A. Evaluation of *Staphylococcus aureus* DNA aptamer by enzyme-linked aptamer assay and isothermal titration calorimetry. *J. Mol. Recognit.* **30**, e2583 (2017).
  113. Neves, M. A. D. *et al.* Optimizing stem length to improve ligand selectivity in a structure-switching cocaine-binding aptamer. *ACS Sensors* **2**, 1539–1545 (2017).
  114. Shoara, A. A. *et al.* Development of a thermal-stable structure-switching cocaine-binding aptamer. *Biochimie* **145**, 137–144 (2018).
  115. Slavkovic, S., Eisen, S. R. & Johnson, P. E. Designed alteration of binding affinity in structure-switching aptamers through the use of dangling nucleotides. *Biochemistry* **59**, 663–670 (2020).
  116. Amato, T. *et al.* Investigating the properties of TBA variants with twin thrombin binding domains. *Sci. Rep.* **9**, 9184 (2019).
  117. Zavyalova, E., Golovin, A., Pavlova, G. & Kopylov, A. Module-activity relationship of G-quadruplex based DNA aptamers for human thrombin. *Curr. Med. Chem.* **20**, 4836–4843 (2013).
  118. Antipova, O. M., Solius, G. M., Panteleev, D. Y. & Reshetnikov, R. V. Interaction between thrombin and oligonucleotide RA36 is a two-stage process. *Biochem. Biophys. Res. Commun.* **522**, 1037–

- 1040 (2020).
119. Kantonen, S. A., Henriksen, N. M. & Gilson, M. K. Evaluation and minimization of uncertainty in ITC binding measurements: Heat error, concentration error, saturation, and stoichiometry. *Biochim. Biophys. Acta - Gen. Subj.* **1861**, 485–498 (2017).
  120. Turnbull, W. B. & Daranas, A. H. On the value of *c*: Can low affinity systems be studied by isothermal titration calorimetry? *J. Am. Chem. Soc.* **125**, 14859–14866 (2003).
  121. Tellinghuisen, J. Isothermal titration calorimetry at very low *c*. *Anal. Biochem.* **373**, 395–397 (2008).
  122. Amano, R. *et al.* Kinetic and thermodynamic analyses of interaction between a high-affinity RNA aptamer and its target protein. *Biochemistry* **55**, 6221–6229 (2016).
  123. Zhang, Z., Oni, O. & Liu, J. New insights into a classic aptamer: Binding sites, cooperativity and more sensitive adenosine detection. *Nucleic Acids Res.* **45**, 7593–7601 (2017).
  124. Li, Y., Liu, B., Huang, Z. & Liu, J. Engineering base-excised aptamers for highly specific recognition of adenosine. *Chem. Sci.* **11**, 2735–2743 (2020).
  125. Sigurskjold, B. W. Exact analysis of competition ligand binding by displacement isothermal titration calorimetry. *Anal. Biochem.* **277**, 260–266 (2000).
  126. Kuo, T. C., Tsai, C. W., Lee, P. C. & Chen, W. Y. Revisiting the streptavidin-biotin binding by using an aptamer and displacement isothermal calorimetry titration. *J. Mol. Recognit.* **28**, 125–128 (2015).
  127. Burnouf, D. *et al.* KinITC: A new method for obtaining joint thermodynamic and kinetic data by isothermal titration calorimetry. *J. Am. Chem. Soc.* **134**, 559–565 (2012).
  128. Di Trani, J. M., Moitessier, N. & Mittermaier, A. K. Measuring rapid time-scale reaction kinetics using isothermal titration calorimetry. *Anal. Chem.* **89**, 7022–7030 (2017).
  129. Piñeiro, Á. *et al.* AFFINImeter: A software to analyze molecular recognition processes from experimental data. *Anal. Biochem.* **577**, 117–134 (2019).
  130. Munoz, E. *et al.* Thermodynamic and kinetic analysis of isothermal titration calorimetry experiments by using kinITC in AFFINImeter. in *Microcalorimetry of Biological Molecules* vol. 1964 225–239 (2019).
  131. Di Trani, J. M. *et al.* Rapid measurement of inhibitor binding kinetics by isothermal titration calorimetry. *Nat. Commun.* **9**, 893 (2018).
  132. Challier, L. *et al.* Kinetic rotating droplet electrochemistry: A simple and versatile method for reaction progress kinetic analysis in microliter volumes. *J. Am. Chem. Soc.* **135**, 14215–14228 (2013).
  133. Guyon, H. *et al.* Use of a redox probe for an electrochemical RNA-ligand binding assay in microliter droplets. *Chem. Commun.* **53**, 1140–1143 (2017).
  134. Xie, S., Chai, Y., Yuan, Y., Bai, L. & Yuan, R. Development of an electrochemical method for Ochratoxin A detection based on aptamer and loop-mediated isothermal amplification. *Biosens. Bioelectron.* **55**, 324–329 (2014).
  135. Cao, H., Fang, X., Li, H., Li, H. & Kong, J. Ultrasensitive detection of mucin 1 biomarker by immuno-loop-mediated isothermal amplification. *Talanta* **164**, 588–592 (2017).
  136. Martin, A., Bouffier, L., Grant, K. B., Limoges, B. & Marchal, D. Real-time electrochemical LAMP: A rational comparative study of different DNA intercalating and non-intercalating redox probes. *Analyst* **141**, 4196–4203 (2016).
  137. Jaeger, J. *et al.* Characterization and Inkjet Printing of an RNA Aptamer for Paper-Based Biosensing of Ciprofloxacin. *Biosensors* **9**, 7 (2019).
  138. Fadock, K. L. & Manderville, R. A. DNA Aptamer-Target Binding Motif Revealed Using a Fluorescent Guanine Probe: Implications for Food Toxin Detection. *ACS Omega* **2**, 4955–4963 (2017).
  139. Heyduk, T., Ma, Y., Tang, H. & Ebright, R. H. Fluorescence anisotropy: Rapid, quantitative assay for protein-DNA and protein-protein interaction. in *Methods in Enzymology* vol. 274 492–503 (Academic Press, 1996).
  140. Zhang, D., Lu, M. & Wang, H. Fluorescence anisotropy analysis for mapping aptamer-protein interaction at the single nucleotide level. *J. Am. Chem. Soc.* **133**, 9188–9191 (2011).

141. Zhao, Q., Bai, Y. & Wang, H. Directing a rational design of aptamer-based fluorescence anisotropy assay for sensitive detection of immunoglobulin E by site-specific binding study. *Talanta* **217**, 121018 (2020).
142. Cui, L. *et al.* Mass amplifying probe for sensitive fluorescence anisotropy detection of small molecules in complex biological samples. *Anal. Chem.* **84**, 5535–5541 (2012).
143. Zhao, Q. *et al.* Nucleic acid aptamers improving fluorescence anisotropy and fluorescence polarization assays for small molecules. *TrAC Trends Anal. Chem.* **110**, 401–409 (2019).
144. Ye, H., Lu, Q., Duan, N. & Wang, Z. GO-amplified fluorescence polarization assay for high-sensitivity detection of aflatoxin B1 with low dosage aptamer probe. *Anal. Bioanal. Chem.* **411**, 1107–1115 (2019).
145. Sun, L. & Zhao, Q. Direct fluorescence anisotropy approach for aflatoxin B1 detection and affinity binding study by using single tetramethylrhodamine labeled aptamer. *Talanta* **189**, 442–450 (2018).
146. Trachman, R. J. *et al.* Structure-guided engineering of the homodimeric mango-IV fluorescence turn-on aptamer yields an RNA FRET pair. *Structure* **28**, 776–785.e3 (2020).
147. Breitsprecher, D. *et al.* Aptamer Binding Studies Using MicroScale Thermophoresis BT - Nucleic Acid Aptamers: Selection, Characterization, and Application. in (ed. Mayer, G.) 99–111 (Springer New York, 2016).
148. Biniuri, Y., Albada, B. & Willner, I. Probing ATP/ATP-Aptamer or ATP-Aptamer Mutant Complexes by Microscale Thermophoresis and Molecular Dynamics Simulations: Discovery of an ATP-Aptamer Sequence of Superior Binding Properties. *J. Phys. Chem. B* **122**, 9102–9109 (2018).
149. Yang, Y., Yin, Y., Wang, S. & Dong, Y. Simultaneous determination of zearalenone and ochratoxin A based on microscale thermophoresis assay with a bifunctional aptamer. *Anal. Chim. Acta* **1155**, 338345 (2021).
150. Sass, S. *et al.* Binding affinity data of DNA aptamers for therapeutic anthracyclines from microscale thermophoresis and surface plasmon resonance spectroscopy. *Analyst* **144**, 6064–6073 (2019).
151. Jauset Rubio, M. *et al.*  $\beta$ -Conglutin dual aptamers binding distinct aptatopes. *Anal. Bioanal. Chem.* **408**, 875–884 (2016).
152. Skouridou, V. *et al.* Aptatope mapping of the binding site of a progesterone aptamer on the steroid ring structure. *Anal. Biochem.* **531**, 8–11 (2017).
153. Prante, M., Schüling, T., Roth, B., Bremer, K. & Walter, J. Characterization of an Aptamer Directed against 25-Hydroxyvitamin D for the Development of a Competitive Aptamer-Based Assay. *Biosensors* vol. 9 (2019).
154. Potyrailo, R. A., Conrad, R. C., Ellington, A. D. & Hieftje, G. M. Adapting selected nucleic acid ligands (aptamers) to biosensors. *Anal. Chem.* **70**, 3419–3425 (1998).
155. Chen, H. *et al.* SERS imaging-based aptasensor for ultrasensitive and reproducible detection of influenza virus A. *Biosens. Bioelectron.* **167**, 112496 (2020).
156. Eissa, S. *et al.* Selection, characterization, and electrochemical biosensing application of DNA aptamers for sepiapterin. *Talanta* **216**, 120951 (2020).
157. Bayramoglu, G., Ozalp, V. C., Oztekin, M. & Arica, M. Y. Rapid and label-free detection of *Brucella melitensis* in milk and milk products using an aptasensor. *Talanta* **200**, 263–271 (2019).
158. Jarczewska, M., Górski, Ł. & Malinowska, E. Electrochemical aptamer-based biosensors as potential tools for clinical diagnostics. *Anal. Methods* **8**, 3861–3877 (2016).
159. Nan, M. N. *et al.* Modification performance and electrochemical characteristics of different groups of modified aptamers applied for label-free electrochemical impedimetric sensors. *Food Chem.* **337**, 127761 (2021).
160. Farjami, E. *et al.* RNA aptamer-based electrochemical biosensor for selective and label-free analysis of dopamine. *Anal. Chem.* **85**, 121–128 (2013).
161. Balamurugan, S., Obubuafo, A., McCarley, R. L., Soper, S. A. & Spivak, D. A. Effect of linker structure on surface density of aptamer monolayers and their corresponding protein binding efficiency. *Anal. Chem.* **80**, 9630–9634 (2008).
162. Shorie, M. *et al.* Plasmonic DNA hotspots made from tungsten disulfide nanosheets and gold

- nanoparticles for ultrasensitive aptamer-based SERS detection of myoglobin. *Microchim. Acta* **185**, 158 (2018).
163. Sun, L., Wu, L. & Zhao, Q. Aptamer based surface plasmon resonance sensor for aflatoxin B1. *Microchim. Acta* **184**, 2605–2610 (2017).
164. Qian, H. *et al.* Fiber optic surface plasmon resonance biosensor for detection of PDGF-BB in serum based on self-assembled aptamer and antifouling peptide monolayer. *Biosens. Bioelectron.* **140**, 111350 (2019).
165. Gao, S., Zheng, X. & Wu, J. A bilayer interferometry-based competitive biosensor for rapid and sensitive detection of saxitoxin. *Sensors Actuators, B Chem.* **246**, 169–174 (2017).
166. Donkor, D. A. *et al.* Selection and characterization of a DNA aptamer inhibiting coagulation factor XIa. *Sci. Rep.* **7**, 2102 (2017).
167. Karlsson, R. SPR for molecular interaction analysis: A review of emerging application areas. *J. Mol. Recognit.* **17**, 151–161 (2004).
168. Chang, A. L., McKeague, M., Liang, J. C. & Smolke, C. D. Kinetic and equilibrium binding characterization of aptamers to small molecules using a label-free, sensitive, and scalable platform. *Anal. Chem.* **86**, 3273–3278 (2014).
169. Schasfoort, R. B. M. Chapter 1: Introduction to surface plasmon resonance. in *Handbook of Surface Plasmon Resonance* 1–26 (2017). doi:10.1039/9781788010283-00001.
170. Minagawa, H. *et al.* Selection, characterization and application of artificial DNA aptamer containing appended bases with sub-nanomolar affinity for a salivary biomarker. *Sci. Rep.* **7**, 42716 (2017).
171. Simon, L., Bognár, Z. & Gyurcsányi, R. E. Finding the optimal surface density of aptamer monolayers by SPR imaging detection-based aptamer microarrays. *Electroanalysis* **32**, 851–858 (2020).
172. Dausse, E. *et al.* Aptamer selection by direct microfluidic recovery and surface plasmon resonance evaluation. *Biosens. Bioelectron.* **80**, 418–425 (2016).
173. Jia, W., Lu, Z., Yang, H., Li, H. & Xu, D. Elimination terminal fixed region screening and high-throughput kinetic determination of aptamer for lipocalin-1 by surface plasmon resonance imaging. *Anal. Chim. Acta* **1043**, 158–166 (2018).
174. Neumann, O. *et al.* Direct optical detection of aptamer conformational changes induced by target molecules. *Anal. Chem.* **81**, 10002–10006 (2009).
175. Cui, X. *et al.* Identifying conformational changes of aptamer binding to theophylline: A combined bilayer interferometry, surface-enhanced Raman spectroscopy, and molecular dynamics study. *Talanta* **217**, 121073 (2020).
176. Bai, C. *et al.* Aptamer selection and application in multivalent binding-based electrical impedance detection of inactivated H1N1 virus. *Biosens. Bioelectron.* **110**, 162–167 (2018).
177. Ying, G. Q. *et al.* Construction and application of an electrochemical biosensor based on an endotoxin aptamer. *Biotechnol. Appl. Biochem.* **65**, 323–327 (2018).
178. Li, H. *et al.* A novel label-free electrochemical impedance aptasensor for highly sensitive detection of human interferon-gamma based on target-induced exonuclease inhibition. *Biosens. Bioelectron.* **142**, 111532 (2019).
179. Paniagua, G. *et al.* Amperometric aptasensor for carcinoembryonic antigen based on the use of bifunctionalized Janus nanoparticles as biorecognition-signaling element. *Anal. Chim. Acta* **1061**, 84–91 (2019).
180. Yu, J. *et al.* Simultaneous detection of streptomycin and kanamycin based on an all-solid-state potentiometric aptasensor array with a dual-internal calibration system. *Sensors Actuators, B Chem.* **311**, 127857 (2020).
181. Eissa, S., Siddiqua, A., Chinnappan, R. & Zourob, M. Electrochemical SELEX technique for the selection of DNA aptamers against the small molecule 11-deoxycortisol. *ACS Appl. Bio Mater.* **2**, 2624–2632 (2019).
182. Lin, K.-C., Jagannath, B., Muthukumar, S. & Prasad, S. Sub-picomolar label-free detection of thrombin using electrochemical impedance spectroscopy of aptamer-functionalized MoS<sub>2</sub>.

- Analyst* **142**, 2770–2780 (2017).
183. Bard, A. J. & Faulkner, L. R. *Electrochemical Methods: Fundamentals and Applications, 2nd Edition*. Wiley (2000).
  184. Hu, Q., Wang, R., Wang, H., Slavik, M. F. & Li, Y. Selection of acrylamide-specific aptamers by a quartz crystal microbalance combined SELEX method and their application in rapid and specific detection of acrylamide. *Sensors Actuators, B Chem.* **273**, 220–227 (2018).
  185. Ali, M. H., Elsherbiny, M. E. & Emara, M. Updates on aptamer research. *International Journal of Molecular Sciences* vol. 20 (2019).
  186. Churcher, Z. R., Neves, M. A. D., Hunter, H. N. & Johnson, P. E. Comparison of the free and ligand-bound imino hydrogen exchange rates for the cocaine-binding aptamer. *J. Biomol. NMR* **68**, 33–39 (2017).
  187. Churcher, Z. R., Garaev, D., Hunter, H. N. & Johnson, P. E. Reduction in dynamics of base pair opening upon ligand binding by the cocaine-binding aptamer. *Biophys. J.* **119**, 1147–1156 (2020).
  188. Verdonck, L. *et al.* Tethered imidazole mediated duplex stabilization and its potential for aptamer stabilization. *Nucleic Acids Res.* **46**, 11671–11686 (2018).
  189. Buyst, D. *et al.* Identification of a pKa-regulating motif stabilizing imidazole-modified double-stranded DNA. *Nucleic Acids Res.* **43**, 51–62 (2015).
  190. Oguro, A. *et al.* Two stems with different characteristics and an internal loop in an RNA aptamer contribute to spermine-binding. *J. Biochem.* **161**, 197–206 (2017).
  191. Duchardt-Ferner, E. *et al.* Structure of an RNA aptamer in complex with the fluorophore tetramethylrhodamine. *Nucleic Acids Res.* **48**, 949–961 (2020).
  192. Slavkovic, S. *et al.* Thermodynamic analysis of cooperative ligand binding by the ATP-binding DNA aptamer indicates a population-shift binding mechanism. *Sci. Rep.* **10**, 18944 (2020).
  193. Marshall, A. G. & Smith, J. L. Nuclear spin-labeled nucleic acids. 1. Fluorine-19 nuclear magnetic resonance of Escherichia coli 5-fluorouracil-5S-RNA. *J. Am. Chem. Soc.* **99**, 635–636 (1973).
  194. Scott, L. G. & Hennig, M. <sup>19</sup>F-site-specific-labeled nucleotides for nucleic acid structural analysis by NMR. in *Methods in Enzymology* vol. 566 59–87 (Elsevier Inc., 2016).
  195. Chrominski, M., Baranowski, M. R., Chmielinski, S., Kowalska, J. & Jemielity, J. Synthesis of trifluoromethylated purine ribonucleotides and their evaluation as <sup>19</sup>F NMR probes. *J. Org. Chem.* **85**, 3440–3453 (2020).
  196. Baranowski, M. R., Warminski, M., Jemielity, J. & Kowalska, J. 5'-fluoro(di)phosphate-labeled oligonucleotides are versatile molecular probes for studying nucleic acid secondary structure and interactions by <sup>19</sup>F NMR. *Nucleic Acids Res.* **48**, 8209–8224 (2020).
  197. Ishizuka, T., Yamashita, A., Asada, Y. & Xu, Y. Studying DNA G-Quadruplex aptamer by <sup>19</sup>F NMR. *ACS Omega* **2**, 8843–8848 (2017).
  198. Bao, H. L. *et al.* Characterization of human telomere RNA G-quadruplex structures in vitro and in living cells using <sup>19</sup>F NMR spectroscopy. *Nucleic Acids Res.* **45**, 5501–5511 (2017).
  199. Yamaoki, Y. *et al.* The first successful observation of in-cell NMR signals of DNA and RNA in living human cells. *Phys. Chem. Chem. Phys.* **20**, 2982–2985 (2018).
  200. Broft, P. *et al.* In-cell NMR spectroscopy of functional riboswitch aptamers in eukaryotic cells. *Angew. Chemie - Int. Ed.* **60**, 865–872 (2021).
  201. Gelinas, A. D., Davies, D. R. & Janjic, N. Embracing proteins: structural themes in aptamer – protein complexes. *Curr. Opin. Struct. Biol.* **36**, 122–132 (2016).
  202. Schmidt, C., Perbandt, M., Klussmann, S. & Betzel, C. Molecular characterization of a ghrelin-L-aptamer complex. *J. Mol. Struct.* **1204**, 127510 (2020).
  203. Stagno, J. R., Bhandari, Y. R., Conrad, C. E., Liu, Y. & Wang, Y. X. Real-time crystallographic studies of the adenine riboswitch using an X-ray free-electron laser. *FEBS J.* **284**, 3374–3380 (2017).
  204. Ding, J., Swain, M., Yu, P., Stagno, J. R. & Wang, Y. X. Conformational flexibility of adenine riboswitch aptamer in apo and bound states using NMR and an X-ray free electron laser. *J. Biomol. NMR* **73**, 509–518 (2019).
  205. Chang, Y. M., Chen, C. K. M. & Hou, M. H. Conformational changes in DNA upon ligand binding monitored by circular dichroism. *Int. J. Mol. Sci.* **13**, 3394–3413 (2012).

206. Zhang, D., Han, J., Li, Y., Fan, L. & Li, X. Aptamer-based K<sup>+</sup> sensor: Process of aptamer transforming into G-quadruplex. *J. Phys. Chem. B* **120**, 6606–6611 (2016).
207. Wiedman, G. R., Zhao, Y., Mustaev, A. & Ping, J. An aptamer-based biosensor for the azole class of antifungal drugs. *mSphere* **2**, 2–11 (2017).
208. Wildner, S. *et al.* Aptamers as quality control tool for production, storage and biosimilarity of the anti-CD20 biopharmaceutical rituximab. *Sci. Rep.* **9**, 1111 (2019).
209. Aljohani, M. M. *et al.* Mapping the binding region of aptamer targeting small molecule: Dabigatran etexilate, an anti-coagulant. *Talanta* **218**, 121132 (2020).
210. Das, R. & Doniach, S. Structural studies of proteins and nucleic acids in solution using small angle X-ray scattering (SAXS). in *Soft Matter Characterization* 1083–1108 (Springer, 2008).
211. Mittelberger, F. *et al.* RAID3 - An interleukin-6 receptor-binding aptamer with post-selective modification-resistant affinity. *RNA Biol.* **12**, 1043–1053 (2015).
212. Szameit, K. *et al.* Structure and target interaction of a G-quadruplex RNA-aptamer. *RNA Biol.* **13**, 973–987 (2016).
213. Tomilin, F. N. *et al.* Four steps for revealing and adjusting the 3D structure of aptamers in solution by small-angle X-ray scattering and computer simulation. *Anal. Bioanal. Chem.* **411**, 6723–6732 (2019).
214. Stojanovic, M. N., De Prada, P. & Landry, D. W. Fluorescent sensors based on aptamer self-assembly. *J. Am. Chem. Soc.* **122**, 11547–11548 (2000).
215. Stojanovic, M. N., Prada, P. De & Landry, D. W. Aptamer-based folding fluorescent sensor for cocaine. *J. Am. Chem. Soc.* **123**, 4928–4931 (2001).
216. McLuckey, S. A., Van Berker, G. J. & Glish, G. L. Tandem mass spectrometry of small, multiply charged oligonucleotides. *J. Am. Soc. Mass Spectrom.* **3**, 60–70 (1992).
217. McLuckey, S. A. & Habibi-Goudarzi, S. Decompositions of multiply charged oligonucleotide anions. *J. Am. Chem. Soc.* **115**, 12085–12095 (1993).
218. Monn, S. T. M. & Schürch, S. New aspects of the fragmentation mechanisms of unmodified and methylphosphonate-modified oligonucleotides. *J. Am. Soc. Mass Spectrom.* **18**, 984–990 (2007).
219. Ickert, S. *et al.* Comparison of the fragmentation behavior of DNA and LNA single strands and duplexes. *J. Mass Spectrom.* **54**, 402–411 (2019).
220. Xu, Z., Shaw, J. B. & Brodbelt, J. S. Comparison of MS/MS methods for characterization of DNA/cisplatin adducts. *J. Am. Soc. Mass Spectrom.* **24**, 265–273 (2013).
221. Syka, J. E. P., Coon, J. J., Schroeder, M. J., Shabanowitz, J. & Hunt, D. F. Peptide and protein sequence analysis by electron transfer dissociation mass spectrometry. *Proc. Natl. Acad. Sci. U. S. A.* **101**, 9528–9533 (2004).
222. Lermyte, F. *et al.* ETD allows for native surface mapping of a 150 kDa noncovalent complex on a commercial Q-TWIMS-TOF instrument. *J. Am. Soc. Mass Spectrom.* **25**, 343–350 (2014).
223. Lermyte, F. & Sobott, F. Electron transfer dissociation provides higher-order structural information of native and partially unfolded. *Proteomics* **15**, 2813–2822 (2015).
224. Smith, S. I. & Brodbelt, J. S. Electron transfer dissociation of oligonucleotide cations. *Int J Mass Spectrom.* **283**, 85–93 (2009).
225. Cekan, P., Jonsson, E. Ö. & Sigurdsson, S. T. Folding of the cocaine aptamer studied by EPR and fluorescence spectroscopies using the bifunctional spectroscopic probe Ç. *Nucleic Acids Res.* **37**, 3990–3995 (2009).
226. Wu, J. & McLuckey, S. A. Gas-phase fragmentation of oligonucleotide ions. *Int. J. Mass Spectrom.* **237**, 197–241 (2004).
227. Gates, K. S. An Overview of Chemical Processes That Damage Cellular DNA: Spontaneous Hydrolysis, Alkylation, and Reactions with Radicals. *Chem. Res. Toxicol.* **22**, 1747–1760 (2009).
228. Neves, M. A. D., Reinstein, O. & Johnson, P. E. Defining a stem length-dependent binding mechanism for the cocaine-binding aptamer. A combined NMR and calorimetry study. *Biochemistry* **49**, 8478–8487 (2010).
229. Tikhomirova, A., Beletskaya, I. V & Chalikian, T. V. Stability of DNA duplexes containing GG, CC, AA, and TT mismatches. *Biochemistry* **45**, 10563–10571 (2006).

230. Peyret, N., Seneviratne, P. A., Allawi, H. T. & SantaLucia, J. Nearest-neighbor thermodynamics and NMR of DNA Sequences with internal A-A, C-C, G-G, and T-T mismatches. *Biochemistry* **38**, 3468–3477 (1999).
231. Hari, Y., Leumann, C. J. & Schürch, S. What hinders electron transfer dissociation (ETD) of DNA cations? *J. Am. Soc. Mass Spectrom.* **28**, 2677–2685 (2017).
232. Luger, K., Mäder, A. W., Richmond, R. K., Sargent, D. F. & Richmond, T. J. Crystal structure of the nucleosome core particle at 2.8 Å resolution. *Nature* **389**, 251–260 (1997).
233. Luger, K., Dechassa, M. L. & Tremethick, D. J. New insights into nucleosome and chromatin structure: An ordered state or a disordered affair? *Nat. Rev. Mol. Cell Biol.* **13**, 436–447 (2012).
234. Yadav, T., Quivy, J.-P. & Almouzni, G. Chromatin plasticity: A versatile landscape that underlies cell fate and identity. *Science* **361**, 1332–1336 (2018).
235. Borg, M., Jiang, D. & Berger, F. Histone variants take center stage in shaping the epigenome. *Curr. Opin. Plant Biol.* **61**, 101991 (2021).
236. Segal, E. *et al.* A genomic code for nucleosome positioning. *Nature* **442**, 772–778 (2006).
237. Li, G. & Widom, J. Nucleosomes facilitate their own invasion. *Nat. Struct. Mol. Biol.* **11**, 763–769 (2004).
238. Buning, R. & van Noort, J. Single-pair FRET experiments on nucleosome conformational dynamics. *Biochimie* **92**, 1729–1740 (2010).
239. Chen, Y. *et al.* Revealing transient structures of nucleosomes as DNA unwinds. *Nucleic Acids Res.* **42**, 8767–8776 (2014).
240. Bilokapic, S., Strauss, M. & Halic, M. Histone octamer rearranges to adapt to DNA unwrapping. *Nat. Struct. Mol. Biol.* **25**, 101–108 (2018).
241. Bilokapic, S., Strauss, M. & Halic, M. Structural rearrangements of the histone octamer translocate DNA. *Nat. Commun.* **9**, 1330 (2018).
242. Saikusa, K. *et al.* Gas-phase structure of the histone multimers characterized by ion mobility mass spectrometry and molecular dynamics simulation. *Anal. Chem.* **85**, 4165–4171 (2013).
243. Saikusa, K. *et al.* Structural diversity of nucleosomes characterized by native mass spectrometry. *Anal. Chem.* **90**, 8217–8226 (2018).
244. Mayanagi, K. *et al.* Structural visualization of key steps in nucleosome reorganization by human FACT. *Sci. Rep.* **9**, 10183 (2019).
245. Hake, S. B. & Allis, C. D. Histone H3 variants and their potential role in indexing mammalian genomes: The “H3 barcode hypothesis”. *Proc. Natl. Acad. Sci.* **103**, 6428–6435 (2006).
246. Sekulic, N. & Black, B. E. Molecular underpinnings of centromere identity and maintenance. *Trends Biochem. Sci.* **37**, 220–229 (2012).
247. Ali-Ahmad, A. & Sekulić, N. CENP-A nucleosome - a chromatin-embedded pedestal for the centromere: lessons learned from structural biology. *Essays Biochem.* **64**, 205–221 (2020).
248. Lowary, P. T. & Widom, J. New DNA sequence rules for high affinity binding to histone octamer and sequence-directed nucleosome positioning. *J. Mol. Biol.* **276**, 19–42 (1998).
249. Harp, J. M. *et al.* X-ray diffraction analysis of crystals containing twofold symmetric nucleosome core particles. *Acta Crystallogr. Sect. D* **52**, 283–288 (1996).
250. Ali-Ahmad, A., Bilokapić, S., Schäfer, I. B., Halić, M. & Sekulić, N. CENP-C unwraps the human CENP-A nucleosome through the H2A C-terminal tail. *EMBO Rep.* **20**, e48913 (2019).
251. Dyer, P. N. *et al.* Reconstitution of nucleosome core particles from recombinant histones and DNA. in *Chromatin and Chromatin Remodeling Enzymes, Part A* vol. 375 23–44 (Academic Press, 2003).
252. Bush, M. F. *et al.* Collision cross sections of proteins and their complexes: A calibration framework and database for gas-phase structural biology. *Anal. Chem.* **82**, 9557–9565 (2010).
253. Marklund, E. G., Degiacomi, M. T., Robinson, C. V., Baldwin, A. J. & Benesch, J. L. P. Collision cross sections for structural proteomics. *Structure* **23**, 791–799 (2015).
254. MathWorks. findpeaks function. <https://nl.mathworks.com/help/signal/ref/findpeaks.html>.
255. Konermann, L. & Douglas, D. J. Unfolding of proteins monitored by electrospray ionization mass spectrometry: A comparison of positive and negative ion modes. *J. Am. Soc. Mass Spectrom.* **9**, 1248–1254 (1998).

256. Bilokapic, S., Strauss, M. & Halic, M. Cryo-EM of nucleosome core particle interactions in trans. *Sci. Rep.* **8**, 7046 (2018).
257. Von Helden, G., Hsu, M. T., Gotts, N. & Bowers, M. T. Carbon cluster cations with up to 84 atoms: Structures, formation mechanism, and reactivity. *J. Phys. Chem.* **97**, 8182–8192 (1993).
258. Wyttenbach, T., Von Helden, G., Batka, J. J., Carlat, D. & Bowers, M. T. Effect of the long-range potential on ion mobility measurements. *J. Am. Soc. Mass Spectrom.* **8**, 275–282 (1997).
259. D'Atri, V., Porrini, M., Rosu, F. & Gabelica, V. Linking molecular models with ion mobility experiments. Illustration with a rigid nucleic acid structure. *J. Mass Spectrom.* **50**, 711–726 (2015).
260. Bleiholder, C., Wyttenbach, T. & Bowers, M. T. A novel projection approximation algorithm for the fast and accurate computation of molecular collision cross sections (I). *Method. Int. J. Mass Spectrom.* **308**, 1–10 (2011).
261. Sekulic, N., Bassett, E. A., Rogers, D. J. & Black, B. E. The structure of (CENP-A-H4)<sub>2</sub> reveals physical features that mark centromeres. *Nature* **467**, 347–351 (2010).
262. Falk, S. J. *et al.* CENP-C reshapes and stabilizes CENP-A nucleosomes at the centromere. *Chromosomes* **348**, 699–704 (2015).
263. Panchenko, T. *et al.* Replacement of histone H3 with CENP-A directs global nucleosome array condensation and loosening of nucleosome superhelical termini. *Proc. Natl. Acad. Sci. U. S. A.* **108**, 16588–16593 (2011).
264. Tachiwana, H. *et al.* Crystal structure of the human centromeric nucleosome containing CENP-A. *Nature* **476**, 232–235 (2011).
265. Vasudevan, D., Chua, E. Y. D. & Davey, C. A. Crystal structures of nucleosome core particles containing the '601' strong positioning sequence. *J. Mol. Biol.* **403**, 1–10 (2010).
266. Zhou, B. R. *et al.* Atomic resolution cryo-EM structure of a native-like CENP-A nucleosome aided by an antibody fragment. *Nat. Commun.* **10**, 2301 (2019).
267. Boopathi, R. *et al.* Phase-plate cryo-EM structure of the Widom 601 CENP-A nucleosome core particle reveals differential flexibility of the DNA ends. *Nucleic Acids Res.* **48**, 5735–5748 (2020).
268. Black, B. E. *et al.* Structural determinants for generating centromeric chromatin. *Nature* **430**, 578–582 (2004).
269. Black, B. E., Brock, M. A., Bédard, S., Woods, V. L. & Cleveland, D. W. An epigenetic mark generated by the incorporation of CENP-A into centromeric nucleosomes. *Proc. Natl. Acad. Sci. U. S. A.* **104**, 5008–5013 (2007).
270. Sever, A. I. M., Yin, V. & Konermann, L. Interrogating the quaternary structure of noncanonical hemoglobin complexes by electrospray mass spectrometry and collision-induced dissociation. *J. Am. Soc. Mass Spectrom.* **32**, 270–280 (2021).
271. Ngo, T. T. M. & Ha, T. Nucleosomes undergo slow spontaneous gaping. *Nucleic Acids Res.* **43**, 3964–3971 (2015).
272. Bosch-Orea, C., Farré, M. & Barceló, D. Biosensors and bioassays for environmental monitoring. *Compr. Anal. Chem.* **77**, 337–383 (2017).
273. Moro, G. *et al.* Covalent immobilization of delipidated human serum albumin on poly(pyrrole-2-carboxylic) acid film for the impedimetric detection of perfluorooctanoic acid. *Bioelectrochemistry* **134**, 107540 (2020).
274. Liu, B., Zhuang, J. & Wei, G. Recent advance in the design of colorimetric sensors for environmental monitoring. *Environ. Sci. Nano* **7**, 2195–2213 (2020).
275. Liu, H., Ge, J., Ma, E. & Yang, L. Advanced biomaterials for biosensor and theranostics. in *Biomaterials in Translational Medicine: A Biomaterials Approach* 213–255 (2019).
276. Patil, S. B., Annese, V. F. & Cumming, D. R. S. Commercial aspects of biosensors for diagnostics and environmental monitoring. in *Advances in Nanosensors for Biological and Environmental Analysis* 133–142 (Elsevier Inc., 2019). doi:10.1016/b978-0-12-817456-2.00008-5.
277. Ateia, M., Maroli, A., Tharayil, N. & Karanfil, T. The overlooked short- and ultrashort-chain poly- and perfluorinated substances: A review. *Chemosphere* **220**, 866–882 (2019).
278. Feng, H., Ruan, Y., Zhang, K. & Lam, P. K. S. Current analytical methodologies and gaps for per- and polyfluoroalkyl substances determination in the marine environment. *TrAC - Trends Anal.*

- Chem.* **121**, 115372 (2019).
279. Wang, Y. *et al.* A review of sources, multimedia distribution and health risks of novel fluorinated alternatives. *Ecotoxicol. Environ. Saf.* **182**, 109402 (2019).
280. Nakayama, S. F. *et al.* Worldwide trends in tracing poly- and perfluoroalkyl substances (PFAS) in the environment. *TrAC - Trends Anal. Chem.* **121**, 115410 (2019).
281. Liu, S., Yang, R., Yin, N., Wang, Y. L. & Faiola, F. Environmental and human relevant PFOS and PFOA doses alter human mesenchymal stem cell self-renewal, adipogenesis and osteogenesis. *Ecotoxicol. Environ. Saf.* **169**, 564–572 (2019).
282. Rovira, J. *et al.* Prenatal exposure to PFOS and PFOA in a pregnant women cohort of Catalonia, Spain. *Environ. Res.* **175**, 384–392 (2019).
283. Sánchez-Soberón, F. *et al.* Multi-box mass balance model of PFOA and PFOS in different regions of San Francisco Bay. *Chemosphere* **252**, 126454 (2020).
284. Barceló, D. & Ruan, T. Challenges and perspectives on the analysis of traditional perfluoroalkyl substances and emerging alternatives. *TrAC - Trends Anal. Chem.* **121**, 2–3 (2019).
285. Wang, Z., Cousins, I. T., Scheringer, M., Buck, R. C. & Hungerbühler, K. Global emission inventories for C4-C14 perfluoroalkyl carboxylic acid (PFCA) homologues from 1951 to 2030, Part I: Production and emissions from quantifiable sources. *Environ. Int.* **70**, 62–75 (2014).
286. Glasscott, M. W., Vannoy, K. J., Kazemi, R., Verber, M. D. & Dick, J. E.  $\mu$ -MIP: Molecularly imprinted polymer-modified microelectrodes for the ultrasensitive quantification of GenX (HFPO-DA) in river water. *Environ. Sci. Technol. Lett.* **7**, 489–495 (2020).
287. Karimian, N. *et al.* Electrochemosensor for trace analysis of perfluorooctanesulfonate in water based on a molecularly Imprinted poly(o-phenylenediamine) polymer. *ACS Sensors* **3**, 1291–1298 (2018).
288. Cheng, Z., Du, L., Zhu, P., Chen, Q. & Tan, K. An erythrosin B-based “turn on” fluorescent sensor for detecting perfluorooctane sulfonate and perfluorooctanoic acid in environmental water samples. *Spectrochim. Acta - Part A Mol. Biomol. Spectrosc.* **201**, 281–287 (2018).
289. Li, X., Wang, X., Fang, T., Zhang, L. & Gong, J. Disposable photoelectrochemical sensing strip for highly sensitive determination of perfluorooctane sulfonyl fluoride on functionalized screen-printed carbon electrode. *Talanta* **181**, 147–153 (2018).
290. Cennamo, N. *et al.* A high sensitivity biosensor to detect the presence of perfluorinated compounds in environment. *Talanta* **178**, 955–961 (2018).
291. Liu, X., Fang, M., Xu, F. & Chen, D. Characterization of the binding of per- and poly-fluorinated substances to proteins: A methodological review. *TrAC - Trends Anal. Chem.* **116**, 177–185 (2019).
292. Wang, Y., Zhang, H., Kang, Y., Fei, Z. & Cao, J. The interaction of perfluorooctane sulfonate with hemoglobin: Influence on protein stability. *Chem. Biol. Interact.* **254**, 1–10 (2016).
293. Liu, Y., Cao, Z., Zong, W. & Liu, R. Interaction rule and mechanism of perfluoroalkyl sulfonates containing different carbon chains with human serum albumin. *RSC Adv.* **7**, 24781–24788 (2017).
294. Chi, Q., Li, Z., Huang, J., Ma, J. & Wang, X. Interactions of perfluorooctanoic acid and perfluorooctanesulfonic acid with serum albumins by native mass spectrometry, fluorescence and molecular docking. *Chemosphere* **198**, 442–449 (2018).
295. Forsthuber, M. *et al.* Albumin is the major carrier protein for PFOS, PFOA, PFHxS, PFNA and PFDA in human plasma. *Environ. Int.* **137**, 105324 (2020).
296. Han, X., Snow, T. A., Kemper, R. A. & Jepson, G. W. Binding of perfluorooctanoic acid to rat and human plasma proteins. *Chem. Res. Toxicol.* **16**, 775–781 (2003).
297. Wu, L. L., Gao, H. W., Gao, N. Y., Chen, F. F. & Chen, L. Interaction of perfluorooctanoic acid with human serum albumin. *BMC Struct. Biol.* **9**, 5–11 (2009).
298. Bischel, H. N., MacManus-Spencer, L. A. & Luthy, R. G. Noncovalent interactions of long-chain perfluoroalkyl acids with serum albumin. *Environ. Sci. Technol.* **44**, 5263–5269 (2010).
299. Haldorai, Y. *et al.* Direct electrochemistry of cytochrome c immobilized on titanium nitride/multi-walled carbon nanotube composite for amperometric nitrite biosensor. *Biosens. Bioelectron.* **79**, 543–552 (2016).
300. Aghamiri, Z. S., Mohsennia, M. & Rafiee-Pour, H. A. Immobilization of cytochrome c and its

- application as electrochemical biosensors. *Talanta* **176**, 195–207 (2018).
301. Murphy, M., Theyagarajan, K., Ganesan, P., Senthilkumar, S. & Thenmozhi, K. Electrochemical biosensor for the detection of hydrogen peroxide using cytochrome c covalently immobilized on carboxyl functionalized ionic liquid/multiwalled carbon nanotube hybrid. *Appl. Surf. Sci.* **492**, 718–725 (2019).
302. Burmester, T., Weich, B., Reinhardt, S. & Hankeln, T. A vertebrate globin expressed in the brain. *Nature* **407**, 520–523 (2000).
303. Ascenzi, P. *et al.* Neuroglobin: From structure to function in health and disease. *Mol. Aspects Med.* **52**, 1–48 (2016).
304. Chen, R. F. Removal of fatty acids from serum albumin by charcoal treatment. *J. Biol. Chem.* **242**, 173–181 (1967).
305. Dewilde, S. *et al.* Expression, purification, and crystallization of neuro- and cytoglobin. *Methods Enzymol.* **436**, 341–357 (2008).
306. Sobott, F., Hernández, H., McCammon, M. G., Tito, M. A. & Robinson, C. V. A tandem mass spectrometer for improved transmission and analysis of large macromolecular assemblies. *Anal. Chem.* **74**, 1402–1407 (2002).
307. Göth, M., Badock, V., Weiske, J., Pagel, K. & Kuropka, B. Critical evaluation of native electrospray ionization mass spectrometry for fragment-based screening. *ChemMedChem* **12**, 1201–1211 (2017).
308. Polasky, D. A., Dixit, S. M., Fantin, S. M. & Ruotolo, B. T. CIUSuite 2: Next-generation software for the analysis of gas-phase protein unfolding data. *Anal. Chem.* **91**, 3147–3155 (2019).
309. Dugaiczuk, A., Law, S. W. & Brewer, H. B. Nucleotide sequence and the encoded amino acids of human serum albumin mRNA. *Proc. Natl. Acad. Sci. U. S. A.* **79**, 71–75 (1982).
310. Curry, S., Brick, P. & Franks, N. P. Fatty acid binding to human serum albumin: new insights from crystallographic studies. *Biochim. Biophys. Acta - Mol. Cell Biol. Lipids* **1441**, 131–140 (1999).
311. Curry, S., Mandelkow, H., Brick, P. & Franks, N. Crystal structure of human serum albumin complexed with fatty acid reveals an asymmetric distribution of binding sites. *Nat. Struct. Biol.* **5**, 827–835 (1998).
312. Beesoon, S. & Martin, J. W. Isomer-specific binding affinity of perfluorooctanesulfonate (PFOS) and perfluorooctanoate (PFOA) to serum proteins. *Environ. Sci. Technol.* **49**, 5722–5731 (2015).
313. Eschweiler, J. D., Martini, R. M. & Ruotolo, B. T. Chemical probes and engineered constructs reveal a detailed unfolding mechanism for a solvent-free multidomain protein. *J. Am. Chem. Soc.* **139**, 534–540 (2017).
314. Li, G., DeLaney, K. & Li, L. Molecular basis for chirality-regulated A $\beta$  self-assembly and receptor recognition revealed by ion mobility-mass spectrometry. *Nat. Commun.* **10**, 5038 (2019).
315. Kagan, V. E. *et al.* Cytochrome c/cardiolipin relations in mitochondria: a kiss of death. *Free Radic. Biol. Med.* **46**, 1439–1453 (2009).
316. Rytömaa, M. & Kinnunen, P. K. J. Evidence for two distinct acidic phospholipid-binding sites in cytochrome c. *J. Biol. Chem.* **269**, 1770–1774 (1994).
317. Rytömaa, M. & Kinnunen, P. K. J. Reversibility of the binding of cytochrome c to liposomes. *J. Biol. Chem.* **270**, 3197–3202 (1995).
318. Pinheiro, T. J. T., Elöve, G. A., Watts, A. & Roder, H. Structural and kinetic description of cytochrome c unfolding induced by the interaction with lipid vesicles. *Biochemistry* **36**, 13122–13132 (1997).
319. Kawai, C. *et al.* pH-dependent interaction of cytochrome c with mitochondrial mimetic membranes: The role of an array of positively charged amino acids. *J. Biol. Chem.* **280**, 34709–34717 (2005).
320. Burns, D. C., Ellis, D. A., Li, H., Mcmurdo, C. J. & Webster, E. Experimental pKa determination for perfluorooctanoic acid (PFOA) and the potential impact of pKa concentration dependence on laboratory-measured partitioning phenomena and environmental modeling. *Environ. Sci. Technol.* **42**, 9283–9288 (2008).
321. Cheng, J., Psillakis, E., Hoffmann, M. R. & Colussi, A. J. Acid dissociation versus molecular

- association of perfluoroalkyl oxoacids: Environmental implications. *J. Phys. Chem. A* **113**, 8152–8156 (2009).
322. Vahidi, S., Stocks, B. B. & Konermann, L. Partially disordered proteins studied by ion mobility-mass spectrometry: Implications for the preservation of solution phase structure in the gas phase. *Anal. Chem.* **85**, 10471–10478 (2013).
323. Roncancio, D. *et al.* A label-free aptamer-fluorophore assembly for rapid and specific detection of cocaine in biofluids. *Anal. Chem.* **86**, 11100–11106 (2014).
324. Neves, M. A. D., Blaszykowski, C., Bokhari, S. & Thompson, M. Ultra-high frequency piezoelectric aptasensor for the label-free detection of cocaine. *Biosens. Bioelectron.* **72**, 383–392 (2015).
325. Smith, J. E. *et al.* Colorimetric detection with aptamer-gold nanoparticle conjugates coupled to an android-based color analysis application for use in the field. *Talanta* **121**, 247–255 (2014).
326. Marmur, J. & Doty, P. Determination of the base composition of deoxyribonucleic acid from its thermal denaturation temperature. *J. Mol. Biol.* **5**, 109–118 (1962).
327. Draper, D. E. & Misra, V. K. On the role of magnesium ions in RNA stability. *Biopolymers* **48**, 113–135 (1998).
328. Lipfert, J., Doniach, S., Das, R. & Herschlag, D. Understanding nucleic acid–ion interactions. *Annu. Rev. Biochem.* **83**, 813–841 (2014).
329. Testa, L., Brocca, S. & Grandori, R. Charge-surface correlation in electrospray ionization of folded and unfolded proteins. *Anal. Chem.* **83**, 6459–6463 (2011).
330. Beveridge, R. *et al.* A mass-spectrometry-based framework to define the extent of disorder in proteins. *Anal. Chem.* **86**, 10979–10991 (2014).
331. Garabedian, A. *et al.* Structures of the kinetically trapped i-motif DNA intermediates. *Phys. Chem. Chem. Phys.* **18**, 26691–26702 (2016).
332. Várnai, P. & Zakrzewska, K. DNA and its counterions: A molecular dynamics study. *Nucleic Acids Res.* **32**, 4269–4280 (2004).
333. Sharawy, M. & Consta, S. How do non-covalent complexes dissociate in droplets? A case study of the desolvation of dsDNA from a charged aqueous nanodrop. *Phys. Chem. Chem. Phys.* **17**, 25550–25562 (2015).
334. Owczarzy, R., Moreira, B. G., You, Y., Behlke, M. A. & Wälder, J. A. Predicting stability of DNA duplexes in solutions containing magnesium and monovalent cations. *Biochemistry* **47**, 5336–5353 (2008).
335. Rosu, F., Pirotte, S., Pauw, E. De & Gabelica, V. Positive and negative ion mode ESI-MS and MS/MS for studying drug-DNA complexes. *Int. J. Mass Spectrom.* **253**, 156–171 (2006).
336. Sannes-Lowery, K. A., Mack, D. P., Hu, P., Mei, H. Y. & Loo, J. A. Positive ion electrospray ionization mass spectrometry of oligonucleotides. *J. Am. Soc. Mass Spectrom.* **8**, 90–95 (1997).
337. Strauch, S. *et al.* Biowaiver monographs for immediate-release solid oral dosage forms: Quinine sulfate. *J. Pharm. Sci.* **101**, 499–508 (2012).
338. Loo, J. A. Electrospray ionization mass spectrometry: A technology for studying noncovalent macromolecular complexes. *Int. J. Mass Spectrom.* **200**, 175–186 (2000).
339. Baird, G. S. Where are all the aptamers? *Am. J. Clin. Pathol.* **134**, 529–531 (2010).
340. World Health Organization. *Global action plan on antimicrobial resistance*. World Health Organization (2015) doi:10.1128/microbe.10.354.1.
341. O'Neill, J. *Tackling drug-resistant infections globally: Final report and recommendations*. (2016).
342. Song, K. M., Jeong, E., Jeon, W., Cho, M. & Ban, C. Aptasensor for ampicillin using gold nanoparticle based dual fluorescence-colorimetric methods. *Anal. Bioanal. Chem.* **402**, 2153–2161 (2012).
343. Gülbakan, B. Oligonucleotide aptamers: emerging affinity probes for bioanalytical mass spectrometry and biomarker discovery. *Anal. Methods* **7**, 7416–7430 (2015).
344. Sakamoto, T., Ennifar, E. & Nakamura, Y. Thermodynamic study of aptamers binding to their target proteins. *Biochimie* **145**, 91–97 (2018).
345. Vogel, M. & Suess, B. Label-free determination of the dissociation constant of small molecule-aptamer interaction by isothermal titration calorimetry. in *Nucleic Acid Aptamers: Selection, Characterization, and Application* 113–125 (2016). doi:10.1007/978-1-4939-3197-2.

346. Cai, S. *et al.* Investigations on the interface of nucleic acid aptamers and binding targets. *Analyst* **143**, 5317–5338 (2018).
347. Kouchakdjian, M., Li, B. F. L., Swann, P. F. & Patel, D. J. Pyrimidine · pyrimidine base-pair mismatches in DNA. A nuclear magnetic resonance study of T · T pairing at neutral pH and C · C pairing at acidic pH in dodecanucleotide duplexes. *J. Mol. Biol.* **202**, 139–155 (1988).
348. Schultze, P., Macaya, R. F. & Feigon, J. Three-dimensional solution structure of the thrombin-binding DNA aptamer d(GGTGGTGTGGTGG). *J. Mol. Biol.* **235**, 1532–1547 (1994).
349. Dieckmann, T., Suzuki, E., Nakamura, G. K. & Feigon, J. Solution structure of an ATP-binding RNA aptamer reveals a novel fold. *RNA* **2**, 628–640 (1986).
350. Neves, M. A. D., Reinstein, O., Saad, M. & Johnson, P. E. Defining the secondary structural requirements of a cocaine-binding aptamer by a thermodynamic and mutation study. *Biophys. Chem.* **153**, 9–16 (2010).
351. Bishop, G. R. *et al.* Energetic basis of molecular recognition in a DNA aptamer. *Biophys. Chem.* **126**, 165–175 (2007).
352. Storhoff, J. J., Elghanian, R., Mucic, R. C., Mirkin, C. A. & Letsinger, R. L. One-pot colorimetric differentiation of polynucleotides with single base imperfections using gold nanoparticle probes. *J. Am. Chem. Soc.* **120**, 1959–1964 (1998).
353. Haiss, W., Thanh, N. T. K., Aveyard, J. & Fernig, D. G. Determination of size and concentration of gold nanoparticles from UV–Vis spectra. *Anal. Chem.* **79**, 4215–4221 (2007).
354. de Jong, M. *et al.* Levamisole: A common adulterant in cocaine street samples hindering electrochemical detection of cocaine. *Anal. Chem.* **90**, 5290–5297 (2018).
355. Carnerero, J. M., Jimenez-Ruiz, A., Castillo, P. M. & Prado-Gotor, R. Covalent and non-covalent DNA–gold-nanoparticle interactions: New avenues of research. *ChemPhysChem* **18**, 17–33 (2017).
356. Zhang, X., Servos, M. R. & Liu, J. Surface science of DNA adsorption onto citrate-capped gold nanoparticles. *Langmuir* **28**, 3896–3902 (2012).
357. Gopinath, S. C. B., Lakshmi Priya, T. & Awazu, K. Colorimetric detection of controlled assembly and disassembly of aptamers on unmodified gold nanoparticles. *Biosens. Bioelectron.* **51**, 115–123 (2014).
358. Zhao, W., Brook, M. A. & Li, Y. Design of gold nanoparticle-based colorimetric biosensing assays. *ChemBioChem* **9**, 2363–2371 (2008).
359. IARC. IARC monographs on the evaluation of carcinogenic risk of chemicals to humans. *World Health Organization, Geneva* vol. 71 (1999).
360. Claridge, T. D. W. *High-resolution NMR techniques in organic chemistry*. (Elsevier, 2016).
361. Fritzing, B. *et al.* In situ observation of rapid ligand exchange in colloidal nanocrystal suspensions using transfer NOE nuclear magnetic resonance spectroscopy. *J. Am. Chem. Soc.* **131**, 3024–3032 (2009).
362. Bain, A. D. Chemical exchange in NMR. *Prog. Nucl. Magn. Reson. Spectrosc.* **43**, 63–103 (2003).
363. Mirau, P. A. *et al.* Structured DNA aptamer interactions with gold nanoparticles. *Langmuir* **34**, 2139–2146 (2018).
364. Robertson, S. A., Harada, K., Frankel, A. D. & Wemmer, D. E. Structure determination and binding kinetics of a DNA aptamer - argininamide complex. *Biochemistry* **39**, 946–954 (2000).
365. Neves, M. A. D., Slavkovic, S., Churcher, Z. R. & Johnson, P. E. Salt-mediated two-site ligand binding by the cocaine-binding aptamer. *Nucleic Acids Res.* **45**, 1041–1048 (2017).
366. Lin, C. H. & Patel, D. J. Encapsulating an amino acid in a DNA fold. *Nat. Struct. Biol.* **3**, 1046–1050 (1996).
367. Gourishankar, A., Shukla, S., Ganesh, K. N. & Sastry, M. Isothermal titration calorimetry studies on the binding of DNA bases and PNA base monomers to gold nanoparticles. *J. Am. Chem. Soc.* **126**, 13186–13187 (2004).
368. Joshi, H., Shirude, P. S., Bansal, V., Ganesh, K. N. & Sastry, M. Isothermal titration calorimetry studies on the binding of amino acids to gold nanoparticles. *J. Phys. Chem. B* **108**, 11535–11540 (2004).
369. Potty, A. S. R. *et al.* Biophysical characterization of DNA aptamer interactions with vascular

- endothelial growth factor. *Biopolymers* **91**, 145–156 (2009).
370. Álvarez-Martos, I., Campos, R. & Ferapontova, E. E. Surface state of the dopamine RNA aptamer affects specific recognition and binding of dopamine by the aptamer-modified electrodes. *Analyst* **140**, 4089–4096 (2015).
371. Daniel, C., Roupioz, Y., Gasparutto, D., Livache, T. & Buhot, A. Solution-phase vs surface-phase aptamer-protein affinity from a label-free kinetic biosensor. *PLoS One* **8**, e75419 (2013).
372. Gosai, A., Hau Yeah, B. S., Nilsen-Hamilton, M. & Shrotriya, P. Label free thrombin detection in presence of high concentration of albumin using an aptamer-functionalized nanoporous membrane. *Biosens. Bioelectron.* **126**, 88–95 (2019).
373. Zhai, L. *et al.* An RNA aptamer-based microcantilever sensor to detect the inflammatory marker, mouse lipocalin-2. *Anal. Chem.* **84**, 8763–8770 (2012).
374. Daprà, J., Lauridsen, L. H., Nielsen, A. T. & Rozlosnik, N. Comparative study on aptamers as recognition elements for antibiotics in a label-free all-polymer biosensor. *Biosens. Bioelectron.* **43**, 315–320 (2013).
375. Rosati, G., Daprà, J., Cherré, S. & Rozlosnik, N. Performance improvement by layout designs of conductive polymer microelectrode based impedimetric biosensors. *Electroanalysis* **26**, 1400–1408 (2014).
376. Wang, H. *et al.* Target-aptamer binding triggered quadratic recycling amplification for highly specific and ultrasensitive detection of antibiotics at the attomole level. *Chem. Commun.* **51**, 8377–8380 (2015).
377. Wang, X., Dong, S., Gai, P., Duan, R. & Li, F. Highly sensitive homogeneous electrochemical aptasensor for antibiotic residues detection based on dual recycling amplification strategy. *Biosens. Bioelectron.* **82**, 49–54 (2016).
378. Yang, Z. *et al.* Second generation of signaling-probe displacement electrochemical aptasensor for detection of picomolar ampicillin and sulfadimethoxine. *Sensors Actuators, B Chem.* **253**, 1129–1136 (2017).
379. Luo, Z. *et al.* Fluorescent aptasensor for antibiotic detection using magnetic bead composites coated with gold nanoparticles and a nicking enzyme. *Anal. Chim. Acta* **984**, 177–184 (2017).
380. Yu, Z. gang, Sutlief, A. L. & Lai, R. Y. Towards the development of a sensitive and selective electrochemical aptamer-based ampicillin sensor. *Sensors Actuators, B Chem.* **258**, 722–729 (2018).
381. Yu, Z. gang & Lai, R. Y. A reagentless and reusable electrochemical aptamer-based sensor for rapid detection of ampicillin in complex samples. *Talanta* **176**, 619–624 (2018).
382. Blidar, A., Feier, B., Tertis, M., Galatus, R. & Cristea, C. Electrochemical surface plasmon resonance (EC-SPR) aptasensor for ampicillin detection. *Anal. Bioanal. Chem.* **411**, 1053–1065 (2019).
383. Liu, X. *et al.* Novel nanoarchitecture of Co-MOF-on-TPN-COF hybrid: Ultralowly sensitive bioplatfrom of electrochemical aptasensor toward ampicillin. *Biosens. Bioelectron.* **123**, 59–68 (2019).
384. Wang, T. *et al.* Electrochemical aptasensor for ampicillin detection based on the protective effect of aptamer-antibiotic conjugate towards DpnII and Exo III digestion. *Talanta* **197**, 42–48 (2019).
385. Li, J. *et al.* Novel sensing platform based on gold nanoparticle-aptamer and Fe-metal-organic framework for multiple antibiotic detection and signal amplification. *Environ. Int.* **125**, 135–141 (2019).
386. Wang, M. *et al.* Covalent organic framework-based electrochemical aptasensors for the ultrasensitive detection of antibiotics. *Biosens. Bioelectron.* **132**, 8–16 (2019).
387. Taghdisi, S. M. *et al.* An electrochemical sensing platform based on ladder-shaped DNA structure and label-free aptamer for ultrasensitive detection of ampicillin. *Biosens. Bioelectron.* **133**, 230–235 (2019).
388. Shayesteh, O. H. & Ghavami, R. Two colorimetric ampicillin sensing schemes based on the interaction of aptamers with gold nanoparticles. *Microchim. Acta* **186**, (2019).
389. Zhang, R. *et al.* Exonuclease III-powered DNA walking machine for label-free and ultrasensitive electrochemical sensing of antibiotic. *Sensors Actuators, B Chem.* **297**, 126771 (2019).

390. Youn, H. *et al.* Aptasensor for multiplex detection of antibiotics based on FRET strategy combined with aptamer/graphene oxide complex. *Sci. Rep.* **9**, 7659 (2019).
391. Han, K., Liu, T., Wang, Y. & Miao, P. Electrochemical aptasensors for detection of small molecules, macromolecules, and cells. *Rev. Anal. Chem.* **35**, 201–211 (2016).
392. Prante, M., Segal, E., Scheper, T., Bahnemann, J. & Walter, J. Aptasensors for point-of-care detection of small molecules. *Biosensors* **10**, 108 (2020).
393. Nasiri Khonsari, Y. & Sun, S. Recent trends in electrochemiluminescence aptasensors and their applications. *Chem. Commun.* **53**, 9042–9054 (2017).
394. Babamiri, B., Bahari, D. & Salimi, A. Highly sensitive bioaffinity electrochemiluminescence sensors: Recent advances and future directions. *Biosens. Bioelectron.* **142**, 111530 (2019).
395. Ma, C., Cao, Y., Gou, X. & Zhu, J. Recent progress in electrochemiluminescence sensing and imaging. *Anal. Chem.* **92**, 431–454 (2020).
396. Forster, R. J., Bertocello, P. & Keyes, T. E. Electrogenerated chemiluminescence. *Annu. Rev. Anal. Chem.* **2**, 359–385 (2009).
397. Zhao, W.-W., Xu, J.-J. & Chen, H.-Y. Photoelectrochemical aptasensing. *TrAC Trends Anal. Chem.* **82**, 307–315 (2016).
398. Shi, H.-W., Wu, M.-S., Du, Y., Xu, J.-J. & Chen, H.-Y. Electrochemiluminescence aptasensor based on bipolar electrode for detection of adenosine in cancer cells. *Biosens. Bioelectron.* **55**, 459–463 (2014).
399. Zhang, H. *et al.* Signal-on electrochemiluminescence aptasensor for bisphenol A based on hybridization chain reaction and electrically heated electrode. *Biosens. Bioelectron.* **129**, 36–41 (2019).
400. Yu, Y., Cao, Q., Zhou, M. & Cui, H. A novel homogeneous label-free aptasensor for 2,4,6-trinitrotoluene detection based on an assembly strategy of electrochemiluminescent graphene oxide with gold nanoparticles and aptamer. *Biosens. Bioelectron.* **43**, 137–142 (2013).
401. Cheng, S. *et al.* Highly sensitive electrochemiluminescence aptasensor based on dual-signal amplification strategy for kanamycin detection. *Sci. Total Environ.* **737**, 139785 (2020).
402. Cheng, S. *et al.* Ultrasensitive electrochemiluminescence aptasensor for kanamycin detection based on silver nanoparticle-catalyzed chemiluminescent reaction between luminol and hydrogen peroxide. *Sensors Actuators B Chem.* **304**, 127367 (2020).
403. Liu, X. *et al.* An electrochemiluminescence aptasensor for analysis of bisphenol A based on carbon nanodots composite as co-reaction of Ru(bpy)<sub>3</sub><sup>2+</sup> nanosheets. *Electrochim. Acta* **319**, 849–858 (2019).
404. Wei, M. *et al.* A simple and sensitive electrochemiluminescence aptasensor for determination of ochratoxin A based on a nicking endonuclease-powered DNA walking machine. *Food Chem.* **282**, 141–146 (2019).
405. Luo, L. *et al.* Monitoring zearalenone in corn flour utilizing novel self-enhanced electrochemiluminescence aptasensor based on NGQDs-NH<sub>2</sub>-Ru@SiO<sub>2</sub> luminophore. *Food Chem.* **292**, 98–105 (2019).
406. Xiong, H. *et al.* Construction of an ultrasensitive electrochemiluminescent aptasensor for ractopamine detection. *Analyst* **144**, 2550–2555 (2019).
407. Feng, X. *et al.* A novel “dual-potential” electrochemiluminescence aptasensor array using CdS quantum dots and luminol-gold nanoparticles as labels for simultaneous detection of malachite green and chloramphenicol. *Biosens. Bioelectron.* **74**, 587–593 (2015).
408. McKeague, M. *et al.* Comprehensive Analytical Comparison of Strategies Used for Small Molecule Aptamer Evaluation. *Anal. Chem.* **87**, 8608–8612 (2015).
409. Liang, S. & Connell, G. J. An electrochemiluminescent aptamer switch for a high-throughput assay of an RNA editing reaction. *RNA* **15**, 1929–1938 (2009).
410. Liang, S. & Connell, G. J. Identification of specific inhibitors for a trypanosomatid RNA editing reaction. *RNA* **16**, 2435–2441 (2010).
411. Duo, J. *et al.* Slow Off-Rate Modified Aptamer (SOMAmer) as a novel reagent in immunoassay development for accurate soluble glypican-3 quantification in clinical samples. *Anal. Chem.* **90**,

- 5162–5170 (2018).
412. Lin, K. & Wu, G. Chapter 19 Isothermal Titration Calorimetry Assays to Measure Binding Affinities In Vitro. in *The Hippo Pathway. Methods in Molecular Biology* vol. 1893 257–272 (Humana Press, New York, NY, 2019).
413. Chambers, J. R. & Sauer, K. Detection of Cyclic di-GMP Binding Proteins Utilizing a Biotinylated Cyclic di-GMP Pull-Down Assay. in *Methods in Molecular Biology* (ed. Sauer, K.) 317–329 (Springer New York, 2017). doi:10.1007/978-1-4939-7240-1\_25.
414. Miao, W. Electrogenenerated chemiluminescence and its biorelated applications. *Chem. Rev.* **108**, 2506–2553 (2008).
415. Decarie, A., Drapeau, G., Closset, J., Couture, R. & Adams, A. Development of digoxigenin-labeled peptide: application to chemiluminoenzyme immunoassay of bradykinin in inflamed tissues. *Peptides* **15**, 511–518 (1994).
416. Hiramoto, K. *et al.* Recent advances in electrochemiluminescence-based systems for mammalian cell analysis. *Micromachines* vol. 11 (2020).
417. Senthil Kumar, S. & Bard, A. J. Background emission of electrogenerated chemiluminescence during oxidation of tri-n-propylamine from the dimeric  $^1\Delta_g$  State of  $O_2$ . *Anal. Chem.* **85**, 292–295 (2013).
418. Wang, M. *et al.* Signal-on electrochemiluminescence biosensor for microRNA-319a detection based on two-stage isothermal strand-displacement polymerase reaction. *Biosens. Bioelectron.* **107**, 34–39 (2018).
419. Global aptamers market size, share, trends, COVID-19 impact and growth analysis report – segmented by type, application, end user and region - industry forecast (2020 to 2025). *Market Data Forecast* <https://www.marketdataforecast.com/market-reports/aptamers-market> (2020).
420. Largy, E. & Gabelica, V. Native hydrogen/deuterium exchange mass spectrometry of structured DNA oligonucleotides. *Anal. Chem.* **92**, 4402–4410 (2020).
421. Brodbelt, J. S., Morrison, L. J. & Santos, I. Ultraviolet photodissociation mass spectrometry for analysis of biological molecules. *Chem. Rev.* **120**, 3328–3380 (2020).
422. Paul, D. *et al.* Probing ligand and cation binding sites in G-quadruplex nucleic acids by mass spectrometry and electron photodetachment dissociation sequencing. *Analyst* **144**, 3518–3524 (2019).
423. Yoo, J., Winogradoff, D. & Aksimentiev, A. Molecular dynamics simulations of DNA–DNA and DNA–protein interactions. *Curr. Opin. Struct. Biol.* **64**, 88–96 (2020).



## Acknowledgements

After more than four years my time as a PhD student is coming to an end. Throughout these years I was surrounded by people who supported me and I had the chance to collaborate with several people.

First of all, I would like to thank my two promotors: Karolien De Wael and Frank Sobott. **Karolien**, I am grateful for the support you provided throughout the years and for involving me in so many projects within the group. I believe that without you I would not have finished this PhD successfully. You always pushed me towards believing more in myself and made sure I focused on the things that were actually working instead of everything that did not work. **Frank**, without you I would never have started my PhD. I'm grateful that you provided me this opportunity and that you made me familiar with the mass spectrometry world. Thank you for believing in me and being optimistic about every project. I also appreciated the opportunities to go to so many different conferences and workshops throughout the years.

I would also like to thank **Rani** for being there all the years. I could always come to your office for any question, to share my frustrations or for our next attempt to organize the lab. I will also never forget all the trips we made together. More than the conferences themselves, I will remember us trying to get home from Cabourg, us running for our flight in Tel Aviv, our attempt to visit Lisbon in one day, our road trip in the USA and so much more.

**Giulia**, I really enjoyed working with you and yes, we do make a perfect team. Although our projects were not always as successful, we never gave up thanks to your never-ending motivation. Thank you for all your encouraging messages and for being the perfect tour guide when we visited your home town. **Rocio**, although we were not working that long together, I always looked forward to our next day of experiments. Even before we started, I knew it would be fun and we would laugh together. **Rui**, thank you for answering all my silly questions on electrochemistry and immobilizing DNA. I admire your way of always being positive in the lab.

Although I shared an office with many people over the years, I would especially like to thank Fabio and Sara. **Fabio**, the two of us were long the aptamer people of the group. Thank you for (sometimes) struggling with the aptamers together and for all the days

at the ITC we spent together. **Sara**, thank you for all our talks and for the chocolate you provided me when needed.

Of course my gratitude also goes to all the other present and past members of the AXES and BAMS research groups. From BAMS I would especially like to thank **Jeroen** for helping me out with instrument-related issues and **Glenn** for keeping the lab running. The AXES group grew so much over the years that it is impossible to mention everyone by name. If I needed to name one person it would be **Oli** for always providing help when needed and doing that many aptamer orders for me.

Next, I would like to thank **Pieter** for trusting me with the ITC instrument and for your guidance on the many days I was in the lab performing experiments. Also a special thanks to **James** and **Rachel** for helping me out in the lab during my many research stays at the University of Leeds.

I would also like to thank my collaborators of different projects. First, **Anne-Mare de Vries**, **Annemieke Madder** and **José Martins** for the many discussions about aptamers and the insights you provided with the NMR experiments. I'm really proud of our joint effort to aim for a better aptamer characterization. Next, **Tom Vennekens** and **Thomas De Vijlder** for the opportunity to perform the ETD experiments with you and for your guidance on the days I came over to J&J for measurements. Furthermore, I can also not forget **Ahmad Ali-Ahmad** and **Nikolina Sekulić**. Your expertise on the nucleosomes improved the work tremendously. **Konstantin Barylyuk**, thank you for joining me to perform the nucleosome experiments and for your valuable feedback. Finally, **Valérie Gabelica** for providing me the opportunity to do a research stay in your group and **Stefano Piccolo** for your guidance in the lab and the fun moments we had in Bordeaux and Antwerp.

I would like to thank the other members of my PhD committee, **Filip Lemière**, **Sylvia De Wilde** and **Yann Sterckx**, and my remaining jury members, **Pascal Gerbaux** and **Thomas De Vijlder**, for taking the time to read my thesis and provide feedback.

Of course there is also my family and friends who I'm grateful for their support throughout the years. Special thanks to my **dad** for always cheering me up with stupid jokes. Also, **mom**, thank you for overwhelming me with food.

And then there is **Mats**. I never imagined we would be where we are now the first time I saw you. Words cannot describe how grateful I am to have you by my side. I went through a lot of ups and downs the past years and you were always there to support me. You can manage my happy crazy times and laugh with my stupid jokes but you can also comfort me and make me smile again every time when I feel sad. I'm sure I wouldn't have finished this without you.



# ELISE DAEMS



Elise Daems  
Keizershofstraat  
2250 Olen  
Belgium



June 30, 1993 | Mol  
elise@daems.eu  
Belgian

7

Peer-reviewed  
publications

6

International  
research stays

9

Conference/workshop  
contributions

## WORK EXPERIENCE

Jan 2017 – current

### Researcher in bioanalytical chemistry

University of Antwerp | Wilrijk, Belgium



*Characterization of biomolecules, mainly oligonucleotides, using e.g. native IM-MS and ITC: experiments & data analysis.*



*6 publications (in e.g. J. Am. Chem. Soc.), 1 manuscript submitted and 2 in preparation.*



*Active participation workshops/conferences in Belgium, France, The Netherlands, UK, and the USA.*



*Supervision of student practicum and guidance of two students (bachelor & Erasmus).*

Sep 2016 – Dec 2016

### Academic assisting personnel (AAP) | 30 %

University of Antwerp | Wilrijk, Belgium

*Preparation and supervision of student practicum.*

Summers 2011 – 2014

Student job: secretariat employee

Belgonucleaire | Dessel, Belgium

*From making copies to arranging work permits for employees.*



## LANGUAGES



## TECHNICAL SKILLS

Native mass spectrometry  
Ion mobility spectrometry  
Isothermal titration calorimetry  
Electrochemical impedance spectroscopy  
Oligonucleotide characterization

## COMPUTER SKILLS

Origin	MS Office
MassLynx	Illustrator
DriftScope	NOVA 2

## EDUCATION

---

*Jan 2017 – current*

PhD fellow in **Chemistry** | FWO-SB Fellowship  
AXES and BAMS research groups  
University of Antwerp | Wilrijk, Belgium

*Sep 2014 – Jun 2016*

Master of Science in **Chemistry** | Great Distinction  
University of Antwerp | Wilrijk, Belgium

*Sep 2011 – Jul 2014*

Bachelor of Science in **Chemistry** | Distinction  
University of Hasselt | Diepenbeek, Belgium

## PUBLICATIONS

---

\* Joint first authors

G. Moro\*, H. Barich\*, K. Driesen\*, N.F. Montiel\*, L. Neven\*, C.D. Mendonça\*, S.T. Shanmugam\*, **E. Daems\*** and K. De Wael. Unlocking the full power of electrochemical fingerprinting for on-site sensing applications. *Anal. Bioanal. Chem.* 2020, 412, 5955–5968.

M. Leemans, C. Galicia, E. Deyaert, **E. Daems**, L. Krause, J. Paesmans, E. Pardon, J. Steyaert, A. Kortholt, F. Sobott, D. Klostermeier and W. Versees. Allosteric modulation of the GTPase activity of a bacterial LRRK2 homolog by conformation-specific Nanobodies. *Biochem J.* 2020, 477, 7, 1203–1218.

F. Bottari\*, **E. Daems\***, A. de Vries\*, P. Van Wielendaele, S. Trashin, R. Blust, F. Sobott, A. Madder, J.C. Martins and K. De Wael. Do aptamers always bind? The need for a multi-faceted analytical approach when demonstrating binding affinity between aptamer and low molecular weight compounds. *J. Am. Chem. Soc.* 2020, 142, 46, 19622–19630.

**E. Daems**, D. Dewaele, K. Barylyuk, K. De Wael and F. Sobott. Aptamer-ligand recognition studied by native ion mobility mass spectrometry. *Talanta* 2021, 224, 121917.

**E. Daems\***, G. Moro\*, H. Berghmans, L.M. Moretto, A. Angelini, S. Dewilde, S. Sobott and K. De Wael. Native mass spectrometry for the design and selection of protein bioreceptors for perfluorinated compounds. *Analyst* 2021, 146, 2065-2073.

L. Maso, M. Trande, S. Liberi, G. Moro, **E. Daems**, S. Linciano, F. Sobott, S. Covaceuszach, A. Cassetta, S. Fasolato, L.M. Moretto, K. De Wael, L. Cendron and A. Angelini. Unveiling the binding mode of perfluorooctanoic acid to human serum albumin. *Protein Sci.* 2021, 30, 4, 830-841.

**E. Daems\***, G. Moro\*, R. Campos and K. De Wael. Mapping the gaps in chemical analysis for the characterisation of aptamer-target interactions. *Trends Analyt. Chem.* 2021, 142, 116311.

R. Cánovas\*, **E. Daems\***, R. Campos, F. Sobott and K. De Wael. Proof-of-concept electrochemiluminescent assay for the aptamer-based detection of small molecules. Submitted to *Biosens. Bioelectron.*

## CONFERENCES & CONTRIBUTIONS

---

Nucleic Acids Forum 2018 | London, UK – Attended  
66th ASMS Annual Meeting 2018 | San Diego, USA – Oral presentation  
Astbury Conversation 2018 | Leeds, UK – Poster  
BSMS Annual Meeting 2018 | Liege, Belgium – Poster  
Dutch Biophysics 2017 | Veldhoven, The Netherlands – Poster  
Aptamers in Bordeaux 2017 | Bordeaux, France – Poster  
BMSS Annual Meeting 2017 | Manchester, UK – Poster  
BSMS Annual Meeting 2017 | Leuven, Belgium – Poster

## RESEARCH STAYS

---

Oct 2019 (1 week)	Astbury Centre – MS facility   University of Leeds   Leeds, UK Native IM-MS of nucleosome tetramers and octamers.
Sep 2018 (1 week)	Astbury Centre – MS facility   University of Leeds   Leeds, UK Native IM-MS of a canonical nucleosome and multiple variants.
Jul 2018 (2 weeks)	Astbury Centre – Stonehouse group   University of Leeds   Leeds, UK Synthesizing large RNA and learning how to handle it.
Jun 2018 (1 week)	INSERM – Gabelica Group   IECB   Bordeaux, France Understanding the behavior of aptamers in the gas-phase using native IM-MS.
Apr 2018 (1 week)	Astbury Centre – MS facility   University of Leeds   Leeds, UK Fast photochemical oxidation of aptamers.
Jan 2018 (1 week)	Astbury Centre – MS facility   University of Leeds   Leeds, UK Fast photochemical oxidation of aptamers.

## COURSES & WORKSHOPS

---

2020, 3 days	Course Solicitation techniques University of Antwerp   Antwerp, Belgium
2018, 2 days	Course Analytic Storytelling University of Antwerp   Antwerp, Belgium
2017, 4 days	Course Writing Academic Papers University of Antwerp   Antwerp, Belgium
2017, 5 days	Structural Mass Spectrometry Workshop Weizmann Institute of Science   Rehovot, Israel – Oral presentation
2016, 3 days	Top Down and Structural Mass Spectrometry: practical course University of Lisbon   Lisbon, Portugal
2016, 4 days	Thematic school: Ion Mobility Mass Spectrometry Cabourg, France – Poster